TECTONIC EVOLUTION OF THE SOUTH TIBETAN DETACHMENT SYSTEM, BHUTAN HIMALAYA

by

Dawn Anne-Marie Kellett

Submitted in partial fulfillment of the requirements
for the degree of Doctor of Philosophy

at

Dalhousie University
Halifax, Nova Scotia
August 2010

DALHOUSIE UNIVERSITY

DEPARTMENT OF EARTH SCIENCES

The undersigned hereby certify that they have read and recommend to the Faculty of Graduate Studies for acceptance a thesis entitled "TECTONIC EVOLUTION OF THE SOUTH TIBETAN DETACHMENT SYSTEM, BHUTAN HIMALAYA" by Dawn Anne-Marie Kellett in partial fulfillment of the requirements for the degree of Doctor of Philosophy.

Dated: August 12, 2010

External Examiner: _____
B. Clark Burchfiel

Research Supervisor: _____
Djordje Grujic

Examining Committee: _____
Rebecca Jamieson

_____
Isabelle Coutand

_____
John Gosse

_____

DALHOUSIE UNIVERSITY

DATE: August 12, 2010

AUTHOR: Dawn Anne-Marie Kellett

TITLE: TECTONIC EVOLUTION OF THE SOUTH TIBETAN DETACHMENT SYSTEM, BHUTAN HIMALAYA

DEPARTMENT OR SCHOOL: Department of Earth Sciences

DEGREE: PhD CONVOCATION: May YEAR: 2011

Permission is herewith granted to Dalhousie University to circulate and to have copied for non-commercial purposes, at its discretion, the above title upon the request of individuals or institutions.

_____

Signature of Author

TABLE OF CONTENTS

LIST OF TABLES

LIST OF FIGURES

ABSTRACT

Syn-convergent low-angle normal-sense detachments (LANDs) are found in many orogens around the world. However, those tectonic processes which result in their formation are little known. The South Tibetan detachment system (STDS) is the best-studied example worldwide of a syn-convergent LAND, and formed in the Miocene due to the continental collision of India and Asia. In Bhutan, eastern Himalaya, the STDS is duplicated.

Here I investigate the tectonic history of the inner STDS and particularly the outer STDS in Bhutan, to determine whether the duplicated STDS can be explained by or used to constrain models of Himalayan orogenesis. A range of geochronometric, thermochronologic, petrologic, structural, thermobarometric, thermometric, and isotopic tools are used to constrain: the onset and cessation of motion on the outer STDS; the cessation of motion on the inner STDS; the peak metamorphic conditions in the hanging wall and footwall of the outer STDS; the pressure-temperature-time paths of tectonites in the hanging wall and footwall of the outer STDS; the structural history of the hanging wall rocks of the outer STDS, and; the paleogeographic affinity of the hanging wall rocks of the outer STDS.

The results of these studies are compared to thermo-mechanical models of Himalayan-type continental collision. Similarities in model predictions of the type and timing of structures, peak metamorphic conditions of hanging wall and footwall tectonites, pressure-temperature-time paths, and other regional tectonic observations lead to two main conclusions. 1. The STDS is a system of three main types of LANDs: those that formed during channel flow of low-viscosity mid-crustal rocks, those that formed by extrusion of cooled channel rocks to the surface, and those that formed by destabilization of the upper crust above a dome of mid-crustal channel rocks. 2. The STDS was duplicated by underthrusting of a crustal ramp into the Himalayan orogen since early Miocene. The underthrusting led to extrusion of a dome of weak mid-crustal above a previously-extruded channel. The crustal ramp may be local to the eastern Himalaya due to higher convergence and/or erosion rates, or due to local underthrusting of relatively strong crust behind weaker crust.

List of Abbreviations Used

Structures

STDS	South Tibetan detachment system
O-STDS	Outer South Tibetan detachment system
I-STDS	Inner South Tibetan detachment system
MCT	Main Central thrust
KT	Kakhtang thrust
MBT	Main Boundary thrust
MFT	Main Frontal thrust
MHT	Main Himalayan thrust
LAND	low-angle normal-sense detachment

Lithotectonic units

TSS	Tethyan sedimentary sequence
GHS	Greater Himalayan sequence
LHS	Lesser Himalayan sequence

ACKNOWLEDGEMENTS

I would like to thank my supervisor, Djordje Grujic, for suggesting this project, inspiring me with his fascination for the geology of the Bhutan Himalaya, supporting me both scientifically and motivationally over the years, and helping me to reach my goals. It will be a pleasure and an honour to collaborate together in the future. Also, sincere thanks to Rebecca Jamieson, who has challenged me to do my best, both on the court and in my research. Her feedback has been invaluable.

Thanks to my other coauthors Clare Warren, Saskia Erdmann and John Cottle for their interest, encouragement, suggestions, and critical reviews. I also appreciate the guidance and feedback that I received from my thesis committee over the years: Peter Reynolds, Rebecca Jamieson, Nick Culshaw, Isabelle Coutand, Mladen Nedimovic.

The following people contributed to individual chapters of this thesis, whether by teaching me a new technique, critically reviewing my writing, engaging me in scientific discussion or assisting me with analyses:

Chapter 2 J. Wooden, F. Mazdab, P Reynolds, K. Taylor, D. Wheeler, A. Grist, Y. Kettanah, I. Coutand, C. Warren, Y. Fedortchouk, R. Carosi, and U. Ring.

Chapter 3 N. McQuarrie, P. Stoffyn, D. Macdonald, M. Horstwood, R. Parrish, L. Ritchie, D. Moynihan, K. Larson, U. Ring, C. Groppo and D. Whitney.

Chapter 4 R. Jamieson, O. Beyssac, I. Coutand, C. Warren, L. Hilchie, K. Hewitt, N. Whynot.

Chapter 5 S. Duchêne, I. Coutand, C. Warren, K. Zoeller.

Chapter 6 R. Jamieson, C. Beaumont.

I am grateful for the support and friendship I received from our Bhutan field crews, and in particular the leadership, good judgement and interest in geology shown by Lhawang Dorji and Tashi Tenzin. Thanks also to the Bhutan Geological Survey for providing me with access to my field areas.

My research was funded by many organizations, including the Natural Science and Engineering Research Council, the Killam Foundation, the Geological Society of America, and the Mineralogical Association of Canada.

I am filled with great memories from my years spent in Halifax with the grad students and post-docs of the LSC, especially Sofie and Konstanze.

I would like to dedicate this thesis to my family, who have loved and supported me throughout my life, and to Ramón, for helping me find something worth celebrating every day, and for encouraging me to focus on the important things.

CHAPTER 1

INTRODUCTION

1.1 GENERAL INTRODUCTION

The South Tibetan detachment system (STDS) is a set of normal-sense structures that cuts through some of the highest peaks on Earth, including Dhaulagiri (Fig. 1.1a), Annapurna, Everest (Fig. 1.1b), and several others. It is located at the crest of the Himalayan mountains (a chain of peaks extending over 2000 km in length, and in places exceeding 8 km in elevation above sea level) where the steep, deeply-incised southern front of the Himalayan mountain chain changes to the broad, undulating high-altitude hills of the Tibetan plateau (Fig. 1.2). In the Kingdom of Bhutan, eastern Himalaya, rocks deformed by the South Tibetan detachment system are accessible at intermediate altitudes (2500-4500 m above sea level) by trekking (Fig. 1.3a) and by road (Fig. 1.3b). In this PhD thesis, I have investigated the STDS in Bhutan in order to understand its contribution to the tectonic evolution of the eastern Himalaya, and how this system of normal structures formed during active convergence in a collisional orogen.

1.1.1 HIMALAYAN OROGEN

The Himalayan-Tibetan orogen is forming as the result of the continental collision of India with Asia following closure of the intervening Tethyan Ocean, and is regarded as the modern-day type example of a large-scale continent-continent collisional orogen (Fig. 1.4a). The timing of initiation of continental collision is bracketed at ∼55-50 Ma (review in Yin, 2006). The southern flank of the orogen, which is hereafter referred to as the Himalaya, or the Himalayan orogen, forms a large-scale, dominantly south-propagating fold and thrust system comprising rocks that were originally deposited on India's northern

Figure 1.1: STDS in central and eastern Nepal. (a) View to the west from Poon Hill, Annapurna region, central Nepal. Shallowly north-dipping rocks of the STDS cut through Dhaulagiri (8167 m) (photo by D. Kellett). (b) View to the east (photo has been flipped) from the west moraine shoulder of the Ngozumba glacier, eastern Nepal. Shallow dip of the STDS cutting through Mt. Everest (8848 m) and Lhotse, eastern Nepal (photo by D. Grujic).

Figure 1.2: STDS in northern Sikkim, India. Panoramic view of the STDS, separating rolling hills of the Tibetan plateau to the north (left) from steep snow-covered peaks of the Himalaya to the south (right), Sikkim-Tibet border, ∼50 km west of Bhutan (photo by D. Kellett).

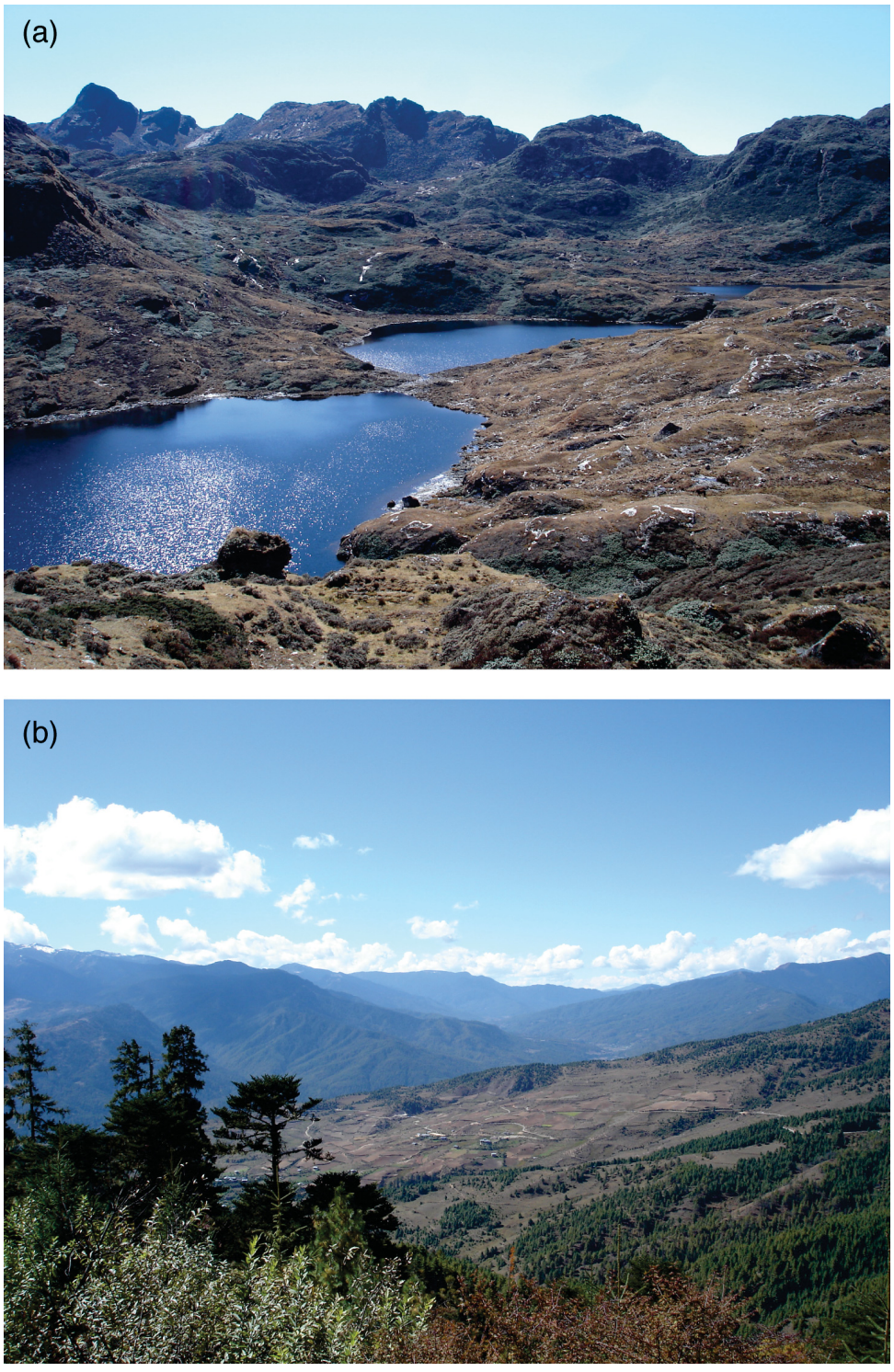

Figure 1.3: STDS in Lingshi and Ura areas, Bhutan. (a) The dip-slope surface of the STDS exposed north of the Druk Path trekking route in the Lingshi klippe, northwest Bhutan. (b) View of the main road passing through the STDS close to the town of Ura, Ura klippe, central Bhutan. These two field locations are discussed in detail in Chapter 2. Photos by D. Kellett

margin (Fig. 1.4b). Crustal thickening and metamorphism followed initial collision, during Eocene to Late Oligocene (Hodges et al., 1996; Godin et al., 2001). This was followed in Early Miocene by the exhumation of material from mid-crustal depths to the southern Himalayan topographic front (Vannay and Hodges, 1996; Hodges et al., 1996).

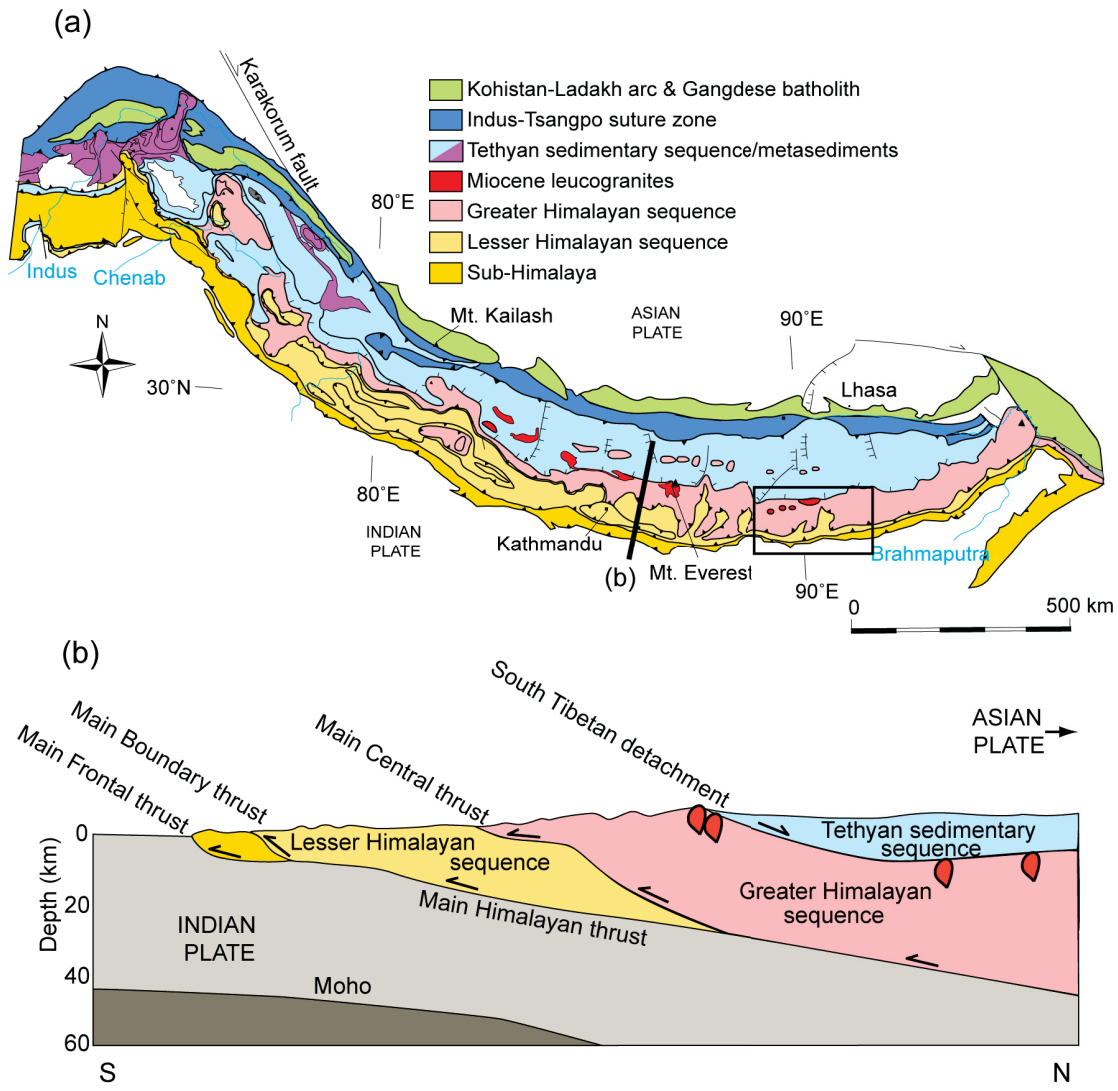

Figure 1.4: (a) Geological map of the Himalayan orogen. Main lithotectonic units and structures are labeled. Adapted from Guillot et al. (2008). (b) Generalized cross-section across the Himalaya. Approximate section line is through central Nepal. Adapted from Hodges et al., 2000.

The structure of the Himalaya summarized below is based on Le Fort (1975) and Hodges (2000). It is characterized by southward-propagating thrusts rooting into a common basal detachment, the Main Himalayan thrust (MHT), as well as one orogen scale

normal-sense detachment system (Fig. 1.4b; Nelson et al., 1996). These structures bound the major lithotectonic units of the Himalaya. The northernmost assemblage, the Tethyan sedimentary sequence (TSS) (also referred to as Tibetan Series, Tibetan sedimentary sequence), is bounded to the north by the India-Asia boundary, the Indus-Yarlung (also Indus-Tsangpo, Indus-Yalu) suture zone. Structurally beneath the TSS are high-grade metamorphic rocks, the Greater Himalayan sequence (GHS) (also referred to as High Himalayan crystalline, Tibetan slab). The boundary between the TSS and the GHS is the STDS, a top-to-the-north normal-sense shear zone. Although it was originally thought to root into the MHT, geophysical data indicate that the STDS may in fact level off more shallowly in the upper- to mid-crust (Fig. 1.4b; Nelson et al., 1996). In places, metasedimentary rocks are exposed between strands of the STDS. Locally these rocks are termed the Chekha Group (Bhutan), the Everest Series (eastern Nepal), the Annapurna Yellow Formation (central Nepal) and the Haimantas Group (NW India) (Fig. 1.4a). The sedimentary Lesser Himalayan sequence (LHS) crops out further to the south, and is separated from the GHS by the Main Central thrust (MCT). The LHS is separated from the Subhimalaya, the deformed foreland basin of the orogen, by the Main Boundary thrust (MBT). The youngest and southernmost thrust of the Himalayan orogen is the active Main Frontal thrust (MFT).

Between the STDS and the India-Asia suture, high-grade metamorphic rocks and granites are exposed in a lateral belt of tectonic windows through the TSS (Fig. 1.4a; Burg et al., 1984b). These gneiss and granite domes are collectively called the North Himalayan gneiss domes, and the exposed rocks may be derived from Indian crust, of GHS affinity (e.g., Lee et al., 2000; Lee et al., 2004; Kawakami et al., 2007).

1.1.2 TECTONIC MODELS OF THE HIMALAYAN OROGEN

Although there is significant orogen-parallel deformation within the greater Himalayan-Tibetan orogen, convergence between India and Asia is largely accommodated in the Himalaya by orogen-perpendicular deformation (Tapponier et al., 2001; Andronicos et al., 2007; Meade, 2007). Models attempting to describe the deformation history of the orogen-perpendicular deformation of the Himalaya should account for all first-order orogen-perpendicular characteristics of the orogen, including: coeval normal- and reverse-sense shear zones bounding the GHS (the STDS and MCT, respectively); an inverted metamorphic sequence across the upper LHS and lower GHS; migmatization of the

GHS; the emplacement of leucogranites at the top of the GHS and into the overlying metasedimentary rocks; the emergence of domes south of the suture and; the preservation of klippen of upper-crustal rocks on top of the GHS (particular to the eastern Himalaya) (Fig. 1.4b; Hodges, 2000; Beaumont et al., 2001). Main end-member models for the evolution of the Himalayan orogen include critical taper models (e.g., Avouac, 2003; Bollinger et al., 2006; Fig. 1.5a) and channel flow models (e.g., Grujic et al., 1996; Beaumont et al., 2001; 2004; 2006; Jamieson et al., 2004; Fig. 1.5b).

Critical taper theory has been successfully used to describe the deformation of plastic frictional material into thin-skinned foreland fold-and-thrust belts and accretionary wedges (Fig. 1.5a, b) (e.g., Boyer and Elliott, 1982). Deformation occurs within a wedge defined by a hinterland-dipping basal detachment and a foreland-dipping topographic surface, and is dominated by foreland-propagating stacked thrusts and fault-bend folds (Dahlen, 1990). The balance of friction at the base of the wedge, erosion, addition of material to the toe of the wedge, rock strength and rate of shortening all interact to influence deformation within the wedge (Dahlen, 1990). The orogen should respond to perturbations in the taper angle, which can occur as a result of changes of any of the above parameters, by propagating thrusting on a new fault in the foreland (in the case of an increase in the taper angle) or by out-of-sequence thrusting in the interior of the orogen (in the case of a decrease in the taper angle) to reestablish the critical taper angle. Critical taper principles have been used in both kinematic models (e.g., Avouac, 2003; Bollinger et al., 2006; Robinson, 2008) and conceptual models (e.g., Yin, 2006; Webb et al., 2007) of the Himalaya, particularly to describe inverted metamorphism and deformation of the LHS and the GHS and movement on the MCT and MBT (e.g., Harrison et al., 1998; Bollinger et al., 2006), but also to describe the orogen as a whole (e.g., Robinson et al., 2006).

Channel flow theory, developed using internally-consistent thermal-mechanical numerical models, has also been applied to the Himalaya (Fig. 1.5c). Results from several viscous channel flow models with boundary conditions similar to the Himalayan orogen have been published (e.g., Model 3—Beaumont et al., 2001; HT1—Beaumont et al., 2004; Jamieson et al., 2004; HT111—Jamieson et al., 2006). In a large, hot orogen, melt-weakened, mid-crustal material bounded by stronger upper and lower crustal layers flows subject to a gravitational pressure gradient towards the foreland. Focused surface denudation can provide a positive feedback to maintain imbalance in the pressure gradient

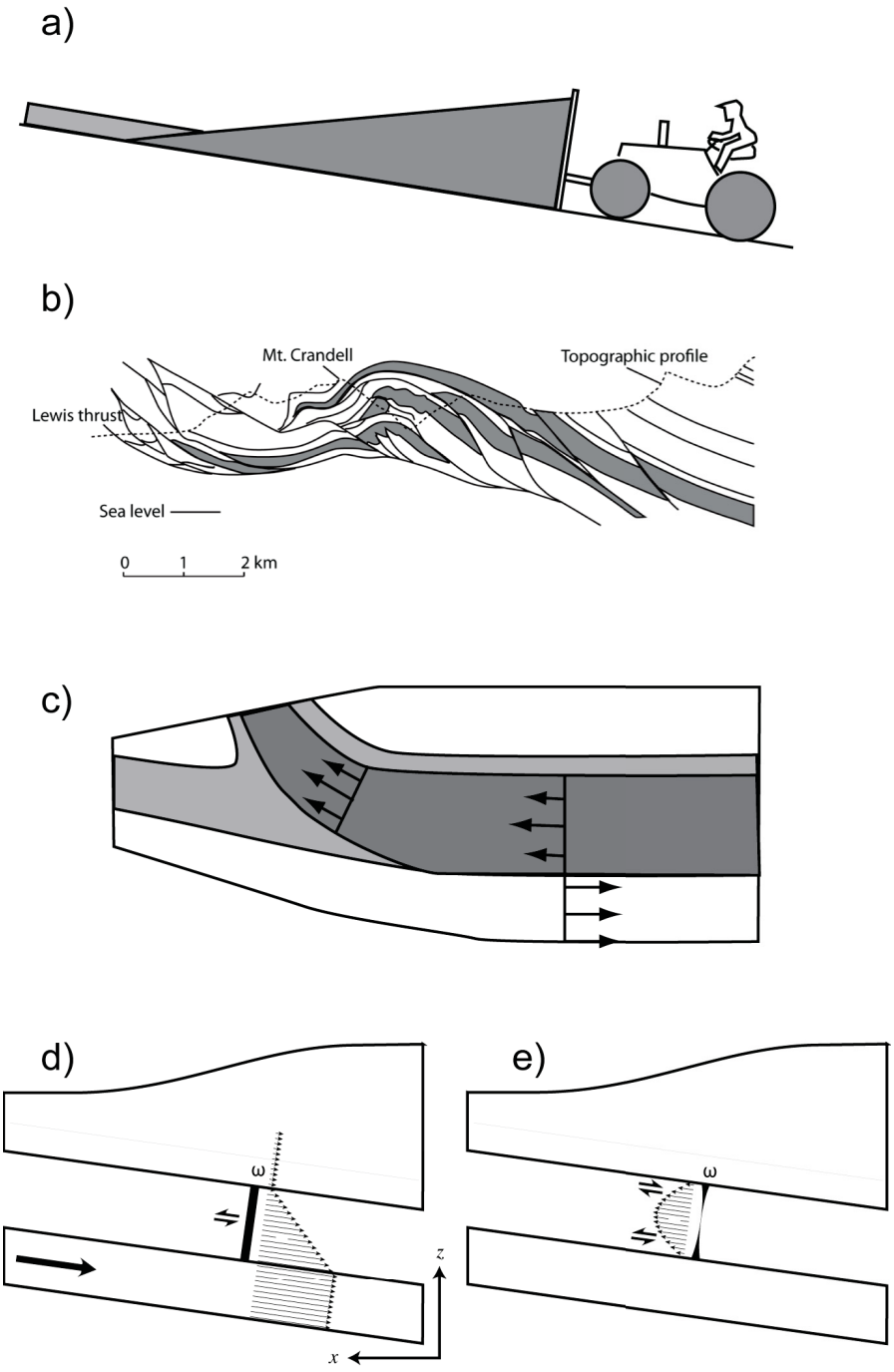

Figure 1.5: End-member models for formation of the Himalayan orogen. (a) Critical taper wedge (image shown from Dahlen, 1990) and (b) example of a foreland fold and thrust belt which can be described as a critical taper wedge (Boyer and Elliott, 1982). (c) Channel flow (adapted from Beaumont et al., 2001) produced by relative components of (d) Couette flow and (e) Poiseuille flow (adapted from Grujic, 2006). Arrows in (c)-(e) are relative velocities of particles within the channel. Shear sense experienced by these particles is indicated in (d) and (e). Bars in (d) and (e) indicate absolute vorticity (ω) values.

and sustain flow. Channel flow is composed of two end-member flow types: Couette and Poiseuille (Fig. 1.5d and e, respectively). Couette flow produces a uniform vorticity across the channel because of the displacement of one channel bounding surface relative to the other, while Poiseuille flow, or "pipe flow" yields the highest velocities in the centre of the channel, no velocity at the boundaries of the channel and a reversal in vorticity from the top to the bottom of the channel (Turcotte and Schubert, 1982; Grujic, 2006).

Channel flow models have been used to describe the evolution of the Himalayan orogen as follows: following the collision of India and Asia, there was a period of crustal shortening and thickening. The decay of radiogenic material in sedimentary rocks buried to mid-crustal depths (tectonically accreted radiogenic material, or TARM; Jamieson et al., 1998) began to produce heat. Over a period of $\sim$20 Ma, thermal evolution brought mid-crustal rocks to partial-melting conditions ($\geq$ 700 °C), significantly reducing their viscosity. The gravitational potential energy difference between the thickened hinterland plateau crust ($\sim$75-80 km) and the "normal" thickness foreland crust ($<$40 km) resulted in an outward lateral flow of the weakened material in a mid-crustal channel bounded by more rigid crustal layers. The upper shear zone boundary to this flow exhibits normal-sense shear, while the lower shear zone boundary exhibits thrust-sense shear (the STDS and MCT, respectively). Focused erosion at the southern flank of the orogen (attributed to the Indian summer monsoon) allowed for the extrusion of mid-crustal channel rocks and eventual exhumation to the surface along the coeval yet opposite-sense shear zones, with the upper boundary exhibiting normal-sense displacement.

1.1.3 Geology of the Bhutan Himalaya

The Eastern Himalaya, particularly Bhutan, shares many characteristics common to the rest of the orogen (Fig. 1.6). However, there are some key distinguishing features. Firstly, Bhutan is dominated by exposure of GHS metamorphic rocks (Fig. 1.6). This is partly due to the shallow dip of the metamorphic package as well as an out-of-sequence thrust, the Kahktang thrust (Fig. 1.6), which duplicates the thickness of the GHS in at least the central part of the country (Grujic et al., 2002). Secondly, the STDS is duplicated in Bhutan. At the northern border of Bhutan and in southern Tibet, the STDS places Paleozoic unmetamorphosed rocks in the hanging wall against high-grade gneiss in the footwall (Burchfiel et al., 1992; Edwards et al., 1996; Edwards et al., 1999). However, to the south, several broad, non-cylindrical synclines within the GHS preserve erosional

klippe in their cores. These erosional klippe contain Chekha Group and TSS rocks, and are soled by top-to-the-north shear zones, and thus have also been identified as preserved segments of the STDS (Grujic et al., 2002). In an orogen-wide review of the STDS, more northern, brittle-ductile structures of the STDS were described as upper STD, while more southern, ductile structures of the STDS were described as lower STD (Godin et al., 2006a). According to this grouping, upper STD structures are younger than lower STD, both were active in the Miocene, and they are distinct structures, not duplications of a single structure. The STDS preserved in erosional klippe in Bhutan has been tentatively described as the lower STD, while the STDS at the northern border of Bhutan has been described as the upper STD (Fig. 1.6) (Hollister and Grujic, 2006).

1.1.4 TESTING MODELS OF CONTINENTAL COLLISION

A range of pressure-temperature-time paths traveled by model points have been published for Himalayan-type channel flow models HT1 (Jamieson et al., 2004) and HT111 (Jamieson et al., 2006). These studies have been used to compare the provenance, metamorphic histories and cooling histories of the LHS, the GHS and the TSS with their model equivalents. The models have also been used to make predictions about the location, timing and kinematics of the MCT and the STDS. Channel flow model predictions indicate that the lower STD is a broad and diffuse shear zone with a range of PTt paths, forming the upper boundary to a channel of partially-melted mid-crustal rocks. Since finite-element models cannot model brittle structures (i.e. discontinuities), the behaviour of structures such as the upper STD, MBT and MFT may not be resolvable from these models.

Although some critical taper models (e.g., Bollinger et al., 2006) do not include the STDS structure in their models, others do. By examining kinematic and/or conceptual models, comparisons with their interpreted evolution of the STDS may be possible. In these models, the STDS, if included, is typically considered to be a thrust fault reactivated as a passive roof fault beneath which the GHS is transported southwards on the MCT (e.g., Robinson et al., 2006; Yin, 2006; Webb et al., 2007). In models for which the STDS and MCT meet in the up-dip direction (e.g., Yin, 2006), the two structures are described as forming a triangle zone (Price, 1986) around the GHS, while in models for which the STDS and MCT meet in the down-dip direction, the two structures bound an extruding wedge (e.g., Royden and Burchfiel, 1987). Kinematic critical taper models must be treated with some caution, however, as dynamical numerical modeling has demonstrated that

Figure 1.6: Geological map of the Bhutan Himalaya. Adapted from Gansser (1983); Grujic et al. (2002); Koike et al. (2002); Chakungal (2006); Long and McQuarrie (2010); Long et al. (*in review*); Tobgay et al. (*in review*); and including all mapping described in this thesis. Boxed areas indicate main study areas of this thesis. Large white dots indicate D. Kellett station locations (described in Appendix A). Small black dots indicate station locations from the Dalhousie Himalayan research working group. All other areas of the map are interpreted and integrated where necessary from the above references.

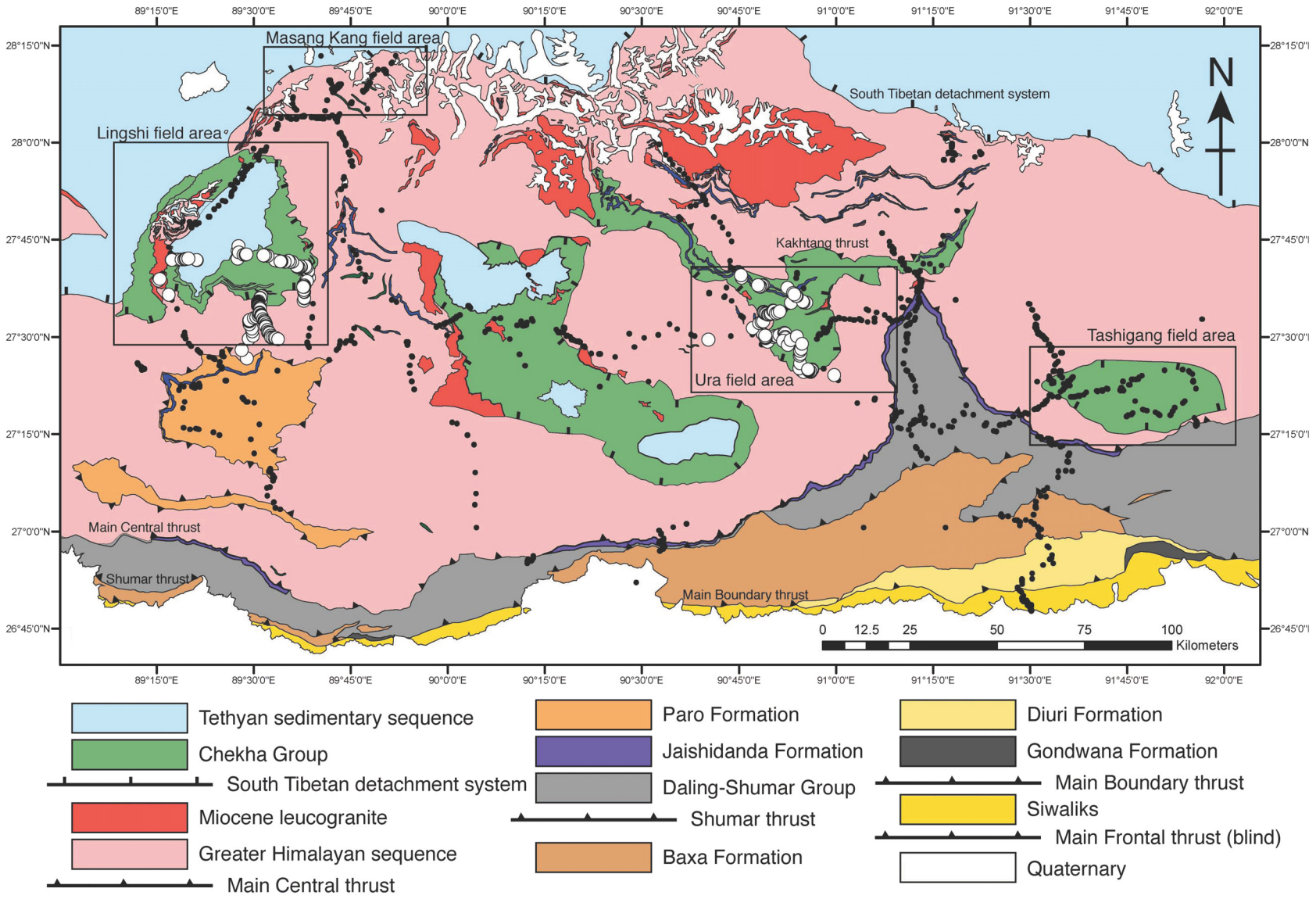
Masang Kang field area
Lingshi field area
South Tibetan detachment system
Kakhtang thrust
Ura field area
Tashigang field area
Main Central thrust
Shumar thrust
Main Boundary thrust
N
0 12.5 25 50 75 100
Kilometers
89°15'0"E
89°30'0"E
89°45'0"E
90°0'0"E
90°15'0"E
90°30'0"E
90°45'0"E
91°0'0"E
91°15'0"E
91°30'0"E
91°45'0"E
92°0'0"E
28°15'0"N
28°0'0"N
27°45'0"N
27°30'0"N
27°15'0"N
27°0'0"N
26°45'0"N
Tethyan sedimentary sequence
Chekha Group
South Tibetan detachment system
Miocene leucogranite
Greater Himalayan sequence
Main Central thrust
Paro Formation
Jaishidanda Formation
Daling-Shumar Group
Shumar thrust
Baxa Formation
Diuri Formation
Gondwana Formation
Main Boundary thrust
Siwaliks
Main Frontal thrust (blind)
Quaternary

structures such as the STDS do not form in critical taper Coulomb wedges under a wide range of model parameter values (Willett, 1999a).

1.2 BACKGROUND: LOW-ANGLE NORMAL-SENSE DETACHMENTS

The formation of normal-sense structures at low angles ($\leq 30^\circ$ dip) is an apparent contradiction of Anderson's theory of basic fault mechanics, which predicts that normal-sense structures will form at approximately 60° dip angles, while low-angle structures should be thrust sense (Fig. 1.7) (Anderson, 1951). For this reason, early geologists did not recognize low-angle normal sense detachments (LANDs, also sometimes referred to as LANFs - low-angle normal faults) in the field until the 1970's and 1980's (e.g., Armstrong, 1972; Davis and Coney, 1979; Wernicke and Burchfiel, 1982).

LANDs are now known to be common structures, and have been mapped in several tectonic environments (e.g., extensional provinces such as the Basin and Range, metamorphic core complexes such as those in the Cordillera, slow-spreading mid-ocean ridges such as the Mid-Atlantic Ridge, and active collisional orogens such as the Himalaya). LANDs from these different tectonic settings share many common features, including: low ($\leq 30^\circ$) dip angles; a contrast in structural style above and below the detachment; pooling of magma in the footwall at the detachment surface (often attributed to decompression melting of footwall rocks as they are denuded and indicating a thermal and rheological contrast across the detachment); and, the juxtaposition of high-grade metamorphic rocks exhumed from the middle or lower crust in the footwall against unmetamorphosed or low-grade upper crustal rocks in the hanging wall.

Some of the first studies on LANDs, in metamorphic core complexes of the Basin and Range extensional province of the southwest USA and the North American Cordillera, pointed to an exclusively extensional tectonic setting for their formation. The LANDs were interpreted to have accommodated as much as tens of kilometers of lithospheric-scale extension (e.g., Wernicke, 1981). Thirty years later, unanswered questions surrounding the formation of extensional LANDs include: their initial orientations (low-angle or high-angle) (Axen, 2007), the relationship between near-surface brittle faulting and ductilely-deformed tectonites exhumed in the footwall (Wernicke, 2009), the dynamics of coupling and decoupling of superstructure and infrastructure (Wernicke, 2009) and the amount of extension accommodated (significant or insignificant at the scale of the lithosphere) (e.g.,

Anders et al., 2006).

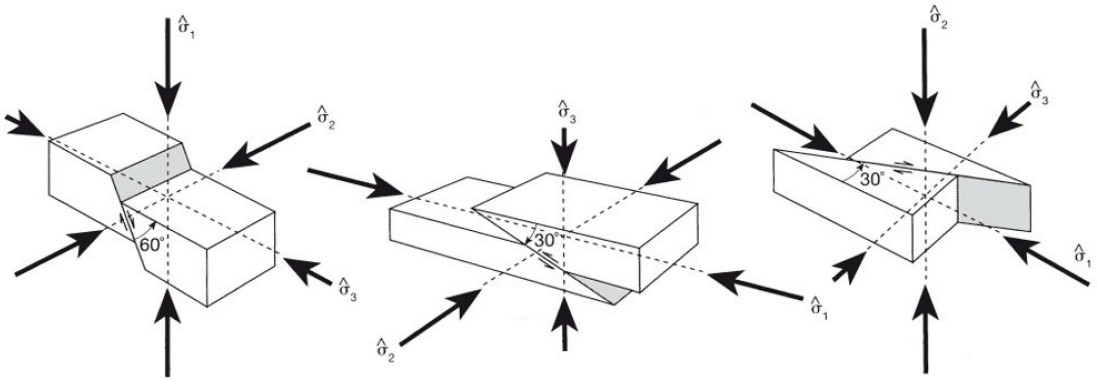

Figure 1.7: Anderson's theory of fault mechanics. In general, principal stress axes are orthogonal to or parallel to the Earths surface. Depending on the orientations of the maximum (σ_1) and minimum (σ_3) compressive stress axes relative to the surface, normal faults (a), thrust faults (b) or strike-slip faults (c) will form. Faults form at an angle of 30° from σ_1, producing high angle normal faults ($\sim$60° dip) in extensional settings, when σ_1 is sub-vertical. (Twiss and Moores, 2007).

More recently, LANDs that accompany lithospheric-scale contraction have been identified in several active and ancient orogens, including: Himalaya (e.g., Burchfiel et al., 1992); Pamir (e.g., Brunel et al., 1994); Trans-Hudson (e.g., St.-Onge et al., 2006); Canadian Cordillera (e.g., Carr et al., 1987; Brown and Gibson, 2006), and Hellenides (e.g., Xypolias and Kokkalas, 2006; Ring et al., 2007). These structures are distinct from the extensional LANDs described above because they formed during lithospheric contraction, and coevally with parallel shortening structures. The fault mechanics behind such LANDs are even more enigmatic, and studies on the longevity and coeval nature of these LANDs with parallel thrust-sense structures are still at a preliminary stage. The questions listed above pertaining to extensional LANDs also remain largely unanswered for these contractional LANDs. Perhaps the best-studied example of a contractional LAND is the South Tibetan detachment system (STDS), a network of low-angle, top-to-the-north faults and shear zones in the hinterland of the Himalayan orogen (e.g., Burg and Chen, 1984; Burchfiel et al., 1992; Hodges et al., 1992; Brown and Nazarchuk, 1993; Makovsky et al., 1996; Carosi et al., 1998; Coleman and Hodges, 1998; Wu et al., 1998; Dèzes et al., 1999; Edwards et al., 1999; Searle et al., 2003; Cottle et al., 2007; Jessup et al., 2008; this study and several others).

1.3 BACKGROUND: SOUTH TIBETAN DETACHMENT SYSTEM

The South Tibetan detachment system was first described by Burg and Chen (1984) and Burg et al. (1984a) as a normal fault that deformed leucogranites at the top of the GHS metamorphic package, and that in places juxtaposes low-grade metamorphosed Jurassic schists against staurolite-kyanite gneiss. Investigating crystallographic preferred orientations in quartz crystals within leucogranites in southern Tibet east of Bhutan, Burg et al. (1984a) demonstrated that the upper boundary of the GHS was a shear zone of gently-dipping mylonite gneisses hundreds of metres thick that had an opposite shear sense to the regional thrusting. They further demonstrated that shearing post-dated emplacement of the leucogranites, which at that time were already suspected to be produced from partial melting within the GHS above the MCT. This timing relationship demonstrated that the normal-sense structure was likely Miocene in age, and thus coeval to either the MCT or the MBT. Burg and colleagues noted the apparent incongruity of a north-directed normal-sense ductile shear zone within the south-directed thrust-sense Himalayan orogen, and explained its formation by sliding of the TSS along a gravity-driven décollement (Fig. 1.8a) (Burg et al., 1984a).

Burchfiel and Royden (1985), noting the along-strike continuity of the normal-sense structure, further suggested that it may have accommodated as much as tens of kilometers of extensional northward displacement of the TSS, and probably formed after development of the TSS fold and thrust belt and coevally with leucogranite intrusion and thrusting on the MCT or MBT. It was later confirmed that the STDS and the MCT were indeed coevally active (Hodges et al., 1992), and that the STDS extends west as far as NW India (Herren, 1987; Kündig, 1988). Burchfiel and Royden (1985) further noted that the normal faults and the MCT together could bound the GHS in a wedge geometry. They demonstrated that loading of a perfectly elastic lithosphere with a topographically high area such as the Himalaya could rotate the principal stress axes, steepening σ_1 (the maximum compressive stress) and orienting σ_2 sub-horizontally on the northern side of the topographic slope, which would favour local low-angle extension produced by gravity acting on the high topography (Fig. 1.8b). It was further suggested that a particular recumbent, north-verging fold exposed at Gyirong and Annapurna (also called Fang nappe) in the immediate hanging wall of the STDS was a product of the postulated gravity sliding.

Microstructural evidence for shear-sense reversal has been documented in the

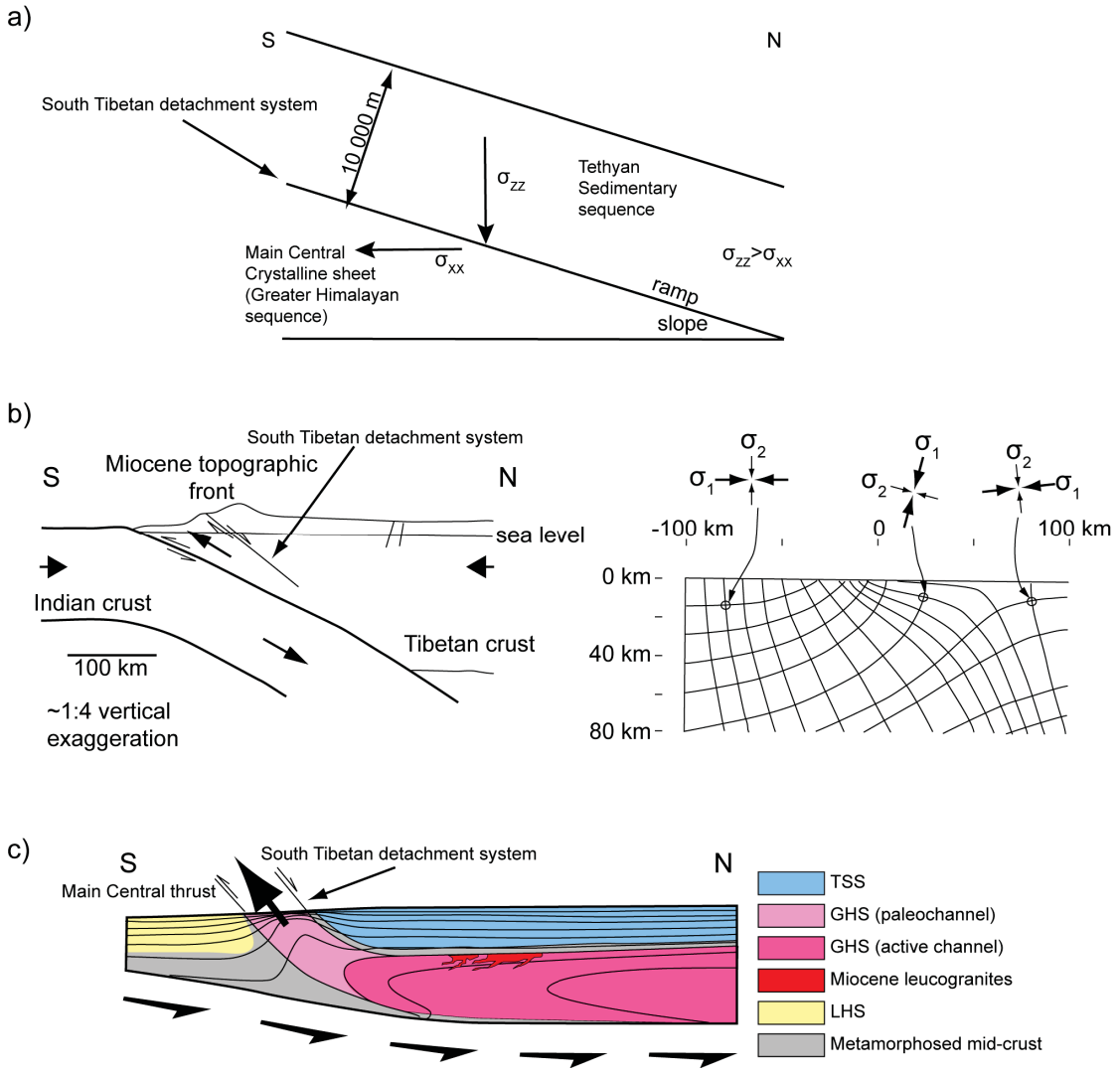

Figure 1.8: Proposed mechanisms for the formation of the STDS: (a) sliding of the TSS down a gravity-driven decollement (Burg et al., 1984a); (b) local rotation of the principal stress axes due to topographic loading favouring local extension along low-angle fault surfaces (Burchfiel and Royden, 1985); (c) channel flow of hot, low-viscosity mid-crustal material resulting a normal-sense of shear on the upper boundary of the channel (adapted from Beaumont et al., 2001).

STDS by numerous authors (Burg et al., 1984a; Burchfiel et al., 1992; Vannay and Hodges, 1996; Carosi et al., 1998; Godin et al., 2001; Grujic et al., 2002; Wiesmayr and Grasemann, 2002, among others). As well, strain and kinematic vorticity data from the STDS in the Everest region indicates significant components of both pure and simple shear (Law et al., 2004), suggesting that the STDS may be a "stretching" fault as defined by Means (1990).

Thermomechanical models of the Himalaya (§1.1.2) suggest that low-angle normal-sense detachments will form during orogenic channel flow. In these models, the flow of mid-crustal material towards the foreland between the relatively stronger upper and lower crust produces pervasive shear throughout the mid-crustal channel, but also focused low-angle shear zones of opposite vergence at the top and base of the channel (Fig. 1.8c). The upper bounding shear zone is analogous to the STDS. In the models, the STDS structure forms because of relative displacement of material beneath it, but both the channel and its hangingwall move toward the foreland in an absolute sense.

The general characteristics of the STDS that must be explained by any model of Himalayan orogenesis are as follows: it juxtaposes high-grade metamorphic rocks in the footwall against low-grade or unmetamorphosed rocks in the hanging wall; the footwall is characterized by a hundreds of metres thick zone of mylonite; the uppermost hanging wall appears little deformed (an exception is the recumbent folds in Nepal); leucogranite dikes and sills are syntectonic and do not penetrate into the uppermost hanging wall; it has an early component of top-to-the-south shear; it is deformed by both pure and simple shear; synthetic normal faults can be found in its hanging wall which place younger on older rocks, it is coeval with the Main Central thrust; it predates EW extensional structures, and; it is duplicated in the Bhutan Himalaya.

1.4 PROBLEM AND OBJECTIVES

1.4.1 STATEMENT OF PROBLEM

The crustal-scale STDS has a normal sense of displacement, but developed within a compressional tectonic regime, challenging traditional concepts of orogenesis. In the eastern Himalaya of Bhutan, the STDS appears to be duplicated. What is the tectonic history of the duplicated STDS in the eastern Himalaya; can it be explained by or used to constrain models of Himalayan orogenesis, and; what are the implications of a duplicated

STDS for the evolution of the Himalayan orogen in general?

1.4.2 OBJECTIVES

To determine the tectonic history of the duplicated STDS, the following research objectives were pursued:

1. Determine the timing and cooling history of the STDS,
2. Characterize the structure and metamorphic field gradient across the STDS
3. Establish pressure-temperature-time paths for tectonites across the STDS
4. Determine the paleo-geographic affinity of the Chekha Group.

To complete these objectives, two field seasons of sampling and structural mapping in the Bhutan Himalaya were conducted during 2006 and 2008. The mapping and sampling locations are shown in Fig. 1.6, and station locations and sample descriptions are catalogued in Appendix A. This thesis comprises four research manuscripts, Chapters 2-5, each an independent study focusing on one or more of the above objectives with the goal of answering the general questions posed in §1.4.1. As such, each chapter contains an abstract, introduction, methods section, results section, discussion and conclusion. My contributions to each chapter, as well as contributions from the various co-authors, are listed in Appendix B. The findings from these four studies are synthesized in a general discussion in Chapter 6, and the final outcomes are summarized in Chapter 7. All references are listed together following Chapter 7. The content of each research manuscript is outlined below.

1.4.3 CHAPTER 2

This chapter is entitled "*Miocene structural reorganization of the South Tibetan detachment, Bhutan Himalaya*. A version of this chapter has been published as: "*Kellett, D.A., Grujic, D. and Erdmann, S., 2009, Miocene structural reorganization of the South Tibetan detachment, eastern Himalaya: implications for continental collision. Lithosphere, 1(5), 259-281.*"

In this chapter, I used U-Pb crystallization ages of igneous rims on zircon grains in small, deformed leucogranite bodies to show that the ductile shearing along two components of the STDS in the eastern Himalaya ceased at different times in the Miocene. The distinct age difference of and other distinguishing features between the two components led

me to demonstrate that the "upper" and "lower" nomenclature could not be applied to these two components. I propose a new nomenclature for the STDS in Bhutan: "outer STDS" for the more southern component and "inner STDS" for the more northern component. I argue that the two structures were once one continuous structure, and that the southern component was isolated from the main structure in the Mid-Miocene.

The U-Pb age data were collected at Stanford University using the Sensitive High-Resolution Ion MicroProbe (SHRIMP). I was able to complement the age data with Ti-in-zircon thermometry and trace element measurements, due to the particular reverse geometry configuration of the Stanford SHRIMP. The thermometry data, combined with $^{40}Ar/^{39}Ar$ cooling ages of muscovite from the same rocks was used to constrain the cooling history of the two components of the shear zone. The trace element data are some of the first data to characterize the geochemistry of zircons formed in fractionated decompression melts.

In the discussion, I consider two possible mechanisms for forming such a duplication of the STDS. The first is hinterland stepping of the STDS to maintain an orogenic critical taper, and the second is foreland translation and exhumation of a mid-crustal dome. Our results favour the second mechanism.

1.4.4 CHAPTER 3

This chapter is entitled "*Metamorphic history of the outer South Tibetan detachment system, Bhutan Himalaya*". A version of this chapter has been published as "*Kellett, D.A., Grujic, D., Warren, C., Cottle, J., Jamieson, R. and Tenzin, T., Metamorphic history of a syn-convergent orogen-parallel detachment: The South Tibetan detachment system, Bhutan Himalaya. Journal of Metamorphic Geology, 28, 785-808*".

In this chapter I combine *in situ* U(-Th)-Pb geochronology of monazite with peak temperature thermobarometric estimates to construct pressure-temperature-time (P-T-t) paths of tectonites along two transects across the outer STDS in Bhutan. In addition, microstructural characterization of tectonites is used to link the P-T-t paths of footwall and hanging wall rocks to their deformation history in the outer STDS. Our monazite age data was also used to constrain the onset of shearing on the outer STDS, and confirms that it was coeval with the MCT. These are some of the first well-constrained geochronological data for the onset of STDS shearing in the eastern Himalaya.

P-T-t paths are directly compared to analogous particle P-T-t paths from a thermomechanical model in which an analogue STDS is separated into two components by foreland translation and exhumation of a mid-crustal dome, showing that our estimated P-T-t histories are compatible with such a tectonic history.

1.4.5 CHAPTER 4

This chapter is entitled "*Defining the South Tibetan detachment system: Structure and metamorphism from mid- to upper crust in the Bhutan Himalaya*". A version of this chapter: "*Kellett, D.A., and Grujic, D., Syn-convergent, low-angle normal-sense detachments: defining the South Tibetan detachment system*" is in preparation for submission to Earth and Planetary Science Letters.

In this chapter I characterize the structural and metamorphic history of the rocks in the hanging wall of the outer STDS in the westernmost preserved klippe. Peak metamorphism is determined by the Raman spectroscopy of carbonaceous material (RSCM) method, and complemented with thermobarometric data from the previous chapter.

In particular I examine evidence for "lower" and "upper" STD structures within the outer STDS, as described in other parts of the orogen. I also discuss the tectonic context and suggest possible mechanisms of formation of the various individual structures within the STD "system" by relating them to various stages of channel flow, extrusion and exhumation.

1.4.6 CHAPTER 5

This chapter is entitled "*Paleogeographic restoration of the eastern Himalaya: knowns and unknowns*". A version of this chapter: "*Kellett, D.A., and Grujic, D., Paleogeographic restoration of the eastern Himalaya: knowns and unknowns*" is in preparation for submission to Earth and Planetary Science Letters.

In this chapter, I examine all available ϵNd and detrital zircon provenance data from the Bhutan Himalaya for the main lithotectonic packages (LHS, GHS and TSS). I also examine provenance data for the Jaishidanda Formation, which is exposed beneath the MCT, and for the Chekha Group, exposed in the outer STDS, for which I have acquired several new ϵNd data from four different transects across the outer STDS.

These data are used to critique a previously published proposal that the GHS, Chekha Group and TSS are preserved their in original stratigraphic positions (Long and

McQuarrie, 2010). I also consider the previously unspecified paleogeographic affinity of Jaishidanda and Chekha Group rocks. Finally, I suggest a possible paleogeographic geometry for the various lithotectonic packages of the Bhutan Himalaya.

CHAPTER 2

MIOCENE STRUCTURAL REORGANIZATION OF THE SOUTH TIBETAN DETACHMENT, BHUTAN HIMALAYA

This chapter has been published as: "*Kellett, D.A., Grujic, D. and Erdmann, S., 2009, Miocene structural reorganization of the South Tibetan detachment, eastern Himalaya: implications for continental collision. Lithosphere, 1(5), 259-281.*"

2.1 ABSTRACT

In the eastern Himalaya (Bhutan) there are two distinct top-down-to-the-north segments of the South Tibetan detachment (STD) system. The outer segment is a diffuse ductile shear zone preserved at the base of klippen of upper crustal rocks. New age constraints show that it was active until at least ca. 15.5 Ma and cooled by ca. 11.0 Ma, as constrained by SHRIMP U-Pb geochronology of magmatic zircon and $^{40}Ar/^{39}Ar$ thermochronology of muscovite in ductily-deformed leucogranite sills. The inner segment is a ductile shear zone active at least until ca. 11.0 Ma (constrained by SHRIMP U-Pb geochronology of magmatic zircon) and overprinted by more recent brittle faulting. These age constraints indicate that ductile deformation continued on the STD more recently in the eastern Himalaya than in central and western parts of the orogen. These improved constraints on timing of STD segments allow for a more detailed reconstruction of continental collision in the

eastern Himalaya in which the outer STD segment was abandoned in the mid-Miocene and passively transported southward in the hanging wall of the Main Himalayan thrust (the basal detachment of the orogen), while top-to-the-north ductile to brittle shearing continued on the inner STD segment. Hinterland stepping of the STD to maintain an orogenic critical taper (frictional wedge model) is a possible mechanism for this tectonic reorganization of the STD during the Miocene. However, our data combined with published geochronologic data for the eastern Himalaya demonstrates that foreland translation and exhumation of a mid-crustal dome (viscous wedge model) is the more tenable mechanism.

2.2 INTRODUCTION

Exposed mid-crustal rocks in the Himalayan orogen are bound by opposing-sense crustal-scale shear/fault systems, the Main Central thrust (MCT) below and the normal-sense South Tibetan detachment system (STDS) above (Fig. 2.1). The discovery that the timing of displacement along these two shear systems was coeval for at least part of the Miocene (Burchfiel et al., 1992; Hodges et al., 1992; review in Godin et al., 2006a), has led to several geodynamic and kinematic models for continental collision in which mid-crustal rocks are exhumed between coeval bounding shear zones (e.g., Grujic et al., 1996; Beaumont et al., 2001; Robinson et al., 2006; Webb et al., 2007). These models mark a major shift in how geologists attempt to explain the tectonic evolution of large hot orogens such as the Himalaya.

In the eastern Himalaya, two geographically and structurally distinct segments of the STDS, an outer, ductile shear zone preserved within broad synformal klippen and an inner ductile/brittle shear zone, have been identified (Edwards et al., 1996; Grujic et al., 2002, Hollister and Grujic, 2006) (Fig. 2.2). This STDS geometry may be unique to the eastern Himalaya. While other klippen are found in the central (Kathmandu, Jajarkot and Dadeldura) (Fig. 2.1a) and western (Simla) Himalaya, there is little agreement about whether the rocks preserved within are soled by top-to-the-north shear zones, whether (in some cases) they are windows rather than klippen, or whether Tethyan strata are preserved (e.g., Upreti, 1999; Johnson et al., 2001; Robinson et al., 2001; Robinson et al., 2003; Bollinger et al., 2006; Webb et al., 2007). In this paper we constrain the timing of ductile shearing of the outer and inner segments of the STDS in Bhutan using U-Pb and $^{40}Ar/^{39}Ar$ geochronological data. By clearly resolving the diachroneity of these two segments, we

are able to propose mechanisms for their formation and preservation, and the consequent implications for geodynamic and kinematic models of the Himalayan orogen.

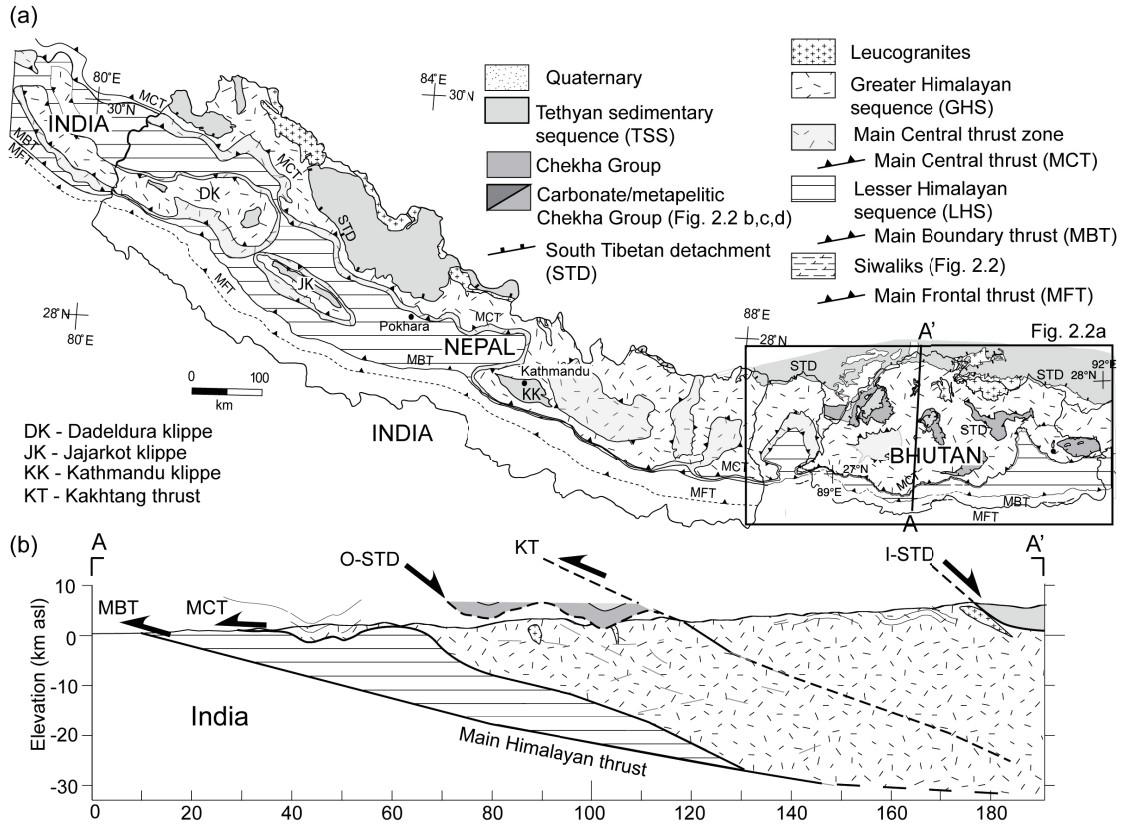

Figure 2.1: (a) Geological map of the Himalayan orogen (modified from McQuarrie et al., 2008). (b) Generalized cross-section through 90° E showing the main structures of the eastern Himalaya, based on the geological map by Gansser (1983), INDEPTH data (Hauck et al, 1998) and our field observations. Grey dashed lines indicate INDEPTH reflectors.

2.3 GEOLOGICAL SETTING

The Himalayan orogen is regarded as the epitome of a continent-continent collisional orogen. Following initiation of the collision in early Eocene (Molnar, 1984; Rowley, 1998; de Sigoyer et al., 2000; Najman et al., 2001; Searle, 2001; Leech et al., 2005), the Eocene to late Oligocene was a period (Eohimalayan) of crustal thickening and Barrovian metamorphism in the mid-crust. Evidence for crustal thickening is recorded by fold-and-thrust deformation in the upper-crust (e.g., Ratschbacher et al., 1994; Aikman et al., 2008; Kellett and Godin, 2009), as well as kyanite-grade metamorphism in the middle

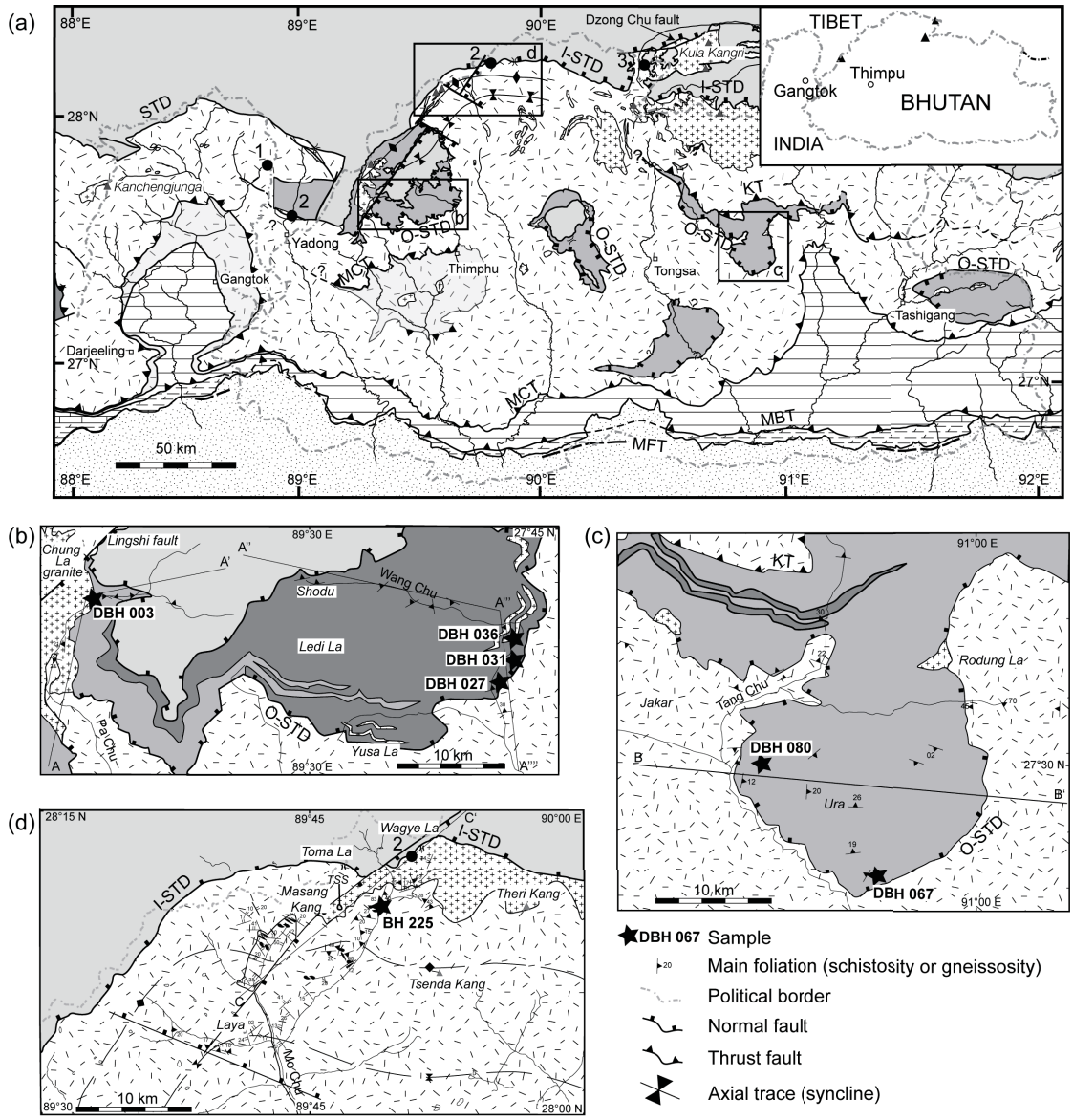

Figure 2.2: (a) Geological map of Bhutan. Inset shows its geographical location and legend is according to Figure 2.1. Mapped transects and structural data are shown for field areas: (b) Lingshi, (c) Ura and (d) Masang Kang. A-A', B-B' and C-C' cross-sections are shown in Figure 2.3. Maps compiled from this study; Gansser, 1983; Wu et al., 1998; Grujic et al., 2002; Chakungal, 2006. Locations of samples from previous geochronology studies are shown: 1. Catlos et al., 2004; 2. Wu et al., 1998; 3. Edwards and Harrison, 1997.

crust (e.g., Simpson et al., 2000; Godin et al., 2001). This was followed in early to mid-Miocene by the (Neohimalayan) exhumation of material from mid-crustal depths to the southern Himalayan topographic front (Vannay and Hodges, 1996; Hodges et al., 1996). Exhumation was facilitated by vigorous surface erosion along the southern front of the orogen cooperating with active thrusting below and normal fault geometry tectonic denudation above the metamorphic rocks (see review in Yin, 2006).

The Himalaya is characterized by a series of southward-propagating, south-verging thrusts rooting into a common basal detachment thrust, the Main Himalayan thrust (MHT) (e.g., Nelson et al., 1996). These thrusts bound the major lithotectonic units of the Himalaya (Fig. 2.1; review in Le Fort, 1975). The northernmost lithotectonic assemblage is the Tethyan sedimentary sequence (TSS), bounded to the north by the Yarlung-Tsangpo suture, which divides Indian from Asian crust. Structurally beneath the TSS is the Greater Himalayan sequence (GHS) of high-grade metamorphic rocks and Miocene leucogranites (Fig. 2.1). The boundary between the TSS and the GHS is the STDS, a system of top-down-to-the-north normal-sense ductile shear zones and brittle faults (e.g., Burchfiel et al., 1992; Carosi et al., 1998; Searle et al., 2003). The dominantly sedimentary Lesser Himalayan sequence (LHS) is separated from the GHS by the Main Central thrust (MCT). Further south, the Neogene Siwalik molasse is separated from the LHS by the Main Boundary thrust (MBT). The Main Frontal thrust (MFT) marks the deformation front of the Himalayan orogen, and consists of a blind active thrust below the Siwalik molasse against Quaternary alluvial sediments (Lavé and Avouac, 2000). Within the eastern Himalaya a distinctive out-of-sequence thrust, the Kakhtang thrust (Fig. 2.1b), doubles the thickness of the GHS (Davidson et al., 1997; Grujic et al., 2002).

2.4 South Tibetan detachment system

The STDS is a laterally continuous network of normal-sense, mainly low-angle detachments, some of which were dominantly active in the Miocene and some of which are still active (Burg and Chen, 1984; Burchfiel and Royden, 1985; Burchfiel et al., 1992; Brown and Nazarchuk, 1993; Hurtado et al., 2001; Wiesmayr et al., 2002; Meyer et al., 2006). In the hanging wall of the detachment system are Cambrian to Eocene sedimentary rocks of the TSS (Garzanti, 1999). In the footwall are migmatite, amphibolite to granulite-grade metamorphic rocks, and Miocene leucogranites of the GHS. Locally, greenschist-

to amphibolite-facies metasedimentary rocks crop out within the STDS. Regionally these rocks are termed the Chekha Group (Bhutan), the Everest Series (eastern Nepal), the North Col Formation (eastern Nepal), the Annapurna Yellow Formation (central Nepal) and the Haimantas Group (NW India) and are probably latest Proterozoic to Ordovician in age (Frank et al., 1973; Gansser, 1983; Colchen et al., 1986; Burchfiel et al., 1992; Lombardo et al., 1993; Bhargava, 1995; Carosi et al., 1999; Searle et al., 2003; Myrow et al., 2009).

2.4.1 South Tibetan detachment system in Bhutan

In Bhutan, there are two segments comprising the STDS. The more internal, northern segment is referred to here as the inner STD (I-STD) and the more external, southern segment is referred to as the outer STD (O-STD). In northwestern Bhutan, the I-STD occurs as two closely-spaced normal-sense faults which dip shallowly (10-30°) to the north, covered by Quaternary deposits (Figs. 2.2d and 2.3c) (Burchfiel et al., 1992). The northern brittle structure separates upper Paleozoic shale, siltstone and limestone of the TSS from metasedimentary rocks, while the southern ductile structure separates metasedimentary rocks from leucogranite, augen gneiss and schist of the GHS. Variably deformed leucogranite sills and dikes increase upwards in abundance, reaching nearly 100 % mylonitic leucogranite in outcrops at the top of the GHS (Burchfiel et al., 1992; Edwards et al., 1996; Chakungal, 2006; our observations). Younger, brittle normal faulting along the Dzong Chu fault occurs north of, and truncates the ductile I-STD (Fig. 2.2) (Edwards et al., 1996; 1999). Normal faulting has continued in northern Bhutan to recent times, documented by faulted Quaternary moraines, although the most recent faulting apparently occurs along NS-striking rather than EW-striking faults (Meyer et al., 2006).

While metasedimentary rocks are only locally present at the I-STD, thick sequences of the metasedimentary Chekha Group are preserved farther south within the O-STD (Figs. 2.2, 2.3). The O-STD, with intensely-folded gneisses of the GHS in its footwall and the Chekha Group in its hanging wall, is a diffuse shear zone exhibiting an upward decrease in metamorphic grade. Conjugate top-to-the-south and top-to-the-northwest shear-bands and strong sub-horizontal crenulation cleavage in the Chekha Group indicate a zone of general shear with components of both vertical shortening and top-to-the-north simple shear (Grujic et al., 2002; Carosi et al., 2006), similar to that described for the well-studied STD in the Everest region (e.g. Law et al., 2004; Jessup et al., 2006). The shear zone is preserved within broad, non-cylindrical synclines in central and southern Bhutan (Fig.

2.1a; Edwards et al., 1996; Grujic et al., 2002). Some of these klippen also preserve TSS rocks in their cores. The contact between the Chekha Group and the TSS marks a seemingly abrupt change in structural style and metamorphic grade, perhaps indicating a fault.

An interpretation of compiled published data from the Himalaya suggests that STD structures may young toward the north (Godin et al., 2006a). Edwards et al. (1996) have suggested that the geometry of the STDS in Bhutan is a result of later, brittle faults cutting an earlier ductile STD, implying synchroneity for both ductile segments of the STD (I-STD and O-STD), with younger brittle faults cutting into the ductile shear zone in the north (I-STD). In this study we constrain the timing of ductile components of the I-STD and O-STD structures in areas where they are well accessible and separated enough to avoid overlapping of geological information.

2.4.2 AGE CONSTRAINTS

The I-STD in the eastern Himalaya has been shown, by Th-Pb and U-Pb dating of monazite in mylonitized granite bodies in the footwall, to have been active at least until ca. 12.5-12.0 Ma in northern Bhutan at Kula Kangri and at Wagye La (Edwards and Harrison, 1997 and Wu et al., 1998, respectively). These ages can also be interpreted as constraining the onset of brittle deformation since the mylonitized granites are cut by brittle STD faults. In the adjacent area of Sikkim (India), zircon and monazite in deformed leucogranites in some component of the STD have been dated at ca. 17 and 15-14 Ma, indicating STD-related ductile deformation may have occurred there until ca. 14 Ma (Fig. 2.2; Catlos et al., 2004). Only slightly younger muscovite $^{40}Ar/^{39}Ar$ cooling ages in granites in these areas of ca. 11-10 Ma (Maluski et al., 1988) indicate rapid cooling of the footwall and constrain the minimum age of ductile deformation on the I-STD. It has been recently suggested that ductile shearing occurred on the O-STD between 24-22 Ma (Chambers, 2008), and 22-17 Ma (Grujic et al., 2002).

2.5 STUDY AREAS

This study comprises three transects across segments of the STDS. The Lingshi and Ura transects cross the O-STD where the Chekha Group is exposed in broad synforms in NW and central Bhutan (Fig. 2.2b, c). The Masang Kang transect in NW Bhutan crosses the

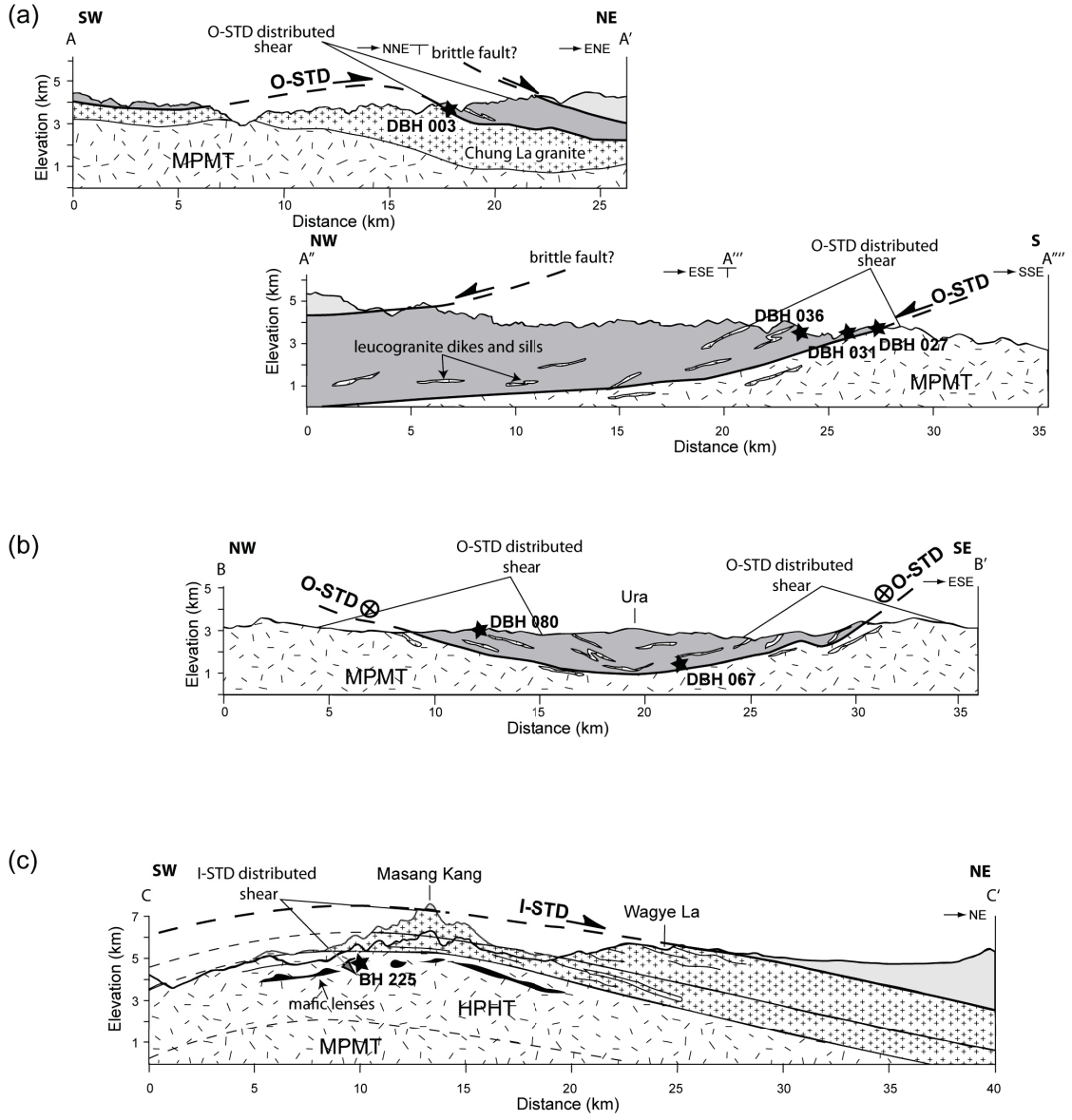

Figure 2.3: Cross-sections across the O- and I-STD. See Figure 2.2 for location of section lines. (a) A-A' and A"'-A"" section across the O-STD in the Lingshi area. (b) B-B' section across the O-STD in the Ura area. (c) C-C' section across the I-STD in the Masang Kang area. Location of high pressure, high temperature metamorphism (HPHT) and medium pressure and temperature metamorphism (MPMT) in the GHS indicated (after Chakungal, 2006).

I-STD where it separates granulite-grade gneisses and leucogranites of the GHS from TSS rocks (Fig. 2.2d). The characteristic metamorphic assemblages observed in each transect are discussed briefly below.

2.5.1 LINGSHI (OUTER SOUTH TIBETAN DETACHMENT)

At the SW side of the Lingshi area, garnet-sillimanite gneiss of the GHS is separated from the Chekha Group by the Chung La leucogranite (Fig. 2.2b), which is a large sill intruded along the contact and tapering toward the east. A slightly deformed component of the Chung La granite has been dated by monazite U-Pb to ca. 23-22 Ma (R. Parrish, 2008, personal commun.). To the east of the Lingshi area, the GHS comprises sheared garnet-bearing metapelite, quartzite, pelitic gneiss and augen gneiss intruded by leucogranite dikes and sills. Near the contact with the Chekha Group, gneisses are migmatized and leucosomes contain garnet, muscovite and sillimanite. Above the GHS are sheared intercalated calc-silicate, garnet and staurolite-bearing metapelitic schist, phyllite and rare quartzite of the Chekha Group, which sharply decrease in metamorphic grade from amphibolite-facies at the base to greenschist-facies further up-section. Above the calc-silicate and schist is a thick sequence of monotonous grey marble. Leucogranite intrusions are common at the base of the Chekha Group and disappear at ca. 2.5 km structurally above the contact. The Chekha Group appears to have a structural thickness of 4-5 km in the Lingshi area (Fig. 2.3a). The stratigraphic thickness is unconstrained because the metasedimentary rocks are isoclinally folded and sedimentary bedding has been transposed (Fig. 2.4a-d). The contact between the Chekha Group and the overlying TSS is characterized by a sharp boundary from marble to immature sandstone in the east and from metapelitic schist to fine-grained graphitic slate, sandstone, and limestone in the west, accompanied by a decrease in metamorphic grade and transition from transposed bedding to preserved right-way-up stratigraphy (see Gansser (1983) for further structural and lithologic details).

2.5.2 URA (OUTER SOUTH TIBETAN DETACHMENT)

In the Ura area, the GHS is characterized by sheared migmatitic garnet-bearing augen gneiss. Leucogranite dikes and sills are common within the augen gneiss. Some leucogranites contain magmatic cordierite, partially replaced by subsolidus sillimanite and muscovite, followed by andalusite. The overlying Chekha Group comprises sheared amphibolite-facies garnet-bearing metapelitic schist and biotite-bearing quartzite. Amphibolite bands are present locally. To the north, two thick white marble bands are present.

Figure 2.4: Macro- and microstructures in deformed leucogranites. (a) Outcrop located at the base of the Chekha Group in the O-STD, Lingshi transect (sample DBH 003). The leucogranite dike cross-cuts the main fabric (S_m) in calc-silicates and metapelites and is folded. (b) Leucogranite dikes cross-cutting folded Chekha Group carbonate and showing little evidence of deformation. Located near to sample DBH 036 on the eastern side of the Lingshi transect. (c) Boudinaged leucogranite sill emplaced in Chekha Group carbonate, near sample DBH 036 on the eastern side of the Lingshi transect. (d) Folded and boudinaged leucogranite dikes in Chekha Group metapelite near the western contact between Chekha Group metapelites and the GHS gneisses within the O-STD in the Ura area. (e) Optical micrograph of DBH 027 showing the sharp contact with Chekha Group metapelite (outlined in white), SGR, GBM, and undulose extinction in Qtz and undulose extinction in muscovite (Ms): crossed polarized light (XL). (f) Optical micrograph of DBH 036 showing deformation tartan twinning in Kfs and SGR recrystallization in Qtz; XL. (g) Optical micrograph of DBH 080 showing brittle fractures in plagioclase filled with Qtz: XL. (h) Optical micrograph of BH 225 showing GBM recrystallization in Qtz, and Sil associated with a top-to-the-north shear band: XL. Mineral abbreviations are according to Kretz (1983).

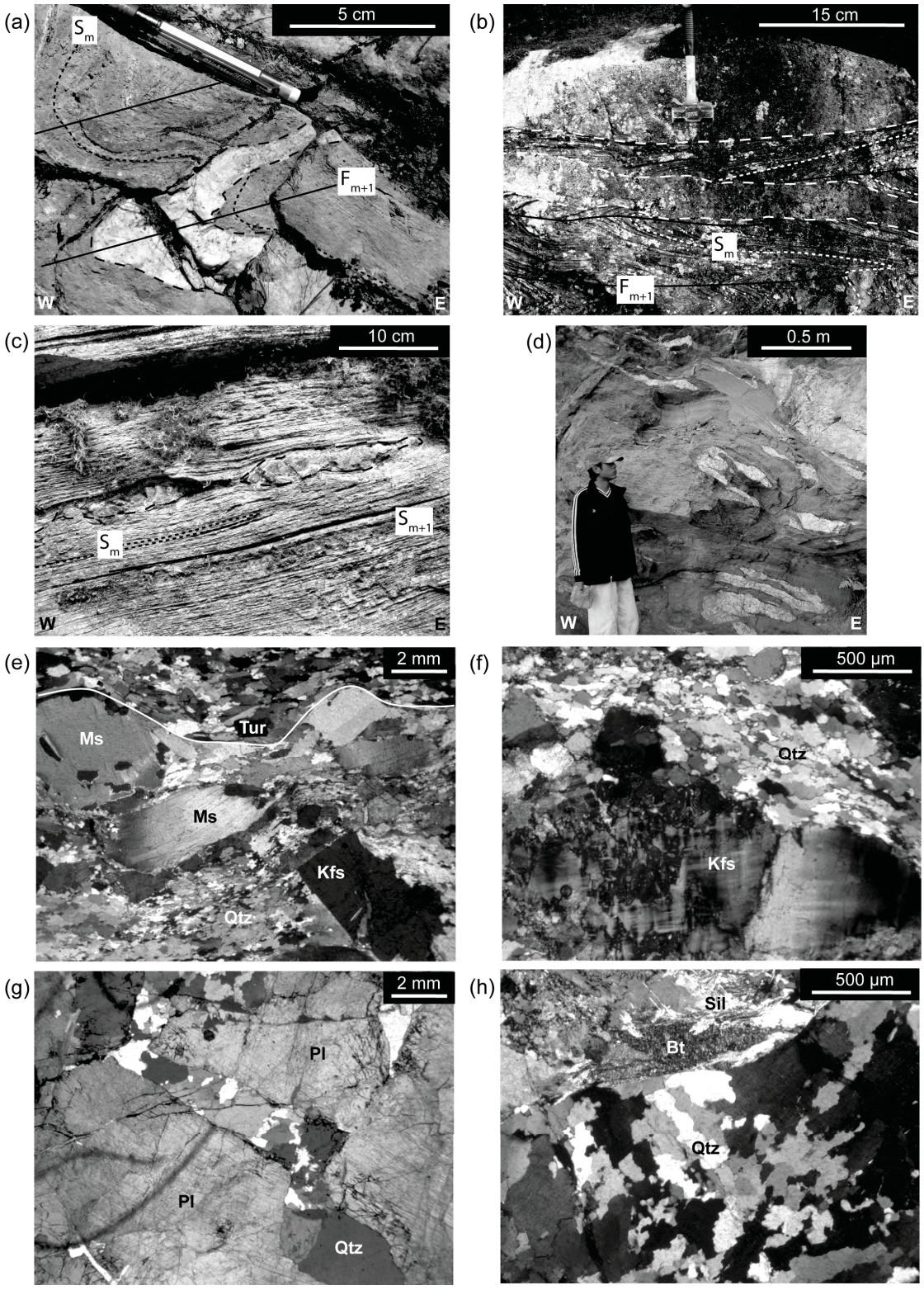
(a)
5 cm
S_m
F_{m+1}
W
E
(b)
15 cm
S_m
F_{m+1}
W
E
(c)
10 cm
S_m
S_{m+1}
W
E
(d)
0.5 m
W
E
(e)
2 mm
Ms
Tur
Ms
Kfs
Qtz
(f)
500 µm
Qtz
Kfs
(g)
2 mm
Pl
Pl
Qtz
(h)
500 µm
Sil
Bt
Qtz

Garnet-staurolite schist becomes abundant (the Naspe Formation of Bhargava (1995)) toward the footwall of the Kakhtang thrust (Fig. 2.1b, 2.2c; Gansser, 1983; Davidson et al., 1997; Grujic et al., 2002). Leucogranite dikes and sills are pervasive throughout the Chekha Group. TSS rocks are not preserved within the Ura klippe.

2.5.3 MASANG KANG (INNER SOUTH TIBETAN DETACHMENT)

The GHS in the Masang Kang area forms an east-west trending open upright antiform-synform pair (Fig. 2.2c). Lithologies within the GHS include migmatite, augen gneiss, orthogneiss, calc-silicate and quartzite with granulite-facies mafic and ultramafic lenses (Chakungal, 2006). Leucogranite dikes and sills intrude the GHS, and a large, variably sheared leucogranite body is exposed to the northeast. The leucogranite intrusions are cut by brittle faults along the I-STD and do not penetrate into the hanging wall TSS rocks.

2.5.4 LEUCOGRANITES

Miocene leucogranite and granite dikes and sills are found throughout the GHS in Bhutan, with the largest bodies occurring at the very top of the sequence, broadly corresponding with the highest metamorphic grades (e.g., Wagye La in NW Bhutan, see Fig. 2.2b) (Gansser, 1983; Lombardo et al., 1993). Variably deformed leucogranite and granite dikes and sills are also found within the lower structural levels of the Chekha Group.

Dikes and sills emplaced within the Chekha Group at the O-STD are generally leucogranitic (to granitic), coarse-grained to bimodal and are characterized by abundant tourmaline and apatite, and minor garnet and retrograde subsolidus sillimanite. Tartan twinning in K-feldspar suggests crystallization at $>$450-550 °C (e.g. Brown and Parsons, 1989), whereas the presence of sillimanite suggests crystallization at $\geq$550 °C (using the aluminosilicate stability field of Pattison (1992)). The leucogranites are hosted by marble, calc-silicate and schist and were therefore clearly injected (i.e. they did not form *in situ*). Leucogranite bodies emplaced within the top of the GHS at the I-STD are characterized by magmatic andalusite and cordierite, and late sillimanite. We suggest that the andalusite crystallized slightly above the solidus (it occurs interstitially and as marginal inclusions in magmatic phenocrysts), and therefore probably at a pressure of $\leq$2.8 kbar (see details in Appendix C).

2.6 STRUCTURE

2.6.1 MACROSTRUCTURES

Samples for this study were collected from deformed leucogranite dikes and sills (Fig. 2.4). In the Lingshi and Ura areas, the sampled leucogranites were emplaced within Chekha Group rocks (Fig. 2.2b, c; Fig. 2.3a, b). Sample DBH 003 was collected from a ca. 5 cm dike at the base of the Chekha Group, 100 m from the Chung La granite (Fig. 2.2b). The dike crosscuts the host calc-silicate, which has been isoclinally folded, and has a pervasive axial planar cleavage (the dominant foliation in the area) that dips 40-50° toward the ENE. The dike is folded into open folds with axial planes dipping 24° toward SSW (Fig. 2.4a). The foliation is folded in a similar manner, although with a higher amplitude and tighter folds, indicating that the intrusion postdated the main foliation but was pre- to synkinematic with the later folding. Samples DBH 027, DBH 031 and DBH 036 were sampled from leucogranite sills progressively structurally up-section from the base of the Chekha Group on the eastern side of the Lingshi transect (Figs. 2.2b, 2.3a). The sills are all weakly folded and boudinaged at the outcrop scale, within the host Chekha Group phyllitic schist (DBH 027) and calc-silicate (DBH 031, DBH 036) foliation dipping ca. 10-20° toward the W-SW (Fig 2.3c). DBH 080 was sampled from a boudin of leucogranite sill emplaced in crenulated metapelitic schist near the western base of the Chekha Group in the Ura transect (Fig. 2.2c). The sill and main foliation of the schist both dip ca. 10° toward ESE. The leucogranites in the Chekha Group show a weakly developed, coarse schistosity mainly defined by sub-parallel mica ± grain shape fabric of quartz grains, and no lineation. The style of deformation exhibited by the leucogranite bodies (boudinage, folding or both) is a function of their emplacement orientation with respect to the O-STD.

Sample BH 225 from the Masang Kang area was collected from a deformed leucogranite emplaced in and cross-cutting migmatitic gneisses of the GHS ca. 1 km below the GHS/TSS contact (Fig. 2.3c). Below this, at the lower/southern deformation front of the I-STD, top-to-the-NW shear bands appear, strain increases progressively northward into a mylonitic top-to-the-NW foliation and S-C fabric accompanied by conjugate shear bands, sillimanite mineral lineation and a consistent stretching lineation. Microstructural evidence (described next) indicates that BH 225 has been deformed by the I-STD.

2.6.2 MICROSTRUCTURES

The leucogranite samples collected from the hanging wall of the O-STD do not have obvious chill margins (Fig. 2.4e). Microstructures include undulose extinction, sub-grain rotation (SGR) and grain boundary migration (GBM) recrystallization in quartz grains (Fig. 2.4e, f). SGR recrystallization dominates, although GBM recrystallization is locally significant. Deformation in feldspar includes undulose extinction, deformed twins, perthite and flame perthite and microfractures (Fig. 2.4f, g). Muscovite is coarse, and generally displays undulose extinction, local recrystallization and rare kinks (Fig. 2.4e). The main planar fabric of the leucogranites is defined by the alignment of muscovite. These microstructures suggest that ductile deformation of the leucogranites occurred at ca. 400-500 °C (Stipp et al., 2002; Passchier and Trouw, 2005).

Sample BH 225, collected from the footwall of the I-STD, is weakly deformed. In thin section, both plagioclase (Pl) and K-feldspar (Kfs) show evidence of crystal-plastic deformation, including myrmekite, recrystallized grains (Kfs), undulose extinction (Pl) and deformation twins (Pl). Quartz grains display dynamic recrystallization dominantly by GBM (Fig. 2.4h), and locally by SGR. Combined, these microstructures suggest that STD-related ductile deformation for this leucogranite occurred at ca. 500-600 °C (Stipp et al., 2002; Passchier and Trouw, 2005). In addition, sillimanite (Fig. 2.4h) is present as slickenfibres in top-to-the-north shear bands and also replaces andalusite. Muscovite replaces cordierite, andalusite and feldspar, and is locally recrystallized.

2.7 SHRIMP ZIRCON U-PB GEOCHRONOLOGY

All six studied leucogranites show evidence of solid-state ductile deformation but also cross-cut earlier, well-developed host rock fabrics; they must have been emplaced late syn-kinematically, and crystallized syn-kinematically with top-to-the-north shearing both in the O- and I-STD in Bhutan, consistent with previous observations (Edwards et al. 1996, Edwards and Harrison, 1997; Davidson et al., 1997; Wu et al., 1998; Grujic et al., 2002; Daniel et al., 2003; Chambers, 2008).

Zircons were analysed for U-Pb and trace-element composition using the SHRIMP-RG (Sensitive High-Resolution Ion MicroProbe-Reverse Geometry) operated by the U.S. Geological Survey and Stanford University. Sample locations are shown in Figures 2.1

and 2.2. Approximately 20 spots from 12-15 zircon grains were analyzed for each sample, except sample BH 225 for which ca. 70 spots were analyzed from ca. 40 zircon grains. Pits were ca. 30 μm in diameter with a depth of ca. 5 μm. Mineral separation (standard and SelFrag for BH 225), analytical procedures and detailed zircon characterization are outlined in Appendix D. In general, the O-STD zircons exhibit dark-under-cathodoluminescence (CL) magmatic growth rims, spongy, inclusion-rich interiors and rare inherited cores, while the I-STD zircons exhibit magmatic growth rims, grey-under-CL interiors and commonly contain inherited cores.

2.7.1 TRACE-ELEMENT GEOCHEMISTRY OF ZIRCON

The reverse geometry arrangement of the SHRIMP-RG at Stanford University allows for the collection of trace-element geochemistry data coincident with U-Pb analyses (Mazdab and Wooden, 2006). For full data tables, see Appendix E.

Zircon rims from leucogranites along the O-STD have a consistent trace-element geochemistry characterized by a small positive Ce anomaly and a large negative Eu anomaly (Fig. 2.5a). Eu anomalies for zircon rims range from Eu/Eu* = 0.17 to as low as Eu/Eu* = 0.001, with most analyses ranging from 0.05 to 0.001 (Fig. 2.5d). Heavy rare earth elements (HREEs) are somewhat to very depleted in zircon rims. In particular, sample DBH 080 yielded an average Yb/Gd ratio of ca. 2 (Fig. 2.5e). Zircon rim Th/U values are uniformly low (< 0.1, Fig. 2.5e).

Such low Eu/Eu* values are likely an indication of crystallization in the presence of feldspar, which will take up all available Eu (Rubatto, 2002). This suggests zircon crystallization simultaneous with or after feldspar. Depletion in HREEs indicates preferred fractionation of HREEs by another mineral phase, probably garnet (Rubatto, 2002), which is present in samples DBH 027 and DBH 080. Assuming HREEs are largely stored in garnet, partial melting of the source rocks in which garnet is left in the residual phase could also cause HREE depletion in the leucogranite, in which case greater HREE depletion would indicate a smaller percentage of partial melt at the source. The consistency of the REE patterns of zircon rims compared to cores (Fig. 2.5b) indicates that mixing of age domains during micro-sampling was not an issue.

Zircon rims and grey-under-CL interiors from sample BH 225 that yield Miocene U-Pb ages (many grey interiors, as will be discussed below, yield early Paleozoic ages) are plotted in Figure 2.5c. The two growth phases are indistinguishable on the basis

of their REE patterns, but can be distinguished from the zircon rims from the O-STD leucogranites by their less pronounced negative Eu anomaly, steeper HREE pattern, and lower Hf values (Fig. 2.5d, e). These zircons likely crystallized from a different protolith than those described above, and perhaps one that experienced a greater percentage of partial melting, consistent with higher country rock metamorphic temperatures in the footwall of the I-STD (Chakungal, 2006).

2.7.2 U-PB GEOCHRONOLOGY RESULTS

Results are presented in Table 2.1, and plotted in Figure 2.6. For all samples from the hanging wall of the O-STD (Fig. 2.6a-d), U-Pb ages of zircon rims do not define a single crystallization age, but rather produce a spread of ages along concordia. This spread is discussed further below. In general, $^{206}Pb/^{238}U$ age ranges to the nearest 0.5 Ma (at the 2σ confidence level) are reported through the text unless otherwise indicated. Zircon rim data that are $> 1\%$ discordant are shown in Table 2.1 and Fig. 2.6, but not used for U-Pb age interpretation. For the Lingshi area, apparent $^{206}Pb/^{238}U$ ages range from ca. 24.5-16.5 Ma, 29.5-19.0 Ma and 24.5-16.5 Ma (DBH 027, 031 and 036, respectively). In the Ura area, sample DBH 080 zircon rims yielded $^{206}Pb/^{238}U$ ages of ca. 20.5-15.5 Ma. BH 225 from the footwall of the I-STD displays a similar spread of ages along concordia (Fig. 2.6e). Dark rim apparent $^{206}Pb/^{238}U$ ages range from ca. 15.5-11.0 Ma, while the grey interior zircon apparent ages range from ca. 29.0-11.5 Ma. Within individual grains dark rims are younger than their grey interiors. Cores and interior zircon from BH 225 yield a significant age population at ca. 500 Ma, as well as many Proterozoic ages, and a few younger discordant Paleozoic ages (Fig. 2.6f). Cores from DBH 003 from the Lingshi area are discordant, but indicate Proterozoic ages (Fig. 2.6g).

2.7.3 INTERPRETATION

Crystallization of the zircon rims is correlated with the presence of melt. Solid-state ductile deformation of the leucogranites must have therefore outlasted the youngest zircon rim crystallization ages. Thus we conclude that ductile deformation continued after ca. 15.5 Ma for the O-STD (based on the youngest zircon ages from DBH 080, DBH 027, DBH 031 and DBH 036) and after ca. 11.0 Ma for the I-STD (based on the youngest zircon ages from BH 225).

With the exception of sample DBH 080, most of the Miocene-aged zircon phases in this study exhibit a high U content of $>$2500 ppm, (Table 2.1). Zircon with U content

Table 2.1: SHRIMP U-Pb isotopic analyses for zircon. Standard text—zircon rims, italic—mottled zircon, light grey shading—cores. For sample BH 225, standard text—dark rims, italic—grey interiors, light grey shading—cores. Percent discordance is calculated for Tertiary ages only. * Uncorrected values, # Corrected for ^{207}Pb. Cm—common.

Spot	U (ppm)	Th (ppm)	$^{232}Th/^{238}U$	$^{204}Pb/^{206}Pb$	Cm ^{206}Pb (%)	$^{238}U/^{206}Pb$*	Error (%)	$^{207}Pb/^{206}Pb$*	Error (%)	$^{206}Pb/^{238}U$ age# (Ma)	Error (%)	Discordance (%)
DBH 003												
3.1	*5993*	*1264*	*0.22*	*5.1E-3*	*9.29*	*276.25*	*0.5*	*.1199*	*7.5*	*21.1*	*0.3*	*9.2*
11.1	5502	69	0.01	5.3E-4	0.33	280.42	0.6	.0491	2.3	22.9	0.1	0.3
2.1	*4307*	*93*	*0.02*	*6.6E-3*	*11.82*	*245.48*	*0.4*	*.1400*	*11.9*	*23.1*	*0.6*	*11.8*
10.1	*5043*	*309*	*0.06*	*3.8E-3*	*6.46*	*213.21*	*0.5*	*.0977*	*5.1*	*28.2*	*0.2*	*6.5*
7.1	*10437*	*10077*	*1.00*	*7.2E-3*	*14.22*	*191.91*	*0.3*	*.1590*	*3.4*	*28.8*	*0.3*	*14.2*
9.1	*13172*	*8414*	*0.66*	*1.5E-2*	*26.65*	*163.78*	*0.6*	*.2574*	*11.3*	*28.8*	*1.5*	*26.6*
4.1	9147	298	0.03	5.0E-4	0.75	209.33	1.1	.0526	1.6	30.5	0.3	0.8
1.1	*22664*	*22717*	*1.04*	*2.2E-2*	*41.55*	*120.27*	*0.6*	*.3753*	*10.4*	*31.3*	*2.7*	*41.4*
5.2C	13117	10515	0.83	1.0E-4	8.67	14.87	2.9	.1243	5.8	384.3	11.5	
8.1	1012	133	0.14	2.6E-5	3.98	8.19	0.3	.0959	0.5	714.7	2.3	
11.2	365	145	0.41	1.1E-4	0.25	6.55	0.5	.0716	0.9	913.3	4.2	
9.2	556	407	0.76	1.6E-4	1.93	6.41	2.1	.0857	1.6	917.4	18.6	
14.2C	210	71	0.35	---	1.57	5.08	0.7	.0910	1.1	1141.8	7.6	
DBH 027												
A-5.1	5067	18	0.00	---	0.08	390.94	0.7	.0470	2.8	16.5	0.1	0.1
A-12.1	4824	26	0.01	3.0E-4	-0.10	376.46	0.6	.0456	2.6	17.1	0.1	-0.1
11.1	5401	18	0.00	3.0E-4	0.16	371.94	0.6	.0477	2.3	17.3	0.1	0.2
A-2.1	3429	20	0.01	9.3E-5	0.09	371.66	0.8	.0471	3.1	17.3	0.1	0.1
A-1.1	3721	17	0.00	1.5E-4	0.24	368.59	0.7	.0483	2.7	17.4	0.1	0.2
19.2	2319	14	0.01	---	0.24	367.45	0.8	.0483	3.4	17.5	0.2	0.2
9.1	3340	15	0.00	3.7E-4	0.23	365.36	0.7	.0482	2.8	17.6	0.1	0.2
A-1.2	4038	17	0.00	5.0E-4	0.02	363.25	0.7	.0465	2.8	17.7	0.1	0.0
A-11.1	3348	10	0.00	1.4E-4	0.09	345.19	0.7	.0471	2.9	18.6	0.1	0.1
A-4.1	3626	12	0.00	-2.4E-4	-0.10	339.62	0.7	.0456	2.9	19.0	0.1	-0.1
1.2	2431	6	0.00	2.5E-4	0.38	336.73	0.9	.0494	3.5	19.0	0.2	0.4
A-11.2	3890	15	0.00	---	0.05	334.62	0.7	.0468	2.7	19.2	0.1	0.0
19.1	2727	21	0.01	---	0.99	329.49	0.8	.0543	2.9	19.3	0.2	1.0
1.1	3317	10	0.00	1.2E-4	0.17	329.73	0.7	.0477	2.9	19.5	0.1	0.2
15.1	2776	21	0.01	1.7E-3	4.33	313.87	0.7	.0806	3.8	19.6	0.2	4.3
A-4.2	2717	5	0.00	---	0.32	321.71	0.8	.0489	3.0	19.9	0.2	0.3

Spot	U (ppm)	Th (ppm)	$^{232}Th/^{238}U$	$^{204}Pb/^{206}Pb$	Cm ^{206}Pb (%)	$^{238}U/^{206}Pb$*	Error (%)	$^{207}Pb/^{206}Pb$*	Error (%)	$^{206}Pb/^{238}U$ age# (Ma)	Error (%)	Discordance (%)
6.1	4598	14	0.00	6.2E-5	0.26	321.72	0.6	.0485	2.5	20.0	0.1	0.3
14.3	2931	12	0.00	---	-0.09	316.15	0.8	.0457	3.9	20.4	0.2	-0.1
5.1	3169	15	0.00	3.2E-4	0.26	309.64	0.7	.0485	2.8	20.7	0.1	0.3
17.1	4153	15	0.00	2.3E-4	0.12	309.24	0.6	.0474	2.6	20.8	0.1	0.1
2.1	4868	19	0.00	3.1E-4	0.80	294.85	0.5	.0528	2.6	21.7	0.1	0.8
20.1	4215	73	0.02	---	-0.17	294.67	0.6	.0451	2.7	21.9	0.1	-0.2
2.2	10737	44	0.00	---	0.18	288.76	0.4	.0479	1.4	22.2	0.1	0.2
3.1	7581	30	0.00	2.8E-5	0.08	284.61	0.4	.0471	1.7	22.6	0.1	0.1
14.1	6820	27	0.00	1.7E-4	-0.02	266.39	0.4	.0464	1.7	24.2	0.1	0.0
9.2	*5842*	*56*	*0.01*	*2.4E-4*	*0.12*	*251.86*	*0.5*	*.0475*	*1.7*	*25.5*	*0.1*	*0.1*
14.2	*6736*	*28*	*0.00*	*3.5E-5*	*0.09*	*241.76*	*0.4*	*.0473*	*1.6*	*26.6*	*0.1*	*0.1*
DBH 031												
10.1	505	44	0.09	6.2E-3	3.24	369.01	2.0	.0719	6.8	16.9	0.4	3.2
4.1	277	20	0.08	3.0E-3	2.55	340.08	2.5	.0666	8.9	18.4	0.5	2.5
15.1	848	32	0.04	6.3E-3	10.19	301.51	1.4	.1269	3.6	19.2	0.3	10.1
28.1	1704	29	0.02	---	-0.04	332.46	1.0	.0461	3.9	19.4	0.2	16.2
12.1	1154	37	0.03	1.2E-3	0.51	312.01	1.2	.0505	5.7	20.5	0.3	-0.1
10.2	609	35	0.06	6.6E-4	1.19	281.85	1.6	.0559	5.9	22.6	0.4	0.5
8.1	2391	47	0.02	9.2E-4	1.22	279.71	0.8	.0561	3.1	22.7	0.2	1.2
15.2	2288	48	0.02	2.7E-4	0.83	276.19	0.7	.0531	2.7	23.1	0.2	1.2
9.1	7796	212	0.03	3.9E-4	0.51	272.39	0.6	.0506	1.9	23.5	0.1	0.8
5.1	*3078*	*44*	*0.01*	*1.5E-4*	*0.20*	*265.04*	*0.6*	*.0481*	*2.9*	*24.2*	*0.2*	*0.5*
2.1	*6054*	*131*	*0.02*	*7.8E-4*	*0.89*	*255.06*	*0.4*	*.0535*	*1.7*	*25.0*	*0.1*	*0.2*
3.1	*5571*	*294*	*0.05*	*3.7E-3*	*6.47*	*235.73*	*0.5*	*.0977*	*14.5*	*25.5*	*0.5*	*0.9*
31.1	2183	65	0.03	9.0E-4	0.93	220.28	1.0	.0540	3.4	28.9	0.3	*0.9*
DBH 036												
19.1	3750	42	0.01	3.3E-4	0.96	383.12	0.8	.0539	3.1	16.6	0.1	0.9
8.1	2684	24	0.01	6.4E-4	0.60	379.20	0.9	.0512	4.4	16.9	0.2	0.6
14.1	3284	33	0.01	2.6E-4	0.01	371.47	0.7	.0464	3.0	17.3	0.1	0.0
4.1	3107	23	0.01	---	-0.11	370.00	0.8	.0455	3.3	17.4	0.1	-0.1
5.2	*8448*	*123*	*0.01*	*2.9E-4*	*0.31*	*367.78*	*0.5*	*.0488*	*2.1*	*17.4*	*0.1*	*0.3*

Spot	U (ppm)	Th (ppm)	$^{232}Th/^{238}U$	$^{204}Pb/^{206}Pb$	Cm ^{206}Pb (%)	$^{238}U/^{206}Pb$*	Error (%)	$^{207}Pb/^{206}Pb$*	Error (%)	$^{206}Pb/^{238}U$ age# (Ma)	Error (%)	Discordance (%)
28.1	4574	39	0.01	1.3E-4	0.16	361.24	0.6	.0477	2.5	17.8	0.1	0.2
9.1	3820	39	0.01	2.4E-4	0.39	358.68	0.7	.0495	2.7	17.9	0.1	0.4
25.1	2636	30	0.01	5.3E-4	0.43	352.21	0.8	.0498	3.2	18.2	0.2	0.4
6.1	2562	31	0.01	2.0E-4	0.24	349.65	0.8	.0483	3.4	18.4	0.2	0.2
1.1	5029	65	0.01	---	-0.11	339.02	0.7	.0455	2.1	19.0	0.1	-0.1
2.1	4206	55	0.01	1.4E-4	0.22	336.11	0.9	.0482	2.2	19.1	0.2	0.2
3.1	4579	42	0.01	---	0.12	331.36	0.6	.0474	2.4	19.4	0.1	0.1
20.1	5632	50	0.01	1.3E-4	0.36	319.29	0.5	.0492	2.2	20.1	0.1	0.4
11.1	7501	84	0.01	5.9E-5	-0.11	303.15	0.5	.0456	1.9	21.3	0.1	-0.1
13.1	5679	40	0.01	2.1E-4	0.87	298.26	0.6	.0534	2.7	21.4	0.1	0.9
10.1	5225	68	0.01	7.5E-5	0.18	284.12	0.5	.0479	2.1	22.6	0.1	0.2
15.1	15977	118	0.01	6.6E-5	0.18	262.93	0.3	.0479	1.1	24.4	0.1	0.2
16.1	*5798*	*119*	*0.02*	*4.0E-4*	*0.69*	*259.31*	*0.6*	*.0520*	*2.0*	*24.6*	*0.1*	*0.7*
10.2	4953	41	0.01	1.0E-5	0.09	13.90	0.2	.0566	1.8	447.5	1.0	1.3
29.1	712	54	0.08	1.4E-5	11.05	9.56	1.5	.1494	0.9	573.4	8.6	13.0
DBH 080												
1.1	1609	9	0.01	1.9E-4	-0.02	406.06	1.3	.0462	3.7	15.9	0.2	0.0
27.1	1821	12	0.01	1.8E-4	0.17	394.36	1.3	.0477	4.5	16.3	0.2	0.2
9.2	1761	10	0.01	5.6E-4	0.15	393.52	1.4	.0475	3.8	16.3	0.2	0.1
5.1	2179	23	0.01	1.4E-4	1.05	384.98	1.1	.0547	3.0	16.5	0.2	1.0
5.3	1960	21	0.01	3.9E-4	0.65	379.74	1.2	.0515	3.3	16.8	0.2	0.6
25.1	1805	10	0.01	---	0.12	379.69	1.2	.0473	3.5	16.9	0.2	0.1
22.2	1978	20	0.01	4.8E-4	0.73	373.20	1.4	.0521	3.4	17.1	0.2	0.7
17.1	2027	21	0.01	5.8E-4	0.42	373.09	1.3	.0497	3.6	17.2	0.2	0.4
15.1	1720	12	0.01	---	-0.22	374.53	1.3	.0447	3.8	17.2	0.2	-0.2
1.2	*3314*	*35*	*0.01*	*1.9E-4*	*0.74*	*358.97*	*0.8*	*.0522*	*2.3*	*17.8*	*0.2*	*0.7*
22.1	3938	35	0.01	6.6E-5	0.24	324.86	0.9	.0483	2.1	19.8	0.2	0.2
5.2	*5551*	*86*	*0.02*	*8.2E-5*	*0.87*	*311.30*	*0.6*	*.0534*	*2.3*	*20.5*	*0.1*	*0.9*
12.1	*7566*	*124*	*0.02*	*1.7E-4*	*0.60*	*311.97*	*0.7*	*.0511*	*1.6*	*20.5*	*0.1*	*0.6*
11.1	*6175*	*63*	*0.01*	*8.5E-5*	*0.06*	*310.33*	*0.6*	*.0469*	*1.7*	*20.7*	*0.1*	*0.1*
9.1	*7479*	*157*	*0.02*	*---*	*0.17*	*306.47*	*0.6*	*.0478*	*1.6*	*21.0*	*0.1*	*0.2*

Spot	U (ppm)	Th (ppm)	$^{232}Th/^{238}U$	$^{204}Pb/^{206}Pb$	Cm ^{206}Pb (%)	$^{238}U/^{206}Pb$*	Error (%)	$^{207}Pb/^{206}Pb$*	Error (%)	$^{206}Pb/^{238}U$ age# (Ma)	Error (%)	Discordance (%)
2.2	*4001*	*47*	*0.01*	*4.8E-4*	*0.23*	*277.28*	*0.7*	*.0483*	*1.9*	*23.2*	*0.2*	*0.2*
BH 225												
13.1DKR	2529	47	0.02	1.6E-3	1.26	580.30	0.6	.0562	6.8	11.0	0.1	1.2
5.1DKR	2600	42	0.02	7.7E-5	0.28	584.29	0.7	.0485	3.2	11.0	0.1	0.3
7.1DKR	3066	381	0.13	7.4E-4	2.24	567.45	0.6	.0639	4.4	11.1	0.1	2.2
35.1GInt	*563*	*60*	*0.11*	*-5.1E-4*	*0.70*	*554.41*	*1.3*	*.0518*	*5.8*	*11.6*	*0.2*	*0.7*
35.3DKR	4022	63	0.02	5.3E-5	1.15	551.14	0.6	.0553	2.6	11.6	0.1	1.1
25.3DKR	3488	58	0.02	-1.3E-4	-0.09	557.39	0.7	.0456	3.2	11.6	0.1	-0.1
46.1DKR	4726	557	0.12	2.0E-4	0.29	552.21	1.9	.0486	2.3	11.6	0.2	0.3
65.1DKR	2862	51	0.02	-1.9E-6	0.19	549.21	0.6	.0478	2.9	11.7	0.1	0.2
2.1DKR	3025	99	0.03	4.4E-5	0.08	548.68	0.6	.0469	2.9	11.7	0.1	0.1
39.1DKR	4522	142	0.03	-7.9E-5	-0.05	542.96	0.5	.0459	2.5	11.9	0.1	-0.1
30.2DKR	5031	29	0.01	-2.3E-6	0.22	533.71	0.5	.0480	2.4	12.1	0.1	0.2
34.1DKR	3098	89	0.03	1.3E-3	1.85	523.35	0.7	.0609	2.4	12.1	0.1	1.8
6.1DKR	3393	1105	0.34	2.6E-3	4.18	510.68	0.6	.0793	2.1	12.1	0.1	4.1
21.2GR	*1873*	*93*	*0.05*	*-2.1E-4*	*0.12*	*531.05*	*0.9*	*.0472*	*4.0*	*12.1*	*0.1*	*0.1*
43.1DKR	2708	87	0.03	1.3E-4	0.10	529.83	0.7	.0471	3.1	12.2	0.1	0.1
27.1DKR	4617	118	0.03	-9.0E-5	0.09	529.09	0.6	.0470	2.6	12.2	0.1	0.1
56.1DKR	3975	963	0.25	3.0E-4	1.21	518.28	0.6	.0558	2.4	12.3	0.1	1.2
33.1DKR	1978	43	0.02	4.0E-4	0.90	518.96	0.9	.0534	3.9	12.3	0.1	0.9
51.1DKR	4211	98	0.02	-9.0E-5	0.53	519.26	0.6	.0504	2.5	12.4	0.1	0.5
31.1GInt	*500*	*44*	*0.09*	*5.6E-4*	*0.15*	*520.79*	*1.5*	*.0475*	*6.8*	*12.4*	*0.2*	*0.1*
42.1DKR	4221	16	0.00	2.8E-4	0.36	510.71	0.5	.0491	2.3	12.6	0.1	0.3
3.1DKR	4386	3840	0.90	1.9E-3	2.23	489.79	0.5	.0639	2.0	12.9	0.1	2.2
54.1G	*1245*	*89*	*0.07*	*-1.1E-3*	*1.08*	*492.12*	*1.0*	*.0548*	*4.4*	*13.0*	*0.1*	*1.1*
22.2DKR	5634	1924	0.35	8.2E-4	1.53	482.71	0.5	.0584	8.3	13.2	0.1	1.5
15.1DKR	3529	6154	1.80	5.0E-3	7.33	430.27	0.6	.1043	2.2	13.9	0.1	7.3
23.1DKR	7821	128	0.02	4.7E-4	0.52	456.95	0.4	.0504	2.1	14.0	0.1	0.5
23.2GInt	*2758*	*41*	*0.02*	*-1.1E-4*	*0.20*	*434.66*	*0.6*	*.0479*	*2.8*	*14.8*	*0.1*	*0.2*
49.1DKR	3169	116	0.04	1.1E-4	0.45	418.98	0.5	.0499	2.4	15.3	0.1	0.4
47.1GInt	*644*	*54*	*0.09*	*4.3E-3*	*9.77*	*332.29*	*1.0*	*.1236*	*3.0*	*17.5*	*0.2*	*9.7*

Spot	U (ppm)	Th (ppm)	$^{232}Th/^{238}U$	$^{204}Pb/^{206}Pb$	Cm ^{206}Pb (%)	$^{238}U/^{206}Pb$*	Error (%)	$^{207}Pb/^{206}Pb$*	Error (%)	$^{206}Pb/^{238}U$ age# (Ma)	Error (%)	Discordance (%)
3.2GInt	*152*	*3*	*0.02*	*-1.2E-3*	*-0.03*	*352.94*	*2.1*	*.0461*	*9.7*	*18.3*	*0.4*	*0.0*
16.1GInt	*984*	*15*	*0.02*	*2.2E-4*	*0.13*	*327.87*	*0.9*	*.0475*	*4.2*	*19.6*	*0.2*	*0.1*
59.1GInt	*610*	*3*	*0.01*	*-1.2E-5*	*0.33*	*307.06*	*1.0*	*.0490*	*6.2*	*20.9*	*0.2*	*0.3*
57.1GInt	*739*	*12*	*0.02*	*-1.9E-4*	*0.07*	*239.81*	*0.8*	*.0471*	*3.8*	*26.9*	*0.2*	*0.1*
21.3GInt	*589*	*4*	*0.01*	*-3.9E-6*	*-0.56*	*227.13*	*1.7*	*.0422*	*4.5*	*28.5*	*0.5*	*-0.5*
45.1DKR	3247	86	0.03	-1.2E-6	1.96	119.47	0.4	.0626	1.5	52.8	0.2	2.0
2.2GInt	*459*	*19*	*0.04*	*-4.5E-6*	*1.12*	*77.37*	*0.6*	*.0566*	*2.5*	*82.0*	*0.5*	
41.1C	955	307	0.33	3.7E-5	0.80	27.79	0.4	.0571	1.1	226.5	0.9	
13.2Int	96	62	0.67	-5.8E-6	1.12	18.95	0.8	.0620	2.5	328.5	2.8	
3.3C	83	55	0.68	-9.3E-5	-0.03	14.70	0.8	.0551	2.5	424.9	3.5	
2.3C	1520	239	0.16	-1.2E-7	0.11	14.30	0.2	.0565	0.6	436.0	0.9	
43.2GInt	282	183	0.67	-3.0E-5	0.22	13.57	0.6	.0579	1.4	458.0	2.6	
1.1C	219	195	0.92	-3.3E-5	0.09	13.03	0.5	.0574	1.4	477.0	2.4	
6.2GInt	184	153	0.86	3.5E-5	-0.02	12.93	0.6	.0566	1.6	481.2	2.7	
21.1GInt	142	92	0.67	1.9E-5	0.12	12.83	0.7	.0578	1.9	483.9	3.4	
5.2GInt	122	109	0.92	-5.4E-5	-0.01	12.82	0.8	.0567	1.9	485.0	3.7	
65.2GInt	190	120	0.65	-8.3E-7	0.05	12.75	0.6	.0573	1.6	487.3	2.8	
15.2GInt	199	172	0.90	-3.6E-5	-0.07	12.62	0.5	.0564	1.5	492.6	2.6	
46.2GInt	239	81	0.35	-2.8E-5	-0.16	12.59	0.5	.0557	1.3	494.4	2.4	
30.1GInt	139	122	0.90	-6.0E-5	-0.17	12.53	0.7	.0558	1.9	496.4	3.4	
23.3C	1605	204	0.13	-5.8E-6	-0.05	12.42	0.7	.0568	0.6	500.3	3.3	
16.2Int	228	145	0.66	-2.1E-4	0.16	12.38	0.6	.0585	1.6	500.9	2.9	
22.1C	218	198	0.94	-1.3E-6	0.06	12.38	0.5	.0577	1.5	501.2	2.7	
28.1GInt	771	327	0.44	-1.1E-7	-0.09	12.39	0.3	.0565	0.8	501.7	1.5	
35.2C	253	380	1.55	1.1E-4	-0.12	12.22	0.5	.0565	1.3	508.4	2.5	
46.3C	539	246	0.47	2.0E-5	-0.02	12.20	0.3	.0573	0.9	508.8	1.6	
50.1C	950	336	0.37	4.1E-6	0.18	12.13	0.2	.0590	1.2	510.6	1.3	
56.2G	138	159	1.19	-2.0E-4	0.04	12.09	0.7	.0579	1.9	512.7	3.5	
15.3Int	191	174	0.94	-4.1E-5	-0.28	12.12	0.7	.0553	1.6	513.4	3.6	
59.2C	1229	977	0.82	4.1E-4	0.70	11.96	0.3	.0633	0.9	514.9	1.4	
49.2C	183	145	0.82	-1.2E-6	-0.16	11.97	0.6	.0564	1.6	518.8	3.0	

Spot	U (ppm)	Th (ppm)	$^{232}Th/^{238}U$	$^{204}Pb/^{206}Pb$	Cm ^{206}Pb (%)	$^{238}U/^{206}Pb$*	Error (%)	$^{207}Pb/^{206}Pb$*	Error (%)	$^{206}Pb/^{238}U$ age# (Ma)	Error (%)	Discordance (%)
42.1GInt	1155	812	0.73	1.0E-4	0.05	11.93	0.2	.0581	0.6	519.4	1.2	
25.2C	196	184	0.97	-4.7E-5	-0.10	11.95	0.6	.0569	1.7	519.5	3.2	
44.1C	528	238	0.47	-1.5E-5	-0.01	11.89	0.4	.0577	1.5	521.2	1.9	
52.1GInt	819	26	0.03	-8.6E-6	-0.21	11.57	0.3	.0564	1.8	536.3	1.8	
32.1GInt	309	100	0.34	-2.0E-5	1.09	11.32	0.5	.0672	1.0	541.0	2.6	
25.1GInt	1339	169	0.13	4.1E-6	-0.26	10.70	0.2	.0572	0.5	578.2	1.3	
27.2BInt	213	63	0.31	-5.3E-7	0.95	10.47	0.6	.0672	4.1	583.4	4.1	
54.2C	104	124	1.23	-8.6E-7	-0.48	9.50	0.7	.0574	3.1	649.3	4.8	
4.2C	155	112	0.74	-3.5E-5	0.51	9.18	0.6	.0659	1.4	664.0	3.9	
10.1C	213	74	0.36	-2.0E-5	0.56	8.47	0.5	.0679	2.4	716.8	4.0	
4.1G	277	111	0.41	1.7E-5	0.07	8.23	0.5	.0645	1.9	740.3	3.9	
32.2C	757	740	1.01	-5.6E-6	0.20	7.79	0.3	.0668	0.6	778.6	2.0	
53.1C	1181	59	0.05	-1.4E-5	-0.26	7.40	1.3	.0643	0.9	819.9	10.5	

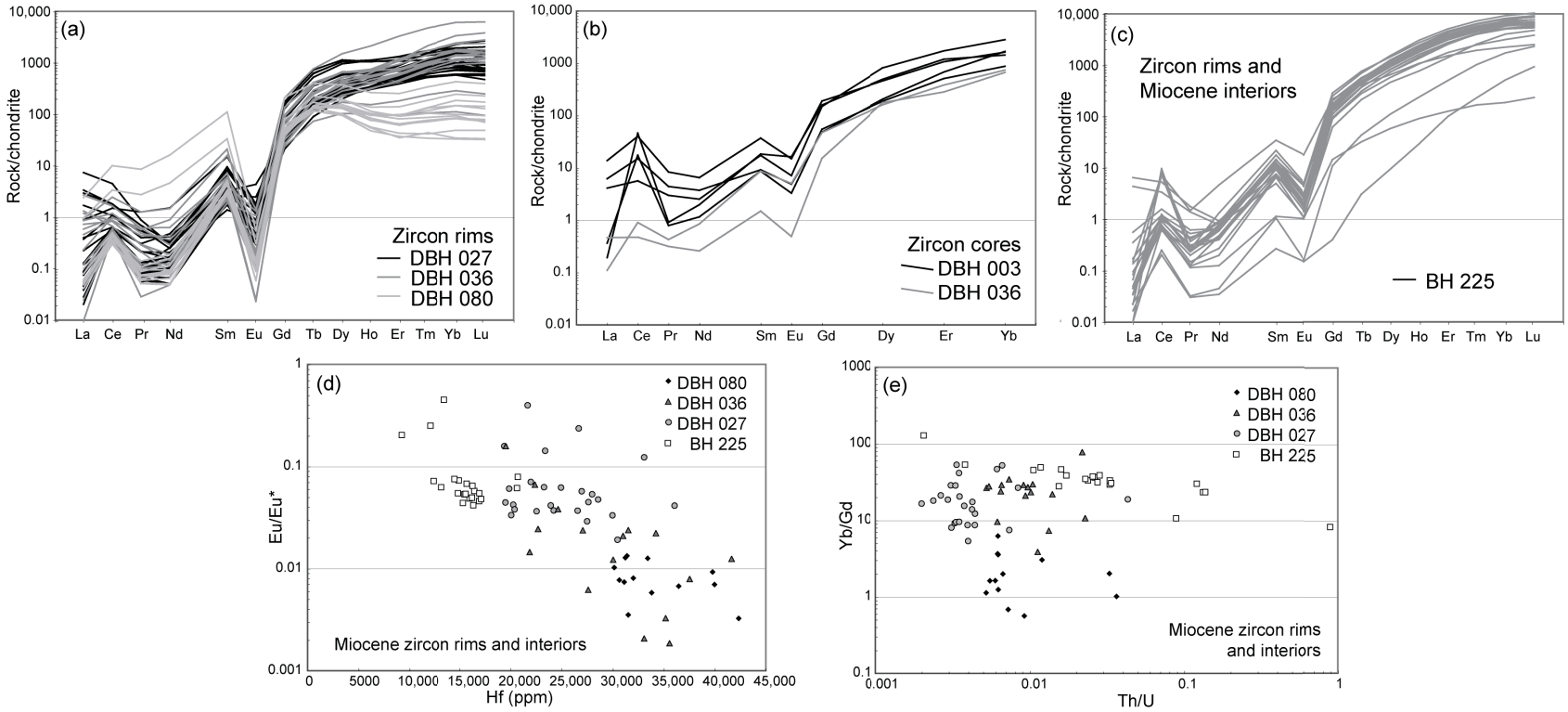

Figure 2.5: SHRIMP-RG trace-element geochemistry of zircon. (a) REE pattern of zircon rims for three samples from the hanging wall of the O-STD. (b) REE patterns of zircon cores from the same samples. (c) REE pattern for zircon rims and Miocene grey zircon interiors from the footwall of the I-STD. (d) Eu/Eu* against Hf indicating an inverse correlation. (e) Yb/Gd against Th/U indicating generally low Th/U ratios and the depletion of HREEs, especially for DBH 080. Analyses that exhibit anomalous zircon trace element geochemistry indicating inclusions and/or problem analyses are shown in the full data tables, but have been removed from the figure plots.

Figure 2.6: SHRIMP-RG U-Pb geochronology of zircon rims and cores. Sample locations are shown in Figures 2.2 and 2.3. For (a)-(e), the left plot is a weighted mean age plot (with calculated mean age), while the right plot is a Tera-Wasserburg concordia diagram of zircon rims. For (a)-(d), only $\geq 99\%$ concordant data are shown in the weighted mean plots. In the Tera-Wasserburg concordia diagrams, discordant data are also shown in grey. For (e), in the weighted mean plots, black bars indicate rims, grey bars indicate grey (under CL) interior zircon, while in the Tera-Wasserburg diagram, the open circles show grey interior zircon, and discordant data are in grey. (f) Concordia diagram showing Paleozoic and Proterozoic cores from sample BH 225. (g) Concordia diagram showing Paleozoic and Proterozoic cores from sample DBH 003. (h) Plot of $^{206}Pb/^{238}U$ zircon age against U indicating high U content ($>$2500 ppm) appears to influence U-Pb SHRIMP ages. *Ages are ^{207}Pb corrected. Zircons are imaged by backscattered electrons (left) and cathodoluminescence (right), and dashed circles denote spots for U-Pb analyses while dotted circles denote spots for both U-Pb and Ti-in-zircon analyses.

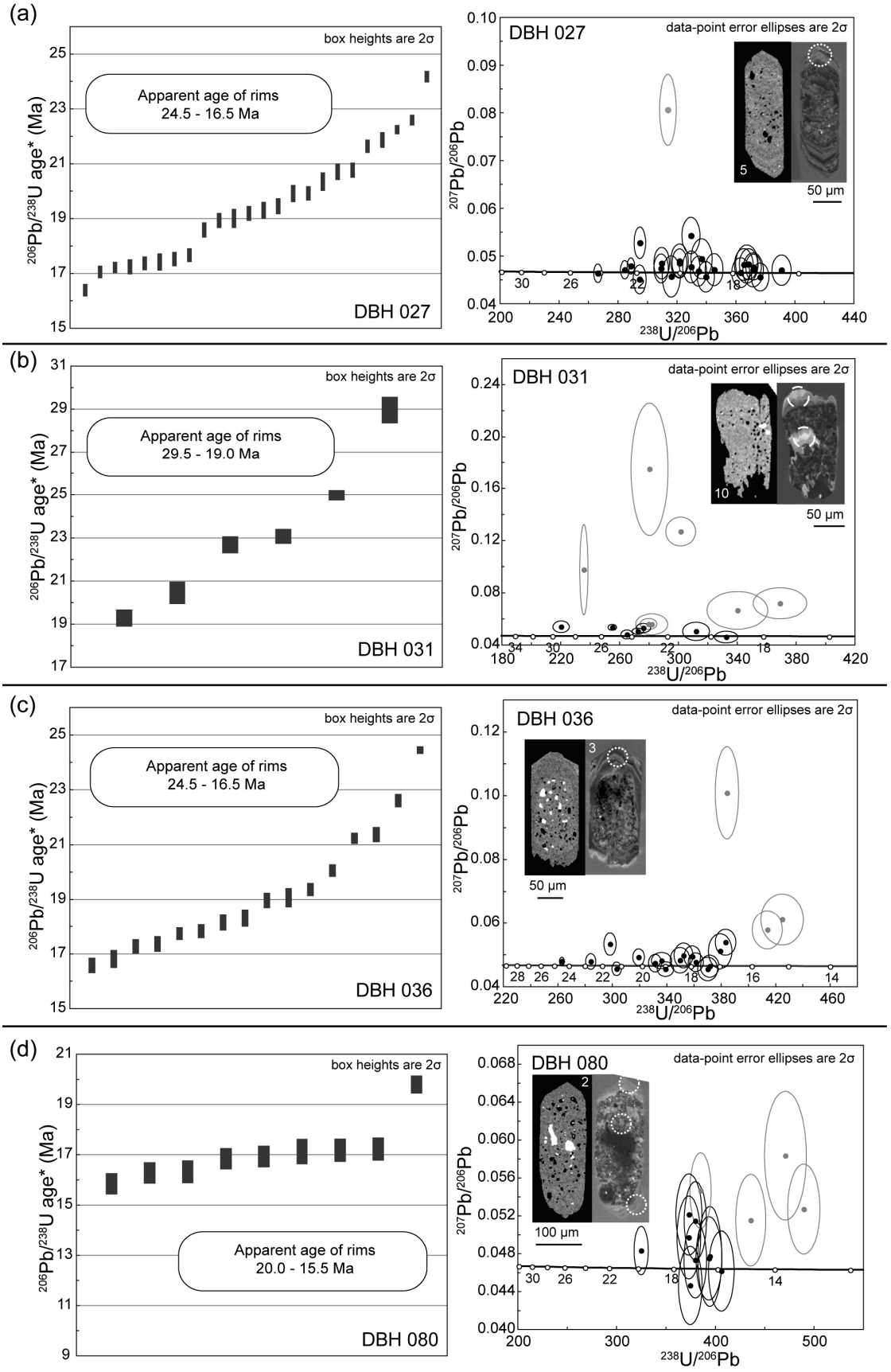
(a)
box heights are 2σ
Apparent age of rims
24.5 - 16.5 Ma
DBH 027
$^{206}Pb/^{238}U$ age* (Ma)
DBH 027
data-point error ellipses are 2σ
5
50 μm
$^{207}Pb/^{206}Pb$
$^{238}U/^{206}Pb$
(b)
box heights are 2σ
Apparent age of rims
29.5 - 19.0 Ma
DBH 031
$^{206}Pb/^{238}U$ age* (Ma)
DBH 031
data-point error ellipses are 2σ
10
50 μm
$^{207}Pb/^{206}Pb$
$^{238}U/^{206}Pb$
(c)
box heights are 2σ
Apparent age of rims
24.5 - 16.5 Ma
DBH 036
$^{206}Pb/^{238}U$ age* (Ma)
DBH 036
data-point error ellipses are 2σ
3
50 μm
$^{207}Pb/^{206}Pb$
$^{238}U/^{206}Pb$
(d)
box heights are 2σ
Apparent age of rims
20.0 - 15.5 Ma
DBH 080
$^{206}Pb/^{238}U$ age* (Ma)
DBH 080
data-point error ellipses are 2σ
2
100 μm
$^{207}Pb/^{206}Pb$
$^{238}U/^{206}Pb$

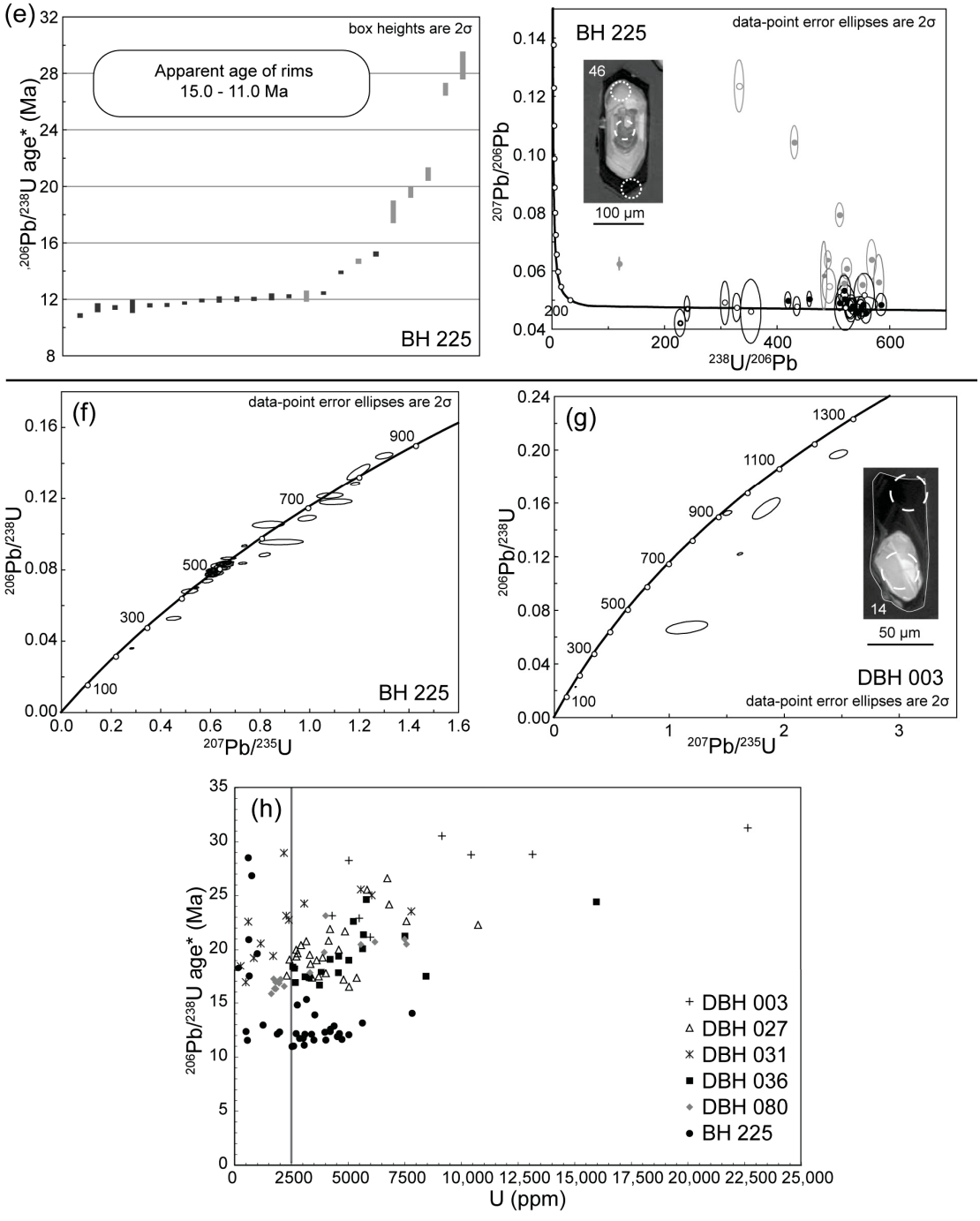
(e)
box heights are 2σ
Apparent age of rims
15.0 - 11.0 Ma
BH 225
$^{206}Pb/^{238}U$ age* (Ma)
BH 225
data-point error ellipses are 2σ
46
100 µm
200
$^{207}Pb/^{206}Pb$
$^{238}U/^{206}Pb$
(f)
data-point error ellipses are 2σ
100
300
500
700
900
BH 225
$^{206}Pb/^{238}U$
$^{207}Pb/^{235}U$
(g)
100
300
500
700
900
1100
1300
14
50 µm
DBH 003
data-point error ellipses are 2σ
$^{206}Pb/^{238}U$
$^{207}Pb/^{235}U$
(h)
DBH 003
DBH 027
DBH 031
DBH 036
DBH 080
BH 225
$^{206}Pb/^{238}U$ age* (Ma)
U (ppm)

>2500 ppm has been reported as causing a systematic bias toward older apparent U-Pb ages in SHRIMP analyses independent of the zircon age (Williams and Hergt, 2000). We observe a broad positive correlation between U content and age in our samples (Fig. 2.6h). This may provide an explanation for the observed spread of ages along concordia. For a systematic analytical bias it should be possible to regress the age data back to a common hinge point at 2500 ppm, giving the "true" age of the zircon rims (e.g., Larson, 2009). However, if there is such a bias in apparent zircon age, it is not consistent within our samples. Furthermore, DBH 080, for which the U content of the zircon rims is entirely below 2500 ppm, still displays a spread along concordia in apparent age from ca. 20.5-15.5 Ma, though a smaller age range than observed in other samples. Thus while we agree that there is likely some bias on U-Pb age due to high U content, we argue that it is not consistent and thus cannot be quantified or corrected for in this data set. Since we use the youngest zircon ages for each sample (all of which have U contents <2500 ppm) to constrain the timing of ductile deformation, this potential bias does not affect our conclusions.

2.7.4 TI-IN-ZIRCON THERMOMETRY

The crystallization temperature of zircon was estimated using Ti-in-zircon thermometry (Watson et al., 2006). Spot locations are adjacent to the spots for U-Pb analyses of the same zircons and have the same labels; analytical procedures can be found in Appendix D. Data collected from zircon rims are shown in Table 2.2 and the results are plotted in Figure 2.7 against coincident SHRIMP U-Pb spot ages using the revised calibration of Ferry and Watson (2007). The calculated Ti-in-zircon temperatures are uncorrected for pressure.

Since quartz is abundant in the leucogranites, a_{SiO2} can be considered to be 1.0. For most igneous rocks, a_{TiO2} is ≥ 0.5 (Watson and Harrison, 2005). The studied leucogranites do not contain any Ti-bearing phases such as rutile, an indication that $a_{TiO2} < 1.0$. Our data are calculated for a_{TiO2} = 0.5 (Fig. 2.7), which probably represent maximum temperatures. For comparison, calculations of Ti-in-zircon temperatures for a_{TiO2} = 1.0 (which represent minimum temperatures) are also listed in Table 2.2, and in general are ca. 30-40 °C lower.

In the Ura area, apparent crystallization temperatures range from ca. 620 to 500 °C for zircons with apparent ages ca. 20.5-15.5 Ma, with no obvious T-t trend (Fig. 2.7a). In the Lingshi area, zircons have slightly higher apparent crystallization temperatures of between ca. 750 and 550 °C during ca. 25.0-16.5 Ma (DBH 036, Fig. 2.7b) and ca. 750

Table 2.2: Ti-in-zircon data. Temperatures calculated using recalibrations from Ferry and Watson, 2007. The range of possible Ti activities are bracketed by a_{TiO2} = 0.5 and a_{TiO2} = 1.0 (see text for further explanation). * estimated from Ferry and Watson (2007) error in empirical correlation.

Spot	^{48}Ti (ppm)	^{49}Ti (ppm)	T (C), a_{TiO2} = 0.5	T (C), a_{TiO2} = 1.0	Error (2σ)*	Age (Ma)	Error (2σ)	Hf (ppm)
DBH 080								
DBH080-1.1	0.1935	0.1803	507.0	470.6	20.0	15.9	0.4	39934
DBH080-27.1	0.2315	0.2016	513.2	476.2	20.0	16.3	0.4	31088
DBH080-9.2	0.2070	0.1598	500.4	464.6	20.0	16.3	0.5	39748
DBH080-5.1	0.4283	0.3370	543.0	503.3	20.0	16.5	0.4	30621
DBH080-5.3	0.8343	0.6845	588.1	543.9	20.0	16.8	0.4	33775
DBH080-25.1	0.2112	0.1489	496.6	461.2	20.0	16.9	0.4	31983
DBH080-22.2	0.6286	0.5460	573.2	530.5	20.0	17.1	0.5	30122
DBH080-17.1	0.1242	0.2140	516.5	479.3	20.0	17.2	0.5	42314
DBH080-15.1	0.1721	0.1707	504.0	467.9	20.0	17.2	0.5	36431
DBH080-1.2	1.1078	1.0869	620.2	572.8	20.0	17.8	0.3	29568
DBH080-22.1	0.3427	0.2816	532.3	493.6	20.0	19.8	0.4	33397
DBH080-5.2	1.0246	1.0215	615.8	568.8	20.0	20.5	0.2	29555
DBH080-12.1	0.4550	0.4464	560.3	518.9	20.0	20.5	0.3	30968
DBH080-11.1	0.4305	0.4125	555.4	514.4	20.0	20.7	0.3	28716
DBH080-9.1	1.2308	1.2853	632.5	583.8	20.0	21.0	0.2	46375
DBH080-2.2B	1.6994	1.9034	662.6	610.7	20.0	23.2	0.3	31463
DBH 036								
DBH036-1.1	0.5273	0.5391	572.3	529.8	20.0	19.0	0.1	37510
DBH036-2.1	4.3483	4.6925	740.0	679.5	20.0	19.1	0.2	35156
DBH036-3.1	0.5991	0.6369	583.2	539.6	20.0	19.4	0.1	34198
DBH036-4.1	1.1801	1.1855	626.5	578.5	20.0	17.4	0.1	21826
DBH036-5.2	3.6385	3.1928	705.4	648.9	20.0	17.4	0.1	26119
DBH036-6.1	0.7996	0.6321	582.7	539.2	20.0	18.4	0.2	33052
DBH036-8.1	4.3681	3.4362	711.8	654.5	20.0	16.9	0.2	31504
DBH036-9.1	1.4272	1.1120	621.9	574.3	20.0	17.9	0.1	27037
DBH036-10.1	2.1335	2.1713	673.1	620.1	20.0	22.6	0.1	19487
DBH036-11.1	1.6549	1.7400	655.5	604.4	20.0	21.3	0.1	27565
DBH036-13.1	2.9755	3.1962	705.5	648.9	20.0	21.4	0.1	22659
DBH036-14.1	0.7730	0.6595	585.6	541.7	20.0	17.3	0.1	35533
DBH036-15.1	1.8477	1.9203	663.3	611.4	20.0	24.4	0.1	24614
DBH036-16.1	5.5719	5.3112	751.6	689.7	20.0	24.6	0.1	64358

Spot	^{48}Ti (ppm)	^{49}Ti (ppm)	T (C), a_{TiO2} = 0.5	T (C), a_{TiO2} = 1.0	Error (2σ)*	Age (Ma)	Error (2σ)	Hf (ppm)
DBH036-19.1	1.7432	1.5998	649.0	598.6	20.0	16.6	0.1	30010
DBH036-20.1	1.9416	1.8146	658.8	607.4	20.0	20.1	0.1	22349
DBH036-25.1	1.0492	0.9362	609.6	563.3	20.0	18.2	0.2	41626
DBH036-28.1	1.3467	1.3447	635.9	586.9	20.0	17.8	0.1	30983
DBH 027								
DBH027-2.2	1.3559	1.3505	636.2	587.1	20.0	22.2	0.2	29951
DBH027-A4.1	1.1044	0.9270	608.9	562.7	20.0	19.0	0.3	27945
DBH027-A2.1	0.8304	0.8535	603.1	557.5	20.0	17.3	0.3	30434
DBH027-6.1	2.3576	1.9230	663.4	611.5	20.0	20.0	0.3	27586
DBH027-2.1	1.2158	1.0749	619.4	572.1	20.0	21.7	0.2	26530
DBH027-14.1	1.3894	1.1895	626.8	578.7	20.0	24.2	0.2	22503
DBH027-17.1	1.6837	1.4962	643.9	594.0	20.0	20.8	0.3	23236
DBH027-1.1	1.1765	1.0781	619.6	572.3	20.0	19.5	0.3	27452
DBH027-14.3	1.1262	1.2513	630.5	582.1	20.0	20.4	0.3	20227
DBH027-19.2	0.9237	0.9289	609.0	562.8	20.0	17.5	0.3	36031
DBH027-A11.1	1.0627	1.0132	615.2	568.3	20.0	18.6	0.3	23904
DBH027-20.1	1.1237	1.1415	623.8	576.0	20.0	21.9	0.3	21937
DBH027-15.1	0.9190	0.7934	598.1	552.9	20.0	19.6	0.3	19454
DBH027-1.2	1.0724	1.0140	615.2	568.4	20.0	19.0	0.3	20351
DBH027-A11.2	0.8130	0.9223	608.5	562.3	20.0	19.2	0.3	23356
DBH027-19.1	1.5735	1.5111	644.7	594.7	20.0	19.3	0.3	21630
DBH027-A4.2	1.1247	1.1168	622.2	574.6	20.0	19.9	0.3	19821
DBH027-A3.1	0.7578	0.7129	590.8	546.4	20.0	22.6	0.2	20022
DBH027-5.1	0.6278	0.3501	545.3	505.4	20.0	20.7	0.3	28530
DBH027-A12.1	0.6593	0.8446	602.4	556.8	20.0	17.1	0.2	24196
DBH027-A1.2	0.6569	0.5968	579.0	535.7	20.0	17.7	0.2	24905
DBH027-A1.1	0.8875	0.6325	582.8	539.2	20.0	17.4	0.2	26923
DBH027-9.1	3.6280	3.6055	716.1	658.3	20.0	17.6	0.3	33052
DBH027-11.1	2.0719	1.9463	664.4	612.3	20.0	17.3	0.2	26639
DBH027-A5.1	0.9701	1.1191	622.3	574.7	20.0	16.5	0.2	19341

and 550 °C during ca. 24.5-16.0 Ma (DBH 027, Fig. 2.7c). Neither sample displays a T-t trend during zircon crystallization. In contrast, apparent crystallization temperatures for BH 225 from the I-STD range from ca. 820 to 670 °C during ca. 15.5-11.0 Ma (Fig. 2.7d). The observed spread in apparent temperature at any given time (100-150 °C) may be due to local variations in Ti concentration during zircon crystallization, or the sampling of Ti-rich and Ti-poor subdomains in various analyses (Fu et al., 2008).

For all samples, there is an inverse correlation between Hf values and Ti-in-zircon crystallization temperatures (Fig. 2.7e). This has been observed in general for zircon (Fu et al., 2008) and can be taken as a reflection of the increasing degree of fractionation from least fractionated (BH 225) to most fractionated (DBH 080) (Claiborne et al., 2006). Thus in general, all the O-STD samples are more fractionated than the I-STD sample.

Some apparent crystallization temperatures calculated for zircon rims from the O-STD samples DBH 036, DBH 027 and especially DBH 080 are lower than even a minimum estimate for the solidus of the leucogranites of ca. 600-650 °C, assuming a pressure of ca. 4-6 kbar at the time of crystallization (Fig. 2.7; Davidson et al, 1997). However, the leucogranites contain abundant apatite and tourmaline, which suggests that the magmas contained high concentrations of B, P, H_2O and possibly other fluxes. At emplacement pressures of $>$ ca. 2.7 kbar, high concentrations of fluxing elements may lower the solidus of granitic-pegmatitic melts to as low as ca. 400-350 °C (Sirbescu and Nabelek, 2003). The Ti-in-zircon temperatures, tartan twinning in K-feldspar and presence of late subsolidus sillimanite indicate that crystallization of the studied leucogranites took place at $>$550 °C, but possibly at or below an average solidus of ca. 650 °C. The Ti-in-zircon thermometer was calibrated for P = 10 kbar, and crystallization at lower pressures may cause temperature to be underestimated by up to 50 °C (Ferry and Watson, 2007). Although there may be other, non-temperature related factors influencing Ti concentrations (see Fu et al., 2008) the apparent Ti-in-zircon temperatures are consistent with our geochemical observations that the leucogranites crystallized at low temperature.

Figure 2.7: Ti-in-zircon thermometry combined with U-Pb zircon ages, $^{40}Ar/^{39}Ar$ cooling ages for muscovite and regional cooling ages for apatite fission track (AFT) from Grujic et al. (2006) and I. Coutand (2008 personal commun.). (a) DBH 080 from the Ura area, including the $^{40}Ar/^{39}Ar$ cooling age for muscovite obtained from the same sample. (b) DBH 036 from the Lingshi area, including the $^{40}Ar/^{39}Ar$ cooling age for other Lingshi samples DBH 003 and DBH 027. (c) DBH 027 from the Lingshi area with $^{40}Ar/^{39}Ar$ cooling age for muscovite from the same sample, and from other Lingshi sample DBH 003 for reference. (d) BH 225 from the Masang Kang area. A steep cooling path can be inferred from regional muscovite and biotite $^{40}Ar/^{39}Ar$ cooling ages of ca. 11-10 Ma (e.g., Maluski et al., 1988; Chakungal, 2006). (e) Ti-in-zircon temperature against measured Hf, indicating that the O-STD zircons (all DBH samples) are more fractionated than the I-STD zircons (BH 225). *Temperatures shown are calculated for a_{TiO2} = 0.5. Granite solidi shown in (a) to (d) are approximated for ca. 3 kbar (after Scaillet et al., 1995; Sirbescu and Nabelek, 2003).

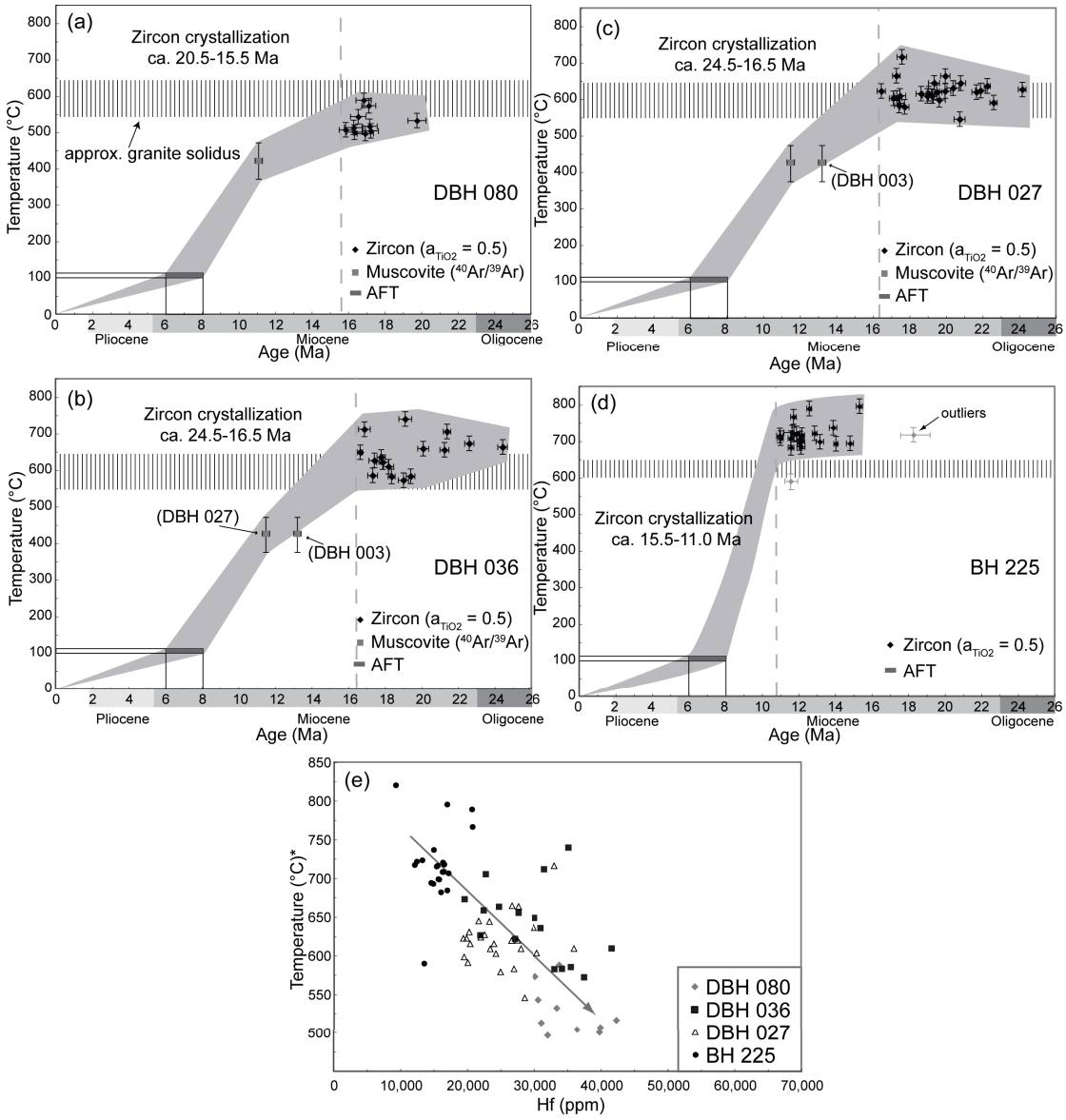
(a)
Zircon crystallization
ca. 20.5-15.5 Ma
approx. granite solidus
DBH 080
Zircon (a_{TiO2} = 0.5)
Muscovite ($^{40}Ar/^{39}Ar$)
AFT
Temperature (°C)
Age (Ma)
Pliocene
Miocene
Oligocene
(c)
Zircon crystallization
ca. 24.5-16.5 Ma
(DBH 003)
DBH 027
(b)
Zircon crystallization
ca. 24.5-16.5 Ma
(DBH 027)
(DBH 003)
DBH 036
(d)
outliers
Zircon crystallization
ca. 15.5-11.0 Ma
BH 225
(e)
Temperature (°C)*
Hf (ppm)
DBH 080
DBH 036
DBH 027
BH 225

2.8 MUSCOVITE ^{40}AR/^{39}AR THERMOCHRONOLOGY

2.8.1 MUSCOVITE CHARACTERIZATION

Muscovite from four leucogranite samples (DBH 003 and DBH 027 from the Lingshi area and DBH 067 and DBH 080 from the Ura area; Figs. 2.2, 2.3) were selected for step heat ^{40}Ar/^{39}Ar thermochronology to determine cooling ages of the leucogranite bodies in the hanging wall of the O-STD. Muscovite makes up between 10-25% of the samples, and is anhedral and coarse grained (up to 500 μm in length), with little recrystallization. Muscovite grains in samples DBH 003, 067 and 080 show a weak preferred orientation. Muscovite in sample DBH 027 has a preferred orientation that, along with deformed Qtz grains, defines a foliation in the granite sub-parallel to the main foliation in the host rock.

The ^{40}Ar/^{39}Ar thermochronology of bulk coarse-grained (ca. 200 μm average diameter) muscovite separates was carried out using a Heine-based Ta double-vacuum furnace at Dalhousie University, Halifax. Sample preparation and experimental procedures are outlined in Appendix F. All plateau ages are reported at the 2σ confidence level.

2.8.2 ^{40}AR/^{39}AR THERMOCHRONOLOGY RESULTS

All samples yield well-constrained plateau ages (Table 2.3, Fig. 2.8). Of the two samples analyzed from the Lingshi transect, sample DBH 003 yields a plateau age of 13.2±0.2 Ma (93.3% of Ar released) while sample DBH 027 yields a plateau age of 11.5±0.2 Ma (97.3% of Ar released). From the Ura transect, sample DBH 067 has a plateau age of 11.7±0.2 Ma (96.8% of Ar released) and sample DBH 080 has a plateau age of 11.1±0.2 Ma (86.0% of Ar released).

2.8.3 INTERPRETATION

Recent advances in the understanding of Ar diffusion and distribution in muscovite warrant a short discussion on the concept of Ar closure temperature. The closure temperature of muscovite to Ar diffusion is nominally reported as ca. 350 °C (Hames and Bowring, 1994). It has been observed that high metamorphic temperatures of 500-600 °C have left Ar undisturbed in muscovite (see review in Villa, 2004), inconsistent with the assumption that Ar will always diffuse out of muscovite at temperatures greater than ca. 350 °C. This observation has been noted particularly in metamorphic rocks bearing multiple phases and

DBH 003

T°C	^{39}Ar(mV)	^{39}Ar(%)	AGE (Ma)±1σ	% ATM	^{37}Ar/^{39}Ar	^{36}Ar/^{40}Ar	^{39}Ar/^{40}Ar	% IIC
700	9.1	1.1	25.2 ± 11.2	96.4	0	0.003262	0.005411	0
800	33.9	4.4	14.5 ± 1.07	79.7	0	0.002699	0.053298	0
825	120.8	15.7	13.4 ± .14	30.6	0	0.001037	0.197618	0
850	226.2	29.4	13.2 ± .1	16.8	0	0.000571	0.239329	0
900	204.9	26.6	13.3 ± .12	15.5	0	0.000525	0.242945	0
950	88.4	11.4	13.1 ± .13	30.6	0	0.001036	0.201276	0
1000	42.9	5.5	13.1 ± .22	42.5	0	0.001438	0.167775	0
1100	32.8	4.2	13.1 ± .27	48.3	0	0.001637	0.150157	0
1250	5.7	0.7	11.3 ± 3.56	94.5	0	0.003198	0.018549	0.01
1450	4	0.5	24.7 ± 22.61	98.2	0	0.003324	0.002699	0

Mean age (825°C-1100°C) = 13.2 ± 0.1 Ma (2σ uncertainty, including error in *J*) *J* = 0.002129 ± 2.129 x 10^{-5}

DBH 027

T°C	^{39}Ar(mV)	^{39}Ar(%)	AGE (Ma)±1σ	% ATM	^{37}Ar/^{39}Ar	^{36}Ar/^{40}Ar	^{39}Ar/^{40}Ar	% IIC
700	9.4	0.9	16.2 ± 11.39	97.7	0	0.003307	0.005336	0
800	78.8	8.3	11.8 ± .69	76.4	0	0.002587	0.07586	0
850	379.9	40	11.6 ± .1	22	0	0.000746	0.256404	0
900	193.6	20.4	11.5 ± .1	17.2	0	0.000583	0.273296	0
950	116.7	12.3	11.5 ± .12	26.2	0	0.000888	0.245033	0
1000	89.3	9.4	11.4 ± .12	29.6	0	0.001002	0.235274	0
1100	61.5	6.4	11.6 ± .19	42.2	0	0.00143	0.189628	0
1200	9.2	0.9	10.5 ± 1.63	90.1	0	0.003051	0.03552	0
1450	8.8	0.9	17.7 ± 14.3	98	0	0.003318	0.004147	0

Mean age (825°C-1100°C) = 11.5 ± 0.1 Ma (2σ uncertainty, including error in *J*) *J* = 0.002126 ± 2.126 x 10-5

DBH 067

T°C	^{39}Ar(mV)	^{39}Ar(%)	AGE (Ma)±1σ	% ATM	^{37}Ar/^{39}Ar	^{36}Ar/^{40}Ar	^{39}Ar/^{40}Ar	% IIC
700	9.1	0.8	26.3 ± 15.18	96.6	0	0.003271	0.004808	0
800	85.4	8.1	12.2 ± .73	78.3	0	0.002653	0.067692	0
900	701	66.5	11.8 ± .1	26.9	0	0.000911	0.235808	0
950	102.2	9.7	11.3 ± .17	41.1	0	0.001392	0.197724	0
1050	68	6.4	11.5 ± .21	48.9	0	0.001655	0.169743	0
1150	62.3	5.9	11.5 ± .21	48.8	0	0.001653	0.169907	0
1450	25.7	2.4	23.3 ± 6.7	94.7	0	0.003205	0.0086	0

Mean age (825°C-1100°C) = 11.7 ± 0.2 Ma (2σ uncertainty, including error in *J*) *J* = 0.002128 ± 2.128 x 10-5

DBH 080

T°C	^{39}Ar(mV)	^{39}Ar(%)	AGE (Ma)±1σ	% ATM	^{37}Ar/^{39}Ar	^{36}Ar/^{40}Ar	^{39}Ar/^{40}Ar	% IIC
700	13.9	1.5	22.8 ± 8.36	95.8	0	0.003242	0.006968	0
800	94.7	10.6	12.1 ± .37	63.9	0	0.002165	0.113824	0
825	142.9	16.1	11.3 ± .18	38.2	0	0.001293	0.208703	0
850	193.3	21.8	11.1 ± .1	23.8	0	0.000807	0.262028	0
900	190	21.4	11.1 ± .1	20	0	0.000679	0.272996	0
950	115.9	13	10.9 ± .1	27	0	0.000915	0.255054	0
1000	66.3	7.4	11.2 ± .15	33.8	0	0.001145	0.22403	0
1100	51.7	5.8	11.1 ± .17	41.1	0	0.001393	0.202462	0
1250	12.5	1.4	10.3 ± 1.32	88.1	0	0.002984	0.043801	0
1450	5	0.5	13.1 ± 15.09	98.5	0	0.003334	0.004276	0

Mean age (825°C-1100°C) = 11.1 ± 0.1 Ma (2σ uncertainty, including error in *J*) *J* = 0.002127 ± 2.127 x 10-5

Table 2.3: ^{40}Ar/^{39}Ar step-heat isotopic data for muscovite. Percent IIC—interfering isotopes correction.

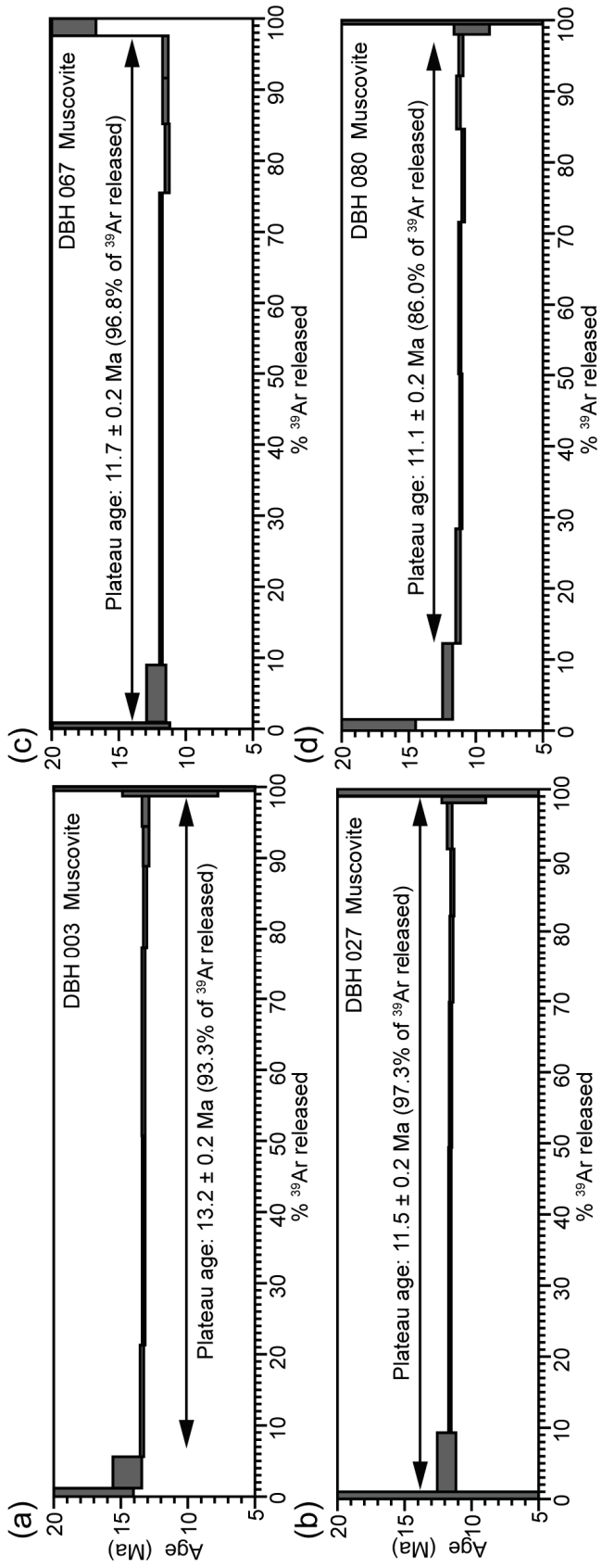

Figure 2.8: $^{40}Ar/^{39}Ar$ step-heat thermochronology of muscovite. Sample locations are shown in Figure 2.2. (a) and (b) are from the Lingshi section, while (c) and (d) are from the Ura section. Plotted error bars are 1σ and plateau ages are reported at the 2σ level.

generations of muscovite (e.g. Di Vincenzo et al., 2004). However, the preponderance of muscovite $^{40}Ar/^{39}Ar$ data for igneous rocks, both within and outside the Himalayan orogen, is consistent with muscovite $^{40}Ar/^{39}Ar$ ages $<$ igneous crystallization ages recorded by minerals such as zircon, arguing for post-igneous-crystallization Ar retention in muscovite. Here, although minor dynamic recrystallization produced fine-grained muscovite, only coarse, igneous grains were selected for $^{40}Ar/^{39}Ar$ analysis. The granites have a relatively simple geologic history of crystallization from a melt, followed by sub-solidus deformation during exhumation, and the well-defined plateaus produced during step-heating suggest Ar systematics have not been disturbed in these grains since initial cooling. Ti-in-zircon data (Fig. 2.7) show that zircon was crystallizing from melt at fairly low temperatures of $\leq$600 °C, near the leucogranite solidus. It is possible, considering the above mentioned studies, that Ar did not diffuse out of the muscovite below 500-600 °C, and thus that the $^{40}Ar/^{39}Ar$ plateaux represent crystallization and not cooling ages of the muscovite, but we argue that in this case, such high closure temperatures are inconsistent with our Ti-in-zircon thermometry and U-Pb zircon ages.

Recent experiments on Ar diffusion in muscovite indicate that in cases where temperature is likely the main factor influencing Ar diffusion, ca. 425 °C may be a more appropriate approximation of Ar closure temperature than 350 °C (for pressures of ca. 5 kbar, muscovite grain diameters of ca. 200 μm and a cooling rate of ca. 60 °C/Ma (determined from average slopes in Fig. 2.7)) (Harrison et al., 2009). Since our samples have experienced minor deformation, equations of volume diffusion may not be a strictly accurate way to estimate closure temperature (deformation may have kept Ar pathways open below the diffusion-controlled closure temperature, thus 425 °C may be an over- rather than underestimate of Ar retention temperature).

A closure temperature of ca. 425 °C is slightly higher than the estimated temperature of the brittle/ductile transition zone of ca. 350 °C for quartzo-feldspathic rocks (e.g., Sibson, 1977; Passchier and Trouw, 2005), and coincides with the estimated temperature of ductile deformation of 400-500 °C for O-STD granites (see above). Thus, the $^{40}Ar/^{39}Ar$ apparent cooling ages can be interpreted as closely preceding cessation of ductile deformation along the O-STD. Since the I-STD experienced ductile deformation until at least after 11.0 Ma, as constrained by U-Pb geochronological data (this study; Edwards and Harrison, 1997; Wu et al., 1998), followed by brittle deformation, then the O-STD ceased operating while

the I-STD was still active as a ductile to ductile/brittle shear zone. A biotite $^{40}Ar/^{39}Ar$ cooling age from a leucogranite near Wagye La beneath the I-STD of ca. 10.2 Ma and muscovite and biotite cooling ages from the Kula Kangri granite of ca. 11.4-10.7 Ma (Chakungal, 2006 and Maluski et al., 1988, respectively) suggest cooling of the I-STD must have been rapid.

2.9 Discussion

2.9.1 Age of the South Tibetan detachment system in the Bhutan Himalaya

A recent review of published geochronological data suggests that orogen-wide the timing of displacement of interpreted *upper* and *lower* components of the STDS can been approximated as ca. 18 and ca. 22 Ma, respectively (Carosi et al., 1998; Godin et al., 2006a). These upper and lower components of the STD (e.g., the Qomolangma and Lhotse detachments, respectively, of the Everest region (Searle et al., 2003; Sakai et al., 2005) and the Phu and Chame detachments of the Annapurna region (Searle and Godin, 2003)) are not considered analogous to the O-STD and I-STD described here. In Nepal, the two detachments are within 1-2 km structurally of each other (e.g., Searle and Godin, 2003; Searle et al., 2003); they may be two components of the same shear zone acting simultaneously or progressively at different structural levels and rheological boundaries. In Bhutan, this might correlate to GHS/Chekha and Chekha/TSS bounding structures in the Lingshi klippe, both part of the O-STD (we suggest that the Chekha/TSS boundary may be a fault although thus far it has been poorly-defined in the field). However, there is a distinct time and geographic separation between the defined *inner* and *outer* detachments in Bhutan. Thus we prefer the terms I-STD and O-STD to distinguish them from previously published *upper* and *lower* STD terminology.

Structural, geo- and thermochronological data, published and ours (Table 2.4) indicate that ductile motion along the O-STD began at ca. 24 Ma, continuing until at least 16.0 (Lingshi) -15.5 (Ura) Ma, but ceasing by ca. 11.0 Ma, while ductile motion along the I-STD remained active through ca. 11.0 Ma. Brittle faulting at the I-STD followed (e.g., Wiesmayr et al., 2002; Meyer et al., 2006), while there is no field or geophysical evidence for any recent deformation associated with the O-STD. These data suggest that the O-STD

Sample	Location	Structural position	Zircon rim U-Pb age range (Ma)	Ti-in-zircon temperature range (°C)	$^{40}Ar/^{39}Ar$ cooling age (Ma) ~425 °C
DBH 003	Lingshi (W)	O-STD HW	N/A	N/A	13.2 ± 0.2
DBH 027	Lingshi (E)	O-STD HW	~24-16	~625	11.5 ± 0.2
DBH 031	Lingshi (E)	O-STD HW	~23-16	N/A	N/A
DBH 036	Lingshi (E)	O-STD HW	~24-16	~600	N/A
DBH 067	Ura (E)	O-STD HW	N/A	N/A	11.7 ± 0.2
DBH 080	Ura (W)	O-STD HW	~18-16	~550	11.1 ± 0.2
BH 225	Masang Kang	I-STD FW	~16-11	~700	N/A

Table 2.4: Summary of analytical results. HW—hanging wall, FW—footwall.

was abandoned in mid-Miocene. As discussed further below, the Kakhtang thrust, an out-of-sequence thrust within the GHS, separates the inner and outer detachments at least in central and eastern Bhutan. Its age has been constrained to younger than 15 Ma by U-Pb dating of monazite in deformed leucogranites (Daniel et al., 2003), and it is postulated to be concurrent with the I-STD (Grujic et al., 2002). Map relationships in central Bhutan indicate that the Kakhtang thrust cuts and therefore postdates the O-STD (Fig. 2.1b, 2.2c).

2.9.2 Implications for tectonic models of the Himalayan orogen

The two main questions arising from this study that have implications for the formation of the Himalayan orogen are: 1. What caused the O-STD to be abandoned? 2. What is the significance of the abandonment for the evolution of the orogen?

We suggest two possible mechanisms for abandonment of the O-STD. Firstly, the STD may have stepped to the hinterland because the O-STD segment of the shear zone became unviable. It has been documented that normal-sense detachment systems can progressively step structurally up-section as older, deeper shear surfaces become rotated towards the horizontal (progressively flattening during footwall exhumation) and, in cases, folded (e.g., Mancktelow and Pavlis, 1994) or they can even step down-section (e.g., Brichau et al., 2007). The O-STD has been folded in a low-amplitude dome and basin geometry and may have been rotated toward the south (Wiesmayr et al., 2002). If both occurred during shearing, the changed orientation of the O-STD surface may have prevented further slip, and caused a new shear plane (I-STD) to initiate. A second possibility is that the O-STD became separated from the STD due to doming within the GHS at depth. Exhumation of the dome would erode through a segment of the

STD, resulting in a laterally continuous "window" of younger and deeper GHS material separating the O-STD from the active STDS.

To examine these two possibilities, two general end-member mechanisms for orogenic wedge development widely applied to describe the Himalayan orogen may be considered: critical taper/frictional wedge theory (e.g., Webb et al., 2007; Kohn, 2008; Robinson, 2008) and channel flow/viscous wedge theory (e.g., Grujic et al., 1996; Beaumont et al., 2004; Carosi et al., 2006). Critical taper theory dictates that deformation in a frictional orogenic wedge occurs to maintain a critical taper angle (CTA) between the hinterland-dipping basal detachment and the topographic surface of the orogen. That angle can decrease either by increased erosion rates or foreland propagation of thrusting or both, and can increase by out-of-sequence thrusting or decreased erosion rates (Dahlen, 1990). It can be argued that hinterland stepping of a normal-sense fault in an orogenic wedge would also reduce the CTA by widening the orogen. During 12-10 Ma, it appears that the O-STD was abandoned synchronously with propagation of thrusting toward the foreland from the MCT to the MBT (at least in the western Himalaya; the age of the MBT has not been well-constrained for the eastern Himalaya) (Meigs et al., 1995; Stüwe and Foster, 2001; Daniel et al., 2003). Intensified erosion also began at ca. 12-10 Ma as indicated by sediment accumulation rates in the Siwaliks (Najman, 2006 and references therein), which may be coincident with the start of the Indian monsoon (Dettman et al., 2003), although the date of the later has been highly disputed, and may have been already established by ca. 24 Ma (e.g., Clift et al., 2008). Thus, both orogen-wide changes in thrusting and erosion rates and an arguably local hinterland stepping of normal-sense displacement all should have resulted in a widening of the orogenic wedge and narrowing of the CTA. The expected tectonic response to these changes would be out-of sequence thrusting to reestablish the CTA. If the Kakhtang thrust arose in response, it was immediate, short-lived and only locally developed. There is no other, later out-of-sequence thrusting in Bhutan. Furthermore, since both foreland propagation and intensified erosion occurred at the orogen scale, so out-of-sequence thrusting within the GHS might be expected to be observable at the orogen scale.

Alternatively, channel flow models propose that in large hot orogens the gravitational potential between the thickened hinterland and the foreland results in an outward lateral flow of weakened mid-crustal material in a channel bound by more rigid crustal

layers (e.g., Beaumont et al., 2004; Beaumont et al., 2006). Focused erosion at the deformation front of the orogen allows for the extrusion of mid-crustal rocks to the surface along coeval yet opposite-sense shear zones; in the Himalayan orogen, these shear zones may be analogous to the MCT and the STD (Beaumont et al, 2001). These models have shown that cool, under-thrusted crust can form a crustal ramp on the basal detachment that will propagate into the orogen (e.g., Jamieson et al., 2006). Crustal ramps do occur in the Himalaya; a crustal ramp is interpreted beneath southern Tibet in the INDEPTH profile (Hauck et al., 1998) and similar, more external (thus younger) ramps may exist in the central Himalaya (Avouac, 2003). Other, more internal ramps may have been consumed. In channel flow models, these ramps are found to destabilize the middle crust, resulting in doming of a weak, partially molten crustal layer; this process has been suggested as a mechanism for the formation of the North Himalayan gneiss domes (Beaumont et al., 2004). In channel flow models, the tectonic fate of such a mid-crustal dome depends on the strength of the upper crust and erosion efficiency. For example, the dome can be translated toward the exhumation front and juxtaposed on top of a previously exposed channel, potentially (but not necessarily) above an apparent out-of-sequence thrust (i.e., Fig. 12e of Beaumont et al., 2004; Jamieson et al., 2006). We suggest that exhumation of such a dome could have caused erosion through the STD, cutting off the outer segment (O-STD) from the enduring STD (I-STD).

2.9.3 TECTONIC INTERPRETATION

We suggest that the now exhumed O-STD was first active as a near-horizontal top-to-the-north detachment deforming lower Chekha Group and upper GHS rocks, accompanied by anatexis at a depth of 10-30 km during ca. 25-16 Ma (Fig. 2.9a; Grujic et al., 2002; Harris et al., 2004; Chambers, 2008). Partially melted GHS in the hinterland flowed southward driven by a pressure gradient between hinterland and foreland (Grujic et al., 1996). Melt pooled at a rheological boundary at the top of the GHS, resulting in the formation of plutons such as the Chung La and Kula Kangri granites (Scaillet and Searle, 2006). During ca. 16-12 Ma, the O-STD began to exhume and cool (Figs. 2.6, 2.8b) due to erosion at the surface, perhaps enhanced by under-thrusting of the LHS beneath the GHS, propagating a ramp on the MHT toward the north. As the ramp advanced into the orogen, it caused the weak mid-crust to destabilize and a dome formed, flattened and extruded to the south. Crystallized leucogranite dikes and sills in the hanging wall of the

O-STD underwent varying amounts of sub-solidus ductile deformation before cooling at ca. 11 Ma (Fig. 2.9b). Coeval with rapid cooling of the O-STD from ca. 12 to 10 Ma, ductile motion ceased on the MCT and thrusting on the MBT began (Meigs et al., 1995; Stüwe and Foster, 2001; Daniel et al., 2003). The dome of GHS material was translated toward the foreland in the hanging wall of the Kakhtang thrust, cutting off the O-STD from the I-STD (Fig. 2.9c) and burying part of the O-STD beneath the Kakhtang thrust. Note that an out-of-sequence thrust is not required in our interpretation, but doming and the corresponding bending of metamorphic isograds are. From that point, the O-STD (and Chekha Group in its hanging wall) were passively carried southward in the hanging wall of the MHT, and displacement occurring along the STD at depth in the hinterland continued to be accommodated along the I-STD. Since 11 Ma, continued displacement along the I-STD, coeval with the MBT, facilitated rapid cooling and exhumation of footwall GHS rocks, and progressive overprinting of the ductile I-STD by younger, brittle normal-sense faulting (Fig. 2.9d) (Edwards et al., 1996). By ca. 8-6 Ma, GHS rocks cooled through the apatite fission-track closure temperature of ca. 110 °C (Grujic et al., 2006). However, the period of fast cooling and exhumation probably ended around the Mio-Pliocene transition (Fig. 2.7; Grujic et al., 2006), allowing for the preservation of the O-STD (appearing as klippen of Chekha Group and TSS rocks) that may have been lost to erosion elsewhere in the Himalaya. Our and published thermochronological data support a break in the cooling slope at around the end of the Miocene (Fig. 2.7).

Cooling through the Ar closure temperature of muscovite of metasedimentary rocks rimming the Kangmar Dome, which is located to the north of NW Bhutan, occurred from 15 to 10 Ma (Maluski et al., 1988; Lee et al., 2000). This dome is thought to be an exhumed northern portion of the STD, brought to the surface by thrusting of that dome along a ramp in the GHS during 11.5-10.0 Ma (Lee et al., 2000). This deformation coincided with thrusting along the MBT, ductile shearing on the I-STD, and possibly with thrusting along the Kakhtang thrust, as well as cessation of the O-STD and the MCT, indicating that there was a major shift in deformation partitioning within the eastern Himalaya at 12-10 Ma.

The O-STD appears to be unique to the eastern Himalaya, either because it did not form elsewhere, or it was not preserved. Erosion levels of the GHS in Bhutan are shallower than in the central Himalaya, most likely due to decreased erosion rates caused by a decline in mean annual precipitation caused by uplift of the Shillong plateau from

Figure 2.9: Schematic illustration of the tectonic history of the STDS in Bhutan from ca. 25 Ma to 9 Ma. The black pattern filled leucogranite is a marker used to track displacement of the mid-crust, and the dashed lines are marker lines. Active shear zones and faults are in black while inactive ones are in grey. (a) 25-16 Ma: the mid-crustal GHS flows southward beneath the TSS. The intervening CG is ductily deformed by top-to-the-north sense shearing. (b) Between 16 and 12 Ma, the more outboard leucogranites have crystallized and continue to experience ductile deformation while new partial melting and magma emplacement continues in the hinterland. The GHS is exhumed toward the foreland and the O-STD is exposed at the surface, comprising top-to-the-north sheared GHS and CG rocks. (c) By 12-10 Ma, the marker granite passes through the brittle/ductile transition. The KT becomes active, cutting off the O-STD from the main STD and causing it to become inactive. CG and TSS rocks are preserved in the footwall of the thrust (as klippen). The southward transport of mid-crustal GHS rocks from the hinterland is now accommodated on the MBT. (d) After 10 Ma ductile motion on the KT and the I-STD ceases. O-STD, I-STD, STD—outer, inner and main STD, respectively; MCT—Main Central thrust; KT—Kakhtang thrust; MHT—Main Himalayan thrust; MBT—Main Boundary thrust; CG—Chekha Group; TSS—Tethyan sedimentary sequence; GHS—Greater Himalayan sequence; LHS—Lesser Himalayan sequence. Position of the MHT inferred from INDEPTH data (Hauck et al., 1998). Depth is in km below sea level. Horizontal scale $\cong$ vertical. Kangmar dome is not shown for simplicity. *Stüwe and Foster (2001); §Meigs et al. (1995).

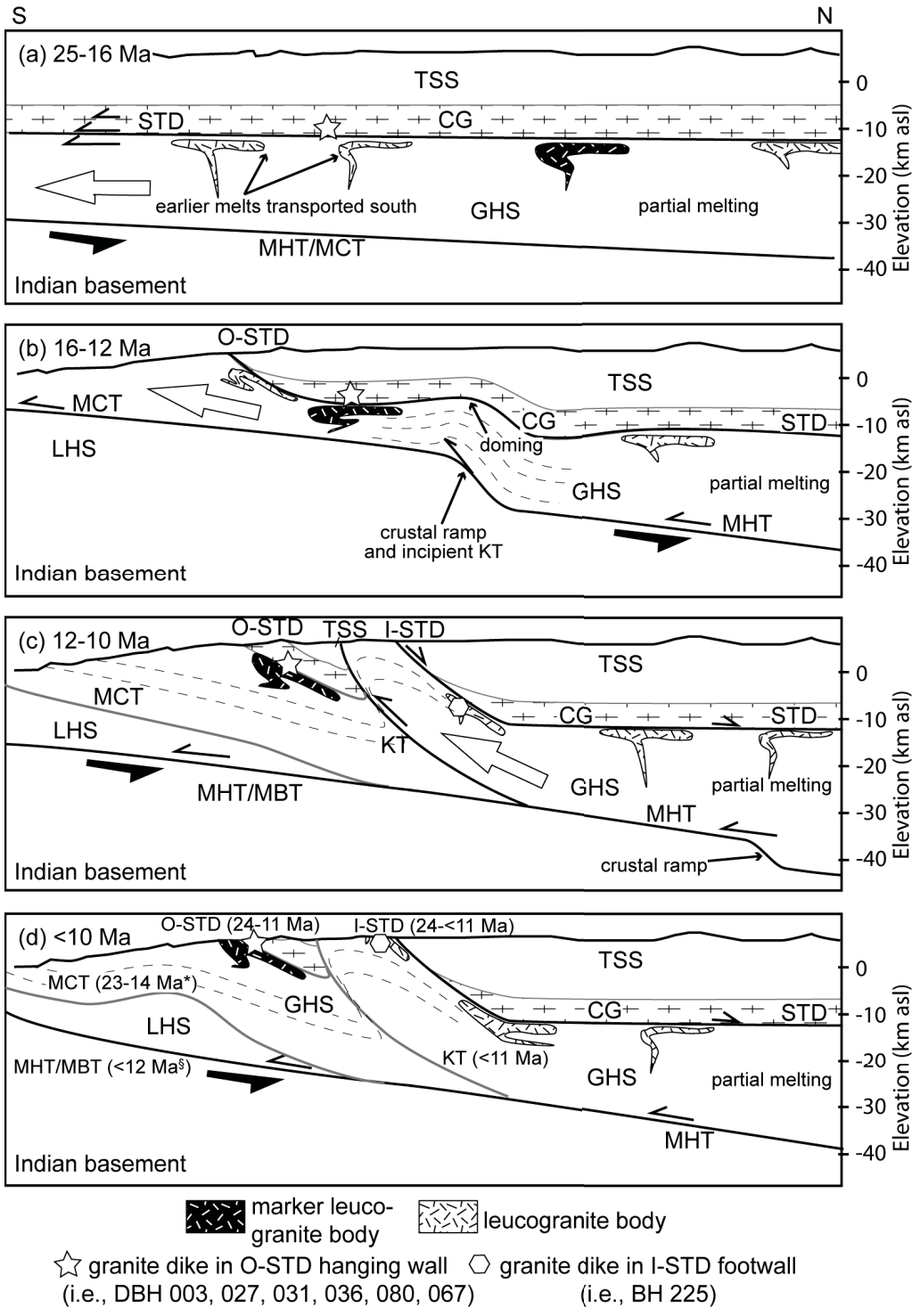
S
N
(a) 25-16 Ma
TSS
STD
CG
earlier melts transported south
GHS
partial melting
MHT/MCT
Indian basement
0
-10
-20
-30
-40
Elevation (km asl)
(b) 16-12 Ma
O-STD
MCT
LHS
TSS
CG
STD
doming
GHS
partial melting
MHT
crustal ramp
and incipient KT
Indian basement
(c) 12-10 Ma
O-STD
TSS
I-STD
MCT
LHS
KT
MHT/MBT
GHS
partial melting
MHT
crustal ramp
Indian basement
(d) <10 Ma
O-STD (24-11 Ma)
I-STD (24-<11 Ma)
MCT (23-14 Ma*)
GHS
LHS
MHT/MBT (<12 Ma§)
KT (<11 Ma)
partial melting
MHT
Indian basement
marker leuco-granite body
leucogranite body
granite dike in O-STD hanging wall (i.e., DBH 003, 027, 031, 036, 080, 067)
granite dike in I-STD footwall (i.e., BH 225)

ca. 6 Ma (Grujic et al., 2006; Biswas et al., 2007). If outer segments of the STD were similarly abandoned elsewhere in the Himalayan orogen, perhaps this difference in erosion level can explain why they are not observed today.

Irrespective of the mechanism, once the O-STD was abandoned in the mid-Miocene, it became coupled to the hanging wall of the MHT, and was transported southward away from the active I-STD. Thus the O-STD is now located more externally in the Himalayan orogen than when it was an active structure in the Miocene: its leading edge today does not mark the edge of the STD in the Miocene.

2.10 CONCLUSIONS

The South Tibetan detachment system in Bhutan is comprised of two distinct structures: the fossil O-STD preserved in the cores of synforms in the GHS, and the younger I-STD along the border between the Himalaya and Tibet.

Weakly deformed leucogranite sills emplaced in the hanging wall of the outer STD are dated by zircon U-Pb SHRIMP geochronology at or prior to 15.5 Ma. Low zircon crystallization temperatures of ca. 500-800 °C as determined by Ti-in-zircon thermometry suggest subsolidus crystallization, but zircon textures and trace-element geochemistry point to magmatic crystallization in a low-temperature, highly-fractionated melt. These rocks cooled through ca. 425 °C by ca. 11.0 Ma, as determined by muscovite $^{40}Ar/^{39}Ar$ thermochronology. Zircon in weakly deformed leucogranite emplaced in the footwall of the inner STD crystallized $\geq$11.0 Ma. Crystallization temperatures for magmatic zircon are ca. 700-800 °C, with more rapid cooling than that observed for leucogranites in the outer STD.

These age constraints for the outer and inner STD indicate that I-STD ductile to brittle faulting coincided with both cessation of motion on the O-STD and local out-of-sequence thrusting within the GHS. Furthermore, ductile shearing on both STD segments appears to have been active more recently than ductile motion along the STDS in the central and western parts of the orogen. The O-STD was abandoned in the mid-Miocene and subsequently transported southward in the hanging wall of the MHT to its present location. While hinterland stepping of the STD (frictional wedge model) is a possible mechanism for O-STD abandonment, our data combined with published geochronologic

constraints for the eastern Himalaya support foreland translation and exhumation of mid-crustal domes (viscous wedge model) as the tectonic mechanism for O-STD abandonment and subsequent southward translation.

CHAPTER 3

METAMORPHIC HISTORY OF THE SOUTH TIBETAN DETACHMENT SYSTEM, BHUTAN HIMALAYA

This chapter has been published as "*Kellett, D.A., Grujic, D., Warren, C., Cottle, J., Jamieson, R.A. and Tenzin, T., Metamorphic history of a syn-convergent orogen-parallel detachment: The South Tibetan detachment system, Bhutan Himalaya, Journal of Metamorphic Geology, 28, 785-808*".

3.1 ABSTRACT

The South Tibetan detachment system (STDS) in the Himalayan orogen is an example of normal-sense displacement on an orogen-parallel shear zone during lithospheric contraction. Here we combine *in situ* monazite U(-Th)-Pb geochronology with metamorphic pressure and temperature estimates to constrain pressure-temperature-time (P-T-t) paths for both the hanging-wall and footwall rocks of a Miocene ductile component of the STDS (outer STDS) now exposed in the eastern Himalaya. The outer STDS is located south of a younger, ductile/brittle component of the STDS (inner STDS), and is characterized by structurally-upward decreasing metamorphic grade corresponding to a transition from sillimanite-bearing Greater Himalayan sequence (GHS) rocks in the footwall with garnets that preserve diffusive chemical zoning to staurolite-bearing Chekha Group rocks in the hanging wall with garnets that record prograde chemical zoning. Monazite ages indicate that prograde garnet growth in the footwall occurred prior to partial melting at 22.6 $\pm$ 0.4

Ma, and that peak temperatures were reached following ca. 20.5 Ma. In contrast, peak temperatures were reached in the Chekha Group hanging wall by ca. 22 Ma. Normal-sense (top-to-the-north) shearing in both the hanging wall and footwall followed peak metamorphism from ca. 23 Ma until at least ca. 16 Ma. Retrograde P-T-t paths are compatible with modeled P-T-t paths for an outer STDS analogue that is isolated from the inner STDS by intervening extrusion of a dome of mid-crustal material.

3.2 INTRODUCTION

The South Tibetan detachment system (STDS) is a major network of low-angle normal-sense ductile shear zones and brittle faults within the Himalayan orogen (Burg et al., 1984a). It formed parallel to the orogenic front during India-Asia convergence and was coeval with, and broadly parallel to Miocene thrusts (Burchfiel et al., 1992; Hodges et al., 1992; Godin et al., 2006a). While many examples of low-angle normal-sense faults have been described from extensional settings (Axen, 2004; 2007), these were not thought to be important structures for accommodating lithospheric contraction prior to the discovery and study of the STDS in the Himalaya (e.g., Burg et al., 1984a; Burchfiel and Royden, 1985; Burchfiel et al., 1992; Hodges et al., 1992). Demonstrably syn-convergent low-angle normal-sense faults have since been recognized in several other contractional settings in which they have accommodated lithospheric contraction rather than extension (i.e. Pamir ranges, Brunel et al., 1994; Canadian Cordillera, Carr et al., 1987; Trans-Hudson Orogen, St-Onge et al., 2006; Hellenides, Ring et al., 2007; Eastern European Alps, Glodny et al., 2008). Thus, conceptual, analogue and numerical models of continental collision should provide testable geodynamic explanations for formation of these large-scale structures during convergence.

Several recent quantitative models have been proposed to account for the formation and timing of, and/or metamorphic conditions, across first order structures of the Himalayan orogen (e.g., Grujic et al., 1996; Beaumont et al., 2001; 2004; Jamieson et al., 2004; Robinson, 2008). However, few of these studies describe satisfactory mechanisms for creating a syn-convergent normal-sense structure like the STDS, and fewer still make testable predictions about the P-T-t histories of related tectonites. Where predictions are provided, the relevance of such models can be tested by appropriate comparisons with field-based data. In this study, empirical data are compared with P-T-t paths predicted for

a set of models in which rocks are deformed in a top-to-the-hinterland shear zone that bounds a mid-crustal channel.

Normal-sense shear zones seen at the Earths surface typically consist of an undeformed or brittlely-deformed hanging wall juxtaposed against a mylonitized footwall (e.g. Mancktelow, 1985). However, in the eastern Himalaya of Bhutan, an exposed Miocene ductile component of the STDS, part of the outer STDS (Fig. 3.1; Grujic et al., 2002; Chapter 2), provides an opportunity to examine the P-T-t history of the shear zone in detail. When combined with information about the trace-element chemical composition and structural context of *in situ* monazite in metamorphic rocks, U-Pb monazite ages can be used to constrain the absolute timing and duration of metamorphism and deformation. Here thermobarometric estimates of the conditions of peak metamorphism and retrograde shearing are combined with *in situ* U-Pb dating of monazite to characterize the P-T-t of tectonites in two transects across the outer STDS in Bhutan. Comparison of these results with P-T-t paths predicted by numerical models of Himalayan orogenesis (e.g., Jamieson et al., 2004; 2006), is a test of whether these models are compatible with field observations. Our results provide an empirical basis for understanding and modeling normal-sense shear during lithospheric contraction.

3.3 GEOLOGICAL BACKGROUND

The first-order structures of the Himalayan orogen comprise north-dipping shear zones and faults that separate major lithotectonic packages of different provenance, deformational character, and metamorphic history (Fig. 3.1, 3.2a; Hodges, 2000; Yin, 2006 and references therein). The motion across these north-dipping structures is thrust-sense (top-to-the-south) except for the uppermost structure, the STDS, which has a normal (top-to-the-north) sense of displacement (Burg et al., 1984a; Burchfiel and Royden, 1985; Burchfiel et al., 1992). The STDS is an orogen-wide network of top-down-to-the-north ductile shear zones and brittle faults that separate Greater Himalayan sequence (GHS) (also referred to as High Himalayan Crystalline or Tibetan slab) amphibolite- and locally granulite-facies gneiss, migmatite gneiss, and Miocene leucogranite intrusions from weakly to unmetamorphosed Tethyan sedimentary sequence (TSS) rocks (Carosi et al., 1998; Edwards et al., 1996; Edwards et al., 1999; Hurtado et al., 2001; Searle and Godin, 2003; Searle et al., 2003; Cottle et al., 2007; Chapter 2).

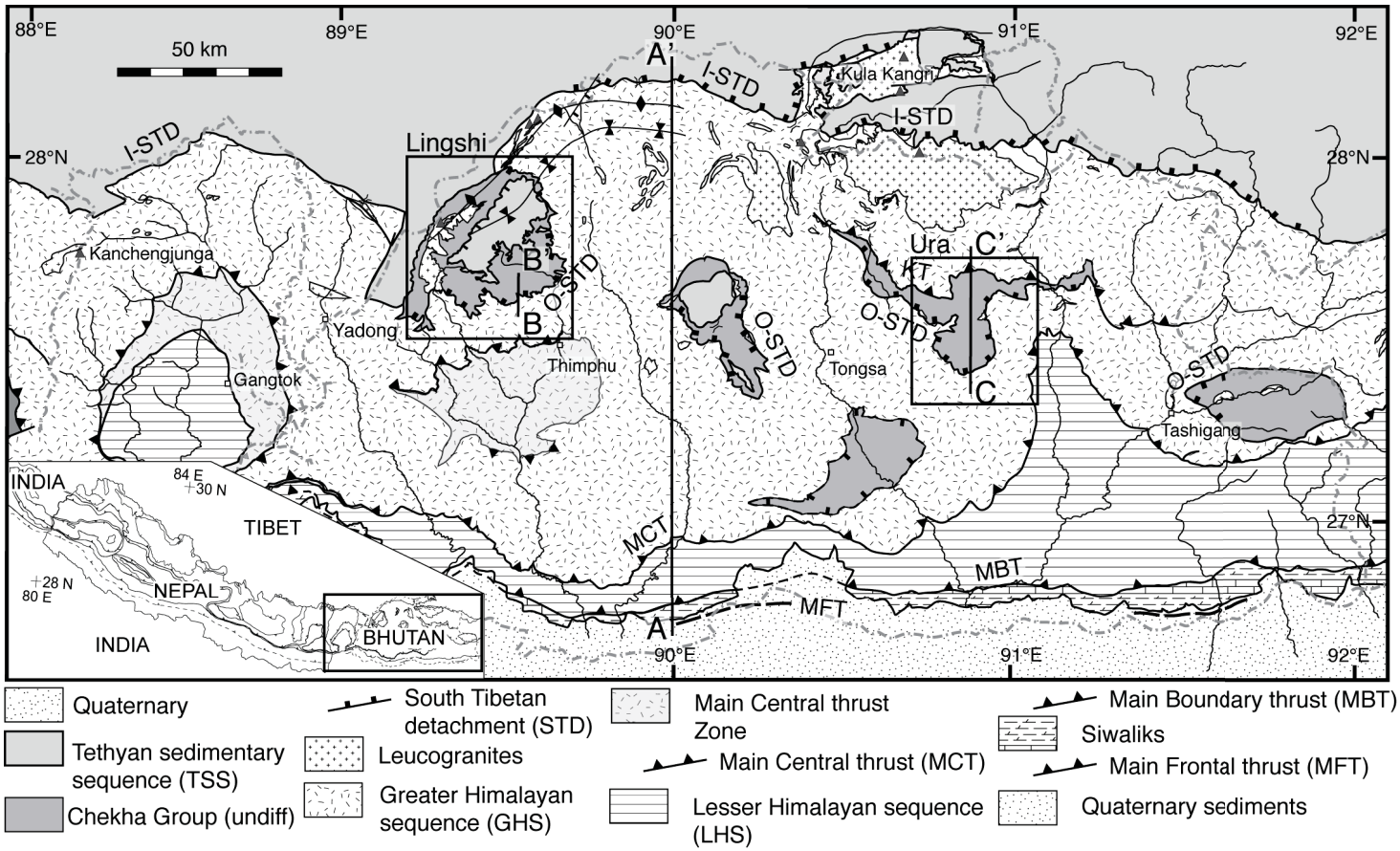

Figure 3.1: Geological map of Bhutan. Lingshi and Ura area sample locations for this study are shown. Map is modified from Gansser, 1983; Grujic et al., 2002; Chapter 2. O-STD - outer South Tibetan detachment system, I-STD - inner South Tibetan detachment system. Inset map of the Himalaya shows the location of the main map.

Figure 3.2: Geological cross-sections. (a) Representative cross-section A-A' through Bhutan at 90 ° E (fills correspond to Fig. 3.1). (b) Cross-section B-B' across the outer STDS in western Bhutan. (c) Cross-section C-C' across the outer STDS in central Bhutan. Section locations are shown in Figure 3.1. Double-pointed arrows span extent of outer STDS ductile top-to-the-north shear. KT - Kakhtang thrust, MHT - Main Himalayan thrust, GHS - Greater Himalayan sequence. Other abbreviations are listed in Figure 3.1.

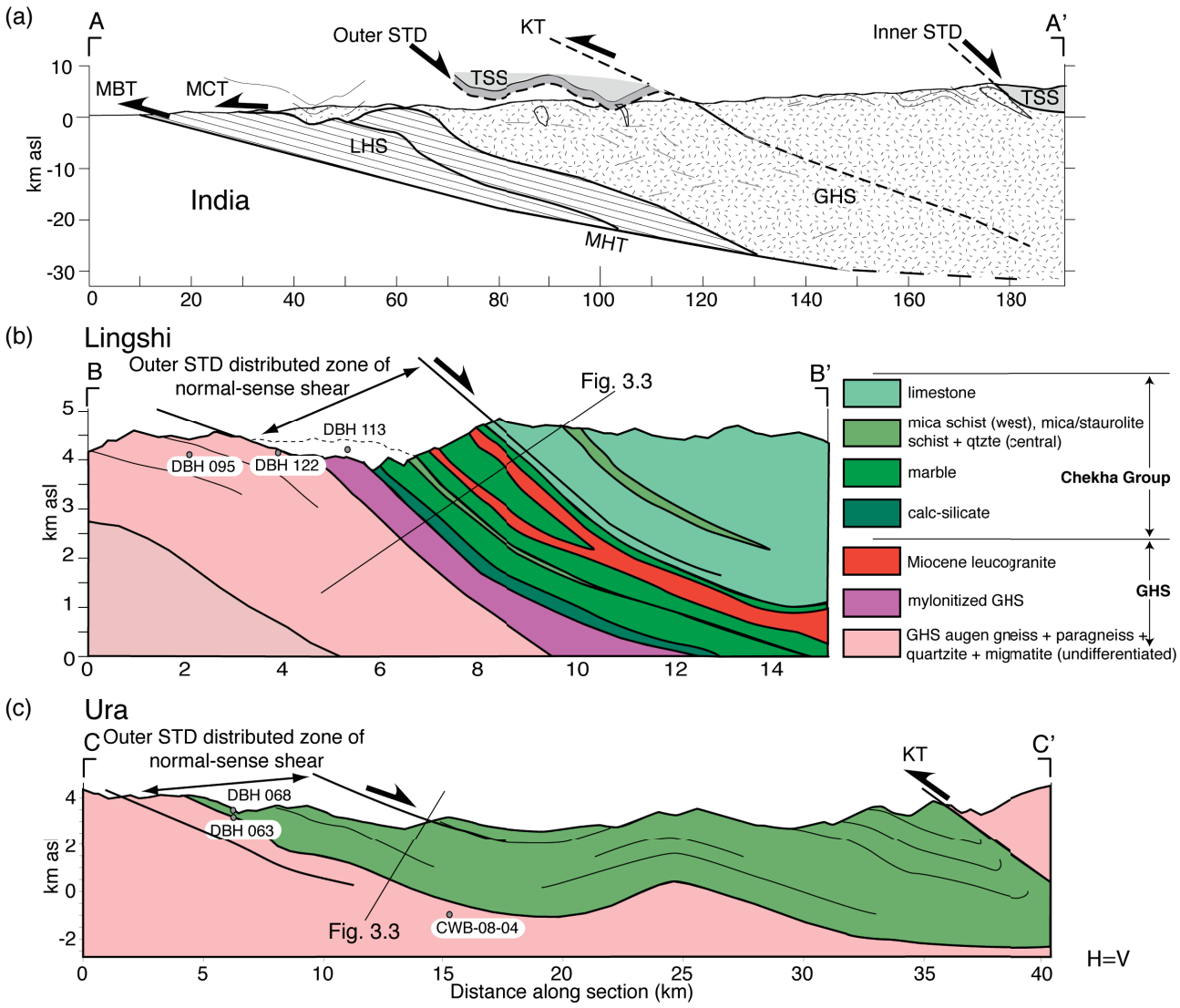
(a)
A
A'
Outer STD
KT
Inner STD
TSS
TSS
MBT
MCT
LHS
India
GHS
MHT
km asl
10
0
-10
-20
-30
0
20
40
60
80
100
120
140
160
180
(b)
Lingshi
B
B'
Outer STD distributed zone of
normal-sense shear
Fig. 3.3
DBH 113
DBH 095
DBH 122
km asl
5
4
3
2
1
0
0
2
4
6
8
10
12
14
limestone
mica schist (west), mica/staurolite
schist + qtzte (central)
marble
calc-silicate
Chekha Group
Miocene leucogranite
mylonitized GHS
GHS
GHS augen gneiss + paragneiss +
quartzite + migmatite (undifferentiated)
(c)
Ura
C
C'
Outer STD distributed zone of
normal-sense shear
KT
DBH 068
DBH 063
Fig. 3.3
CWB-08-04
km asl
4
2
0
-2
0
5
10
15
20
25
30
35
40
Distance along section (km)
H=V

A package of amphibolite to greenschist facies metasedimentary rocks of variable thickness crops out locally between the GHS and the TSS, above the large Miocene leucogranite intrusions. The rocks are generally pervasively ductilely sheared by the STDS, and can be distinguished from GHS rocks by their position structurally above the leucogranite intrusions, the absence of sillimanite, and a lack of *in situ* anatexis (e.g., Searle and Godin, 2003; Searle et al., 2003), and from the TSS by their higher metamorphic grade and contrasting structural style (sheared and transposed vs. preserved bedding and upright to recumbent folds). They are referred to regionally as Chekha Group (Bhutan), Everest Series (eastern Nepal), North Col Formation (eastern Nepal), Annapurna Yellow Formation (central Nepal), Haimantas Group (NW India), and the original sediments were probably deposited during the Proterozoic to Ordovician (Frank et al., 1973; Gansser, 1983; Colchen et al., 1986; Burchfiel et al., 1992; Lombardo et al., 1993; Bhargava, 1995; Carosi et al., 1999; Searle et al., 2003; Myrow et al., 2009).

It is now well established that the STDS was active during the Miocene concurrently with the Main Central Thrust (MCT; Fig. 3.1), particularly during 22-18 Ma (Godin et al., 2006a and references therein). The MCT is a thrust-sense shear zone that separates GHS rocks in its hanging wall from generally older, less deformed and lower metamorphic grade metasedimentary rocks of the Lesser Himalayan sequence in its footwall (e.g., McQuarrie et al., 2008).

3.3.1 Outer South Tibetan detachment system

In the eastern Himalayan Kingdom of Bhutan, the STDS comprises two main structures. The structure located closer to the orogenic front, the outer STDS (Chapter 2), is ductile, forms the base of synformal klippen, and separates migmatites and gneisses of the GHS below from the metasedimentary Chekha Group above (Grujic et al., 2002). The inner STDS is younger, ductile/brittle, and separates the GHS from the Paleozoic and Mesozoic sedimentary TSS (Fig. 3.2a). Unlike the inner STDS, the outer structure has not been overprinted by more recent brittle faults. The timing of normal-sense displacement across the outer STDS has been constrained by U-Pb ages from zircon and $^{40}Ar/^{39}Ar$ cooling ages from muscovite in deformed leucogranites, and U-Pb ages from metamorphic monazite in metapelite. It is thought to have initiated at ca. 24-22 Ma (Grujic et al., 2002; Chambers, 2008), remained active as a ductile shear zone until at least ca. 16 Ma, and cooled below the Ar closure temperature of muscovite by ca. 11 Ma (Chapter 2). The inner STDS was

active as a ductile shear zone after 11 Ma (Edwards et al., 1996; Wu et al., 1998; Edwards et al., 1999; Chapter 2), and is still the locus of brittle faulting (Wiesmayr et al., 2002; Meyer et al., 2006). It has been proposed that the outer STDS was passively translated towards the foreland in the late Miocene by thrusting along the Main Himalayan thrust, the basal detachment to the orogen (Chapter 2). Meanwhile, normal-sense shearing continued on the inner STDS, which is now exposed along the northern border of Bhutan (Chapter 2). This normal-sense shearing may have coincided with out-of-sequence thrusting along the Kakhtang thrust (KT) which locally places high-grade gneiss of the GHS over Chekha Group schist (Figs. 3.1, 3.2). As the outer STDS preserves a record of the Miocene history of the STDS that was not truncated or overprinted by later faults as in most other areas of the Himalayas, it therefore provides an opportunity to study the early stages of shearing along the detachment system.

3.3.2 THERMOBAROMETRIC CONSTRAINTS

Peak temperatures and pressures of sillimanite and kyanite-bearing pelitic gneisses exposed at the top of the GHS and deformed in the STDS in both the central and eastern Himalaya are reported as $>$620 °C, 5-14 kbar, and garnets display little core-rim chemical zoning (Daniel et al., 2003; Searle et al., 2003; Jessup et al., 2008). The presence of abundant anatectite at the top of the GHS further indicates temperatures compatible with partial melting. At the base of the staurolite-bearing Chekha Group and laterally equivalent rocks, peak temperatures and pressures are $>$620 °C, 3-7 kbar, and garnets generally preserve prograde growth zoning (Chambers et al., 2009; Jessup et al., 2008).

3.3.3 LOCAL GEOLOGY

Two transects across the outer STDS in Bhutan were investigated in order to characterize the change in P-T-t history from footwall to hanging wall (Fig. 3.1, 3.2b, c). Both transects comprise amphibolite-facies, migmatitic GHS rocks in the footwall of the detachment and amphibolite- to greenschist-facies Chekha Group rocks in the hanging wall. Reported thicknesses are structural only as the sedimentary bedding is isoclinally folded and transposed.

In the Lingshi area of western Bhutan (Fig. 3.2b), the GHS consists of intercalated augen gneiss, garnet-biotite$\pm$sillimanite paragneiss, quartzite, leucogranite, and migmatite gneiss. Just below the boundary with the Chekha Group is a zone of mylonitized orthogneiss and leucogranite $\sim$1 km thick. At the base of the Chekha Group, a 100-200 m

thick layer of calc-silicate schist is overlain by >1 km of white marble with intercalated mica schist. The sequence is intruded by thick (100-200 m) leucogranite sills as well as smaller deformed Miocene leucogranite dykes and sills (Grujic et al., 2002; Chapter 2). The upper part of the Chekha Group consists of >4 km pale grey marble that grades upward into grey limestone. The orientations of C'-type shear bands, mineral lineations, σ-type porphyroclasts of garnet, asymmetric boudins and vergence of folds in deformed leucogranites indicate a transition from predominantly top-to-the-south shear with minor pure shear and top-to-the-north shear $\sim$1 km structurally below the lithostratigraphic boundary, to predominantly top-to-the-north shear from $\sim$500 m below the GHS/Chekha Group contact (i.e., samples DBH 095 and DBH 122 respectively, Fig. 3.3b, c) to at least 2 km structurally above the contact.

The outer STDS in the Ura transect in central Bhutan (Fig. 3.2c) juxtaposes GHS augen gneiss, garnet-biotite$\pm$sillimanite$\pm$kyanite paragneiss, quartzite, leucogranite, and migmatite in its footwall with intercalated garnet+mica$\pm$staurolite schist and quartzite, as well as rare quartz conglomerate, marble and amphibolite lenses of the Chekha Group in its hanging-wall. The Chekha Group and GHS in the Ura area are also intruded by deformed Miocene leucogranite dykes and sills (Chapter 2). A top-to-the-north sense of shear in the uppermost GHS and lowermost Chekha Group is indicated by the orientation of C'-type shear bands, asymmetric pressure shadows on σ-type garnet porphyroclasts, asymmetric boudins, and the vergence of folds in deformed leucogranite bodies (Grujic et al., 2002).

3.4 SAMPLE DESCRIPTIONS

3.4.1 OBSERVATIONS

Sample locations for this study are shown in map view and cross-section (Figs. 3.1 and 3.2, respectively, sample locations in Appendix G) and their approximate structural positions with respect to each other and to the GHS/Chekha Group contact within the STDS are represented in Figure 3.3. Samples used to determine P-T-t paths are described below, while those used for P-T estimates alone are described in Appendix H. All samples used for P-T-t estimates are metapelitic and contain both garnet and monazite (Table 3.1). They are discussed below sequentially from structurally highest to structurally lowest.

Figure 3.3: Structural sections through the outer STDS. Lingshi (left) and Ura (right) sections showing approximate structural position of samples. (a)-(f) optical micrographs under plane-polarized light showing microstructural context of minerals used for thermobarometry and sense of shear. Stretching lineations, L(str), are shown with an arrow in the bottom left (where possible), and their trends and plunges are reported in the top right. For legend, see Figure 3.2. Shaded area shows zone of outer STDS top-to-the-north ductile shearing.

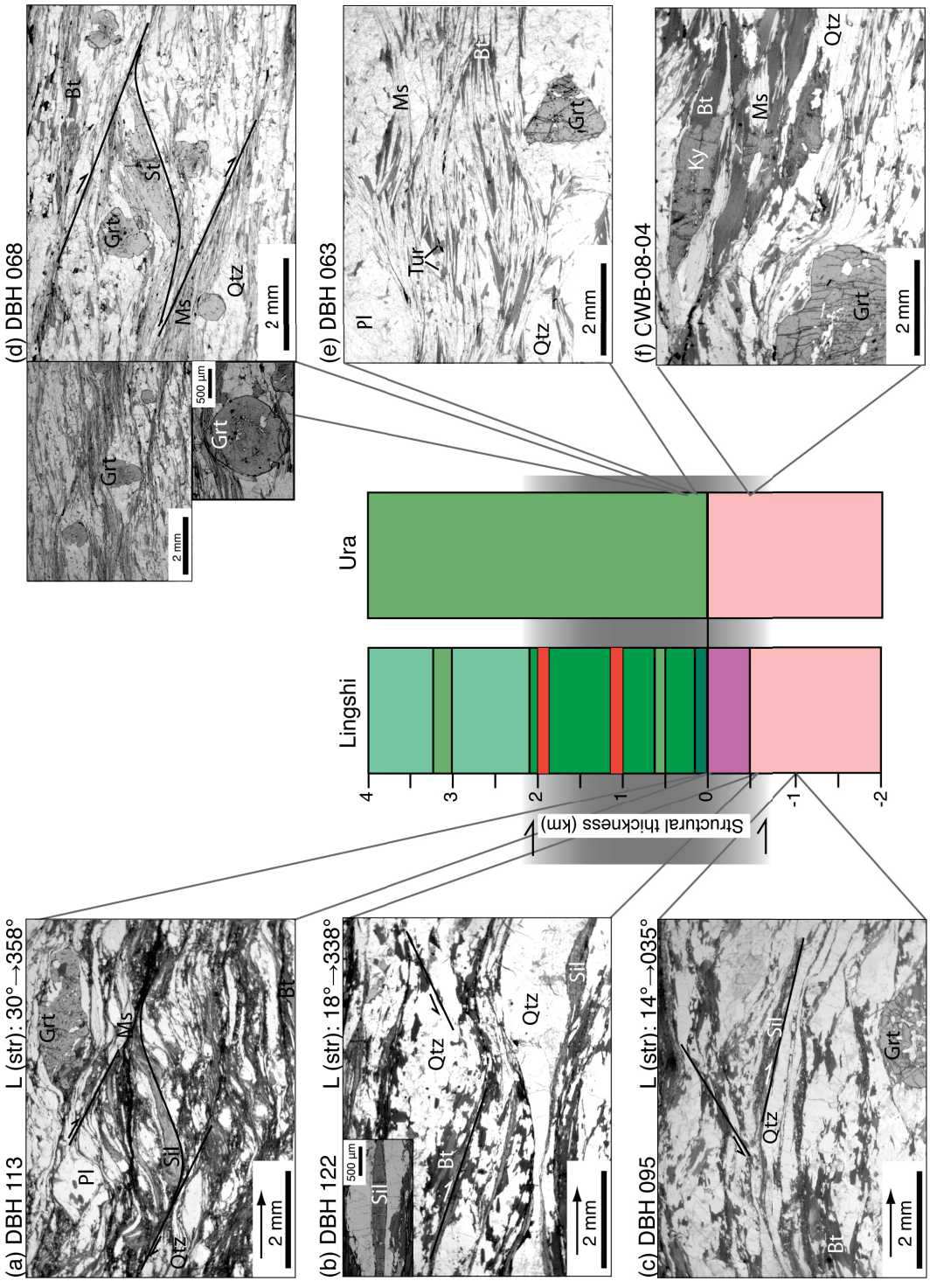
(a) DBH 113
L (str): 30°→358°
Grt
Pl
Ms
Sil
Qtz
Bt
2 mm
(b) DBH 122
L (str): 18°→338°
500 µm
Sil
Qtz
Bt
Qtz
Sil
2 mm
(c) DBH 095
L (str): 14°→035°
Qtz
Sil
Grt
Bt
2 mm
(d) DBH 068
Bt
Grt
St
Ms
Qtz
2 mm
Grt
2 mm
500 µm
Grt
(e) DBH 063
Ms
Bt
Tur
Pl
Grt
Qtz
2 mm
(f) CWB-08-04
Qtz
Ky
Bt
Ms
Grt
2 mm
Lingshi
Ura
4
3
2
1
0
-1
-2
Structural thickness (km)

Sample		Qz	Bt	Pl	Kfs	Ms	Grt	St	Sil	Ky	Ilm	Rt	Chl	Tur	Mnz	Xtm	Ap	Zrn
DBH 068	CG	X	X	X		X	X	X			X	X	X	?	GB, M, FM		X	X
DBH 063	CG	X	X	X		X	X				X	X	X	X	GB, M, FM, K		X	X
DBH 113	GHS	X	X	X	X	X	X		X		X		X	X	SB, GB, M, IG	X	X	X
CWB0804	GHS	X	X	X		X	X			X	X	?			GB, M, IK, IG	?	?	X
DBH 122	GHS	X	X	X	X	X	X		X	?	?	?	?	?	SB, GB, M, F		X	X
DBH 095	GHS	X	X	X	X		X		X		?	?	X	?	SB, GB, M, FF, IG	X	X	X

Table 3.1: Mineral data and monazite structural positions. Samples are ordered according to structural position. CG-Chekha Group, GHS-Greater Himalayan sequence. Mineral abbreviations are according to Whitney and Evans (2010). Monazite structural positions: SB-shear band, GB-grain boundary, M-in mica, FM-in fractured mica, F-in feldspar, FF-in fractured feldspar, K-associated with kinking, IK-in kyanite, IG-in garnet. X-mineral present.

Chekha Group: DBH 068 and 063 are coarse-grained garnet-biotite schists in the hanging wall of the outer STDS in the Ura klippe (Figs. 3.2c, 3.3). DBH 068 contains both garnet and staurolite (Figs. 3.3d, 3.4). Schistosity is defined by aligned biotite and muscovite, and is deflected around garnet grains. Garnet porphyroblasts are $\sim$1 mm in diameter, idioblastic to subidioblastic, and are characterized by inclusion-rich cores and relatively inclusion-poor rims. Inclusions of biotite, plagioclase, quartz, ilmenite and apatite form sinuous inclusion trails that, near the rims, are broadly continuous with the surrounding external foliation (Fig. 3.5a). Most garnets have weakly developed strain shadows of quartz, biotite, and muscovite, and strain caps of biotite and muscovite (Fig. 3.3d). Staurolite grains in DBH 068 contain straight inclusion trails that are continuous with the schistosity (Fig. 3.3d). Staurolite grains are xenoblastic, and also have small pressure shadows around them. Some garnets in sample DBH 063 are idioblastic whereas others are skeletal and elongate parallel to the foliation. Inclusion trails in garnet are poorly defined but appear to align at the rim with the external schistosity defined by biotite and muscovite (Fig. 3.5b). Monazite in DBH 068 and 063 occurs at grain boundaries, in mica, and adjacent to late fractures (Table 3.1), but was not found included in garnet.

GHS: DBH 113 is the structurally highest sample from the GHS (Fig. 3.2b). It is a sillimanite-rich S-C mylonite with sillimanite, quartz, biotite and muscovite folded and cut by top-down-to-the-north C'-type shear bands (Fig. 3.3a). Retrograde chlorite is present in pressure shadows of feldspar and in shear bands. Rare garnets are either skeletal and inclusion-rich, with an internal fabric at an angle to the external mylonitic fabric and 2-3 mm in diameter, or fractured to 100-200 μm in diameter within shear bands. Inclusions within garnet include quartz, plagioclase, biotite, ilmenite, zircon and monazite. They appear to be solid-state inclusions, and lack textures such as feldspar grain-boundary films, or shapes controlled by the host garnet (Sawyer, 1999). Thus this sample does not preserve evidence for partial melting, although it may have been obliterated by solid-state deformation (Vernon, 2000). Monazite in DBH 113 occurs at grain boundaries, in mica, in shear bands and in garnet grains near the rim.

CWB-08-04 is a kyanite-bearing schist collected from a schistose layer within augen gneiss west of, and structurally beneath the Ura klippe. Garnets in this sample are subidioblastic, polygonal and 2-5 mm in diameter. They are, in general, pervasively fractured at a high angle to the gneissic fabric, only rarely show a well-developed internal

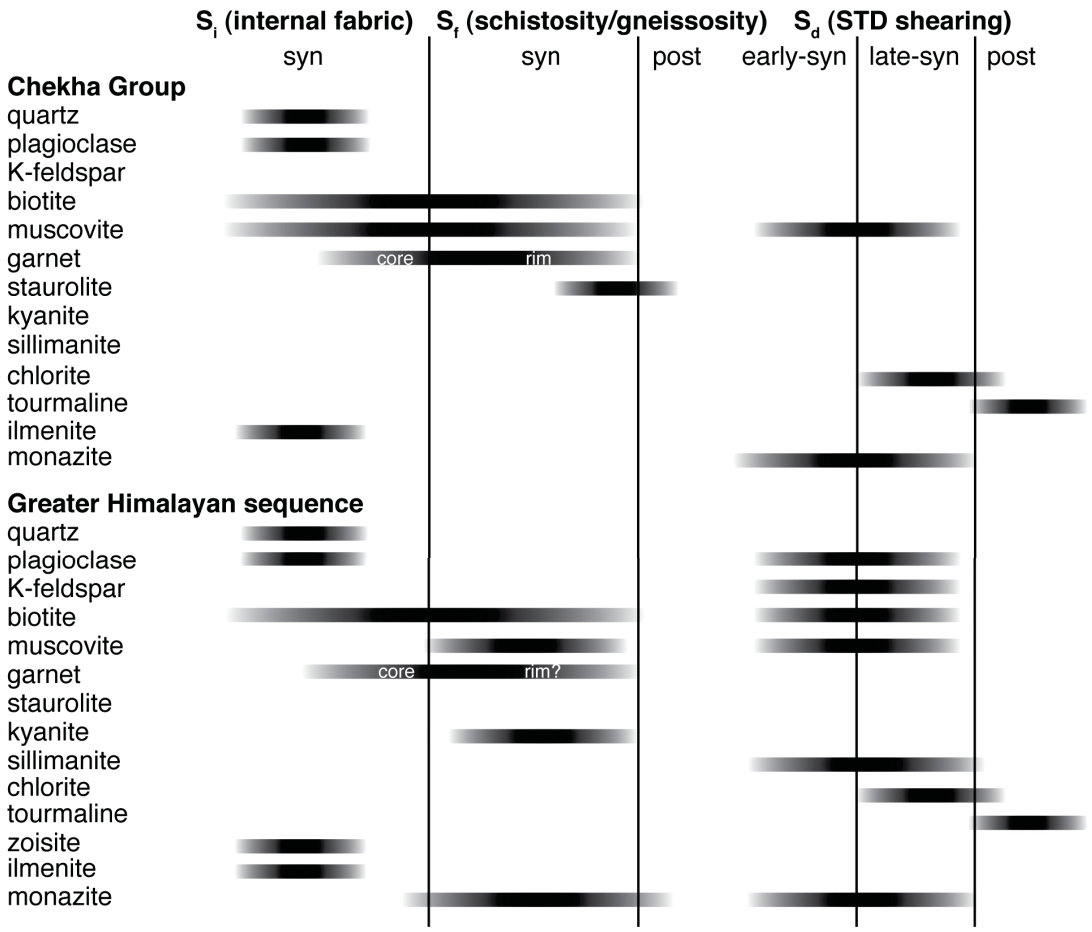

Figure 3.4: Summary of microstructural data. Generalized structural histories for Chekha Group and GHS samples used to determine equilibrium assemblages.

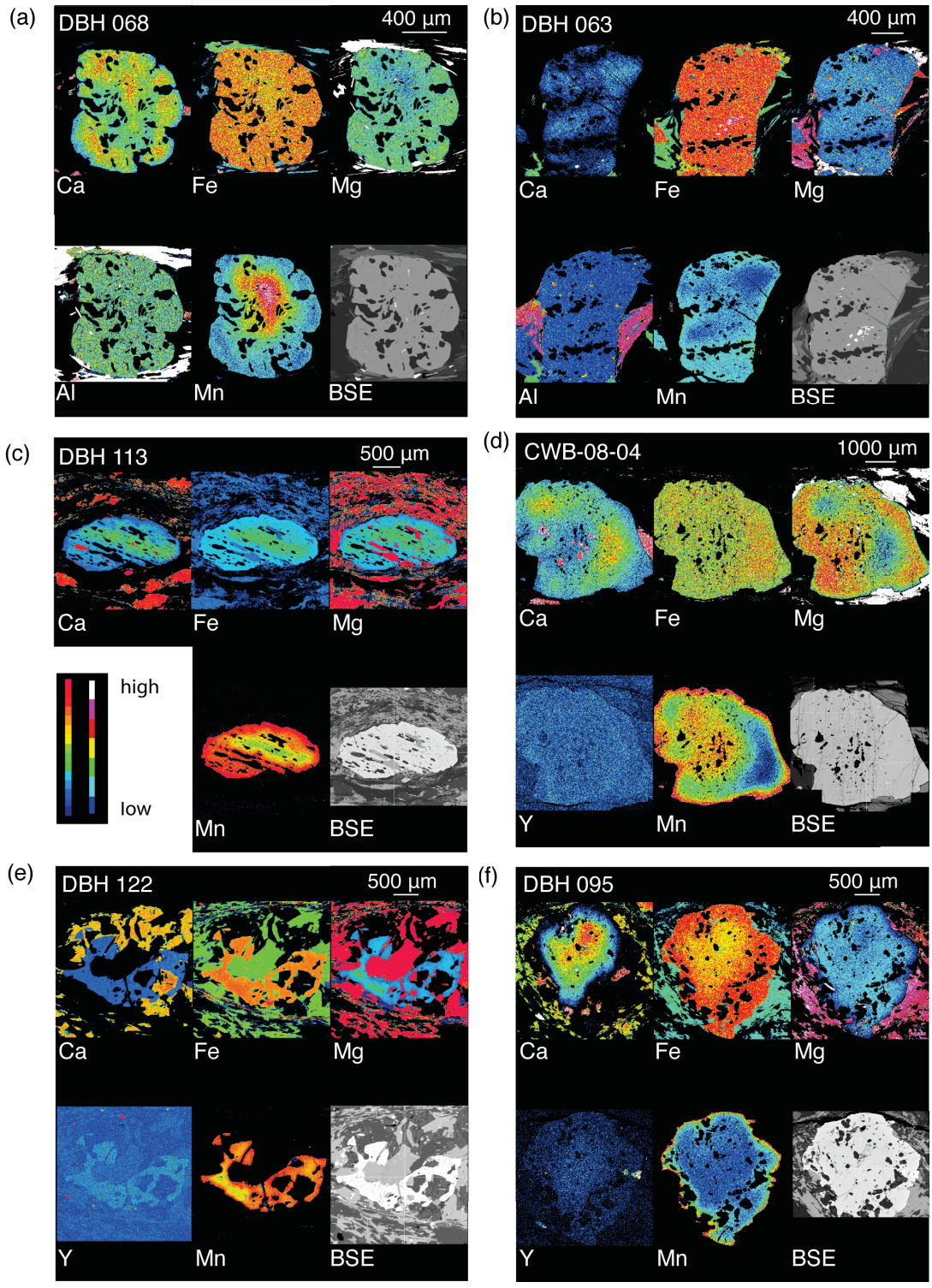

Figure 3.5: Element distribution maps and BSE images of garnets used for thermobarometric estimates.

fabric, and have inclusion-rich cores and inclusion-poor rims (Fig. 3.3f). Inclusions in garnet cores are both monomineralic and polymineralic, and composed of quartz, biotite, plagioclase, ilmenite, and zircon. Kyanite is coarse-grained, aligned with the gneissic fabric and exhibits undulose extinction. Aligned intergrown muscovite and biotite, kyanite and quartz grains define the gneissic foliation, which is cut by shear bands that contain recrystallized mica (Fig. 3.3c). Monazite in CWB-08-04 occurs at grain boundaries, in mica and kyanite and in garnet grains near the rim.

Sample DBH 122 (Figs. 3.2b, 3.3b) is a sheared biotite-sillimanite gneiss. Fibrolitic sillimanite is present in both top-down-to-the-NW and top-down-to-the SE conjugate shear bands (Fig. 3.3b). It also forms local pseudomorphs after either early sillimanite or kyanite. Garnets are rare, have a skeletal morphology, are $\sim$2 mm in diameter, lack an internal fabric and contain few inclusions. Muscovite is rare in this sample, and where present, is intergrown with biotite. Textures such as small relict sillimanite grains mantled by K-feldspar mantled by plagioclase, and large K-feldspar grains containing small sillimanite pods and rounded quartz inclusions are suggestive of crystallization from a melt. Monazite occurs at grain boundaries, in mica and feldspar and in shear bands.

DBH 095 is the structurally lowest sample in this study. It contains subidioblastic garnet 1-2.5 mm in diameter. Garnet grains contain abundant inclusions of quartz, biotite, plagioclase, zoisite (in the garnet core only), monazite (in garnet rims) and zircon, but well-defined inclusion trails are rarely present (Fig. 3.3c). Coarse-grained quartz, K-feldspar and biotite form pressure shadows around garnet grains. Sillimanite in the sample occurs within top-down-to-the-NE and top-down-to-the-SW conjugate shear bands. Both the gneissic fabric and the shear bands bend around garnet grains. Possible melt-present textures are preserved in garnet inclusions, including grain-boundary films of plagioclase around quartz and inclusion shapes controlled by host garnet. Furthermore, the irregular shapes of the garnet grains may indicate resorption of garnet during crystallization of melt. Monazite occurs at grain boundaries, in mica, in feldspar, in garnets near the rim, in shear bands, and adjacent to small late fractures.

3.4.2 MICROSTRUCTURAL INTERPRETATIONS

The three main fabrics preserved in the microstructure of both the Chekha Group and GHS samples are an internal fabric in garnets (S_i), the gneissic/schistose matrix fabric (S_f) and an overprinting fabric defined by STDS-related shear bands and mylonite zones (S_d)

(Fig. 3.4). In Chekha Group samples, the S_i fabric defined by inclusions of ilmenite, biotite, plagioclase, and quartz in garnet cores is sinuous, and finer-grained than the matrix and inclusions in the garnet rims, indicating that S_i predates growth of the minerals defining S_f. Garnet rims contain included fabrics that are generally continuous with the external fabric, with similar mineralogy but smaller grain size, indicating they are early syn-S_f. S_f is defined by fabric-aligned biotite, muscovite and staurolite (Fig. 3.3d). Chlorite occurs in pressure shadows and shear bands, and is therefore interpreted to be retrograde, and late-syn-S_d. Tourmaline, where present, overgrows all fabrics, and thus post-dates S_d (e.g. Fig. 3.3e). Monazite growth is interpreted to post-date early S_f, as it is not found included in early syn-S_f garnet rims.

In GHS samples, garnet cores contain fine-grained inclusions of ilmenite, biotite, plagioclase, and quartz, forming an internal foliation, S_i. Similarly to the Chekha Group rocks, S_i is interpreted to be a relict pre-S_f fabric, while garnet rims, mica, kyanite and monazite are syn-S_f (Fig. 3.4). As described above, garnet textures in samples DBH 095 and DBH 122 are consistent with crystallization in the presence of melt. Similar evidence in the matrix has been largely obliterated by deformation, indicating that any melting occurred prior to latest S_d, and may be syn-S_f. Muscovite, biotite, sillimanite, feldspar, monazite and quartz are all dynamically recrystallized in mylonite bands (Fig. 3.3a), and found within shear bands (Fig. 3.3a-c). Monazite is found in garnet rim zones, as well as in the matrix and shear bands, and as is shown below, is chemically zoned. Thus it is interpreted to be both syn-S_f and syn-S_d. For those samples that preserve evidence for partial melt, monazite inclusions in garnet may have grown in equilibrium with the melt.

3.5 THERMOBAROMETRY

3.5.1 MINERAL COMPOSITIONS AND ZONING

Selected garnet grains from each sample were imaged using backscattered electron (BSE) microscopy, and then mapped for Ca, Mg, Mn, Fe, $\pm$Y, $\pm$Al by wavelength-dispersive spectrometry on the JEOL 8200 electron microprobe at Dalhousie University, using an accelerating voltage of 15 kV and a beam current of $\sim$10 nA. The resulting compositional maps were used to characterize chemical zoning patterns and to guide quantitative point analyses (Table 3.2; Fig. 3.5).

Sample	Anal.	Field area	Approx. structural distance above CG/GHS contact (m)	Assemblage	AX conditions (P, T)	T (°C)	2σ Error (°C)	P (kbar)	2σ Error (kbar)	Rho	Fit (95% conf.)
DBH 088	PT	Ura	1000	grt, bt, plag, ms, st	7.0, 600	650	26	8.4	1.1	0.78	0.77
DBH 088	PT	Ura	1000	grt, bt, plag, ms, ksp	7.0, 600	558	32	6.9	1.2	0.78	1.27
DBH 086	PT	Ura	600	grt, bt, plag, ms	8.0, 600	607	27	7.7	1.0	0.75	0.44
DBH 086	PT	Ura	600	grt, bt, plag, ms	9.0, 650	618	31	8.6	1.2	0.76	1.13
DBH 071	PT	Ura	250	grt, bt, plag, ms	9.0, 600	604	27	8.6	1.1	0.72	0.83
DBH 071	PT	Ura	250	grt, bt, plag, ms	9.0, 600	576	44	8.7	1.9	0.75	1.69
DBH 068	PTt	Ura	100	grt, bt, plag, ms, st	8.1, 645	642	72	7.2	1.2	0.53	1.64
DBH 068	PTt	Ura	100	grt, bt, plag, ms	8.0, 600	620	67	7.6	2.2	0.85	3.36
DBH 063	PTt	Ura	50	grt, bt, plag, ms	7.7, 665	664	30	7.7	1.2	0.73	0.6
DBH 005	PT	Lingshi	50	grt, bt, plag, ms, ksp	7.0, 700	721	90	8.7	2.9	0.83	2.78
DBH 113	PTt	Lingshi	-20	grt, bt, plag	8.0, 700	622	49	(7)	-	-	0.6
DBH 061	PT	Lingshi	-50	grt, bt, plag, ms	7.0, 700	725	49	6.2	1.7	0.71	1.17
DBH 061	PT	Lingshi	-50	grt, bt, plag, ms	7.0, 700	748	41	8.1	1.6	0.69	0.91
CWB08-04	PTt	Ura	-500	grt, bt, plag, ms, ky	9.5, 725	789	21	9.1	1.0	0.82	0.65
CWB08-04	PTt	Ura	-500	grt, bt, plag	8.0, 550	560	40	(8)	-	-	0.1
DBH 122	PTt	Lingshi	-800	grt, bt, plag, ms, sill	6.9, 786	785	49	6.9	1.4	0.82	1.88
DBH 020	PT	Lingshi	-1500	grt, bt, plag, ms	7.0, 750	673	40	5.5	1.1	0.73	0.68
DBH 095	PTt	Lingshi	-1600	grt, bt, plag, ksp, sill	8.8, 746	741	26	9	0.8	0.22	0.74
DBH 095	PTt	Lingshi	-1600	grt, bt, plag	7.0, 650	630	156	10.9	5.2	0.99	1.99

Table 3.2: P-T estimates determined by THERMOCALC. Note: Shaded rows denote measurements for garnet cores and inclusions, plain rows denote rim and matrix measurements for Chekha Group samples and near rim and matrix measurements for GHS samples. Where pressures are given in brackets, THERMOCALC was run in average-T mode, and the pressure reported is that which yields the best fit in T. All other results were determined by THERMOCALC in average P-T mode ($XH_20 = 1$).

3.5.1.1 Chekha Group samples

In general, garnet grains in Chekha Group metapelitic schists from all studied locations in Bhutan are almandine-rich and characterized by prograde zoning from Mn-rich cores to Mn-depleted rims (Table 3.2; see Appendix H for details). Sample DBH 068 shows chemical zoning typical of growth during progressive medium-grade metamorphism (Yardley, 1977), with spessartine decreasing from core to rim and pyrope and almandine components increasing from core to rim (Table 3.2, Fig. 3.5a). The distribution of the grossular component is patchier throughout, but decreases at the rim. This chemical zoning indicates that garnet rims represent peak or near-peak temperature conditions (Hollister, 1966). The skeletal garnet grains in DBH 063 (Fig. 3.5b) do not exhibit chemical zoning for the elements measured. DBH 068 garnet is not affected by post-growth diffusional homogenization, while DBH 063 garnet (which lacks compositional zoning) may have been. Biotite in strain caps and slight embayments in garnet rims suggests local garnet breakdown during retrogression.

Matrix minerals in contact with each other and with garnet rims are assumed to be in equilibrium. Garnet point analyses in Chekha Group samples were made at the rim to estimate P-T conditions of equilibration with the matrix, and at the core (highest grossular and spessartine, lowest pyrope and almandine components) to constrain earliest prograde P-T conditions. Point analyses were also made to determine adjacent and matrix muscovite, biotite, staurolite and plagioclase compositions. Since there was little variation in the composition of matrix minerals (no zoning was observed for plagioclase or biotite), analyses were generally averaged, but for particularly coarse-grained minerals (i.e., staurolite, plagioclase), rim compositions were used for thermobarometric calculations. Biotite and plagioclase included in garnet are assumed to be in equilibrium with adjacent garnet, so their compositions were combined with garnet core measurements. Biotite inclusions were only measured where they were shielded by quartz and not in direct contact with garnet, to avoid retrograde exchange effects.

3.5.1.2 Greater Himalayan sequence samples

GHS garnets (samples DBH 113, 122, 095 and CWB-08-04) have more uniform compositions than Chekha Group garnets (Fig. 3.5c-f). Some garnet grains exhibit spessartine enrichment at garnet rims, while several grains also have elevated grossular components in their cores (Fig. 3.5c, d, f). The subdued zoning profiles indicate complete to near-complete

diffusional re-equilibration of original prograde zoning in these grains during higher-T metamorphic conditions, or of growth at high T, while spessartine enrichment at the rims points to retrograde effects (Yardley, 1977; Kohn and Spear, 2000). For these grains, near-rim garnet compositions (just interior to the high-Mn rims) were used to represent peak T conditions, combined with adjacent and matrix biotite, K-feldspar, plagioclase and muscovite average compositions. For samples DBH 095 and 122, indications of partial melt during garnet rim crystallization suggest that near-rim and matrix mineral compositions rather represent post-peak T recrystallization conditions.

The presence of staurolite and absence of sillimanite in Chekha Group samples, and the presence of sillimanite and absence of staurolite in GHS samples, suggests an apparent metamorphic isograd at approximately the structural contact between the GHS and the Chekha Group (Table 3.1). The contrast in garnet zoning from prograde in the Chekha Group to mostly homogeneous in the GHS across the same contact is similar to that described by Yardley (1977) for the staurolite-sillimanite transition zone at ca. 640 °C in Dalradian metasedimentary rocks in Ireland. The Everest Series, laterally equivalent to the Chekha Group, is also distinguished from the GHS by the preservation of prograde zoning in garnet, as well as by the presence of staurolite and absence of sillimanite (Jessup et al., 2008).

3.5.2 PRESSURE-TEMPERATURE ESTIMATES

Pressures and temperatures for interpreted stable metamorphic assemblages were calculated using THERMOCALC version 3.26i (© rp/tjbh 2005) in average PT mode with the internally consistent thermodynamic database of Holland and Powell (1998). Table 3.2 lists the resulting calculated P-T conditions; corresponding electron microprobe analyses can be found in Appendix I. Uncertainties in P and T are reported at the 2σ level as calculated by THERMOCALC.

3.5.2.1 Results

Metamorphic temperatures determined for rim and near-rim (GHS samples) garnet and matrix mineral compositions yield peak T estimates of ∼780 °C at the base of top-to-the-north sheared rocks in the GHS to ∼600 °C in the Chekha Group across a structural thickness of 850 m (Table 3.2; Fig. 3.6). Near rim/matrix pressures are poorly constrained, ranging by 5-10 kbar across the same structural section (Table 3.2; Fig. 3.6). Several of

the samples analyzed also contain garnets with inclusions suitable for calculating P-T conditions (Table 3.2). For the Chekha Group samples these may be prograde assemblages, as the garnet compositions indicate prograde chemical zoning is preserved. The calculated P-T conditions (Table 3.2) are within error of the rim/matrix P-T conditions (DBH 086, DBH 071, DBH 068), with only one sample indicating lower P-T conditions of 6.9 $\pm$ 1.2 kbar, 558 $\pm$ 32 °C (DBH 088). For the GHS samples studied, garnet cores and inclusions yield large errors for P-T calculations, suggesting they are not equilibrium compositions, consistent with post-growth chemical modification by diffusion. Though they indicate slightly lower metamorphic temperatures, the large errors indicate that prograde metamorphic equilibrium compositions are not preserved in the reequilibrated garnet cores.

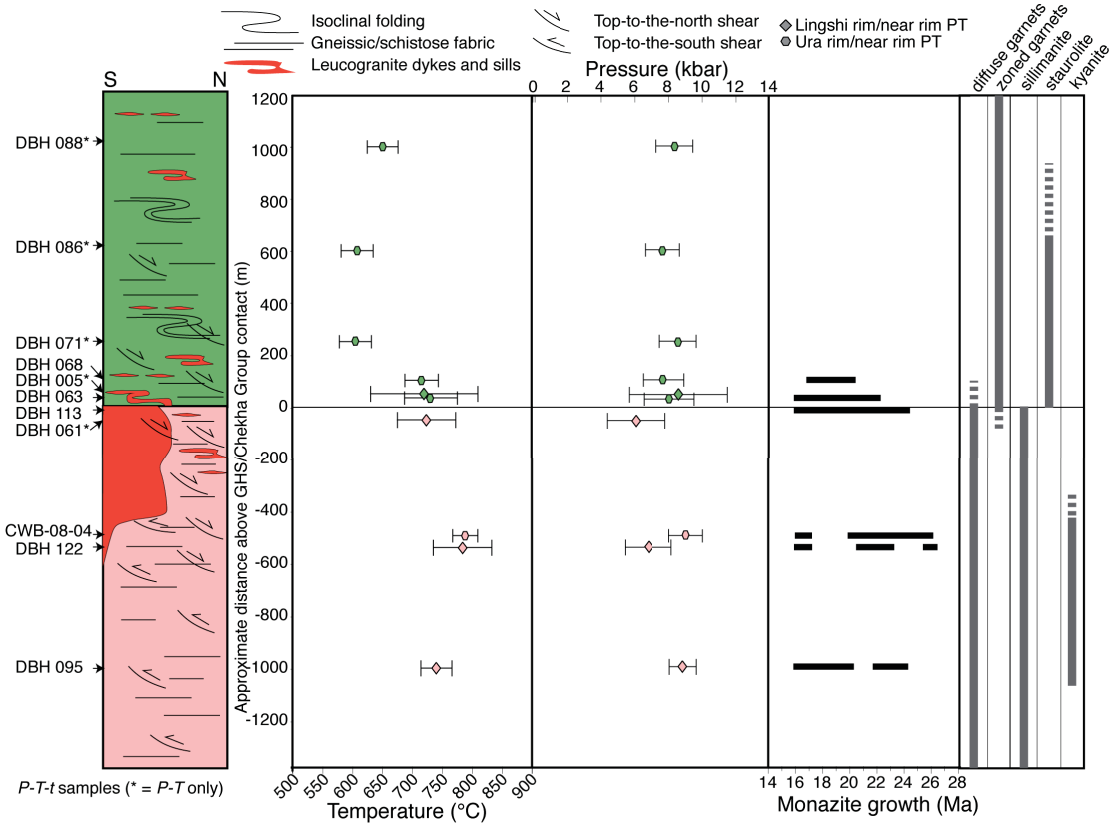

Figure 3.6: P-T estimates across the STDS. Garnet rim and near rim P-T estimates plotted against distance above the GHS/Chekha Group contact. Error bars are 2σ, calculated from THERMOCALC. Timing of monazite growth is also shown for P-T-t samples. Fills correspond to legend in Fig. 3.1.

3.6 U(-Th)-Pb monazite geochronology

3.6.1 Monazite zoning

Monazite grains were located in polished thin section by reconnaissance mapping on the electron microprobe (Dalhousie); 15 mm x 15 mm reconnaissance maps of Ca, Ce, Mg, Y and P were made at 15 kV and ∼200 nA to identify monazite populations in several samples. Six samples containing the largest and most abundant monazite grains and favorable mineralogy for thermobarometry were then selected for detailed monazite elemental mapping by electron microprobe (Dalhousie) and U-Th-Pb geochronology by LA-MC-ICP-MS (Laser Ablation Multi-Collector Inductively-Coupled Plasma Mass Spectrometry; NIGL). These samples form a ∼1.5 km structural transect across the outer STDS including the GHS and the Chekha Group (Fig. 3.3). Between 13 and 20 monazite grains from each sample were mapped at high resolution (15 kV, ∼200 nA) for Th, Nd, Y and U. BSE images were also collected at low magnification to determine the textural context of the *in situ* monazite grains. These data are summarized in Table 3.1.

Y mapping of monazite is a powerful tool for linking monazite growth to metamorphism in metapelites. Y zoning has been found to correlate with age domains within single monazite grains (Foster et al., 2002; Gibson et al., 2004), indicating that in some cases the range in U-Pb ages observed in single monazite grains is due to protracted or episodic growth or recrystallization of monazite due to radiogenic Pb. This suggests that Y domains in monazite may have different ages and should be considered separately during U-Pb spot selection. In other studies, monazite grown prior to garnet growth and during garnet breakdown has been found to be high in Y, while monazite growing in the presence of stable garnet is found to be relatively low in Y, since garnet has a higher partition coefficient for Y than monazite (Foster et al., 2002). Xenotime (YPO_4), which may also influence the Y budget of metapelites, is also present in the matrix of many of the studied samples (Table 3.1).

Monazite grains from Chekha Group samples DBH 068 and DBH 063 range in diameter from 20-120 μm, and are zoned with relatively high Th cores and low Th rims (Fig. 3.7a, b). Monazite crystals in these two samples are not zoned in Y, and Y content is high relative to GHS samples. The GHS samples analyzed (DBH 113, DBH 122, DBH 095, CWB-08-04) contain both matrix monazite and monazite inclusions in garnet. Matrix

monazite grains are all zoned in Y, with generally low Y cores and high Y rims (Fig. 3.7d-f), except for DBH 113, which contains mostly high Y monazite with less pronounced zoning (Fig. 3.7c). Th zoning is much less pronounced than Y zoning, but where present is inversely correlated with Y zoning (i.e. low Th zones correspond to high Y zones). Monazite inclusions in garnet are zoned in Th, weakly zoned in Y, and do not exhibit high Y rims (e.g., Fig. 3.7f).

3.6.2 U(-TH)-PB GEOCHRONOLOGY

U(-Th)-Pb geochronology of monazite in polished thin sections was conducted using a LA-MC-ICP-MS system operated at the NERC Isotope Geosciences Laboratory, UK (Tables 3.3, 3.4). Instrumentation consists of a Nu Plasma MC-ICP-MS (Nu Instruments, Wrexham, UK) and a UP193SS laser ablation system (New Wave Research (ESI), UK). The analytical protocol used is similar to that described in Simonetti et al. (2006) and the detailed instrumental configuration is outlined in Cottle et al. (2009b). For U-Pb analyses, 15 μm diameter spots were ablated for 40 s at 5 Hz and 2.6 J/cm^2 fluence (equating to crater depths of approximately 12 μm). Procedures for U-Th-Pb dating were the same as those reported by Cottle et al. (2009a). Spots of diameter 15 μm were analyzed for U-Pb (30 s) and U-Th (30 s) at 4-5 Hz and 3.1 J/cm^2 fluence. Microprobe BSE images and elemental maps guided spot selection. U(-Th)-Pb data were normalized to primary reference material "Manangotry" monazite (554 Ma ID-TIMS age) (Paquette et al., 1994). An in-house secondary reference material FC-1 monazite (55.6$\pm$1.3 Ma ID-TIMS age) (Horstwood et al., 2003) was analyzed concurrently to monitor data accuracy. Overall uncertainties achieved on the secondary reference material throughout the analytical period were 3% (2σ) for U-Pb data and 4% (2σ) for Th-Pb data. All quoted uncertainties include contributions from the external reproducibility of the standard for ^{206}Pb/^{238}U and ^{208}Pb/^{232}Th ratios. For common-lead correction purposes, ^{207}Pb/^{206}Pb ratios were measured in feldspar grains (which contain no radiogenic Pb) in sample DBH 063, averaging 0.824$\pm$0.004 for 5 measurements on different grains.

3.6.2.1 Results

Because of their young age, radiogenic Pb signals in the samples are low (^{207}Pb < 0.1 mV). This results in a relatively imprecise ^{207}Pb/^{235}U age and difficulty in applying an accurate common-Pb correction. Data are therefore plotted on Tera-Wasserburg diagrams

Table 3.3: U-Pb geochronology results. §Textural position: GB—monazite is at grain boundaries; M—monazite is in mica grain; FM—monazite is in fractured mica; K—kinking around monazite grain; IK—monazite inclusion in kyanite; IG—monazite inclusion in garnet.. *Rho is the $^{206}Pb^{238}U$ - $^{207}Pb/^{235}U$ error correlation coefficient calculated following K.R. Ludwig (unpublished data, 1993). †$^{207}Pb/^{235}U$ calculated using ($^{207}Pb/^{206}Pb$)/($^{238}U/^{206}Pb$*1/137.88).

						Ratios							Ages					
Analysis	§	U (ppm)	204 (cps)	206 (mV)	207 (mV)	207/206	2σ (%)	206/238	2σ (%)	207/235†	2σ (%)	Rho*	207/206 (Ma)	2σ abs	206/238 (Ma)	2σ abs	207/235 (Ma)	2σ abs
DBH068																		
DBH068_grn12-2	GB	2443	509	0.7	0.11	0.1845	4.64	0.003552	3.54	7161.2935	5.84	0.61	2694	75	22.9	0.8	87.8	4.9
DBH068_grn6-1	GB	3052	399	0.9	0.13	0.1668	11.72	0.003550	4.50	6479.1047	12.55	0.36	2526	184	22.8	1.0	79.7	9.6
DBH068_grn12-1	GB	2513	374	0.7	0.1	0.158	4.7	0.003496	2.38	6231.3928	5.27	0.45	2434	78	22.5	0.5	74.5	3.8
DBH068_grn8-1	GB	3176	32	0.9	0.07	0.0979	2.92	0.003384	4.48	3989.0625	5.35	0.84	1585	54	21.8	1.0	45.4	2.4
DBH068_grn2-3	FM	1559	766	0.6	0.06	0.1316	2.98	0.003333	0.86	5444.7726	3.10	0.28	2119	51	21.4	0.2	59.6	1.8
DBH068_grn3-1	M	2113	308	0.6	0.05	0.1058	3.46	0.003306	2.24	4412.3428	4.12	0.54	1728	62	21.3	0.5	47.8	1.9
DBH068_grn12-4	GB	2967	120	0.8	0.07	0.1028	8.22	0.003277	3.04	4325.6409	8.76	0.35	1675	145	21.1	0.6	46.1	3.9
DBH068_grn1-4	FM	2686	825	0.9	0.08	0.0934	3.98	0.003265	2.48	3944.0138	4.69	0.53	1496	73	21.0	0.5	41.8	1.9
DBH068_grn1-1	FM	2544	426	0.9	0.07	0.0943	3.52	0.003265	3.50	3982.5383	4.96	0.71	1514	65	21.0	0.7	42.2	2.1
DBH068_grn3-4	M	2390	242	0.6	0.05	0.0858	4	0.003259	3.30	3629.4759	5.19	0.64	1334	75	21.0	0.7	38.4	2.0
DBH068_grn7-2	FM	2462	293	0.7	0.05	0.0874	3.7	0.003252	2.80	3706.1965	4.64	0.60	1369	70	20.9	0.6	39.0	1.8
DBH068_grn7-1	FM	2231	279	0.6	0.04	0.0879	3.88	0.003233	2.82	3749.0931	4.80	0.59	1380	73	20.8	0.6	39.0	1.8
DBH068_grn13-2	GB	2717	379	0.7	0.07	0.1109	3.24	0.003217	2.04	4753.7854	3.83	0.53	1814	58	20.7	0.4	48.8	1.8
DBH068_grn3-3	M	2467	341	0.7	0.05	0.0897	3.46	0.003212	2.98	3849.9837	4.57	0.65	1419	65	20.7	0.6	39.6	1.8
DBH068_grn12-3	GB	2867	23	0.7	0.05	0.0841	5.5	0.003185	2.08	3640.8204	5.88	0.35	1295	103	20.5	0.4	36.8	2.1
DBH068_grn4-7	GB	2424	202	0.6	0.04	0.0782	4.18	0.003163	2.20	3408.4741	4.72	0.47	1152	81	20.4	0.4	34.1	1.6
DBH068_grn4-6	GB	2320	489	0.6	0.05	0.0884	3.94	0.003158	2.06	3859.6395	4.45	0.46	1391	74	20.3	0.4	38.3	1.7
DBH068_grn5-1	GB	1789	34	0.5	0.04	0.0878	5.12	0.003150	1.82	3843.6118	5.43	0.33	1378	95	20.3	0.4	38.0	2.0
DBH068_grn3-5	M	2967	787	0.8	0.06	0.0871	4.68	0.003141	3.40	3823.0558	5.78	0.59	1363	88	20.2	0.7	37.6	2.1
DBH068_grn2-2	FM	3128	806	1	0.09	0.0993	3.02	0.003101	0.92	4414.5452	3.16	0.29	1611	55	20.0	0.2	42.2	1.3
DBH068_grn4-5	GB	2375	630	0.6	0.04	0.0792	4.72	0.003100	2.18	3522.0586	5.20	0.42	1177	91	20.0	0.4	33.8	1.7
DBH068_grn2-4	FM	2429	733	0.8	0.06	0.088	3.08	0.003095	0.90	3920.7998	3.21	0.28	1382	58	19.9	0.2	37.4	1.2
DBH068_grn4-1	GB	1470	437	0.4	0.02	0.0753	6.72	0.003087	2.28	3362.9515	7.10	0.32	1077	129	19.9	0.5	32.0	2.2
DBH068_grn4-2	GB	1543	324	0.4	0.03	0.0766	6.84	0.003070	2.32	3440.3382	7.22	0.32	1111	131	19.8	0.5	32.4	2.3
DBH068_grn9-1	GB	2684	249	0.7	0.05	0.0884	3.58	0.003062	2.20	3980.4285	4.20	0.52	1391	67	19.7	0.4	37.2	1.5
DBH068_grn5-3	GB	1780	274	0.4	0.03	0.0826	5.74	0.003059	1.76	3723.4830	6.00	0.29	1260	108	19.7	0.3	34.8	2.1
DBH068_grn4-3	GB	2081	311	0.5	0.03	0.0765	5.68	0.003051	2.70	3456.7316	6.29	0.43	1108	109	19.6	0.5	32.2	2.0
DBH068_grn2-5	FM	2359	603	0.8	0.05	0.0811	3.4	0.003047	1.16	3670.1784	3.59	0.32	1224	65	19.6	0.2	34.0	1.2
DBH068_grn4-4	GB	2673	388	0.7	0.05	0.0862	5.8	0.003040	2.62	3909.6550	6.36	0.41	1343	108	19.6	0.5	36.0	2.3
DBH068_grn11-2	GB	3873	-47	1	0.08	0.0978	7.9	0.003018	2.72	4468.4131	8.36	0.33	1583	141	19.4	0.5	40.5	3.3
DBH068_grn3-2	M	2745	235	0.7	0.06	0.1003	3.28	0.002952	2.02	4684.8353	3.85	0.52	1630	60	19.0	0.4	40.6	1.5
DBH068_grn2-1	FM	2851	798	0.9	0.05	0.0732	3.86	0.002938	1.02	3435.3927	3.99	0.26	1020	76	18.9	0.2	29.7	1.2
DBH068_grn8-2	GB	3540	318	0.8	0.06	0.0912	3.22	0.002928	3.40	4294.4965	4.68	0.73	1451	60	18.8	0.6	36.7	1.7
DBH068_grn11-1	GB	3885	337	0.9	0.06	0.0731	5.7	0.002921	2.28	3450.4544	6.14	0.37	1017	111	18.8	0.4	29.5	1.8
DBH068_grn13-1	GB	2567	290	0.6	0.04	0.0714	5.12	0.002819	2.46	3492.2848	5.68	0.43	969	101	18.1	0.4	27.8	1.6
DBH063																		
DBH063_grn9-2	GB	4214	735	1.1	0.1	0.0957	4.78	0.003610	2.58	3655.0471	5.43	0.47	1542	87	23.2	0.6	47.3	2.5
DBH063_grn2-4	GB	3973	834	1.1	0.07	0.07	3.32	0.003587	3.12	2690.6730	4.56	0.68	928	67	23.1	0.7	34.6	1.5
DBH063_grn7-2	FM	2860	693	0.8	0.06	0.0843	5.04	0.003570	2.60	3255.6818	5.67	0.46	1299	95	23.0	0.6	41.3	2.3
DBH063_grn3-3	GB	2981	452	0.8	0.05	0.0724	6.5	0.003475	1.56	2872.8671	6.68	0.23	997	127	22.4	0.3	34.6	2.3

						Ratios							Ages					
Analysis	§	U (ppm)	204 (cps)	206 (mV)	207 (mV)	207/206	2σ (%)	206/238	2σ (%)	207/235†	2σ (%)	Rho*	207/206 (Ma)	2σ abs	206/238 (Ma)	2σ abs	207/235 (Ma)	2σ abs
DBH063_grn3-1	GB	2681	761	0.7	0.04	0.0597	4.58	0.003459	1.54	2379.3789	4.83	0.32	593	96	22.3	0.3	28.5	1.4
DBH063_grn5-2	K	2653	626	0.7	0.05	0.0761	5.4	0.003418	2.58	3069.8399	5.98	0.43	1098	104	22.0	0.6	35.8	2.1
DBH063_grn8-1	FM	3514	508	0.9	0.06	0.0785	7.24	0.003203	2.50	3378.6887	7.66	0.33	1160	137	20.6	0.5	34.6	2.6
DBH063_grn12-2	M	3760	170	0.9	0.06	0.0724	3.6	0.003171	1.82	3147.8853	4.03	0.45	997	71	20.4	0.4	31.6	1.3
DBH063_grn13-1	FM	4493	212	1.1	0.06	0.068	3.34	0.003168	3.54	2959.9527	4.87	0.73	869	68	20.4	0.7	29.7	1.4
DBH063_grn9-1	GB	3890	456	0.9	0.05	0.0631	3.46	0.003163	2.52	2751.0121	4.28	0.59	712	72	20.4	0.5	27.6	1.2
DBH063_grn2-2	GB	4172	795	1	0.06	0.0679	4.16	0.003108	2.50	3011.7721	4.85	0.52	866	84	20.0	0.5	29.1	1.4
DBH063_grn7-1	FM	3546	556	0.8	0.06	0.0805	6.9	0.003048	2.76	3642.0264	7.43	0.37	1209	130	19.6	0.5	33.8	2.5
DBH063_grn2.1	GB	4836	518	1.1	0.08	0.087	6.14	0.003019	5.40	3972.9295	8.18	0.66	1361	114	19.4	1.0	36.1	2.9
DBH063_grn12-1	M	4400	-46	1	0.06	0.0691	3.12	0.002974	2.80	3203.7198	4.19	0.67	902	63	19.1	0.5	28.4	1.2
DBH063_grn8-2	FM	3992	422	0.9	0.06	0.0785	3.88	0.002885	3.20	3751.8858	5.03	0.64	1160	75	18.6	0.6	31.2	1.5
DBH063_grn3-2	GB	3754	785	0.8	0.07	0.1061	3.08	0.002780	1.78	5262.6609	3.56	0.50	1733	55	17.9	0.3	40.5	1.4
DBH063_grn11-1	FM	3071	44	0.6	0.04	0.0712	5.8	0.002700	1.58	3635.6485	6.01	0.26	963	114	17.4	0.3	26.6	1.6
DBH063_grn17-1	M	5065	373	1	0.06	0.0716	3.66	0.002581	1.80	3824.4934	4.08	0.44	975	73	16.6	0.3	25.6	1.0
DBH113																		
DBH113_grn7-3	SB	4922	160	1.3	0.08	0.0715	2.32	0.003744	2.56	2633.3812	3.45	0.74	972	47	24.1	0.6	36.8	1.2
DBH113_grn5-1	M	3289	177	0.9	0.05	0.065	4.06	0.003677	2.82	2437.6288	4.94	0.57	774	83	23.7	0.7	32.9	1.6
DBH113_grn4-2	SB	2984	-146	0.8	0.04	0.0629	3.92	0.003665	2.92	2366.0729	4.89	0.60	705	81	23.6	0.7	31.8	1.5
DBH113_grn4-3	SB	2963	-4	0.8	0.04	0.0644	3.94	0.003626	2.56	2448.8696	4.70	0.54	755	81	23.3	0.6	32.2	1.5
DBH113_grn4-1	SB	2537	329	0.6	0.09	0.1696	1.96	0.003620	2.84	6460.4214	3.45	0.82	2554	32	23.3	0.7	82.5	2.7
DBH113_grn1_2	GB	3223	-439	0.8	0.05	0.0655	3.76	0.003575	2.60	2526.4614	4.57	0.57	790	77	23.0	0.6	32.3	1.5
DBH113_grn14-1	GB	3925	-138	1	0.06	0.0658	3.06	0.003564	2.60	2545.5632	4.02	0.65	800	63	22.9	0.6	32.3	1.3
DBH113_grn10-1	GB	4360	-106	1.1	0.06	0.0637	2.98	0.003533	2.92	2486.1914	4.17	0.70	732	62	22.7	0.7	31.0	1.3
DBH113_grn1_1	GB	2846	33	0.7	0.04	0.0652	4.3	0.003532	3.32	2545.5450	5.43	0.61	781	88	22.7	0.8	31.7	1.7
DBH113_grn2_4	SB	4175	633	1	0.14	0.1516	1.88	0.003491	4.48	5988.1791	4.86	0.92	2364	32	22.5	1.0	71.5	3.3
DBH113_grn1_3	GB	3197	52	0.8	0.06	0.0904	2.94	0.003460	3.00	3602.0731	4.20	0.71	1434	55	22.3	0.7	42.9	1.8
DBH113_grn15-1	SB	4978	158	1.2	0.07	0.0645	2.62	0.003449	2.70	2578.5118	3.76	0.72	758	54	22.2	0.6	30.7	1.1
DBH113_grn5-2	M	3402	-55	0.8	0.05	0.0735	3.64	0.003425	2.80	2959.0792	4.59	0.61	1028	72	22.0	0.6	34.6	1.6
DBH113_grn12-1	SB	4025	441	0.9	0.05	0.0661	3.26	0.003331	3.50	2736.4389	4.78	0.73	810	67	21.4	0.7	30.4	1.4
DBH113_grn7-1	SB	4514	62	1	0.07	0.0723	2.76	0.003281	3.66	3038.2677	4.58	0.80	994	55	21.1	0.8	32.7	1.5
DBH113_grn8-2	GB	4187	58	1	0.1	0.1213	11.68	0.003246	3.10	5152.7572	12.08	0.26	1975	195	20.9	0.6	53.7	6.3
DBH113_grn11-1	SB	4123	421	0.9	0.05	0.0692	3.2	0.003122	3.76	3056.4588	4.94	0.76	905	65	20.1	0.8	29.8	1.4
DBH113_grn11-2	SB	4679	196	0.9	0.06	0.0707	2.96	0.002977	3.56	3274.3922	4.63	0.77	949	59	19.2	0.7	29.0	1.3
DBH113_grn8-1	GB	4372	485	0.9	0.11	0.148	1.64	0.002902	2.92	7031.3781	3.35	0.87	2323	28	18.7	0.5	58.4	1.9
DBH113_grn9-1a	GB	5134	551	1	0.11	0.1211	1.78	0.002893	5.50	5772.5795	5.78	0.95	1973	31	18.6	1.0	47.9	2.7
DBH113_grn15-2	SB	5590	554	1.1	0.11	0.12	1.64	0.002866	2.78	5772.2635	3.23	0.86	1956	29	18.5	0.5	47.0	1.5
DBH113_grn2_2	SB	4751	-147	0.9	0.07	0.0878	2.7	0.002609	2.82	4639.6934	3.90	0.72	1378	51	16.8	0.5	31.6	1.2
DBH113_grn3_2	SB	3960	-62	0.7	0.05	0.0822	4.12	0.002562	2.70	4423.7838	4.93	0.55	1250	79	16.5	0.4	29.1	1.4
DBH122																		
DBH122_grn1-1	GB	1593	287	0.5	0.03	0.0528	6.44	0.004140	1.56	1758.4995	6.63	0.24	320	140	26.6	0.4	30.2	2.0
DBH122_grn18-1	GB	3613	373	1.2	0.06	0.0528	3.18	0.004012	5.56	1814.4104	6.41	0.87	320	71	25.8	1.4	29.2	1.8

						Ratios							Ages					
Analysis	§	U (ppm)	204 (cps)	206 (mV)	207 (mV)	207/206	2σ (%)	206/238	2σ (%)	207/235†	2σ (%)	Rho*	207/206 (Ma)	2σ abs	206/238 (Ma)	2σ abs	207/235 (Ma)	2σ abs
DBH122_grn1-2	GB	1948	753	0.6	0.03	0.0538	5.94	0.003547	1.22	2091.4893	6.06	0.20	363	129	22.8	0.3	26.4	1.6
DBH122_grn6-1	M	2966	411	0.8	0.04	0.0529	4.3	0.003439	3.66	2121.0522	5.65	0.65	325	95	22.1	0.8	25.2	1.4
DBH122_grn14-1	M	3241	717	0.9	0.04	0.0512	4.12	0.003406	1.12	2072.4445	4.27	0.26	250	92	21.9	0.2	24.1	1.0
DBH122_grn7-1	F	2130	694	0.6	0.03	0.0539	5.82	0.003375	3.78	2202.0965	6.94	0.54	367	126	21.7	0.8	25.2	1.7
DBH122_grn5-1	F	2260	530	0.6	0.03	0.0585	6.12	0.003367	2.92	2395.2734	6.78	0.43	549	128	21.7	0.6	27.2	1.8
DBH122_grn11-1	GB	3793	373	1.1	0.04	0.0485	3.82	0.003351	1.20	1995.3876	4.00	0.30	124	88	21.6	0.3	22.5	0.9
DBH122_grn11-2	GB	3573	640	1	0.04	0.0496	4.06	0.003309	1.26	2066.7683	4.25	0.30	176	92	21.3	0.3	22.7	1.0
DBH122_grn12-1	GB	3444	288	0.9	0.05	0.0582	5.72	0.003276	1.50	2449.4338	5.91	0.25	537	120	21.1	0.3	26.3	1.5
DBH122_grn10-1	SB	2126	685	0.6	0.07	0.1419	5	0.003076	3.12	6359.6592	5.89	0.53	2251	84	19.8	0.6	59.3	3.4
DBH122_grn8-1a	GB	1715	1125	0.4	0.05	0.141	5.46	0.003026	1.48	6424.8881	5.66	0.26	2240	91	19.5	0.3	58.0	3.2
DBH122_grn16-1	GB	2197	-29	0.5	0.03	0.0537	6.32	0.002985	2.56	2480.3923	6.82	0.38	358	137	19.2	0.5	22.2	1.5
DBH122_grn4-1	SB	1880	564	0.4	0.04	0.1057	4.54	0.002679	6.18	5439.1312	7.67	0.81	1727	81	17.2	1.1	38.9	2.9
DBH095																		
DBH095_grn11_2	FF	4502	349	2.9	0.19	0.0763	1.98	0.003870	1.66	2718.7467	2.58	0.64	1103	39	24.9	0.4	40.5	1.0
DBH095_grn2_4a	SB	4860	100	2.7	0.16	0.0886	4.52	0.003800	4.22	3214.4403	6.18	0.68	1396	84	24.5	1.0	46.1	2.8
DBH095_grn2_1	SB	5169	127	2.9	0.15	0.0662	3.72	0.003774	2.36	2418.5550	4.41	0.54	813	76	24.3	0.6	34.4	1.5
DBH095_grn8_1	SB	3214	268	2	0.1	0.0547	2.06	0.003734	1.92	2019.7572	2.82	0.68	400	46	24.0	0.5	28.2	0.8
DBH095_grn3-1	GB	3711	145	2.4	0.12	0.0579	1.82	0.003712	1.82	2150.8478	2.57	0.71	526	39	23.9	0.4	29.6	0.8
DBH095_grn11_1	FF	4833	82	3	0.17	0.065	2.26	0.003698	1.48	2423.2893	2.70	0.55	774	47	23.8	0.4	33.1	0.9
DBH095_grn1_1	FF	3621	-96	2	0.09	0.05	2.12	0.003621	2.54	1904.1228	3.31	0.77	195	49	23.3	0.6	25.0	0.8
DBH095_grn1_3	FF	3589	43	1.9	0.1	0.0497	2.62	0.003588	2.60	1909.7611	3.69	0.70	181	60	23.1	0.6	24.7	0.9
DBH095_grn10_2	GB	3573	117	2.1	0.11	0.0599	1.96	0.003578	1.40	2308.4764	2.41	0.58	600	42	23.0	0.3	29.6	0.7
DBH095_grn10_1	GB	3158	77	1.8	0.09	0.0544	2.22	0.003453	1.42	2172.4946	2.64	0.54	388	49	22.2	0.3	26.0	0.7
DBH095_grn5-4	FF	3800	42	2.2	0.12	0.0629	3.32	0.003443	1.48	2518.7116	3.63	0.41	705	69	22.2	0.3	29.9	1.1
DBH095_grn4_2	M	1558	268	0.7	0.05	0.093	3.38	0.003023	1.52	4241.1543	3.71	0.41	1488	63	19.5	0.3	38.6	1.4
DBH095_grn13_1	GB	1613	129	0.8	0.04	0.0534	4.7	0.002987	4.38	2464.5474	6.42	0.68	346	103	19.2	0.8	22.1	1.4
DBH095_grn5-3	FF	2861	-165	1.5	0.07	0.055	6.02	0.002958	1.44	2563.8717	6.19	0.23	412	129	19.0	0.3	22.5	1.4
DBH095_grn14_1	SB	3404	-54	1.6	0.08	0.0554	3.1	0.002953	4.10	2586.5665	5.14	0.80	428	68	19.0	0.8	22.7	1.2
DBH095_grn1_4	FF	2295	-44	1	0.07	0.0658	2.84	0.002933	2.86	3092.9073	4.03	0.71	800	58	18.9	0.5	26.7	1.1
DBH095_grn4_1	M	1549	-6	0.7	0.04	0.0716	8.78	0.002910	1.86	3392.0907	8.97	0.21	975	169	18.7	0.3	28.8	2.5
DBH095_grn6-2	GB	2895	149	1.4	0.09	0.0732	2.42	0.002784	1.46	3625.4404	2.83	0.52	1020	48	17.9	0.3	28.1	0.8
DBH095_grn5-1	FF	2380	-205	1.1	0.05	0.0534	3.6	0.002676	1.40	2751.1809	3.86	0.36	346	79	17.2	0.2	19.8	0.8
DBH095_grn5-2	FF	2597	-236	1.2	0.06	0.0558	3.24	0.002666	1.44	2885.6006	3.55	0.41	444	70	17.2	0.2	20.6	0.7
DBH095_15-1	IG	3673	143	1.7	0.08	0.0626	9.22	0.003770	6.22	2289.7081	11.12	0.56	695	185	24.3	1.5	32.5	3.6
DBH095_16-1	IG	4121	125	1.9	0.09	0.0992	3.9	0.003724	6.24	3672.5982	7.36	0.85	1609	71	24.0	1.5	50.4	3.6
DBH095_16-2f	IG	4588	509	2	0.14	0.1387	23.24	0.003677	6.28	5201.1423	24.07	0.26	2211	356	23.7	1.5	69.0	15.9
DBH095_16-3f	IG	4180	373	1.8	0.11	0.1144	19.46	0.003685	6.28	4280.6048	20.45	0.31	1870	315	23.7	1.5	57.4	11.3
DBH095_16-4f	IG	5450	68	2.4	0.11	0.0644	4.58	0.003625	6.22	2449.4911	7.72	0.81	755	94	23.3	1.4	32.2	2.4
DBH095_16-5f	IG	2235	-8	1	0.05	0.0822	24.5	0.003633	6.36	3119.3842	25.31	0.25	1250	417	23.4	1.5	41.0	10.1
DBH095_16-6f	IG	2153	428	1	0.07	0.125	25.98	0.003841	6.44	4487.6493	26.77	0.24	2029	400	24.7	1.6	65.1	16.7
DBH095_17-1	IG	4904	189	2.1	0.1	0.0693	6.44	0.003647	6.28	2620.2907	9.00	0.70	908	127	23.5	1.5	34.8	3.1

						Ratios							Ages					
Analysis	§	U (ppm)	204 (cps)	206 (mV)	207 (mV)	207/206	2σ (%)	206/238	2σ (%)	207/235†	2σ (%)	Rho*	207/206 (Ma)	2σ abs	206/238 (Ma)	2σ abs	207/235 (Ma)	2σ abs
DBH095_17-2	IG	5059	193	2.1	0.1	0.0666	4.06	0.003625	6.26	2533.0776	7.46	0.84	825	83	23.3	1.5	33.3	2.4
DBH095_17-3	IG	4787	240	2	0.09	0.0537	3.24	0.003637	6.22	2035.9948	7.01	0.89	358	72	23.4	1.5	27.0	1.9
DBH095_17-4	IG	4803	206	2	0.09	0.0538	3.44	0.003642	6.28	2036.8191	7.16	0.88	363	76	23.4	1.5	27.1	1.9
DBH095_17-5	IG	2019	297	0.8	0.05	0.0652	5.88	0.003449	6.24	2606.3159	8.57	0.73	781	119	22.2	1.4	31.0	2.6
DBH095_17-6	IG	3075	273	1.3	0.06	0.0797	6.94	0.003569	6.32	3079.2378	9.39	0.67	1190	131	23.0	1.4	39.1	3.6
DBH095_17-7	GB	3262	-12	0.9	0.04	0.0831	6.16	0.002476	6.28	4626.9001	8.80	0.71	1272	116	15.9	1.0	28.4	2.5
CWB08-4																		
CWB08-4_grn8-2	GB	3501	631	1.3	0.08	0.0761	2.26	0.004230	1.50	2480.4667	2.71	0.55	1098	45	27.2	0.4	44.1	1.2
CWB08-4-grn1-3	M	2592	639	0.9	0.06	0.073	3.56	0.004228	1.28	2380.5299	3.78	0.34	1014	71	27.2	0.3	42.3	1.6
CWB08-4_grn9-3	GB	3278	474	1.2	0.07	0.0655	2.74	0.004110	2.64	2197.4570	3.80	0.69	790	56	26.4	0.7	37.0	1.4
CWB08-4-grn4-3	-	4192	730	1.5	0.08	0.0653	2.22	0.004106	2.02	2192.8180	3.00	0.67	784	46	26.4	0.5	36.9	1.1
CWB08-4-grn4-4	-	4835	668	1.6	0.09	0.0683	2.14	0.003911	2.08	2407.6965	2.98	0.70	878	44	25.2	0.5	36.7	1.1
CWB08-4-grn3-3	IK	6690	472	2.2	0.12	0.0618	1.7	0.003795	3.82	2245.1941	4.18	0.91	667	36	24.4	0.9	32.3	1.3
CWB08-4_grn8-1	GB	5600	393	1.7	0.1	0.0658	2.02	0.003625	1.84	2502.9224	2.73	0.67	800	42	23.3	0.4	32.9	0.9
CWB08-4_grn7-3	IK	3896	292	1.2	0.07	0.0718	2.78	0.003542	2.04	2794.8080	3.45	0.59	980	56	22.8	0.5	35.0	1.2
CWB08-4-grn4-2	-	5932	515	1.8	0.11	0.0692	1.78	0.003529	2.10	2703.6216	2.75	0.76	905	36	22.7	0.5	33.6	0.9
CWB08-4-grn1-2	M	4203	569	1.3	0.07	0.0674	2.54	0.003505	1.32	2651.6036	2.86	0.46	850	52	22.6	0.3	32.5	0.9
CWB08-4_grn7-2	IK	4171	431	1.2	0.08	0.0712	2.6	0.003484	2.82	2817.4951	3.84	0.74	963	52	22.4	0.6	34.2	1.3
CWB08-4-grn1-1	M	3805	482	1.1	0.07	0.0719	2.58	0.003468	1.32	2858.5785	2.90	0.46	983	52	22.3	0.3	34.3	1.0
CWB08-4_grn9-1	GB	6348	417	1.9	0.1	0.0642	1.82	0.003456	3.50	2561.5617	3.94	0.89	748	38	22.2	0.8	30.6	1.2
CWB08-4-grn2-3	M	5314	850	1.6	0.12	0.0873	5.06	0.003453	2.04	3486.3747	5.46	0.37	1367	94	22.2	0.5	41.3	2.2
CWB08-4-grn4-5	-	6960	775	2	0.12	0.0708	1.66	0.003334	2.34	2928.3760	2.87	0.82	952	34	21.5	0.5	32.5	0.9
CWB08-4-grn1-4	M	3887	542	1.1	0.07	0.0728	2.72	0.003309	1.58	3033.0809	3.15	0.50	1008	54	21.3	0.3	33.2	1.0
CWB08-4_grn7-1	IK	4378	266	1.2	0.08	0.0782	2.26	0.003273	1.36	3294.6139	2.64	0.52	1152	44	21.1	0.3	35.2	0.9
CWB08-4-grn3-1	IK	5849	727	1.7	0.12	0.0812	2.14	0.003266	1.64	3428.0591	2.70	0.61	1226	41	21.0	0.3	36.5	1.0
CWB08-4_grn9-2	GB	5079	230	1.3	0.08	0.0697	2.52	0.003088	3.38	3112.2749	4.22	0.80	920	51	19.9	0.7	29.7	1.2
CWB08-4-grn2-2	M	6103	481	1.6	0.1	0.0718	2	0.003087	3.50	3206.6390	4.03	0.87	980	40	19.9	0.7	30.6	1.2
CWB08-4_grn9-4	GB	5791	580	1.5	0.09	0.0689	2.12	0.003011	1.44	3155.1174	2.56	0.56	896	43	19.4	0.3	28.6	0.7
CWB08-4_grn6-2	GB	4856	542	1.1	0.08	0.0804	2.38	0.002702	1.82	4102.7628	3.00	0.61	1207	46	17.4	0.3	30.0	0.9
CWB08-4_grn6-1	GB	4588	478	1	0.07	0.0763	2.66	0.002560	3.84	4110.2593	4.67	0.82	1103	52	16.5	0.6	27.0	1.2
CWB08-4-grn2-1	M	6101	399	1.3	0.08	0.0757	2.2	0.002484	2.12	4201.3089	3.06	0.69	1087	43	16.0	0.3	26.0	0.8

				Ratios									Ages							
Anal.	§	Th (ppm)	Th/U	207/206	2σ (%)	206/238	2σ (%)	207/235†	2σ (%)	Rho*	208/232	2σ (%)	207/206 (Ma)	2σ abs	206/238 (Ma)	2σ abs	207/235 (Ma)	2σ abs	208/232 (Ma)	2σ abs
15-1	IG	61604	16.8	0.05284	2.68	0.00377	6.22	0.02747	6.77	0.56	0.00110	13.08	321.9	59.8	24.26	3.01	27.51	1.84	22.22	5.81
16-1	IG	50515	12.3	0.05889	3.06	0.00372	6.24	0.03021	6.95	0.85	0.00117	8.96	563.1	65.3	23.94	2.98	30.22	2.07	24.24	4.34
16-2f	IG	12602	2.7	0.08058	4.20	0.00368	6.28	0.04089	7.56	0.26	0.00117	10.34	1211.2	80.6	23.68	2.97	40.69	3.01	24.24	5.01
16-3f	IG	15699	3.8	0.06932	2.34	0.00368	6.28	0.03518	6.70	0.31	0.00138	23.9	908.4	47.5	23.68	2.97	35.10	2.31	28.28	13.50
16-4f	IG	78621	14.4	0.05410	1.85	0.00363	6.22	0.02708	6.49	0.81	0.00111	7.6	375.4	41.0	23.36	2.90	27.13	1.74	22.22	3.38
16-5f	IG	14403	6.4	0.05619	4.63	0.00363	6.36	0.02812	7.87	0.25	0.00121	28.74	459.8	99.6	23.36	2.97	28.16	2.18	24.24	13.92
16-6f	IG	5708	2.7	0.08579	8.07	0.00384	6.44	0.04542	10.32	0.24	0.00140	29.1	1333.4	148.6	24.71	3.18	45.10	4.54	28.28	16.44
17-1	IG	91461	18.7	0.05645	2.02	0.00365	6.28	0.02841	6.60	0.70	0.00109	12.58	470.0	44.0	23.49	2.94	28.44	1.85	22.22	5.59
17-2	IG	83506	16.5	0.05370	2.24	0.00363	6.26	0.02688	6.65	0.84	0.00114	10.64	358.6	49.9	23.36	2.92	26.93	1.77	22.22	4.73
17-3	IG	89659	18.7	0.05388	2.50	0.00364	6.22	0.02704	6.70	0.89	0.00108	6.96	366.0	55.3	23.42	2.91	27.09	1.79	22.22	3.09
17-4	IG	90597	18.9	0.05395	2.42	0.00364	6.28	0.02708	6.73	0.88	0.00109	6.94	368.9	53.5	23.42	2.94	27.13	1.80	22.22	3.08
17-5	IG	63165	31.3	0.07864	6.41	0.00345	6.24	0.03741	8.94	0.73	0.00094	6.9	1163.1	122.0	22.20	2.77	37.29	3.27	18.18	2.51
17-6	IG	58145	18.9	0.06090	5.06	0.00357	6.32	0.02998	8.10	0.67	0.00114	7.98	635.6	105.3	22.97	2.90	29.99	2.39	22.22	3.54
17-7	GB	55899	17.1	0.05284	5.48	0.00248	6.28	0.01807	8.33	0.71	0.00077	6.66	322.1	119.8	15.97	2.00	18.18	1.50	16.16	2.15

Table 3.4: U(-Th)-Pb geochronology results, DBH 095. §Textural position: GB—monazite is at grain boundaries; IG—monazite inclusion in garnet. *Rho is the $^{206}Pb^{238}U$ - $^{207}Pb/^{235}U$ error correlation coefficient calculated following K.R. Ludwig (unpublished data, 1993). †$^{207}Pb/^{235}U$ calculated using ($^{207}Pb/^{206}Pb$)/($^{238}U/^{206}Pb$*1/137.88).

uncorrected for common-Pb, but with common-Pb lines of slope determined by direct measurement of the $^{207}Pb/^{206}Pb$ ratio in feldspar grains (Fig. 3.8). All monazite grains large enough to sample multiple spots show a range in U-Pb age within individual grains (i.e., Fig. 3.7) with low Y cores (high Th for Chekha Group samples) up to 10 million years older than high Y rims (Fig. 3.8). Monazite grains in the GHS samples yielded consistently older core U-Pb ages than the Chekha Group samples, at 26.4-23.1 Ma vs. 21.8-19.7 Ma, respectively (Fig. 3.8). All samples contain monazite as young as ca. 16-15 Ma. Typically the high-Y rims yield the youngest ages (e.g., Fig. 3.8c-f), while there does not appear to be a correlation between Th concentration and age (e.g., Fig. 3.8a-b).

Monazite in Chekha Group sample DBH 068 yields a spread of U-Pb ages from 19.7 $\pm$ 0.2 Ma (MSWD=1.1, n=9) to ca. 17.6 Ma. Similarly, sample DBH 063 also yields a spread of U-Pb monazite ages from 21.8 $\pm$ 0.3 Ma (MSWD=1.8, n=6) to ca. 16.1 Ma.

Monazite growth in GHS sample DBH 113 began at 23.1 $\pm$ 0.3 Ma (MSWD=0.5, n=4). Monazite grains included in silicate minerals (mica, kyanite, feldspar) yield ages as young as ca. 21 Ma, and high Y monazite occurring within shear bands is as young as ca. 15.7 Ma. In sample CWB-08-04, monazite growth began at 26.0 $\pm$ 0.2 Ma (MSWD=1.5, n=5). Monazite included in silicates is as young as ca. 20.3 Ma, and the youngest monazite, a high Y rim on monazite at a grain boundary in the matrix, yields an age of ca. 15.4 Ma. Monazite growth in DBH 122 initiated at ca. 26.4 Ma. Monazite included in silicate minerals grew until ca. 21.7 Ma. The youngest monazite in this sample yields an age of ca. 15.9 Ma. In the structurally lowest sample analyzed, DBH 095, monazite growth began at 23.5 $\pm$ 0.3 Ma (MSWD=2.0, n=8), monazite grains included in garnet yield ages of 22.6 $\pm$ 0.4 Ma (MSWD=1.0, n=9), and the youngest U-Pb age, from a high Y rim on a monazite grain at a grain boundary between garnet and the matrix, is ca. 15.2 Ma.

3.6.2.2 Interpretation

A correspondence was observed between U-(Th)-Pb age and elemental zoning, particularly Y zoning, pointing to the importance of elemental mapping prior to *in situ* dating, as it can be used as a tool for preventing inadvertent mixing of different age domains within single crystals. These data indicate that for those studies of *in situ* monazite in which elemental mapping is not conducted, mixing of age domains is likely to be the rule rather than the exception. Unlike grain separates, which are selected for their similar size and then polished to reveal approximate cross-sections of grains, *in situ* grains are randomly

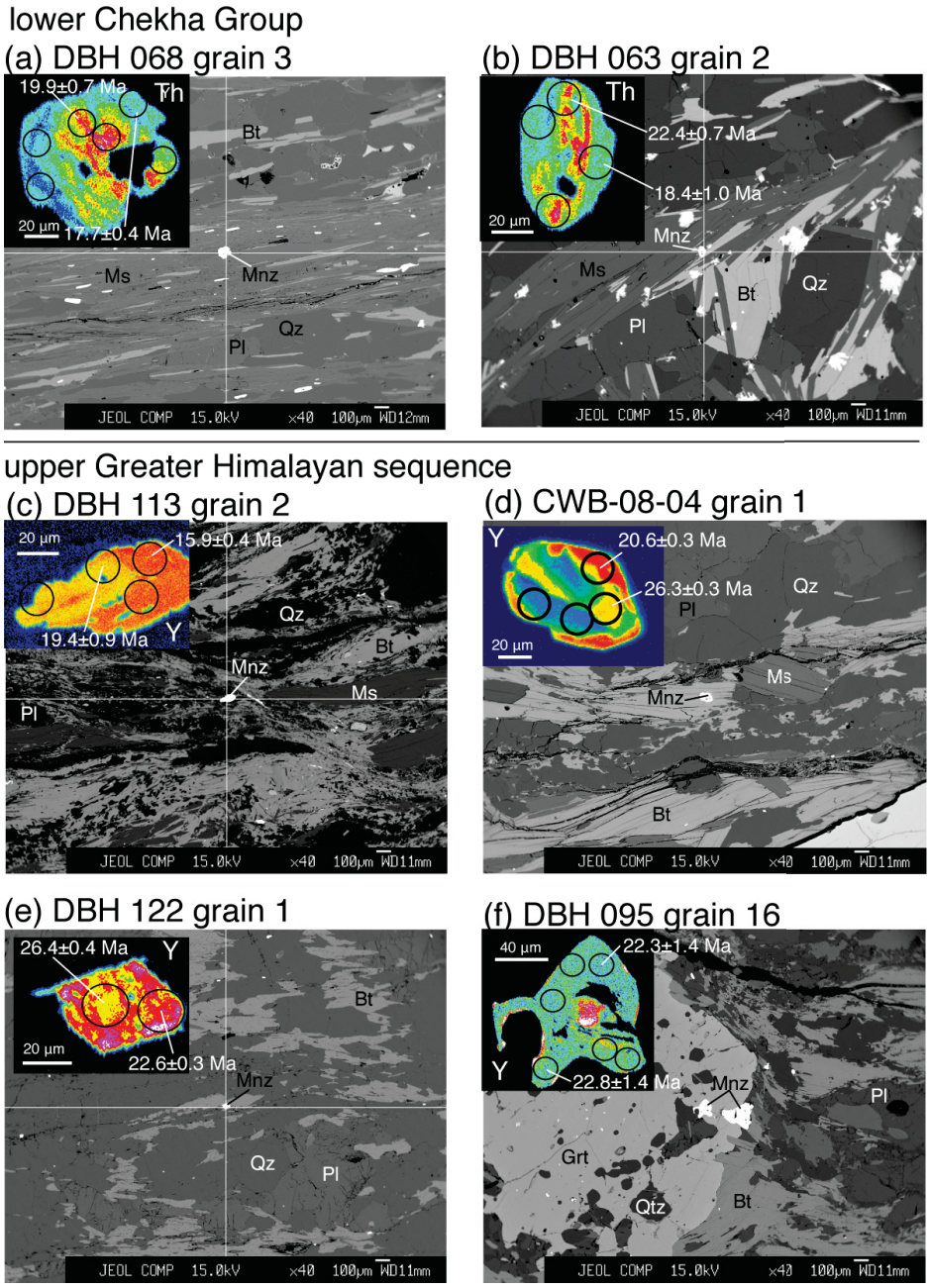

Figure 3.7: Monazite characterization. Y or Th elemental maps illustrating chemical zoning and representative spot analysis locations are inset in BSE images showing the microstructural context of *in situ* monazite. For the elemental maps, white/red=high Y or Th and blue/black=low Y or Th.

Figure 3.8: U(-Th)-Pb geochronology results. Data are plotted in Tera-Wasserburg diagrams. Data point error ellipses are 2σ. Ellipses are coloured according to monazite microstructure and high Y zones (*except for (a) and (b) which do not exhibit Y zoning and are coloured for high Th zones). For clarity, younger data points are not shown for (e) but are high Y monazite spots in shear bands and at grain boundaries. (h) are U-Pb results for monazite inclusions in garnet from DBH 095, while (g) shows the $^{208}Pb/^{232}Th$ age for the same points. CmPb lines for all plots correspond to CmPb $^{207}Pb/^{206}Pb = 0.824$ (see section 3.6.2 for details).

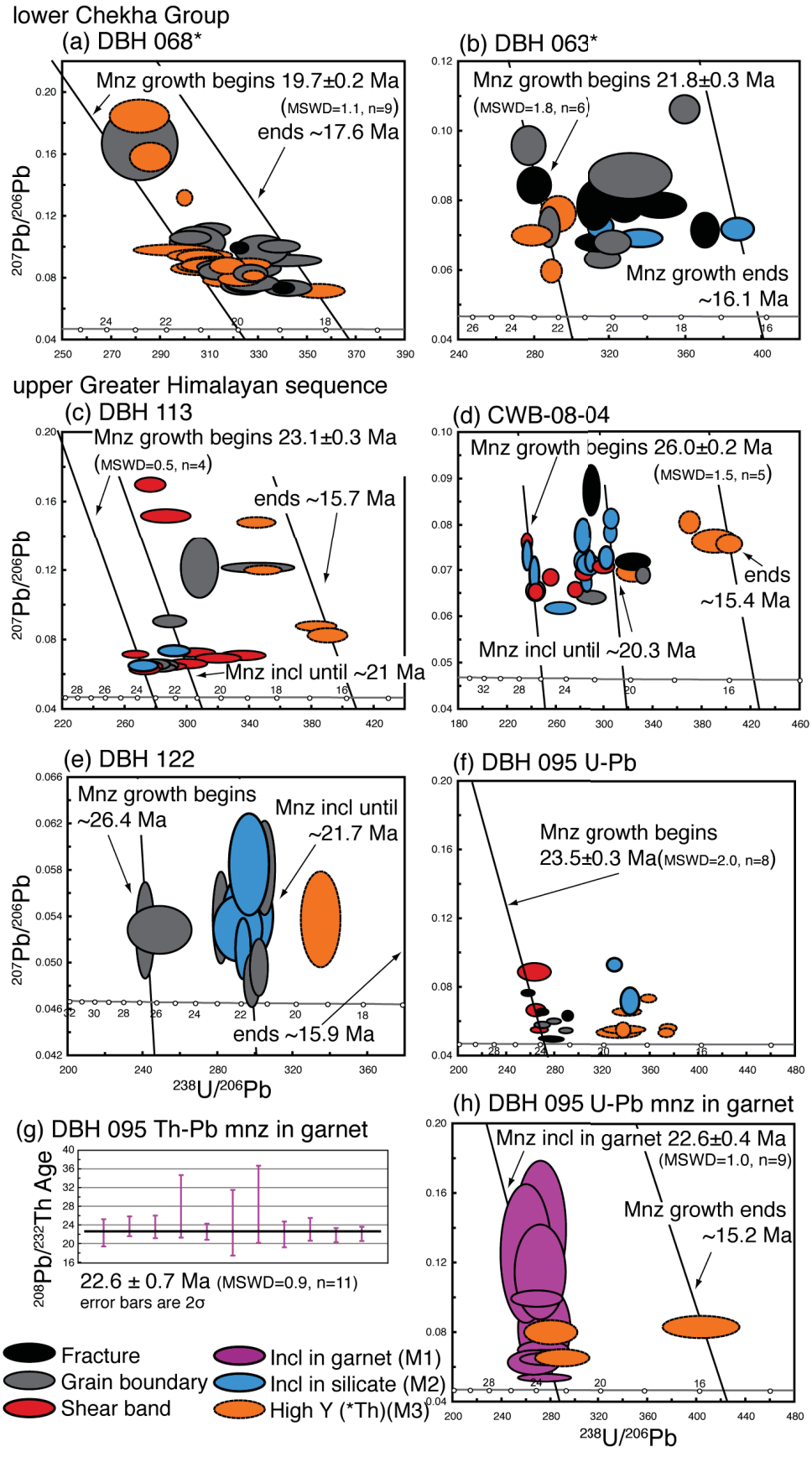
lower Chekha Group
(a) DBH 068*
Mnz growth begins 19.7±0.2 Ma
(MSWD=1.1, n=9)
ends ~17.6 Ma
(b) DBH 063*
Mnz growth begins 21.8±0.3 Ma
(MSWD=1.8, n=6)
Mnz growth ends
~16.1 Ma
upper Greater Himalayan sequence
(c) DBH 113
Mnz growth begins 23.1±0.3 Ma
(MSWD=0.5, n=4)
ends ~15.7 Ma
Mnz incl until ~21 Ma
(d) CWB-08-04
Mnz growth begins 26.0±0.2 Ma
(MSWD=1.5, n=5)
ends
~15.4 Ma
Mnz incl until ~20.3 Ma
(e) DBH 122
Mnz growth begins
~26.4 Ma
Mnz incl until
~21.7 Ma
ends ~15.9 Ma
(f) DBH 095 U-Pb
Mnz growth begins
23.5±0.3 Ma(MSWD=2.0, n=8)
(g) DBH 095 Th-Pb mnz in garnet
22.6 ± 0.7 Ma (MSWD=0.9, n=11)
error bars are 2σ
(h) DBH 095 U-Pb mnz in garnet
Mnz incl in garnet 22.6±0.4 Ma
(MSWD=1.0, n=9)
Mnz growth ends
~15.2 Ma
Fracture
Grain boundary
Shear band
Incl in garnet (M1)
Incl in silicate (M2)
High Y (*Th)(M3)
207Pb/206Pb
238U/206Pb
208Pb/232Th Age

oriented and true cross-sections are probably rare. Furthermore, laser ablation samples a volume of material, while elemental mapping only characterizes the exposed near-surface of the grain. Thus, data interpretation is made with the conservative assumption that mixing of age domains is more common than not, and "mixed" ages may be analytically indistinguishable from a spread of ages resulting from continuous monazite growth.

Initial U-Th disequilibrium caused by the incorporation of excess ^{230}Th during crystallization may lead to excess ^{206}Pb in young monazite (Schärer, 1984). Excess ^{206}Pb yields an apparent increase in the measured ^{206}Pb/^{238}U age compared with the ^{207}Pb/^{235}U and ^{208}Pb/^{232}Th ages that can be difficult to resolve. However, the ^{232}Th decay system is unaffected by excess ^{206}Pb. A comparison of the average ^{206}Pb/^{238}U age of monazite inclusions in garnet from sample DBH 095 (22.6 $\pm$ 0.4 Ma, MSWD = 1.0) (Fig. 3.8h) with the weighted average ^{208}Pb/^{232}Th age for the same inclusions (22.6 $\pm$ 0.7 Ma, MSWD = 0.9) (Fig. 3.8g) shows the ages to be identical within uncertainty (including decay constant uncertainties for both systems). Furthermore, the youngest ages in all samples measured by both U-Pb and U-Th-Pb are ca. 16 Ma, coinciding with the youngest U-Pb ages measured for zircon in nearby leucogranites (Chapter 2). Thus, we argue that excess ^{206}Pb is insignificant in these samples. To simplify the interpretation of our U(-Th)-Pb age data, we assume that any excess ^{206}Pb exists in similar amounts both in time and between samples, such that the relative age differences shown in Fig. 3.8 are real. Considering these caveats, the ages reported below may be over-estimated by no more than ca. 0.5 Ma.

Attempts to link monazite ages to the P-T path must consider both textural relationships of monazite and chemical zonation (Martin et al., 2007). Here, monazite growth appears to have initiated in the GHS at ca. 26 Ma. Most U-Pb ages fall into broad groups of ca. 26 Ma, 24-22 Ma, 20-18 Ma and 16 Ma. In GHS samples, monazite inclusions in feldspar, biotite and kyanite yield U-Pb ages $\geq$20.3 Ma. In particular, the nine U-Pb analyses from three monazite inclusions in a single garnet grain, which may shield monazite from further growth or dissolution, together yield an age of 22.6 $\pm$ 0.4 Ma (Fig. 3.8h). In DBH 095, monazite inclusions in garnet do not yield the young ages found in the matrix. For at least two of the inclusions there were no apparent cracks connecting the inclusions to the matrix, and since multiple spots per grain from multiple grains yield identical ages, it is interpreted that the included monazite constrains the maximum age of garnet rim growth (Martin et al., 2007). Based on their textures and compositions (see

above), garnet rims in all dated samples appear to be syn-tectonic with respect to external gneissosity and schistosity, and pre-tectonic to top-to-the-north shearing. Thus, the 22.6 $\pm$ 0.4 Ma age of monazite inclusions within garnet provides an upper age limit for the onset of shearing within the outer STDS. Since the garnet rim which contains the dated monazite preserves textures consistent with partial melting, this age also provides a time constraint for partial melting in the GHS, and post-peak-P-T equilibrium preserved during recrystallization of the garnet rims and the matrix of the rocks (Fig. 3.9; Table 3.2). This timing constraint on the onset of partial melting agrees with zircon crystallization ages from leucogranites in the outer STDS (Chapter 2), and also coincides with the onset of granite melt generation west of Bhutan (Schärer, 1984; Simpson et al., 2000; Searle et al., 2003), contradicting earlier observations that partial melting occurred more recently east of the Yadong cross structure (Daniel et al., 2003; Harris et al., 2004).

The youngest monazite ages ($<$19 Ma and particularly those ca. 16-15 Ma) are from high Y monazite rims. This is consistent with garnet breakdown during monazite growth/recrystallization (Foster et al., 2002), linking these ages to the retrograde path for both the GHS and the Chekha Group (Fig. 3.9). Retrograde monazite has also been observed in the lower GHS in central and western Nepal (Bollinger and Janots, 2006; Martin et al., 2007). These young ages are not confined to monazite grains adjacent to fractures, but are also recorded by monazites within shear bands and mylonite zones. This suggests that normal-sense ductile shearing on the outer STDS outlasted monazite growth, confirming earlier work that indicates that latest movement on the outer STDS was after 15.5 Ma (Chapter 2). SIMS depth profiling of monazite and zircon rims in migmatite from a Cordilleran metamorphic core complex has revealed that fluid infiltration may also play a role in the late crystallization of accessory minerals during leucogranite crystallization and/or amphibolite-facies devolatilization (Gordon et al., 2009).

Figure 3.9: Pressure-temperature-time diagrams. Representative P-T-t diagrams for DBH 068, DBH 113 and CWB08-4 incorporating thermobarometry and monazite U-Pb age data, as well as zircon U-Pb crystallization and muscovite $^{40}Ar/^{39}Ar$ cooling age data from deformed leucogranites emplaced in the Chekha Group (Chapter 2). Al_2SiO_5 triple point is according to Pattison (1992). Model results for points G2, G3 from thermomechanical numerical model HT1 (Jamieson et al., 2004), and D3 and D4 from HT111 (Jamieson et al., 2006) are shown for comparison. Average T measurements are shown as parallelograms centred at P with best fit of T, with width indicating error in T at that P.

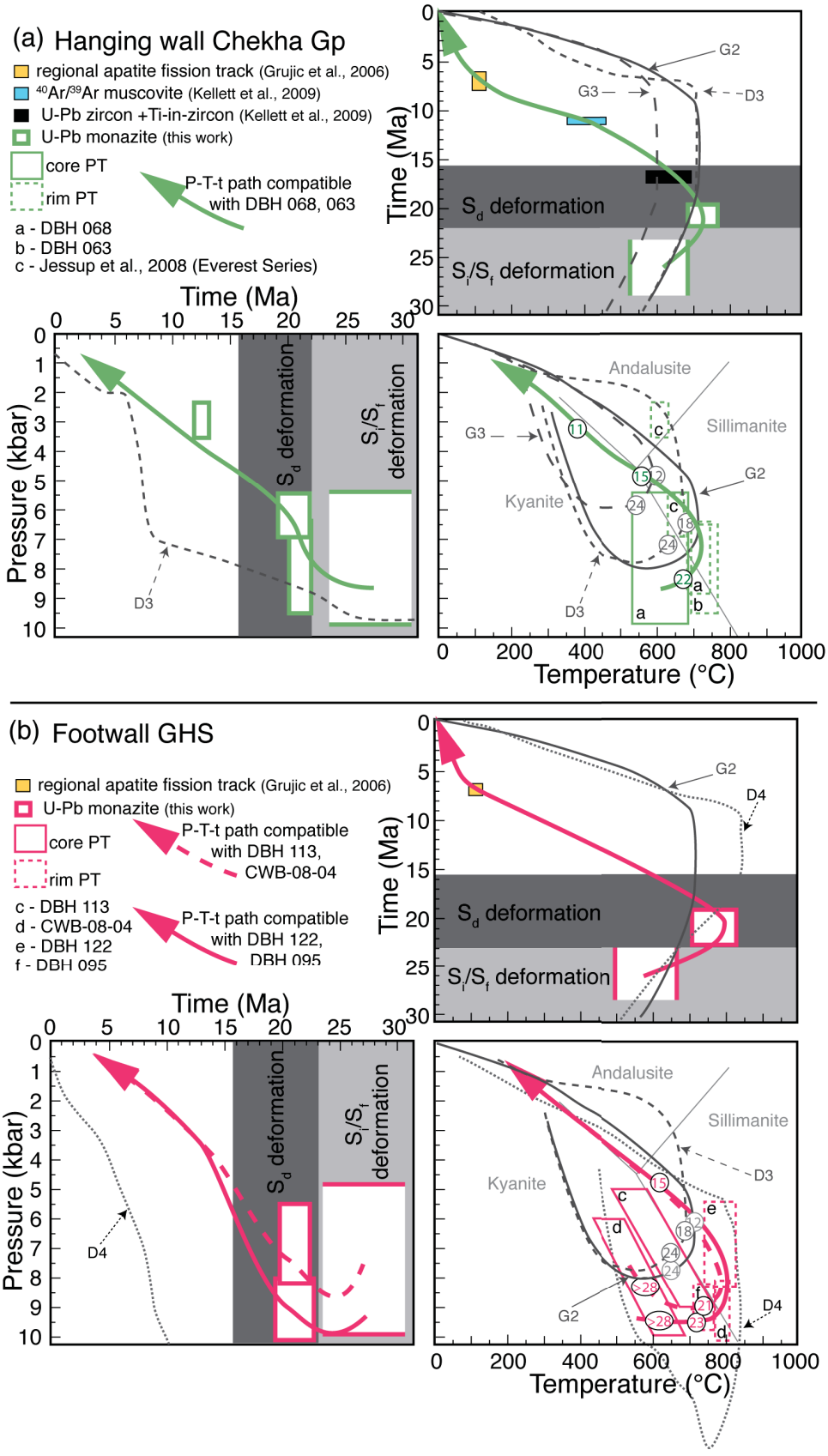
(a) Hanging wall Chekha Gp
regional apatite fission track (Grujic et al., 2006)
40Ar/39Ar muscovite (Kellett et al., 2009)
U-Pb zircon +Ti-in-zircon (Kellett et al., 2009)
U-Pb monazite (this work)
core PT
rim PT
P-T-t path compatible with DBH 068, 063
a - DBH 068
b - DBH 063
c - Jessup et al., 2008 (Everest Series)
Time (Ma)
Pressure (kbar)
Sd deformation
Si/Sf deformation
G2
G3
D3
Andalusite
Sillimanite
Kyanite
Temperature (°C)
(b) Footwall GHS
regional apatite fission track (Grujic et al., 2006)
U-Pb monazite (this work)
core PT
rim PT
P-T-t path compatible with DBH 113, CWB-08-04
P-T-t path compatible with DBH 122, DBH 095
c - DBH 113
d - CWB-08-04
e - DBH 122
f - DBH 095
D4

3.7 DISCUSSION

3.7.1 MIOCENE P-T-T HISTORY OF THE OUTER SOUTH TIBETAN DETACHMENT

3.7.1.1 Hanging wall

In the hanging wall, garnets in Chekha Group rocks generally preserve prograde zoning (see Appendix H). Staurolite growth followed garnet growth. In contrast with the Everest Series exposed further west, Chekha Group rocks do not contain sillimanite or andalusite (Fig. 3.9a; Jessup et al., 2008). Garnets do not appear to contain monazite inclusions, and the earliest preserved monazite ages of ca. 22 Ma (Fig. 3.8a-b) broadly coincide with the age of widespread leucogranite emplacement in the Himalaya (e.g., Deniel et al., 1987; France-Lanord and Le Fort, 1988; Searle et al., 2003), as well as the onset of top-to-the-south shearing along the MCT (Catlos et al., 2004; Harris et al., 2004; Daniel et al., 2003). As the monazites studied from the Chekha Group do not exhibit Y zoning, and do not occur within garnet, it is inferred that earliest monazite growth coincided with or followed peak T and P at peak T (P_{Tmax}) conditions of $\sim$650 °C at $\sim$7.5 kbar (Table 3.2; Fig. 3.9) (Fitzsimons et al., 2005). However, prograde chemical zoning preserved in garnets indicates that the rocks did not experience conditions $>$ $\sim$640 °C for an extended period of time (Yardley, 1977). Decompression and shearing occurred along the retrograde path during 22-16 Ma (Fig. 3.9), and cooling through the muscovite $^{40}Ar/^{39}Ar$ closure temperature occurred at ca. 11 Ma (Chapter 2). Although these data do not constrain the prograde P-T-t path, they are compatible with pre-Miocene crustal thickening and Barrovian metamorphism resulting in garnet growth and early fabric development $>$22 Ma ($>$38-28 Ma; e.g., Simpson et al., 2000; Jessup et al., 2008, Cottle et al., 2009c), and are also compatible with pre-Miocene shortening and cleavage development in the overlying TSS (Ratschbacher et al., 1994; Aikman et al., 2008; Kellett and Godin, 2009). The 2 Ma lag in monazite growth between DBH 063 (structurally lower) and DBH 068 (structurally higher) may be an indication that peak T, leucogranite intrusion, and shearing in the Chekha Group began earlier closer to the lithologic contact with the GHS and that the STDS shear zone shifted (or widened) during 22-20 Ma to include higher structural levels.

3.7.1.2 Footwall

In the footwall rocks of the outer STDS, samples exhibit increasing peak T and P_{Tmax} conditions with increasing structural distance below the lithologic contact with the Chekha Group (Fig. 3.9b), preserving a right-way-up metamorphic field gradient. The higher grade P-T loop includes those samples that preserve evidence of partial melt (DBH 095, DBH 122), while the lower grade P-T loop includes those that do not (DBH 113, CWB-08-04). Garnets in the footwall preserve only minor relicts of prograde chemical zoning, indicating that they experienced temperatures >640 °C for a protracted period. GHS samples yield monazite ages as old as ca. 26 Ma. However, given the lower Y contents of that monazite, the monazite grains probably coexisted with garnet, forming during or after prograde garnet growth, or growing from melt during recrystallization following partial melting. A transition from inclusion-rich (syn-S_i) to inclusion-poor (syn-S_f) garnet growth occurred before 22.6 $\pm$ 0.4 Ma (the age of monazite inclusions in inclusion-poor rims). This transition may reflect the initiation of partial melting and advection of melt and/or fluid within the GHS prior to ca. 23 Ma, which might have facilitated both a change in garnet growth characteristics and conditions favorable for monazite growth. Monazite inclusions in kyanite dated at ca. 20.5 Ma indicate that peak T and P_{Tmax} conditions within the sillimanite stability field may have been reached post-20.5 Ma, (Fig. 3.9b). Peak T was during or followed by a period of decompression and melt-present, top-to-the-north shearing until at least ca. 15 Ma. The latest stage of decompression was accompanied by garnet breakdown, releasing Y to produce high-Y rims on monazite in mylonite and shear bands. Top-to-the-north shearing and decompression occurred in the sillimanite stability field, with subsequent cooling in the andalusite stability field, indicated by andalusite in leucogranite sills within the uppermost GHS of the outer-STDS (Chapter 2).

By ca. 16 Ma, all leucogranitic melt in the outer STDS had crystallized, increasing the strength (viscosity) of the shear zone (Rosenberg and Handy, 2005), and by ca. 12-11 Ma, ductile shearing on the outer STDS had ceased (Chapter 2). The absence of brittle faulting recorded in the outer STDS indicates that no further displacement occurred within that portion of the shear zone. Thus GHS footwall rocks and Chekha Group hanging wall rocks were mechanically coupled by ca. 11 Ma and continued to exhume and cool as a coherent package. Deformation of the GHS and along its roof shear zone shifted to higher structural levels (Chapter 2).

3.7.2 COMPARISONS WITH MODEL PREDICTIONS

3.7.2.1 Channel flow models

Numerical models for homogeneous channel flow applied to the Himalayan-Tibetan system (e.g., Beaumont et al. 2001; 2004) predict that low-viscosity middle crust flowed outward from beneath the Tibetan plateau and was exhumed between the Main Central Thrust (MCT) and South Tibetan Detachment system (STDS) in response to focused denudation at the erosion front. In the models, the protolith boundary between incoming (Indian) pro-crust and the outflowing channel is referred to as the "MCT" (analogous to the Main Central Thrust system), and the boundary between the extruded channel and the overlying upper crust is referred to as the "STD" (analogous to the South Tibetan Detachment system) (Hodges et al. 2000; Jamieson et al., 2004). Models HT1 and HT111 represent members in a spectrum of channel flow model styles that could be applied to different parts of the Himalayan-Tibetan system and/or to different stages in its evolution (Jamieson et al., 2006). Here predicted P-T-t paths from models HT1 and HT111 are compared with the P-T-t data documented above (Fig. 3.9).

Model HT111 is identical to HT1 except that the upper crust contains an embedded weak layer, which facilitates detachment and outward flow of the upper crust overlying the channel. Consequently, the model orogen propagates much further to the south in HT111 than it does in HT1, creating a foreland fold-thrust-belt. Domes are formed where plateau upper crust is destabilised during transport of the channel flow zone over a ramp of cooler underthrust material (cooler because the orogen advances more quickly over the incoming plate). Domes can be expelled rapidly over the ramp and earlier exhumed channel material (Fig. 3.10). This deactivates the older exhumed channel structures and shifts extrusion to higher structural levels. As one dome is expelled, a new one forms above the mid-crustal ramp. For clarity, model output will be referred to in bold, and empirical data in regular text. In both models, collision begins at ca. **54 Ma**, channel flow initiates at ca. **30 Ma** and extrusion begins at ca. **15 Ma**, exhuming melt-weakened rocks ("GHS") between bounding thrust ("MCT") and normal-sense ("STD") shear zones. However, in model HT111, a dome formed at ca. **10 Ma** is translated southward along with the channel and extruded at the erosion front after **5 Ma**. The previously exhumed stage 1 "GHS" becomes progressively shortened as it is overridden from the north, forming an upright syncline. Model HT111 therefore predicts that the exhumed GHS should comprise structurally lower

stage 1 and structurally higher stage 2 components, each bounded by basal thrust- and roof normal-sense shear zones (Fig. 3.10; Jamieson et al., 2006). The structural style predicted by model HT111 is comparable to that observed in the study area (Fig. 3.2), with the model stage 1 "GHS" analogous to the lower part of the GHS, between the MCT and outer STDS, and the model stage 2 "GHS" comparable to the upper part of the GHS, between the KT and inner STDS.

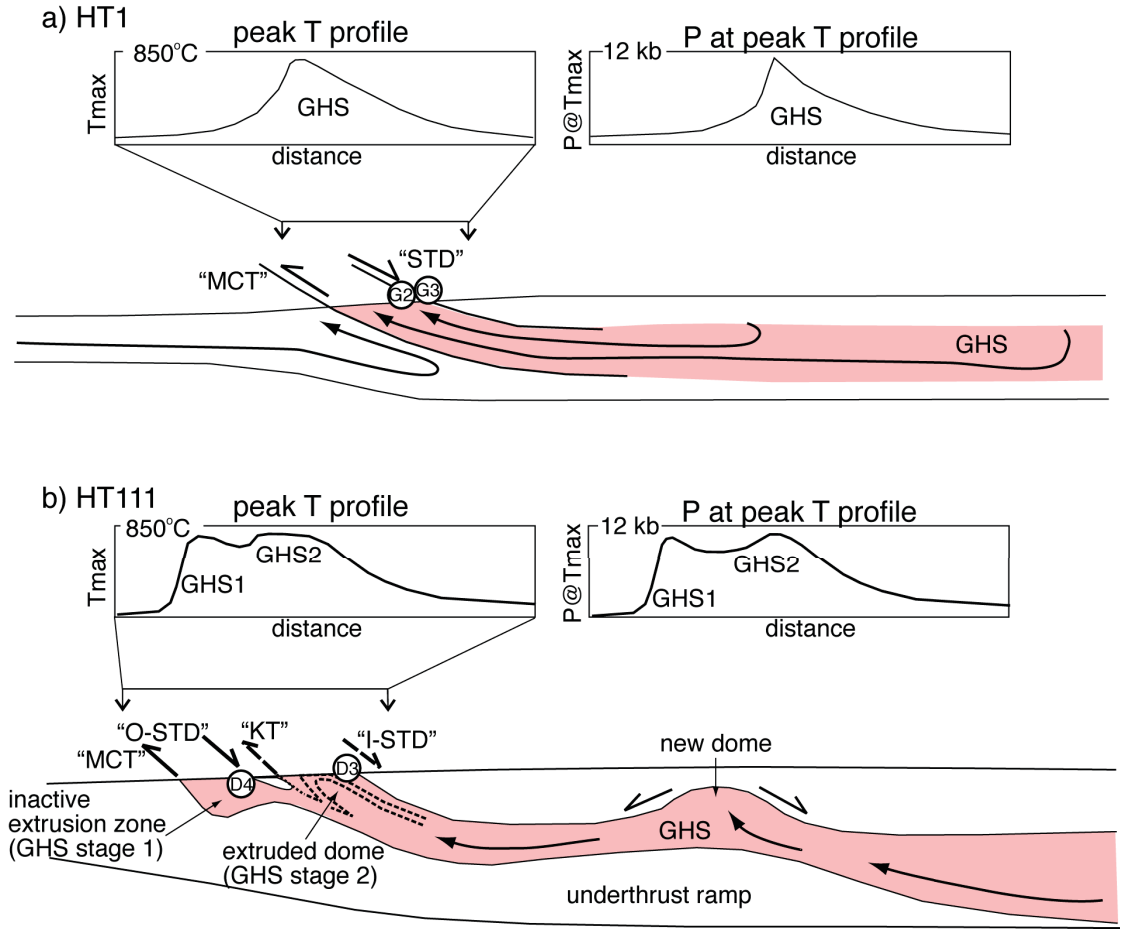

Figure 3.10: Schematic diagrams of channel flow models HT1 (Jamieson et al., 2004) and HT111 (Jamieson et al., 2006) with particle end points for model P-T-t paths G2, G3, D3 and D4 illustrated in Figure 3.9. Pink shading indicates channel and paleo-channel material. Analogous structures are labeled: "MCT" Main Central thrust; "STD" South Tibetan detachment; "O-STD" Outer South Tibetan detachment; "KT" Kakhtang thrust; "I-STD" Inner South Tibetan detachment.

Although the tracked model "particles" are much larger than the field observation scale (they are placed at intersection nodes of model elements of dimension 0.75 x 10 km),

there are several first-order comparisons that can be made between the model P-T-t output and the P-T-t data determined above (Figs. 3.9, 3.10). Points G2 and G3 (model HT1) are considered analogous to samples from the outer STDS, with G2 in the footwall and G3 in the hanging wall (Fig. 3.10a). Point D4 from model HT111 is considered analogous to the outer STDS while D3 is analogous to the footwall of the upper STDS (Fig. 3.10b).

Points G2 and G3 (HT1; Fig. 3.10a) exhibit broad P-T-t loops with prograde isobaric heating (Fig. 3.9). Their prograde paths pass from the kyanite to the sillimanite stability field, with exhumation mainly in the sillimanite stability field with a short excursion through the andalusite stability field. Peak T of **723 °C** is reached for G2 at **6.6 kbar** and **15.2 Ma**, and for G3 peak T is **605 °C** at **5.1 kbar** and **16.9 Ma** (Jamieson et al., 2004). The retrograde P-T path for Chekha Group samples is constrained by the onset of monazite growth at ca. 22 Ma following garnet growth at or near peak T (∼700-750 °C), shearing ending at ca. 16 Ma in the sillimanite stability field, and cooling through ∼350 °C at ca. 11 Ma (Fig. 3.9a; Chapter 2). For GHS samples, timing is constrained by prograde garnet growth during 23 Ma and monazite growth in the kyanite stability field at 20.5 Ma. Peak T of 700-800 °C occurs post-20.5 Ma in the sillimanite stability field. Thus HT1 model peak T conditions are similar to, but younger than, those indicated by field data, although peak T in the model hanging wall (G2) precedes peak T in the model footwall (G3) by 1-2 Ma, consistent with the field observations. In the model, this is the result of more efficient cooling of the upper crust above the channel, which advects isotherms and therefore stays at high temperature for a longer period.

In contrast, the pinched loop of D4, and open loop of D3 (HT111; Fig. 3.10), both exhibit a significant stage of isothermal decompression (Fig. 3.9; Jamieson et al., 2006). D4 reaches peak T of **843 °C** at **9.4 kbar** and **12.7 Ma**, during near-isothermal decompression from ∼**14 kbar** to ∼**5 kbar**, before cooling along a retrograde path similar to those displayed by points G2 and G3. In contrast, point D3, from a position analogous to the inner STDS footwall (Fig. 3.9a; 3.10b), reaches peak T of **708 °C** at **6.3 kbar** and **15.9 Ma** (Jamieson et al., 2006). Near-isothermal decompression to ca. **3 kbar** is followed by near-isobaric cooling in the andalusite stability field. Because GHS and Chekha Group samples from the outer STDS do not exhibit isothermal decompression, it is concluded that the P-T-t history of the outer STDS most closely resembles paths G2 and G3 from model HT1. This is consistent with the interpretation that the GHS exposed in the region

between the MCT and outer STDS in the study area represents an extruded channel that was subsequently overridden at higher structural levels by an extruded dome of the deeper and more internal part of the channel. Results from the stage 2 GHS in model HT111 are more likely to be applicable to higher structural levels in the region between the KT and inner STDS. For comparison, P-T estimates from the Everest region indicate that the retrograde path experienced by some Everest Series rocks (Jessup et al., 2008), along-strike equivalent to the Chekha Group, is comparable to D3 (Fig. 3.9a), and thus may represent an inner STDS. In eastern Nepal, no outer STDS is preserved, but the postulated stage 2 GHS extruded dome and its basal thrust may be the Upper-Plate and High Himal thrust, respectively, of Goscombe et al. (2006).

$^{40}Ar/^{39}Ar$ muscovite cooling ages in deformed leucogranites and regional apatite fission track ages of hanging wall and footwall rocks are significantly older than those predicted by either model (Fig. 3.9; Jamieson et al., 2004; Jamieson et al., 2006; Chapter 2). This discrepancy suggests that model erosion rates post **20-15 Ma** are higher than in nature. Erosion rates in Bhutan since ca. 5 Ma have been found to be approximately half that of the Himalayas west of Bhutan (0.55-0.85 mm/yr vs. 1.0-1.8 mm/yr) due to its sheltered position behind the Shillong Plateau (Grujic et al., 2006; Biswas et al., 2007). This difference in erosion rate is not incorporated into either model, and could be expected to produce a divergence of model and observed cooling paths since ca. 5 Ma. However, cooling ages for the set of channel flow type models discussed are found to be younger for observations both prior to 5 Ma, and outside of the influence of the Shillong Plateau (Jamieson et al., 2004).

Model HT1 predicts that the highest peak T and P conditions should be recorded in the lower GHS, just above the MCT (Fig. 3.10a; Jamieson et al., 2004). In contrast, model HT111 predicts a broad peak P-T profile between the MCT and the inner STDS resulting from duplication of the GHS section by dome extrusion (Fig. 3.10b, Jamieson et al., 2006). Both the peak grade profile and the P-T conditions recorded (ca. **850 °C** at $\geq$**12 kbar**) are consistent with the preservation of young, 14-13 Ma granulite-grade rocks north of the Linghsi klippe beneath the inner STDS in Bhutan (Warren et al., *in review*).

In summary, P-T-t data from across the outer STDS show several striking similarities with P-T-t paths predicted by models HT1 and HT111 for model features analogous to the outer STDS, but contrast with the P-T-t path associated with model features analogous

to the inner STDS. This comparison suggests that channel flow with dome extrusion above an underthrust ramp, producing a repetition of the STDS, is consistent with the evolution of Bhutan Himalaya.

3.8 CONCLUSIONS

The outer STDS in the Bhutan Himalaya is a segment of the STDS that was isolated in the mid-Miocene and preserved at the base of synformal klippe. It preserves the earliest stages of top-to-the-north shearing, and is characterized by a diffuse shear zone and gradually decreasing metamorphic grade from footwall GHS rocks into hanging wall Chekha Group rocks. Footwall GHS rocks contain garnets that lack prograde chemical zonation, while hanging wall Chekha Group rocks contain garnets that typically preserve prograde chemical zoning.

U(-Th)-Pb dating of *in situ* monazite combined with P-T estimates indicate that prograde garnet growth in the upper GHS, followed by a transition in garnet composition and texture, occurred before 22.6 $\pm$ 0.4 Ma. The peak T conditions were reached in Chekha Group rocks before or at ca. 22 Ma, and in upper GHS rocks just after 20.5 Ma. In both cases, peak metamorphic conditions were followed by ductile shearing under retrograde metamorphic conditions. Ductile shearing in both hanging wall Chekha Group and footwall GHS rocks continued until ca. 16-15 Ma. This indicates coeval high-T ductile shearing along the MCT and STDS between ca. 23 and 16-15 Ma.

Retrograde P-T-t paths determined here correspond well with numerical model P-T-t paths for the model analogue to the STDS in homogeneous channel flow models. However, the complex deformation and metamorphic history of the STDS in Bhutan suggests that the evolution of the eastern Himalaya may rather be the result of channel flow in which an underthrust ramp causes extrusion of a dome of mid-crustal material above a previously extruded channel. If ductile channel flow is indeed the mechanism by which the high-grade metamorphic core of the Himalaya has exhumed, then these data imply that the amount and rate of channel flow may be temporally and spatially variable across the Himalayas. The ability to distinguish and compare the timing at which peak T was reached, and differences in metamorphic grade between the footwall and hanging wall of the South Tibetan detachment provides critical field data on mid-crustal normal-sense faulting parallel to and contemporaneous with lithospheric contraction.

CHAPTER 4

DEFINING THE SOUTH TIBETAN DETACHMENT SYSTEM: STRUCTURE AND METAMORPHISM FROM MID- TO UPPER CRUST IN THE BHUTAN HIMALAYA

4.1 ABSTRACT

The South Tibetan detachment system (STDS) is a network of low-angle normal sense detachments (LANDs) that formed parallel to contractional structures in the Miocene during lithospheric contraction accompanying development of the Himalayan orogen. Historically, research on LANDs has focused on those that are interpreted to have accommodated crustal or lithospheric extension. In the eastern Himalaya of Bhutan, the STDS, perhaps the best-studied system of syn-contractional LANDs, is exposed in two different strands, an outer STDS and an inner STDS, distinguished by: different metamorphic grades in their footwalls and hanging walls; different numbers of individual structures; different amounts of ductile versus brittle deformation, and; different times of activity. These two strands are also distinct from putative exhumed portions of the STDS exposed in the North Himalayan gneiss domes. Here we use new and published metamorphic and structural data, including Raman spectroscopy of carbonaceous material (RSCM) thermometry, to highlight the different syn-contractional LAND structures present in the outer and inner

STDS in NW Bhutan, and to suggest mechanisms for their formation.

4.2 INTRODUCTION

Low-angle normal sense detachments (LANDs) are now known to be common structures in several orogenic and post-orogenic tectonic environments. These structures typically juxtapose infrastructural rocks exhumed from the middle or lower crust in the footwall against superstructural upper crustal rocks in the hanging wall, and in many cases are thought to accommodate lithospheric-scale extension. The formation of normal-sense structures at low angles ($\leq 30°$) contradicts conventional fault mechanics, which for a time delayed the recognition of LANDs in the field (e.g., Armstrong, 1972; Davis and Coney, 1979; Wernicke and Burchfiel, 1982). Although extensional LANDs have now been studied intensively for several decades, debate continues about their initial orientations (low-angle or high-angle) (Axen, 2007), the relationship between near-surface brittle faulting and ductilely-deformed tectonites exhumed in the footwall (Wernicke, 2009), the dynamics of coupling and decoupling of superstructure and infrastructure (Wernicke, 2009) and the amount of extension accommodated (significant or insignificant at the scale of the lithosphere) (e.g., Anders et al., 2006).

In the last couple of decades it has become increasingly clear that LANDs can also form during crustal- and lithospheric-scale contraction. Understanding of the tectonic development of LANDs in contractional settings is at an even more preliminary stage of research than LANDs in extensional settings. While they have been identified in several orogens (Himalaya—e.g., Burg, 1984a; Pamir—e.g., Brunel et al., 1994; Trans-Hudson—e.g., St.-Onge et al., 2006; Canadian Cordillera—e.g., Carr et al., 1987; Brown and Gibson, 2006, Kuiper et al., 2006; Hellenides—e.g., Xypolias and Kokkalas, 2006, Ring et al., 2007; Central Alps—e.g. Keller et al., 2006), detailed geochronological studies are only now demonstrating their longevity and synchroneity with parallel shortening structures during lithospheric-scale contraction. Perhaps the best-studied example of a syn-contractional LAND is the South Tibetan detachment system (STDS), a network of low-angle, top-to-the-north faults and shear zones in the hinterland of the Himalayan orogen (e.g., Burg and Chen, 1984; Burchfiel et al., 1992; Hodges et al., 1992; Brown and Nazarchuk, 1993; Makovsky et al., 1996; Carosi et al., 1998; Coleman and Hodges, 1998; Wu et al., 1998; Dèzes et al., 1999; Edwards et al., 1999; Searle et al., 2003; Cottle et al.,

2007; Jessup et al., 2008; Chapters 2, 3).

Finite element thermomechanical modeling of collisional orogenesis has demonstrated the fundamental role that syn-contractional LANDs play in the tectonic evolution of a large hot orogen such as the Himalaya (e.g. Beaumont et al., 2001; Jamieson et al., 2004). There are two different functions of syn-contractional LANDs in these models: one is to accommodate channel flow as the upper, lateral, top-to-the-hinterland sense-of-shear component of a low-viscosity mid-crustal channel; the other is to exhume (i.e. extrude) the channel to the surface. These two processes may form distinct LAND structures. However, within the Himalayan orogen, these LANDs are typically grouped under the term STDS, leading to ambiguity and disagreement about the definition of the STDS, and which structure in the system is the "true" STD (e.g., Searle, 2010). As for extensional LANDs, it is important to determine the initial orientation, the relationship between near-surface brittle faults and ductiley-deformed tectonites exhumed in the footwall (e.g. is one the up-dip equivalent of the other?), the timing of coupling and decoupling of superstructure and infrastructure, and the amount of displacement accommodated by these structures. In this study of the STDS in the eastern Himalaya, we address these questions by examining the structural history of rocks within the STDS, and by comparing peak metamorphic grade across the system.

The STDS is the most internal orogen-scale structure in the Himalayan orogen south of the suture (Fig. 4.1), and passes through some of its highest peaks. Access to the STDS and the base of Himalayan superstructure in its immediate hanging wall is therefore limited to few narrow valley transects across the orogen. In Bhutan, the STDS is duplicated, with pro-ward klippe of superstructural rocks soled by the STDS comprising an "outer STDS", and the more retro-ward exposure of the STDS comprising an "inner STDS" (Fig. 4.1; Edwards et al., 1996; Wu et al., 1998; Edwards et al., 1999; Grujic et al., 2002; Chapter 2). The preserved klippe provide easier access to the STDS than can be obtained in many other parts of the orogen. However, several faulting and folding events have combined to form a multiphase structural geometry that is, in places, further obscured by dense vegetation cover. Furthermore, the sedimentary superstructure of the STDS hanging wall lacks those metamorphic index minerals commonly used in geothermobarometry (e.g., garnet, biotite, feldspar). In this study we employ RSCM thermometry (Beyssac et al., 2002; Beyssac et al., 2007) to determine both peak temperatures and the peak metamorphic temperature field

gradient across the STDS within the westernmost klippe, the Lingshi klippe (Figs. 4.1, 4.2). The RSCM method is based on changes in the Raman spectrum of carbonaceous material with increasing metamorphic temperature. Here we complement structural observations and measurements with RSCM data and published thermometric data to examine the structural and metamorphic transition from infrastructure to superstructure in the Bhutan Himalaya, and the timing of coupling/decoupling of superstructure from infrastructure along the STDS during continental collision. Finally, we relate the different structures within the inner and outer STDS to channel flow and exhumation (i.e. extrusion).

4.3 GEOLOGY

4.3.1 REGIONAL GEOLOGY

The Himalayan orogen began to form ca. 50-54 Ma with the initial collision of the Indian craton with the Lhasa plate, the southern margin of Asia, following consumption of the intervening Tethys Ocean (Rowley, 1996; de Sigoyer et al., 2000; Leech et al., 2005; Guillot et al., 2007). The extensive and still active orogenic belt now forms the highest peaks on Earth. Several north-dipping first-order structures within the belt separate sequences of rock of differing metamorphic grade, deformation history and/or provenance. South of the Indus-Yarlung suture, separating Indian and Asian-derived crust, the northernmost sequence of rock in the Himalayan orogen is the Tethyan sedimentary sequence (TSS) (Fig. 4.1). These unmetamorphosed to low-grade Paleozoic to Mesozoic sedimentary rocks form the superstructure of the orogen, and are separated from the Greater Himalayan sequence (GHS) high-grade metamorphic infrastructure to the south by the STDS, a network of north-dipping LANDs. The GHS rocks are separated from lower metamorphic grade Proterozoic to Mesozoic sedimentary rocks of the Lesser Himalayan sequence (LHS) by the Main Central thrust (MCT). The STDS and the MCT, opposite-verging structures, were contemporaneously active during the Miocene from 22 Ma to at least 18 Ma orogen-wide (i.e. Godin et al., 2006a and references therein), and at least 16 Ma in the Bhutan Himalaya (Stüwe and Foster, 2001; Daniel et al., 2003; Chapter 2). The base of the LHS is the late Miocene-Pliocene Main Boundary thrust (MBT) (Meigs et al., 1995). The southernmost sequence of rocks deformed by the Himalayan orogen is the Sub-Himalaya, composed of deformed Tertiary foreland basin sediments, and the leading

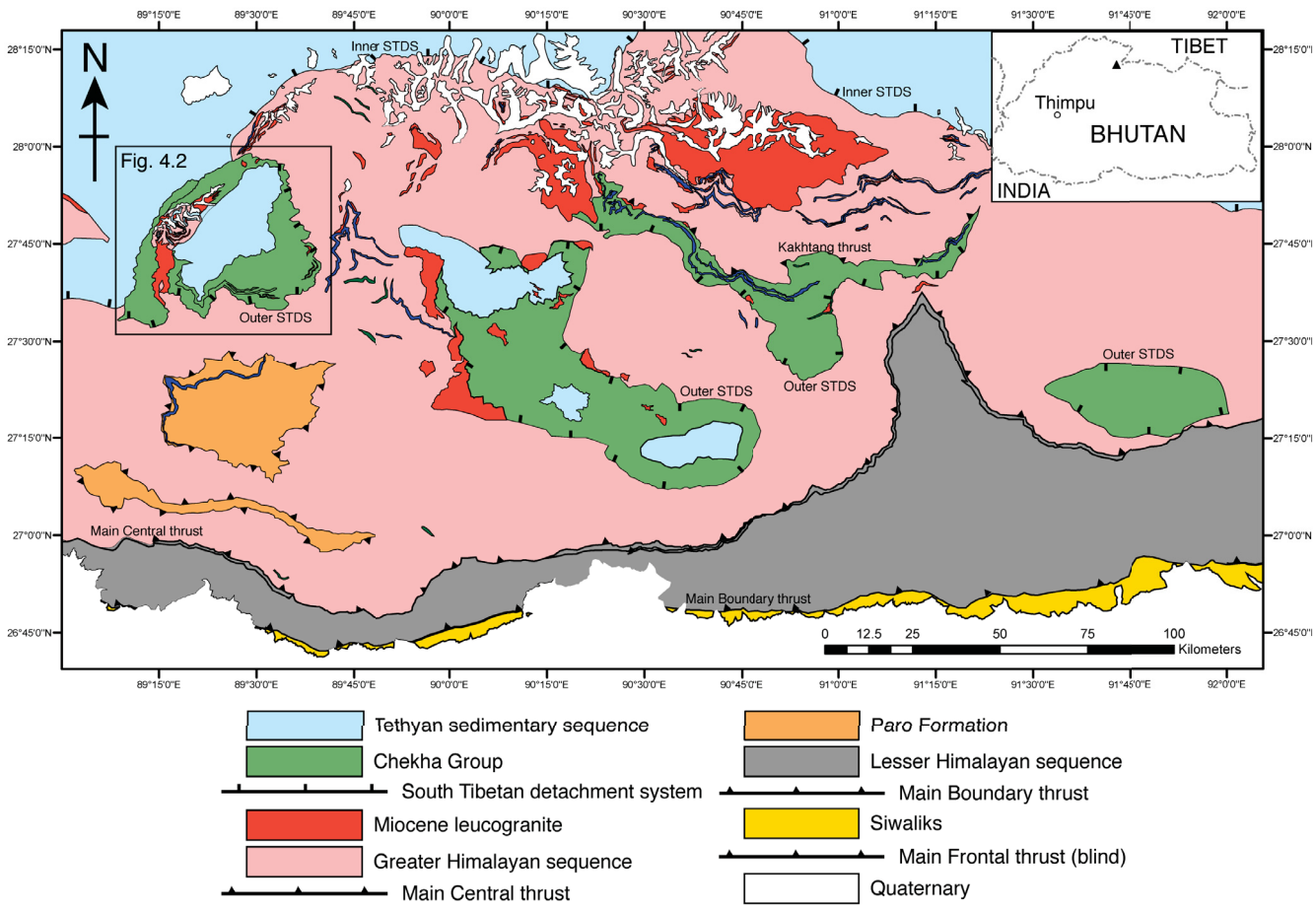

Figure 4.1: Geological map of the Bhutan Himalaya. The study area is boxed. Map is adapted from Gansser (1983); Grujic et al. (2002); Koike et al. (2002); Chakungal (2006), Chapter 2; Long and McQuarrie (2010); Long et al. (*in review*); Tobgay et al. (*in review*). Dark blue bands are marble bands and dark green bands are amphibolite bands.

edge of deformation is the Main Frontal thrust. All thrusts appear to root at depth into the Main Himalayan thrust (MHT), the north-dipping basal detachment of the orogen (Nelson et al., 1996).

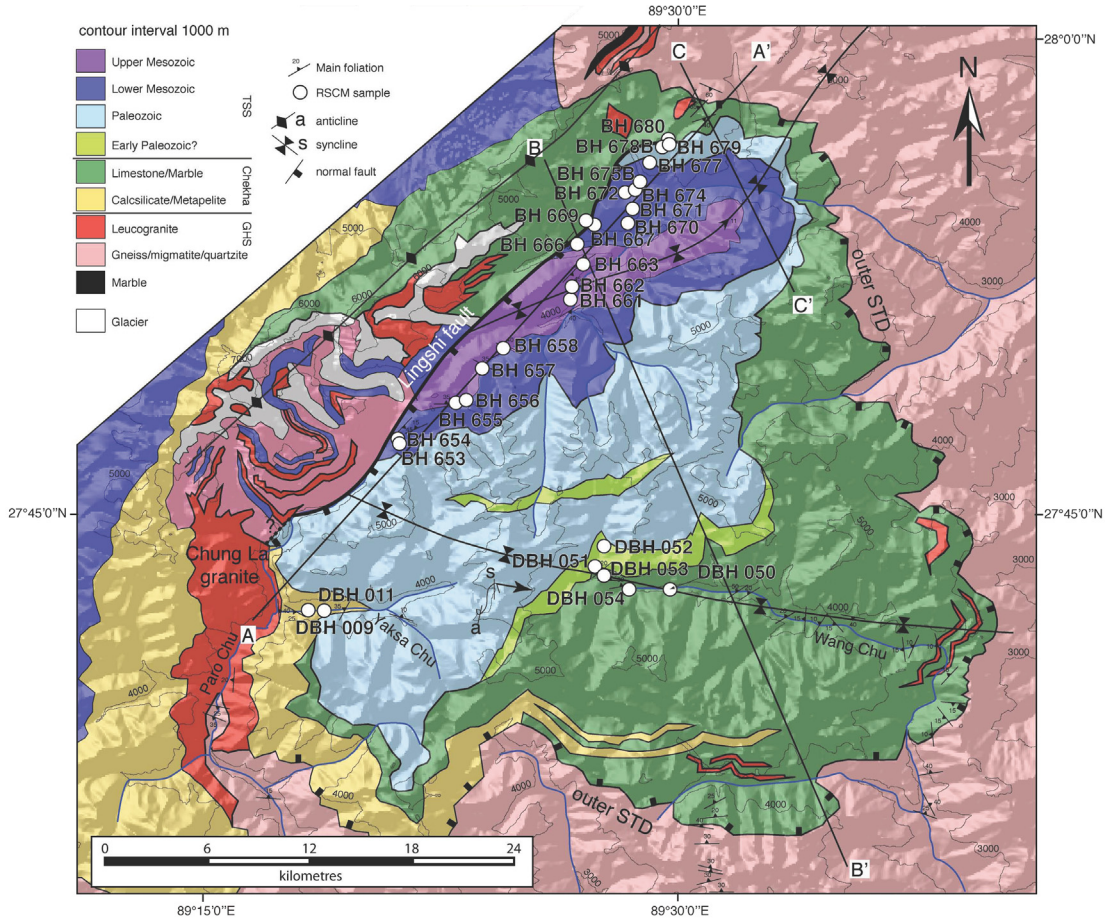

Figure 4.2: Geological map of the Lingshi klippe, northwest Bhutan. Sample locations and structural data are shown. A-A', B-B' and C-C' cross-sections are shown in Figure 4.3. Map compiled from this study; Grujic et al., 2002; Gansser, 1983.

The STDS is termed a detachment "system" because along the length of the orogen it comprises one to several normal-sense brittle faults and/or ductile shear zones. For example, in the Everest region, the STDS comprises a lower ductile shear zone (Lhotse detachment) and an upper ductile/brittle structure (Qomolongma detachment) (Searle et al., 2003). In general, the lowest structural levels containing top-to-the-north shear sense indicators are ductiley-deformed tectonites of the upper GHS, while the uppermost hanging wall of the STDS comprises unmetamorphosed to weakly metamorphosed TSS rocks. When the complexity of the STD system was recognized, the different structures

were categorized as “lower” (and generally older) and “upper” (and generally younger) (see review in Godin et al., 2006a). However, we argue below that in light of several recent studies of the STDS, and channel flow models of the evolution of the Himalaya, it may be more informative to consider the mechanisms of formation of the specific normal-sense structures within the “system”, rather than just their structural position.

In Bhutan, eastern Himalaya (Fig. 4.1), the outer STDS is exposed at the base of a klippe of metasedimentary and sedimentary rocks (Gansser, 1983; Grujic et al., 2002; Chapter 2). The outer STDS comprises a diffuse ductile shear zone, in which the footwall deformation front is within GHS amphibolite-facies ortho- and paragneiss, and migmatite. The high strain zone penetrates into overlying metamorphosed calc-silicate, mica schist, marble and quartzite, which grade upward with decreasing strain into limestone and phyllite. In Bhutan, this package of metasedimentary rocks is termed the Chekha Group. Above the Chekha Group, in the core of some of the klippen, are slate, sandstone, and carbonate of the TSS, remnants of TSS superstructure. The shear zone was active during the Miocene from ca. 22 Ma and it ceased activity by ca. 12 Ma (Chapter 2; Chapter 3). A lack of brittle overprint suggests that the exposed part of the outer STDS was active only under ductile conditions. In contrast, the inner STDS, exposed in northernmost Bhutan and southern Tibet, comprises a ductile normal-sense shear zone that was active after 12 Ma and has since been cut by younger brittle normal faults (Edwards et al., 1996; Wu et al., 1998; Edwards et al., 1999; Chapter 2).

4.3.2 Local geology: Lingshi klippe

The TSS in the Lingshi klippe comprises Paleozoic to Mesozoic slate and shale with minor greywacke, conglomerate, quartzite, and limestone (Fig. 4.2). Original bedding is locally preserved, and the rocks are weakly metamorphosed. However, slaty cleavage is generally well developed and can make bedding difficult to recognize.

The Chekha Group in the Lingshi klippe varies in both composition and thickness along strike from west (Yaksa Chu) to east (Wang Chu) (Fig. 4.3). In the west, the lower Chekha Group comprises garnet-biotite schist with large biotite porphyroblasts (Fig. 4.4g). Some samples contain abundant tourmaline overgrowing the schistosity. This is overlain in structural sequence by amphibole-chlorite-biotite-garnet-titanite calc-silicate, chlorite-biotite-muscovite schist and biotite-calcite-bearing quartzite (Fig. 4.4e). In the east, the lower Chekha Group is characterized by biotite-plagioclase-garnet schist

(Fig. 4.4h), overlain by biotite-muscovite schist and intruded by leucogranitic sills and dykes. Tourmaline is present locally. Above the schist are amphibole-chlorite-biotite-titanite calc-silicate, rare recrystallized calcite-clinopyroxene-titanite calc-silicate, and biotite-muscovite calcarenite (Fig. 4.4f). This grades upward into a few kilometers-thick sequence of muscovite- and quartz-bearing marble (Fig. 4.4d).

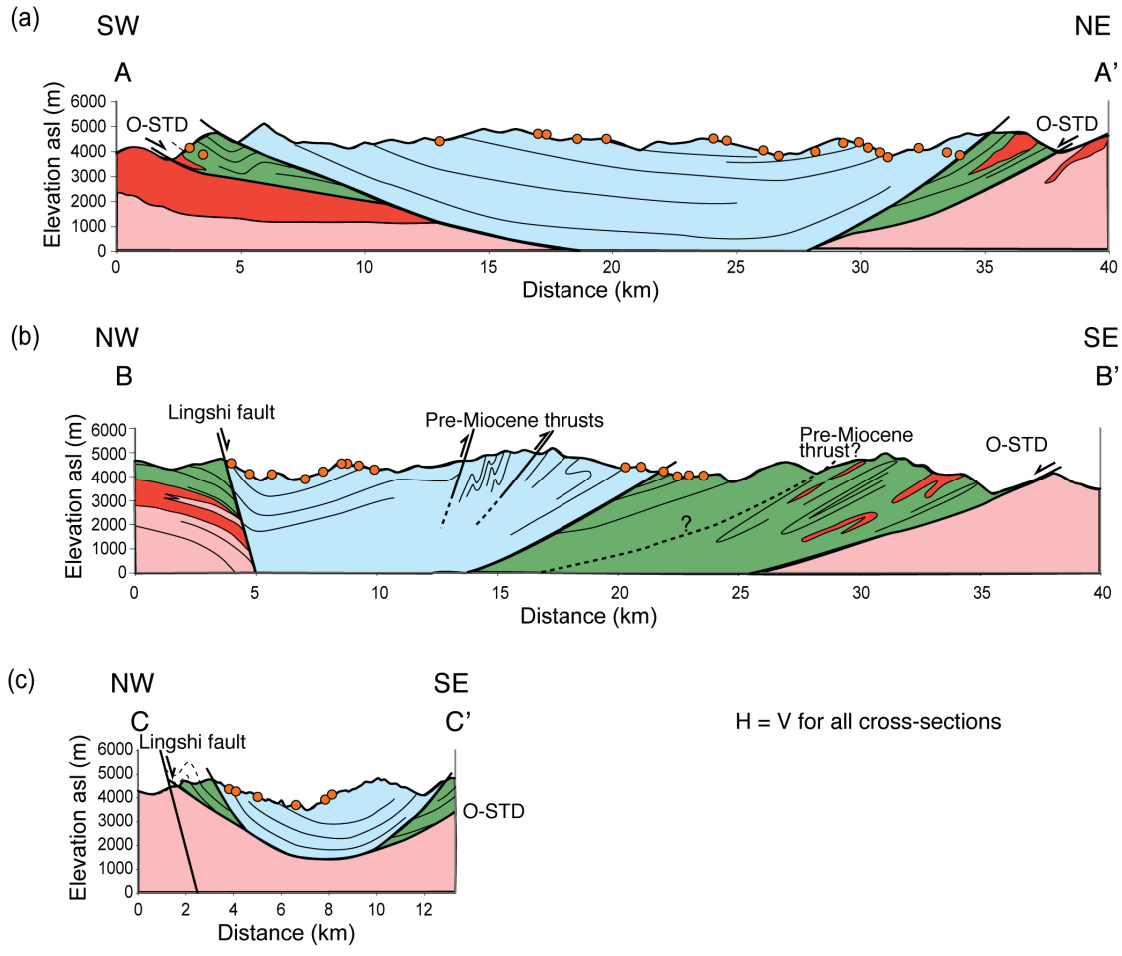

Figure 4.3: Cross-sections across the Lingshi klippe. RSCM sample locations are shown as orange circles. Cross-sections are located in Figure 4.2 and the legend is according to Figure 4.1.

Figure 4.4: Photomicrographs of the Chekha Group and TSS. Photomicrographs illustrate the lithology and change in metamorphic grade and deformation from unmetamorphosed at the base of the TSS (a and b), to isoclinally folded and weakly metamorphosed at the top of the Chekha Group (c and d) to amphibolite-facies metamorphosed at the base of the Chekha Group (e and f). Photomicrographs in the left column are collected at the south-west side of the Lingshi klippe along Yaksa Chu, and those in the right column are collected at the south-east and central portions of the Lingshi klippe, along the Wang Chu (Fig. 4.2).

Lowermost TSS WEST EAST

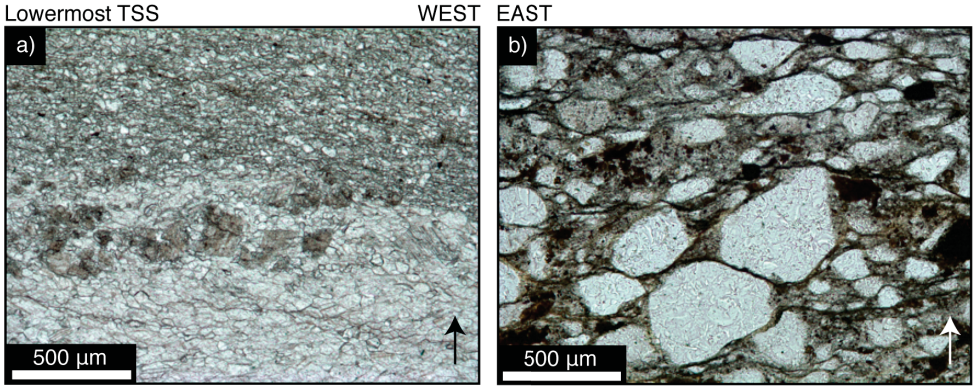

TSS, DBH 014 limestone. TSS, DBH 051 sandstone.

Uppermost Chekha Group WEST EAST

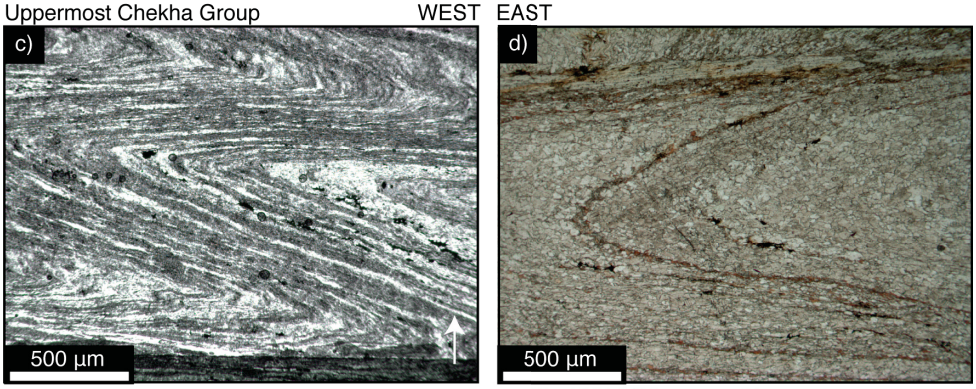

Chekha, DBH 011 phyllite/slate Chekha, DBH 046 impure marble.

Middle Chekha Group WEST EAST

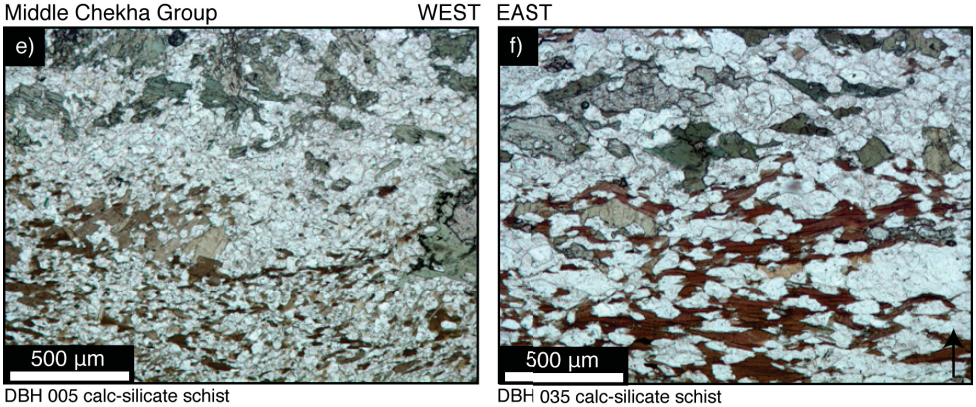

DBH 005 calc-silicate schist DBH 035 calc-silicate schist

Lowermost Chekha Group WEST EAST

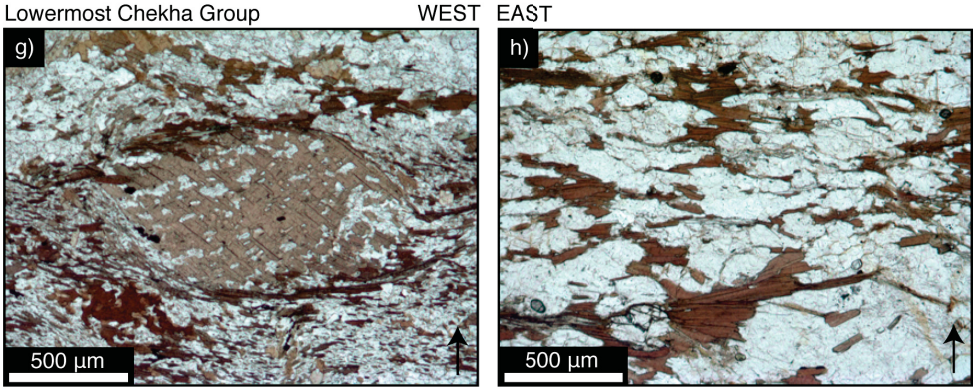

DBH 001 biotite-chlorite metapelitic schist with biotite porphyroblasts. DBH 026 biotite metapelitic schist

4.4 STRUCTURAL OBSERVATIONS AND INTERPRETATIONS

4.4.1 PRE-MIOCENE DEFORMATION

The earliest deformation in the TSS and Chekha Group of the Lingshi klippe predates Miocene normal-sense ductile shearing and faulting along the STDS. There are several indications of early deformation in Chekha Group rocks. At the lowest structural levels, garnets preserve prograde chemical zoning, have both curved and straight internal fabrics that are at high angle to the external schistose fabric, and contain inclusions that are finer-grained than the matrix (Chapter 3). Sedimentary bedding is not preserved, and the rocks are isoclinally folded at both the outcrop (Fig. 4.5a) and microscopic scales (Fig. 4.4c, d), with fold axial planes parallel to the main foliation, resulting in generally monoclinally north to northwest dipping strata (Fig. 4.5b, c).

Within the TSS, pre-Miocene shortening structures are also evident. Preserved original bedding is folded (Fig. 4.3b) into upright antiforms and synforms with wavelengths of a few hundreds of metres (Fig. 4.5f). Pioneering mapping of the area by Gansser (1983) also indicated several small S- to SE-directed thrusts within the TSS that duplicate the lower Paleozoic section (Fig. 4.2, 4.3). Slaty cleavage in the TSS is not axial planar to the broad open folds of the klippe, nor could it be produced by such a minor amount of strain. We suggest that the slaty cleavage also formed during an early stage of folding and thrusting. Where it is possible to distinguish between cleavage and bedding, the cleavage is everywhere found to be steeper than bedding. However, more detailed structural mapping is needed to unravel the geometry of these early structures.

These structures in the Chekha Group and TSS indicate early crustal shortening and thickening, likely following initial collision of the Himalaya in the Eocene, and preceding Miocene normal-sense shearing on the outer STDS. TSS shortening elsewhere in the orogen has been constrained to Eocene-Oligocene (Ratschbacher et al., 1994; Wiesmayr and Grasemann, 2002; Neumayer et al., 2004; Aikman et al., 2008; Kellett and Godin, 2009). A structural transition from more recumbent structures in the Chekha Group to more upright structures in the TSS may reflect lower and higher structural levels, respectively, of a single shortening episode. A similar transition in geometry is observed in the TSS in central Nepal (Godin, 2003). South-vergent thrust structures in the TSS suggest that shortening was approximately in the NS direction, compatible with the general shortening within the orogen. Although in general the sequence youngs upwards from Chekha Group

Figure 4.5: Outcrop photographs and stereographic projections illustrating the main structural styles and cleavage for the Chekha Group (schistose cleavage) and TSS (slaty cleavage). Chekha Group isoclinal folding and monoclinally-dipping beds are shown in (a) and (c), while an inclined anticline-syncline pair and undeformed sandstone photomicrograph are shown in (e). The coin in photograph (a) has a diameter of 2.5 cm. People are shown for scale in (c). In (e) the outcrop is approximately 600 m across. Stereographic projection, lower hemisphere, of poles to cleavage in (b). For (d), the TSS is dominated by slate, for which cleavage and bedding are difficult to distinguish from one another. Thus the data represent a mixture. Contour intervals on stereonets are 2.0%/1% area. Photos by D. Kellett.

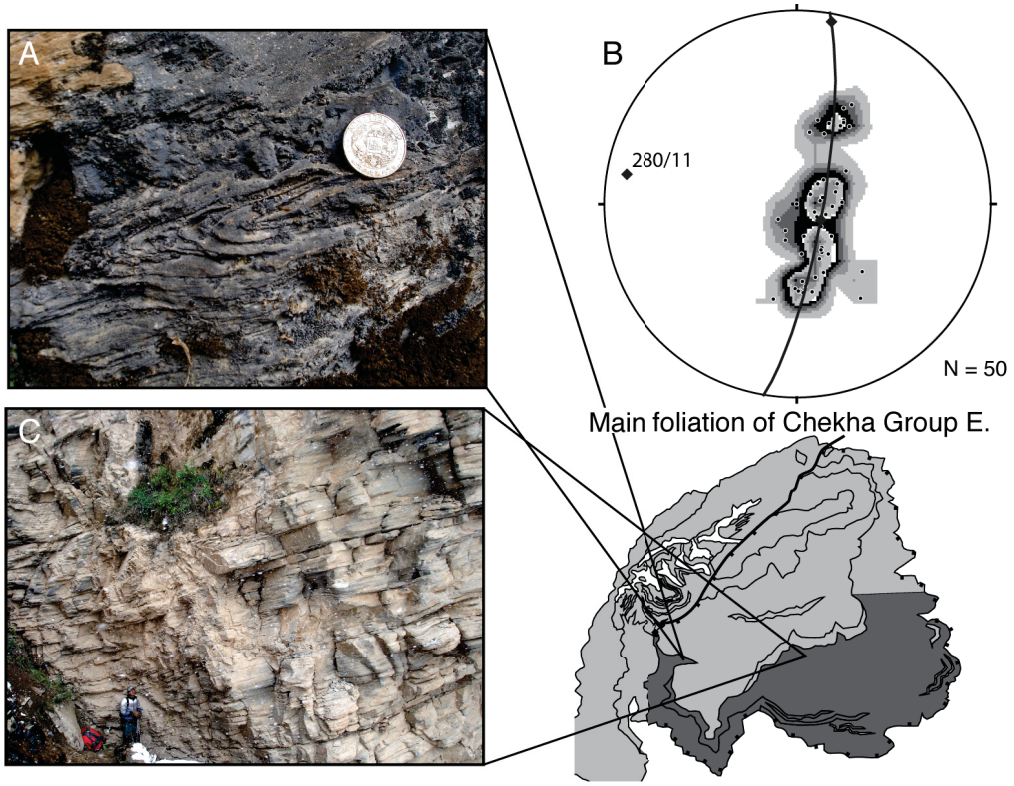
A
B
280/11
N = 50
Main foliation of Chekha Group E.
C

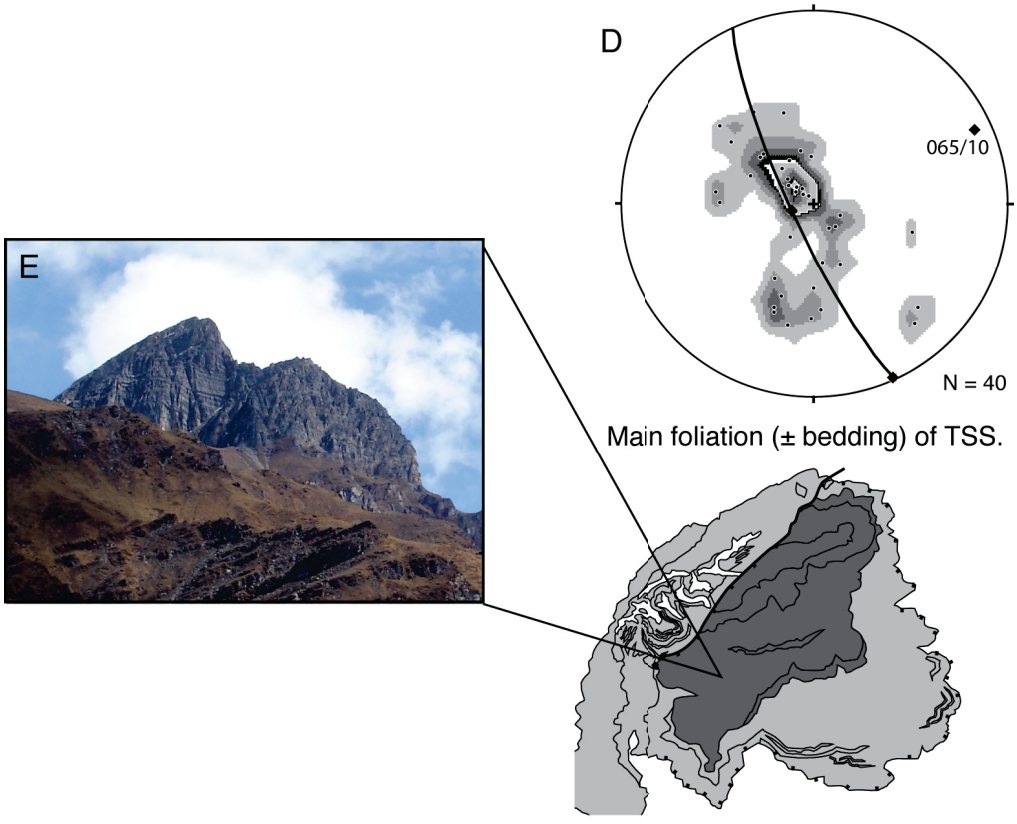
D
065/10
N = 40
Main foliation (± bedding) of TSS.
E

to TSS rocks, isoclinal folds and transposed bedding in the Chekha Group indicate that the observed continuous stratigraphy is only apparent, and that the Chekha Group was tectonically thickened prior to STDS shearing.

4.4.2 South Tibetan detachment system

In Bhutan, two distinct segments of the STDS are preserved, the outer STDS at the base of klippe, and the inner STDS near the Bhutan-Tibet border (Fig. 4.1). The outer STDS is accessible along several transects in the Lingshi area. It comprises a ductile shear zone of variable thickness, deforming GHS gneiss and migmatite in its footwall and calc-silicate, marble and metapelitic schist in its hanging wall. Miocene leucogranitic dykes and sills are also deformed by ductile shear. Shearing of the footwall rocks occurred in the sillimanite stability field, and during retrograde metamorphism. The episode of shearing is ca. 22-12 Ma, as determined by U-Pb dating of zircon and monazite, and by muscovite $^{40}Ar/^{39}Ar$ cooling ages (Chapter 2; Chapter 3). Mineral lineations and stretching lineations, best exposed in the south central part of the klippe, indicate top-down-to-the-north transport.

Brittle normal faults have been identified along several segments of the STDS. For example, the inner STDS in Bhutan is characterized by brittle faults in the uppermost part of the system (Edwards et al., 1996; Edwards et al., 1999). However, we have identified no direct evidence for a similar shallowly-dipping upper brittle normal fault separating Chekha Group rocks from TSS rocks in the Lingshi klippe. Neither has such a structure been described from the Tang Chu klippe, although there is a similar sharp transition in structural style from Chekha Group to TSS. The contact of the TSS with the Chekha Group along the western Yaksa Chu (Fig. 4.2) is characterized by isoclinally-folded phyllite of the Chekha Group below (Fig. 4.4c) and fine-grained, quartz- and muscovite-bearing recrystallized limestone with preserved sedimentary bedding above (Fig. 4.4a). Along the eastern Wang Chu, there is a sharp boundary separating monoclinally-dipping isoclinally-folded recrystallized Chekha group limestone below (Fig. 4.4d) from TSS lithic sandstone and sandy siltstone above (Fig. 4.4b). The TSS and the Chekha Group are further distinguished by the absence of leucogranitic dykes or sills within the TSS, and their presence in the Chekha Group. Initial mapping of the Lingshi klippe by Gansser (1983) identified the contact described above between the Chekha Group and the TSS along the Wang Chu as a thrust fault located just north of Shodu. We concur that a thrust of small displacement occurs at this location, similar to several other small thrusts mapped

with the TSS (Gansser, 1983) (Fig. 4.2), but no major detachment has been observed.

At different locations in the Himalayan orogen, the STDS has been described as ranging from a broad, diffuse ∼1 km-thick shear zone (e.g., Dzakaa Chu section, Cottle et al., 2007) to multiple discrete faults and shear zones (e.g., Everest section, Searle et al., 2003). Where the STDS is described as comprising separate upper and lower structures (e.g., the Qomolongma and Lhotse detachments at Everest, Searle et al., 2003), the lower structure is ductile, and comprises a broad zone of distributed normal-sense shear. The zone is characterized by a progressive upward decrease in metamorphic grade from amphibolite- to granulite-facies gneiss, migmatite, and Miocene granitoids in the footwall to greenschist- to amphibolite-facies schist in the hanging wall. In contrast, the upper structure is ductile-brittle and separates the lower ductile shear zone and overlying schists from unmetamorphosed TSS rocks in the hanging wall. As in the Dzakaa Chu section, there appears to be a single diffuse ductile shear zone within the outer STDS, in contrast to the multiple structures of the inner STDS. Although an upper structure was not identified in the field, its presence could be inferred from a contrast in structural style from isoclinally folded, transposed and recrystallized metasedimentary rocks of the Chekha Group in the footwall and upright open to close folded, unrecrystallized sedimentary rocks with preserved sedimentary bedding of the TSS in the hanging wall. However, we interpret those observations to reflect only a progressive change from lower to higher structural levels, and not a discrete structure. The contact between Chekha Group and TSS rocks is also mapped in the Black Mountain klippe, the southernmost klippe preserving upper-crustal rocks in Bhutan. Here the contact between the Chekha Group and the TSS is reported as conformable (Long and McQuarrie, 2010). Assuming that the klippen were originally continuous, that observation is consistent with our conclusion that there is no LAND separating the Chekha Group from the TSS in the outer STDS.

It appears that while there is an upwards-decreasing strain gradient of top-to-the-north shear through the Chekha Group, the TSS is unaffected structurally by the outer STDS. The dip of the outer STDS varies across the Lingshi klippe, as it was folded by late buckling. However, based on the orientations of stretching and mineral lineations, and shear bands related to STDS shearing, we propose that the initial orientation of the structure was likely dipping ∼20° or shallower towards NW-NE.

4.4.3 LOW-AMPLITUDE BUCKLING

Structural mapping of Bhutan has revealed several large-scale, upright, low amplitude, non-cylindrical folds with both N-S and E-W strike, resulting in a broad dome-and-basin geometry (Fig 4.1; Gansser 1983; Grujic et al., 2002). Within the Lingshi klippe, there are at least two large synclines at high angle to one another. The axial plane of the southern syncline strikes ∼E-W and tilts Chekha Group rocks (Fig. 4.2). Along the Wang Chu, the fold axis of this syncline plunges 11° towards 280° (Fig. 4.5b). The more northern syncline strikes NE-SW, and folds TSS and Chekha Group rocks, as well as GHS rocks northeast of the Lingshi klippe (Fig. 4.2). In the northeast portion of the TSS, the hinge of this syncline plunges 10° towards 065° (Fig. 4.5e). Although our structural data do not constrain a through-going NS-striking fold within the Lingshi klippe, the overall map pattern of Bhutan (Fig. 4.1) suggests buckling with a NS-striking fold axis and wavelength of ∼75 km. This folding has produced a regular spacing of structural basins preserving superstructural klippe in their cores for at least 250 km of orogen strike from western to eastern Bhutan.

As in central Nepal (Godin et al., 2006b), the E-W and N-S striking buckling of the GHS, Chekha Group and TSS rocks together with the outer STDS across Bhutan indicates recoupling of the mid-crust with upper crustal rocks following cessation of shear on the outer STDS. Shearing on the outer STDS ceased by 12 Ma (Chapter 2), which provides an upper age constraint for the buckling. The inner STDS also appears to be folded (Edwards et al., 1999), suggesting the buckling may be even younger.

4.4.4 RECENT FAULTING: LINGSHI FAULT

Present-day faulting in Bhutan is dominated by strike-slip displacements (Drukpa et al., 2006), in contrast to thrusting observed further to the west (Ni and Barazangi, 1984; Avouac, 2003). The oblique-slip Lingshi fault can be traced from northern Bhutan, where it cuts the inner STDS, south through the Lingshi klippe (Figs. 4.1, 4.2). The fault is sinistral strike-slip with upthrow of the W block (Gansser, 1983). The tip of the fault reaches the southern edge of the Lingshi klippe, and there appears to step west. In Sikkim, several faults of similar orientation have been observed. The southernmost segment, the Gish fault, apparently offsets even the MBT (Mukul et al., 2010). The Lingshi fault may actually consist of several right-stepping en-echelon segments that strike parallel

to the normal faults bounding the Yadong-Gulu graben (Armijo et al., 1989). However, its opposite dip and dip-slip movement have resulted in a horst of the Chomolhari range (Figs. 4.1, 4.2). The Lingshi fault is an active structure, most recently causing an M 5.4 earthquake in 2003, (Drukpa et al., 2006). The focal solution of this and nearby historic events indicate N-S shortening; most other historic earthquake events in Bhutan have E-W trending P axes.

4.5 RAMAN SPECTROSCOPY OF CARBONACEOUS MATERIAL

Changes in Raman spectra of carbonaceous material have been recognized as indicative of metamorphic grade for some time (i.e., Wopenka and Pasteris, 1993); they have recently been quantified and calibrated for use a peak-temperature thermometer (Beyssac et al., 2002). The Raman spectroscopy of carbonaceous material (RSCM) method is ideal for use in metasedimentary rocks which lack metamorphic indicator minerals, yet commonly contain carbonaceous material (Beyssac et al., 2002; 2004; Rantitsch et al., 2005; Negro et al., 2006). Carbonaceous material produces several peaks in the first-order region (1100-1800 cm^{-1}) of the Raman spectra: three disorder peaks D1, D2 and D3 and the graphite peak G (Fig. 4.6). The RSCM thermometer has been calibrated against the systematic decrease in R2 (D1/(G+D1+D2) peak area) ratio in the first-order Raman shift between 330-650 °C (Beyssac et al., 2002; Rahl et al., 2005). Below 330 °C there is no change in R2 ratio; however, it has been observed that the R1 ratio (D1/G peak height) does appear to increase between about 100-350 °C permitting an extension of the thermometer down to 100 °C by calibrating against changes in both R1 and R2 ratios (Rahl et al., 2005). Here we report calculated R1 and R2 ratios, and estimate temperatures using both the calibration of Beyssac et al. (2002):

$$T(^{\circ}\mathrm{C}) = -455R2 + 641 \tag{4.1}$$

and that of Rahl et al., (2005):

$$T(^{\circ}\mathrm{C}) = 737.3 + 320.9R1 - 1067R2 - 80.638R1^2 \tag{4.2}$$

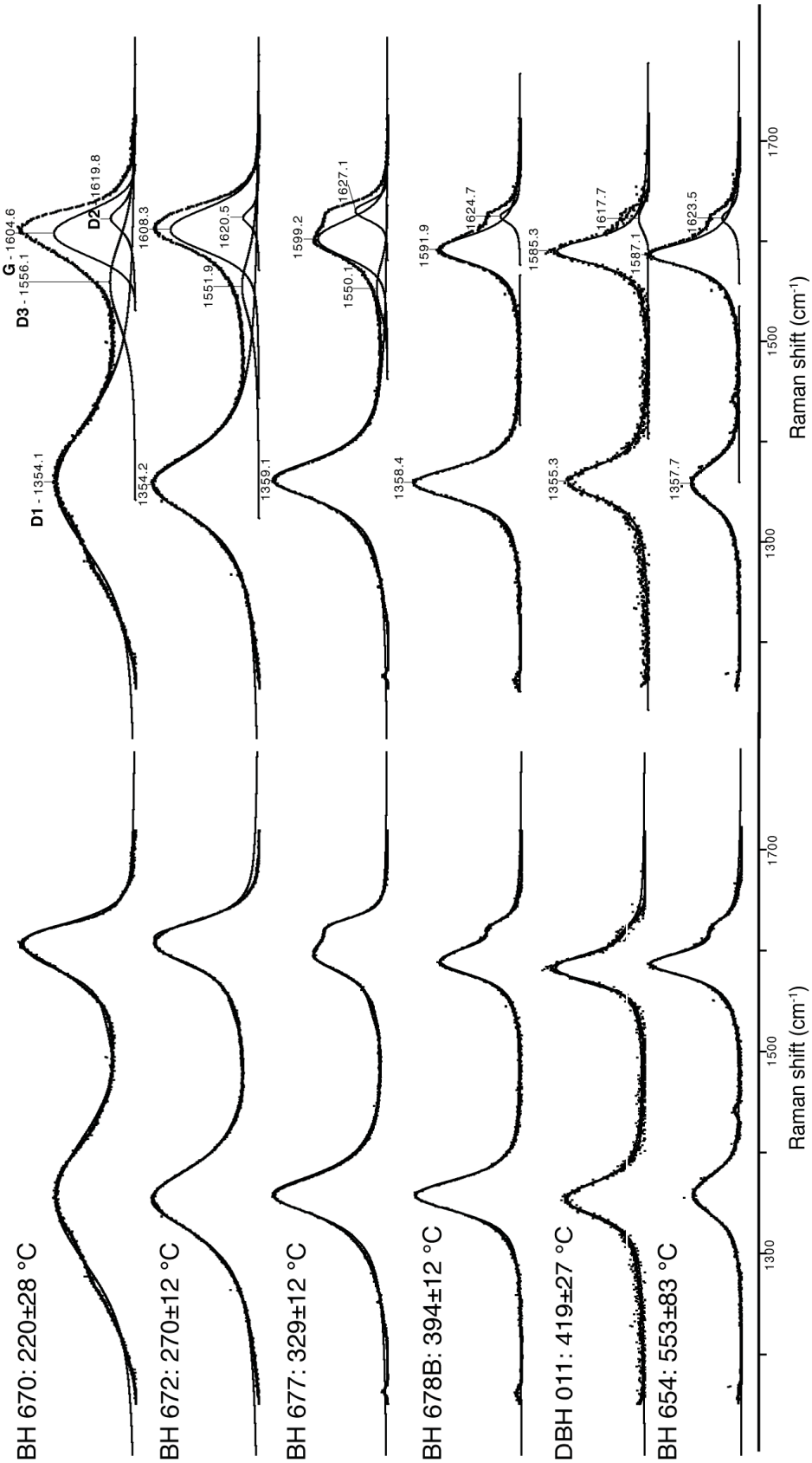

Figure 4.6: Evolution of Raman spectrum with increasing metamorphic temperature.

4.5.1 SAMPLE DESCRIPTIONS AND PREPARATION

Oriented carbonaceous material-bearing samples were collected from the TSS and the Chekha Group (Fig. 4.2; Table 4.1). The 24 samples from the TSS and upper Chekha Group are black shale to slate, grey limestone and rare brown sandstone, and contain disseminated fine-grained carbonaceous material. Samples DBH 009 and DBH 011 from the lower Chekha Group are fine-grained mica schist and graphitic phyllite, respectively, and both contain discrete graphite crystals.

All samples were cut perpendicular to foliation and parallel to lineation (where present) in order to account for any structural heterogeneity (Beyssac et al., 2002). Highly-polished thick (30-100 μm) sections were prepared from these cuts. For those samples with discrete graphite crystals, the crystals were photographed using a reflected light microscope at 50x magnification, and the resulting photomicrographs were used to guide analyses.

4.5.2 SPECTRA ACQUISITION AND DATA PROCESSING

A Jobin Yvon T64000 Raman triple spectrometer set with a 514.532 nm λ excitation Ar laser and a CCD detector at Dalhousie University was used to create and collect Raman scatter. Most samples were placed under a microscope beneath a 100x objective to focus the excitation beam onto the sample and collect the Raman scatter; some samples, indicated in Table 4.1, were measured using a 50x long working distance (LWD) objective. A grating of 1800 gr/mm was used to filter Raman scatter. Power at the sample was measured at $\sim$3 mW (1-2 mW for the 50x LWD objective), and the laser beam size had a diameter of $\sim$2 μm at the sample surface. Carbonaceous material/graphite was characterized by first-order peaks occurring in the 1000-1800 cm^{-1} spectral window of Raman shift (or wavenumber offsets). In each sample, 12-15 spectra were collected for 120 s each. Analyses were distributed across the strike of the samples to account for any heterogeneity that might be present due to intrasample structural anisotropy (Beyssac et al., 2004). Raman spectra were collected from carbonaceous material present beneath clear grains (typically quartz) where possible, to avoid any possible heating effects that may have occurred at the surface of the sample during polishing. Samples for which it was not possible to analyze beneath transparent grains are indicated in Table 4.1.

Peak fitting of Raman spectra was done using Peak Fit®, to calculate R1 and R2 ratios for each analysis (12-15 per sample). Results were combined to produce a mean

Sample	Lithology	Tectonic Assemblage	Spectra acquis.	R1 (mean)	Error (±1σ)	R2 (mean)	Error (±1σ)	T (°C)* (mean)	Error (°C) (±1σ)	T (°C)† (mean)	Error (°C) (±1σ)
654	slate	TSS	s	0.56	0.22	0.36	0.16	505	49	553	83
655	slate	TSS	b	1.19	0.08	0.68	0.02	335	8	274	17
656	slate	TSS	b	1.30	0.04	0.69	0.01	333	3	280	7
657	slate	TSS	b	1.36	0.12	0.68	0.01	339	5	300	10
658	slate	TSS	b	1.26	0.10	0.74	0.01	311	6	222	20
661	slate	TSS	b	1.21	0.06	0.71	0.02	324	7	248	13
662	slate	TSS	b	0.98	0.04	0.66	0.01	346	3	266	2
663	slate	TSS	b	0.83	0.10	0.66	0.01	347	3	243	12
666	slate	TSS	b	1.17	0.22	0.66	0.06	345	27	290	38
667	slate	TSS	b	1.06	0.04	0.70	0.01	329	4	242	14
670	slate	TSS	b	0.83	0.09	0.68	0.03	338	15	220	28
671	slate	TSS	b	0.85	0.10	0.62	0.02	367	11	293	15
672	slate	TSS	b	1.25	0.07	0.70	0.02	331	7	270	12
674	slate	TSS	b	1.30	0.06	0.72	0.01	321	6	251	10
675B	slate	TSS	b	1.3	0.10	0.73	0.03	315	15	231	43
677	slate	TSS	b	1.68	0.26	0.67	0.01	343	5	329	12
678B	slate	TSS	b	1.63	0.17	0.61	0.02	370	10	394	12
680	slate	TSS	b	0.62	0.08	0.44	0.03	444	13	432	17
DBH 009	schist	Chekha	s	0.59	0.30	0.51	0.10	414	46	354	95
DBH 011	phyllite	Chekha	s	0.84	0.08	0.50	0.04	420	16	419	27
DBH 050	limestone	Chekha	s	1.92	0.31	0.69	0.02	336	10	317	20
DBH 051	sandstone	TSS	s	1.42	0.07	0.69	0.01	332	4	290	10
DBH 052	slate	TSS	s	1.65	0.08	0.75	0.02	309	11	252	26
DBH 053	limestone	Chekha	s	1.82	0.15	0.70	0.01	328	5	302	12
DBH 054	limestone	Chekha	s	1.91	0.12	0.69	0.02	335	10	322	23

Table 4.1: Raman spectroscopy of carbonaceous material results. *Beyssac et al. (2002). †Rahl et al. (2005). For spectra acquisition, "s" denotes that spectra were collected from the polished surface, while "b" denotes that spectra were collected from beneath transparent grains.

value and standard deviation for each sample. Individual peak fit results are included in Appendix J.

4.5.3 RESULTS

The samples analyzed yielded a range of Raman spectra (Fig. 4.6) indicating a range of peak temperatures for TSS and Chekha Group rocks from 200-600 °C (Table 4.1, Fig. 4.7). Since several of the samples were of sufficiently low metamorphic grade that they exhibited a change in R1 ratio only, with no change in R2 ratio (<330 °C according to RSCM calibrations (Rahl et al., 2005)), all temperatures reported below are calculated using Eq. 4.2 (for comparison, temperatures calculated using Eq. 4.1 are reported in Table 4.1). In general, the TSS rocks exhibit uniformly low peak temperatures of 200-350 °C. Within the Chekha Group, samples close to the Chekha Group/TSS contact are ∼300 °C, with one sample >400 °C. Those close to the GHS/Chekha Group contact are 300-450 °C. Two TSS samples (BH 653 and BH 654) yielded high temperatures of 400-600 °C (Fig. 4.7a). These samples are located less than 200 m from the Lingshi fault (Fig. 4.2). Samples BH 677, 678B and 680 also yield higher temperatures of ∼320-450 °C (Fig. 4.7b). These samples are the three structurally lowest TSS samples collected from the northeastern corner of the Lingshi klippe, where the STDS is thinnest (Fig. 4.2). For comparison, Crouzet et al. (2007) report a similar range of peak metamorphic temperatures for Devonian to Triassic age TSS rocks in central Nepal of 250-450 °C using illite and chlorite "crystallinity", vitrinite reflectance, calcite-dolomite and chlorite-chloritoid geothermometers.

4.6 DISCUSSION

4.6.1 STRUCTURAL HISTORY OF BHUTAN HIMALAYA SUPERSTRUCTURE

The evolution of Himalayan superstructure preserved within the Lingshi klippe, including both the Chekha Group and the overlying TSS, can be simplified into three main stages of deformation, summarized in Fig. 4.8. The first deformation stage included the development of schistosity in the Chekha Group and slaty cleavage within the TSS, although an earlier deformation fabric is preserved in the Chekha Group as an internal fabric within garnet cores (Fig. 4.8). This core internal fabric is at high angle to a rim fabric that is continuous

Figure 4.7: Compilation of all metamorphic temperature constraints summarized in a vertical structural section. Sample locations are shown in Figure 4.2. Since thickness of the Chekha Group varies considerably along strike, a nominal structural thickness of 3000 m is displayed. Samples DBH 050 and higher are positioned relative to the Chekha Group/TSS contact, while samples below are positioned relative to the GHS/Chekha Group contact. Structural thickness of the Chekha Group varies in the Lingshi klippe from ca. 1.5 km to ca. 5 km. Outliers are circled, and their significance is discussed in the text. Fills correspond to Figure 4.1. Apparent temperature gradient is intended to be a first-order approximation only. RSCM temperatures are calculated using Eq. 4.2 (Rahl et al., 2005). Error bars are $\pm 1\sigma$.

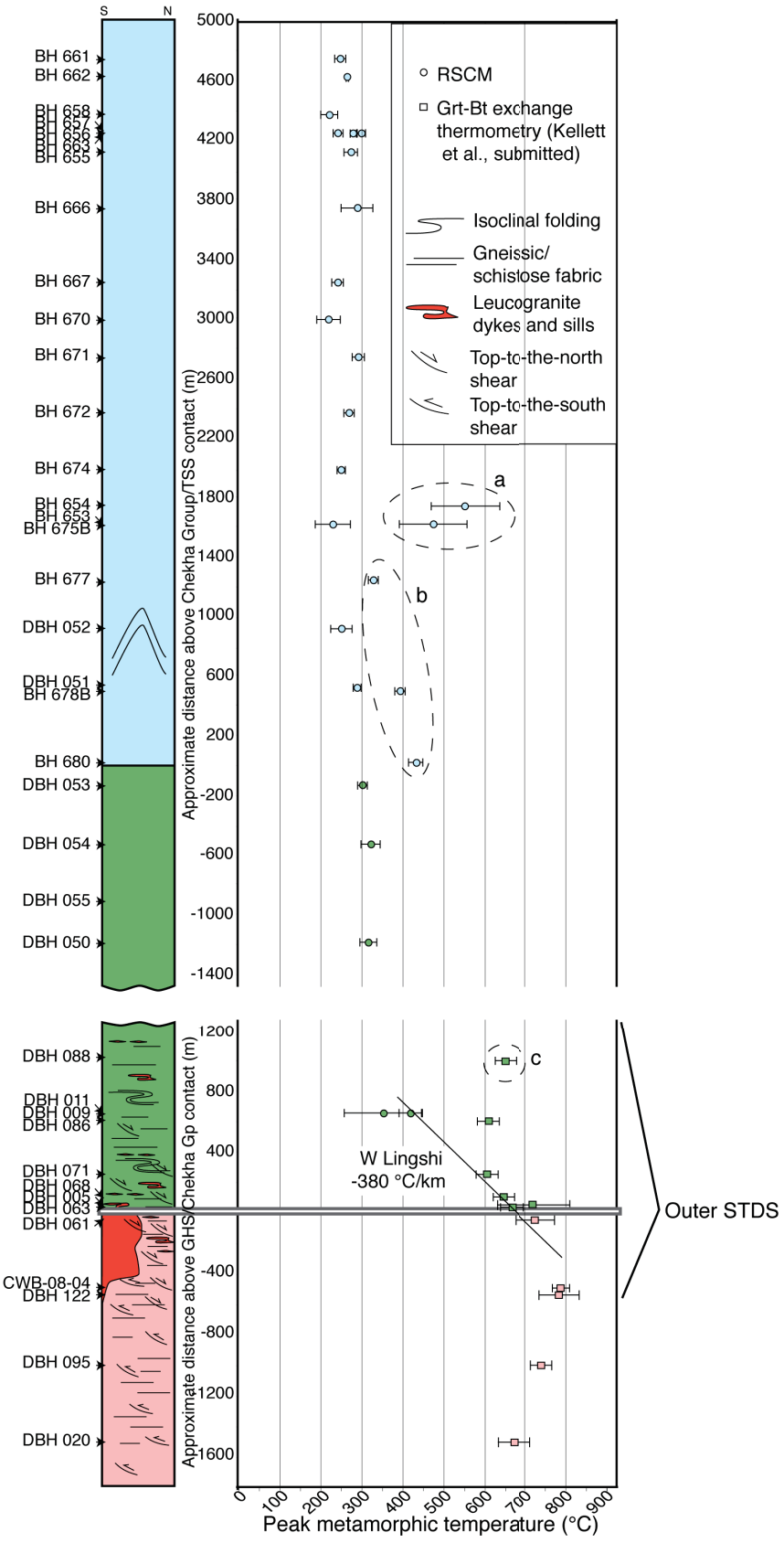
S
N
BH 661
BH 662
BH 658
BH 657
BH 656
BH 663
BH 655
BH 666
BH 667
BH 670
BH 671
BH 672
BH 674
BH 654
BH 653
BH 675B
BH 677
DBH 052
DBH 051
BH 678B
BH 680
DBH 053
DBH 054
DBH 055
DBH 050
Approximate distance above Chekha Group/TSS contact (m)
5000
4600
4200
3800
3400
3000
2600
2200
1800
1400
1000
600
200
-200
-600
-1000
-1400
RSCM
Grt-Bt exchange thermometry (Kellett et al., submitted)
Isoclinal folding
Gneissic/ schistose fabric
Leucogranite dykes and sills
Top-to-the-north shear
Top-to-the-south shear
a
b
DBH 088
DBH 011
DBH 009
DBH 086
DBH 071
DBH 068
DBH 005
DBH 063
DBH 061
CWB-08-04
DBH 122
DBH 095
DBH 020
Approximate distance above GHS/Chekha Gp contact (m)
1200
800
400
-400
-800
1200
1600
c
W Lingshi
-380 °C/km
Outer STDS
0
100
200
300
400
500
600
700
800
900
Peak metamorphic temperature (°C)

with the schistosity. The northwest-dipping axial-planar schistosity preserved in Chekha Group rocks, and northeast-dipping slaty cleavage and small, south- and southeast-directed thrusts preserved in TSS rocks may have formed at similar times, with differences in style of deformation (isoclinal folds in the Chekha Group vs. open folds in the TSS) reflecting different structural levels (lower vs. higher), and differences in orientation of principal finite strain axes reflecting the effects of late folding. However, synchronous development of these structures has yet to be demonstrated.

The second deformation stage involved deformation during Miocene top-to-the-north shearing along the STDS. A broad zone of ductile shear, evidenced by top-to-the-north shear bands and internal boudinage, mineral and stretching lineations and folding or boudinage of Miocene leucogranite bodies, characterizes both the lower Chekha Group and the top of the GHS (Fig. 4.8; Chapter 3). There is no definitive evidence for a related top-to-the-north brittle fault at the Chekha Group/TSS boundary (based on both structural observations and RSCM data discussed in §5.2), suggesting that the outer STDS section bears greater similarity to the Dzakaa Chu STDS section, for example, than the Everest STDS section (Hodges et al., 1996; Searle et al., 2003; Searle and Godin, 2003; Cottle et al., 2007). Although STDS shearing occurred during the Early Miocene across the orogen, it remained active into the Middle Miocene in the eastern Himalaya, several million years longer than in central parts of the orogen (Godin et al., 2006a; Chapter 2; Chapter 3).

The final deformation stage in the Lingshi klippe included km-scale interference folding of the GHS, Chekha Group and TSS into a dome-and-basin geometry and oblique-slip faulting along the Lingshi and related faults. Although there are no absolute constraints on the timing of buckling, relative age constraints indicate that it followed cessation of motion on the outer STDS (which is folded by the buckling) at ca. 15.5-12 Ma, and may also have followed cessation of motion on the inner STDS (which is also folded; Edwards et al., 1999) at ca. 10 Ma. Paleomagnetic remnance data from the Lingshi klippe indicates that it has experienced a 40.2° clockwise rotation around a vertical axis since ∼13 Ma, possibly synchronously with either the interference folding, or the oblique-slip faulting (Baule, 2004). The Lingshi fault and large transverse structures such as the Yadong-Gulu graben (Fig. 4.1) also offset the younger inner STDS. Some of these structures are seismically active now (Drukpa et al., 2006; Mukul et al., 2010), making this the most recent deformation to affect the Himalayan superstructure in this region.

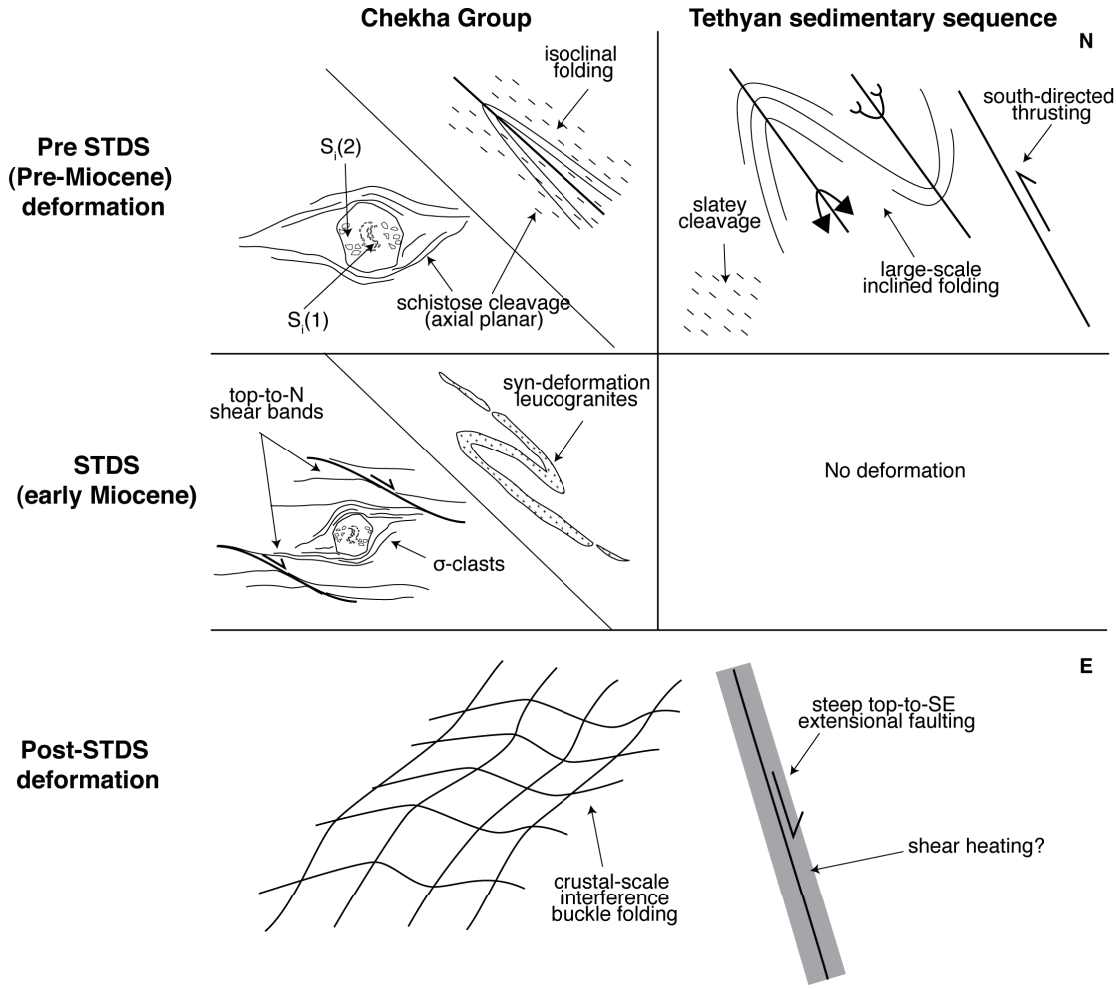

Figure 4.8: Schematic illustration of the structural history of the Chekha Group and TSS in the Lingshi klippe.

These three deformation stages influenced the coupling/decoupling history of the infrastructure and superstructure of the Himalaya. Pre-Miocene south-directed shortening structures observed in the TSS and Chekha Group may have been synchronous with pre-Miocene regional prograde metamorphism in the GHS (Chapter 3), signifying a period of thickening and shortening throughout the upper and middle crust, probably during Eocene-Oligocene. Once the STDS became active in the Miocene, the superstructural TSS was effectively decoupled from the infrastructural GHS, which underwent south-directed flow, presumably due to significant weakening of the GHS relative to the TSS. Once motion on the outer STDS ceased, infrastructure and superstructure were mechanically recoupled, evidenced by km-scale folding of the TSS, GHS and outer STDS. This may

have been a result of cooling and hence strengthening of the GHS.

4.6.2 RSCM AND THE THERMAL FIELD GRADIENT ACROSS BHUTAN HIMALAYA SUPERSTRUCTURE

Samples BH 653 and BH 654 (Fig. 4.7a) yielded elevated RSCM temperatures compared to the other TSS samples. While several other TSS samples yielded pre-Himalayan illite K/Ar ages, a sample collected close to BH 653 and 654 yielded a K/Ar age for illite of 13.1 Ma, (Baule, 2004), consistent with these two samples having been heated to higher temperatures. BH 653 and 654 are in the immediate hanging wall of the Lingshi fault. We suggest that hot fluids traveling along the fault may explain the higher temperature of these samples. Several other analyzed samples NE of BH 653 and 654 are also located proximal to the Lingshi fault (e.g., BH 666, BH 667) and do not yield elevated temperatures. However, in the NE the fault juxtaposes TSS rocks against footwall Chekha Group rocks, while near BH 653 and 654, it juxtaposes TSS rocks against hotter GHS and anatectite in the footwall.

Samples BH 677, 678B and 680 (Fig. 4.7b) indicate a peak temperature increase towards the base of the TSS section in the northernmost portion of the Lingshi klippe. Such an increase is not observed along either of the southern transects along the Yaksa Chu and the Wang Chu. It is possible that these elevated temperatures indicate a shallow pluton beneath the attenuated Chekha Group sequence.

The outlier identified in Fig. 4.7c was collected from the Ura klippe, $\sim$150 km east of the Lingshi klippe (Chapter 3). Compared to the RSCM data for samples DBH 011 and DBH 009 from the Lingshi klippe, this suggests that high peak metamorphic temperatures may have extended to higher structural levels in the Ura klippe than in the Lingshi klippe.

By comparing the RSCM data with published garnet-biotite temperature estimates determined from samples collected across the STD in the Lingshi and Ura klippen (Fig. 4.1; Chapter 3), it is possible to establish an apparent peak temperature field gradient across the entire outer STDS. Though the great variability in thickness of the Chekha Group along strike of the STDS within the Lingshi klippe precludes estimation of a single field gradient representative of the klippe, it can be characterized to a first order. Peak metamorphic temperature decreases steeply but continuously across the outer STDS from $\sim$800°C near the top of the GHS to $\sim$300 °C in the Chekha Group over a structural thickness of $<$2 km (Fig. 4.7). Within the Chekha Group high peak metamorphic temperatures coincide with

the presence of Miocene leucogranitic dykes and sills, while low temperatures coincide with their absence higher in the section. The apparent peak temperature gradient across the outer STD is an order of magnitude greater than a "normal" continental geothermal gradient (i.e. ∼200-500°C/km compared to 25-40°C/km).

This steep thermal field gradient is evidently the result of displacement along a ductile normal-sense shear zone. However, quantifying the amount of down-dip displacement required to produce this gradient is non-trivial because:

- Exhumation of the GHS (and the STDS) was not achieved by crustal extension, rather it occurred in a collisional setting with net uplift of rocks in the footwall relative to rocks in the hanging wall.

- The geothermal gradient in an active collisional orogen is non-linear and non-steady-state in time and space.

- In addition to perfect simple shear, it has been demonstrated that there is a significant component of pure shear across the STDS (e.g. Law et al., 2004), consistent with our observation of microfabrics.

- As indicated by schematic particle velocity diagrams (Grujic 2006) and calculated particle displacement paths (e.g. Jamieson et al., 2004) associated with channel flow, points near the base of the shear zone have undergone greater exhumation than points near the top of the shear zone; there is a progressive increase of particle path transport distance with structural depth. Therefore the finite juxtaposition of points with different peak metamorphic temperatures results from systematic variations in the Poiseuille ("pipe") flow component across the STDS. In addition, even in a simple system the finite displacement path varies down-dip within a single shear zone.

Collectively, these factors preclude calculation of displacement from temperature differences between points in the hanging wall and footwall of the STDS.

4.6.3 SYN-CONTRACTION LANDS

Finite element thermomechanical models of collision for large hot orogens predict three different mechanisms that can produce LANDs during contraction in a large hot orogen

such as the Himalaya: (1) channel flow; (2) extrusion of a paleo-channel, and; (3) destabilization of the upper crust above an exhuming dome of channel material (Beaumont et al., 2001; Beaumont et al., 2004; Jamieson et al., 2004; Beaumont et al., 2006). Comparisons of the structures predicted by the above mechanisms with field data allows us to interpret the origin of various types of LANDs within the STDS, and make comparisons between contrasting along and across-strike exposures of the STDS.

4.6.3.1 Channel LAND

Channel flow (1) in a large hot orogen is caused by the combined effects of Couette and Poiseuille flow acting on a weak crustal layer bounded by stronger layers. During channel flow, rocks within the channel experience pervasive shear, with shear sense controlled by the relative components of Couette and Pouseuille flow, which in turn are determined by the displacement rates of bounding plates, viscosity of the channel rocks, thickness of the channel, and pressure gradient along the channel (e.g., Grujic, 2006). Where the component of Poiseuille flow is significant the upper part of the channel should preserve an opposite shear sense compared to the lower part.

Several researchers have noted both the pervasiveness of shear across the GHS, as well as the reversal in sense-of-shear recorded near the top of the sequence and within overlying metasedimentary rocks (e.g., Burg et al., 1984a; Law et al., 2004). We suggest that the broad, sub-horizontal, top-to-the-north ductile shear zones that characterize the STDS at the outer STDS in Bhutan, at Dzakaa Chu, at the basal part of the STDS at Everest (Lhotse detachment) and at Annapurna (Annapurna detachment) can be explained as the upper part of a laterally-flowing channel (e.g., Beaumont et al., 2001; Grujic et al., 2002; Jamieson et al., 2004; Searle et al., 2003; Cottle et al., 2007; Chapter 3). We propose that this component of the STDS, sometimes referred to in the literature as a "lower STD", is a "channel LAND", the preserved upper part of an active channel, which probably had an initial near-horizontal orientation. Because the relative strength of the two flow components can vary in time and along a channel, a channel LAND may or may not preserve a reversal in sense of shear. A particular distinction between these structures and typical normal-sense structures is that the former may not cut down-section, but rather carry superstructure above the deforming infrastructure. Another distinction is that they are expected to form at high T in the mid-crust, and therefore are more likely to be ductile than brittle structures.

4.6.3.2 Extrusion LAND

(2) Extrusion in the context of Himalayan-style channel flow has been defined as a process of paleo-channel exhumation acting close to the denudation front beyond the rheological tip of the active channel, in which the paleo-channel is exhumed along discrete structures (Godin et al., 2006a).

As mid-crustal rocks flow from a high- to a low-pressure area, in this case the orogenic front, rocks cool, pass through the rheological tip of the channel, and form a paleo-channel. The paleo-channel is preferentially exhumed towards the surface, controlled by focused surface erosion and focused shearing/faulting on bounding discrete thrust and normal faults. Since normal faults cut down-section, they can cut into and expose different sections of the channel LAND. For example, the extrusion LAND may juxtapose non-metamorphic upper crustal rocks in its hanging wall against the hanging wall metasediments of a channel LAND in its footwall, or against footwall high-grade gneisses of the channel LAND. These extrusion structures are associated with both brittle and ductile deformation, as the paleo-channel is exhumed through the brittle-ductile transition towards the surface. Latest motion on an extrusion LAND should post-date motion on the channel LAND it exhumes.

4.6.3.3 Doming and destabilization LAND

(3) Doming of a mid-crustal channel and associated destabilization of the upper crust, if it is sufficiently weak, will occur above a ramp or indentor passing beneath the channel (Jamieson et al., 2006). Poiseuille flow within a mid-crustal channel produces shear traction on the base of the overburden resulting in a horizontal force (Gemmer et al., 2004) which may further destabilize the upper crust and facilitate the formation of the domes. This force, a function of the ratio of overburden thickness to channel thickness and of the overburden strength, may lead to the failure of the upper crust (Beaumont et al., 2004; Gemmer et al., 2004), producing discrete conjugate LANDs. Like extrusion LANDs, they likely also cut down-section, and contain both brittle and ductile components.

The North Himalayan gneiss domes are bounded by one or conjugate LANDs (e.g., Kangmar Dome, Chen et al., 1990; Lee et al., 2000). These LANDs have formed due to destabilization and local extension of the upper crust, exposing domes of mid-crustal rocks, putative channel material (e.g., Beaumont et al., 2004; Jamieson et al., 2006). In this case, we propose that destabilization LANDs have tectonically denuded and exposed a

channel LAND.

4.6.3.4 LANDs and the STDS of the eastern Himalaya

The outer STDS is preserved at the base of several klippe in Bhutan that, taken together, expose ∼100 km of the shear zone across its strike. Yet, there is little increase in metamorphic grade of the footwall across this distance from south to north, suggesting thet the structure does not cut down-section. We interpret the outer STDS to comprise a single LAND that fits the characteristics of a channel LAND (§4.6.3.1). The lack of an obvious upper STD structure in the Lingshi klippe suggests that an extrusion LAND did not develop in the outer STDS. In contrast, the inner STDS contains a diffuse ductile high strain zone that is cut by discrete faults. Furthermore, the inner STDS of NW Bhutan exposes Chekha Group rocks only locally, and we suggest that they may have been cut out by ductile-brittle and brittle normal faults along an extrusion LAND. Thus, the inner STDS comprises both channel and extrusion LANDs, while the outer STDS comprises only an exhumed channel LAND. By comparison, the Himalayan gneiss domes are bounded by destabilization LANDS, conjugate low-angle structures that also cut down-section, denuding and exposing a channel LAND.

4.7 CONCLUSIONS

In the Lingshi klippe of Bhutan, the outer STDS hanging wall Chekha Group and TSS rocks are characterized by pre-Miocene shortening structures. Although there is a transition in structural style from structurally-lower isoclinally-folded and transposed Chekha Group rocks to structurally-higher upright-folded TSS rocks with preserved bedding, there is no definitive evidence for a brittle detachment between Chekha Group and TSS rocks in the hanging wall of the outer STDS. Late low-wavelength buckling of the GHS, Chekha Group and TSS, and oblique-slip faulting have deformed both the outer and the inner STDS.

RSCM thermometry data from the Lingshi klippe yield peak metamorphic temperatures of ∼200-350 °C for TSS rocks and >300 °C for Chekha Group rocks. The data show a very gradual decrease in peak T across the Chekha Group/TSS boundary. We tentatively conclude that there is no structural boundary of significant displacement at this contact. In contrast, there is a steep peak T field gradient preserved across the GHS/Chekha Group contact, consistent with a LAND of significant displacement.

We propose that the STDS is a system of LAND structures formed by three different processes:

1. Channel LANDs, formed by channel flow in the mid-crust, characterized by a diffuse, ductile shear zone that may not cut down-section, and that locally preserves a reversal in shear sense (e.g., the outer STDS).

2. Extrusion LANDs, formed by extrusion of a paleo-channel, characterized by ductile-brittle to brittle faulting post-dating and partly cutting-out a channel flow LAND (e.g., the inner STDS).

3. Destabilization LANDs, formed by destabilization and local extension of the upper crust accompanying doming of a mid-crustal channel, characterized by conjugate ductile-brittle to brittle structures that exhume a channel LAND (e.g., the Kangmar dome).

CHAPTER 5

PALEOGEOGRAPHIC RESTORATION OF THE BHUTAN HIMALAYA: KNOWNS AND UNKNOWNS

5.1 ABSTRACT

Provenance characterization of the main lithotectonic units of the Bhutan Himalaya, from Sm-Nd isotopes and detrital zircon U-Pb age populations, indicates that there are more similarities than differences between them. Here we compare new whole rock ϵNd data from the Chekha Group with a now extensive dataset of published ϵNd and detrital zircon age data from several other lithotectonic units in Bhutan.

While the oldest units of the Lesser Himalayan sequence (LHS), the Daling and Shumar Group, are clearly distinct in terms of depositional age, ϵNd signature and detrital zircon U-Pb age distribution, most other rocks in the Bhutan Himalaya (LHS Baxa and Diuri Formations, Jaishidanda Formation, Greater Himalayan sequence (GHS), Chekha Group and Tethyan sedimentary sequence (TSS)) are indistinguishable on the basis of provenance signatures alone.

From these observations we conclude the following: all units except the Daling and Shumar Group were deposited simultaneously for at least parts of the Paleozoic in an extensive and continuous passive margin basin; age equivalent units in the GHS, Chekha Group and TSS indicate that their original stratigraphic order has not been preserved; and the structural boundaries of the GHS (the Main Central thrust and the South Tibetan detachment system) do not coincide with protolith boundaries.

5.2 INTRODUCTION

In the Himalayan orogen, Sm-Nd isotope systematics combined with detrital zircon U-Pb age distributions have been successfully used to characterize and compare lithotectonic units of varying metamorphic grade and deformation history, as these provenance signals are largely unaffected by crustal processes such as deformation, metamorphism, and weathering. Within the Himalaya, these tools have been used to determine along-strike continuity of lithotectonic units in the absence of recognizable marker horizons (e.g., Richards et al., 2006); to locate structural breaks separating lithotectonic units (e.g., Ahmad et al., 2000; Martin et al., 2005); to propose pre-orogenic paleogeographic distributions of lithotectonic protoliths (e.g., DeCelles et al., 2000; Long et al., *in review*); and to determine exhumation histories of lithotectonic packages recorded in the sedimentary record (e.g., DeCelles et al., 2004). In combination, detrital zircon U-Pb age distributions and whole-rock ϵNd values have proven especially useful for constraining protolith boundaries in pervasively-sheared, tectonically-transposed, and/or metamorphosed rocks.

The exhumed metamorphic core of the Himalayan orogen, the GHS, is bound by major coeval structures, the South Tibetan detachment system (STDS) of low-angle normal shear zones and faults above, and the Main Central thrust (MCT) below (Fig. 5.1). These structures are thought to have accommodated both channel flow and the extrusion of the GHS (e.g., Grujic et al., 1996; Beaumont et al., 2001). There is little consensus on the magnitudes of displacement across these two structures, and application of several different conventional methods has resulted in displacement estimates that range by more than an order of magnitude (e.g., Srivastava and Mitra, 1994; Edwards et al., 1996; Grujic et al., 2002; Robinson et al., 2006). The identification of equivalent rocks astride these structures would improve displacement estimates (e.g., GHS rocks above and below the MCT or the STDS). However, it has been difficult to formulate a consistent relationship orogen-wide between these structures and the protolith boundaries of the GHS. Here we examine whether the protolith boundaries of the GHS are coincident with its structural boundaries.

In Bhutan (eastern Himalaya), two packages of deformed metasedimentary rocks, the Chekha Group and the Jaishidanda Formation, are exposed above and below the GHS, respectively (Fig. 5.2; Gansser, 1983; Dasgupta, 1995).

The Chekha Group, preserved in a series of klippen in Bhutan, is structurally

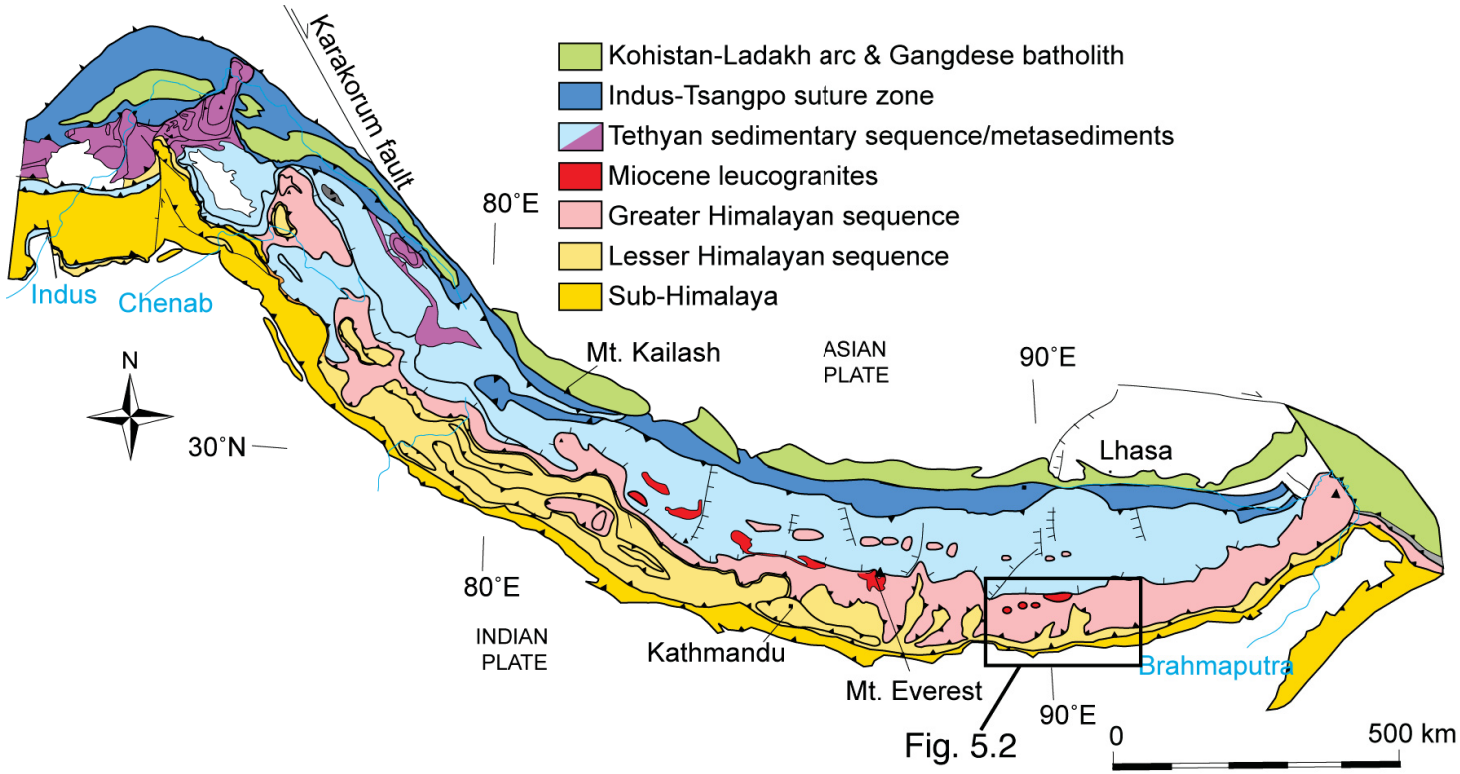

Figure 5.1: Map of the Himalayan orogen showing the basic lithotectonic units (adapted from Guillot et al., 2008).

Figure 5.2: ϵNd and detrital zircon sample locations in Bhutan. Both new sample locations for ϵNd geochemistry and published ϵNd and detrital zircon sample locations are shown. Chekha Group klippen are numbered: 1-Lingshi; 2-Pele La; 3-Black Mountain; 4-Ura and; 5-Tashigang. TSS rocks in the Pele La klippe are at *a*-Tang Chu and *b*-Wachi La. White circles indicate detrital zircon sample locations, and red lines and red dots delineate the transects and locations, respectively, that ϵNd samples were analyzed from. Dark blue lenses are marble bands, and dark green lenses are amphibolite bands. Some areas of the map are interpreted and integrated where necessary from the references listed below. In particular, it is disputed in previous mapping whether the Pele La (2) and Black Mountain (3) klippe are connected (Koike et al., 2002) or not (Long and McQuarrie, 2010). Though they are shown here as continuous, they are treated as separate klippe for the discussion of paleoprovenance signatures in the text. Published data include McQuarrie et al., 2008; Long et al., 2010; Myrow et al., *in review*, Richards et al., 2006. Map is adapted from Gansser (1983); Grujic et al. (2002); Koike et al. (2002); Chakungal (2006); Long and McQuarrie (2010); Long et al. (*in review*); Tobgay et al. (*in review*); and including all mapping described in this thesis.

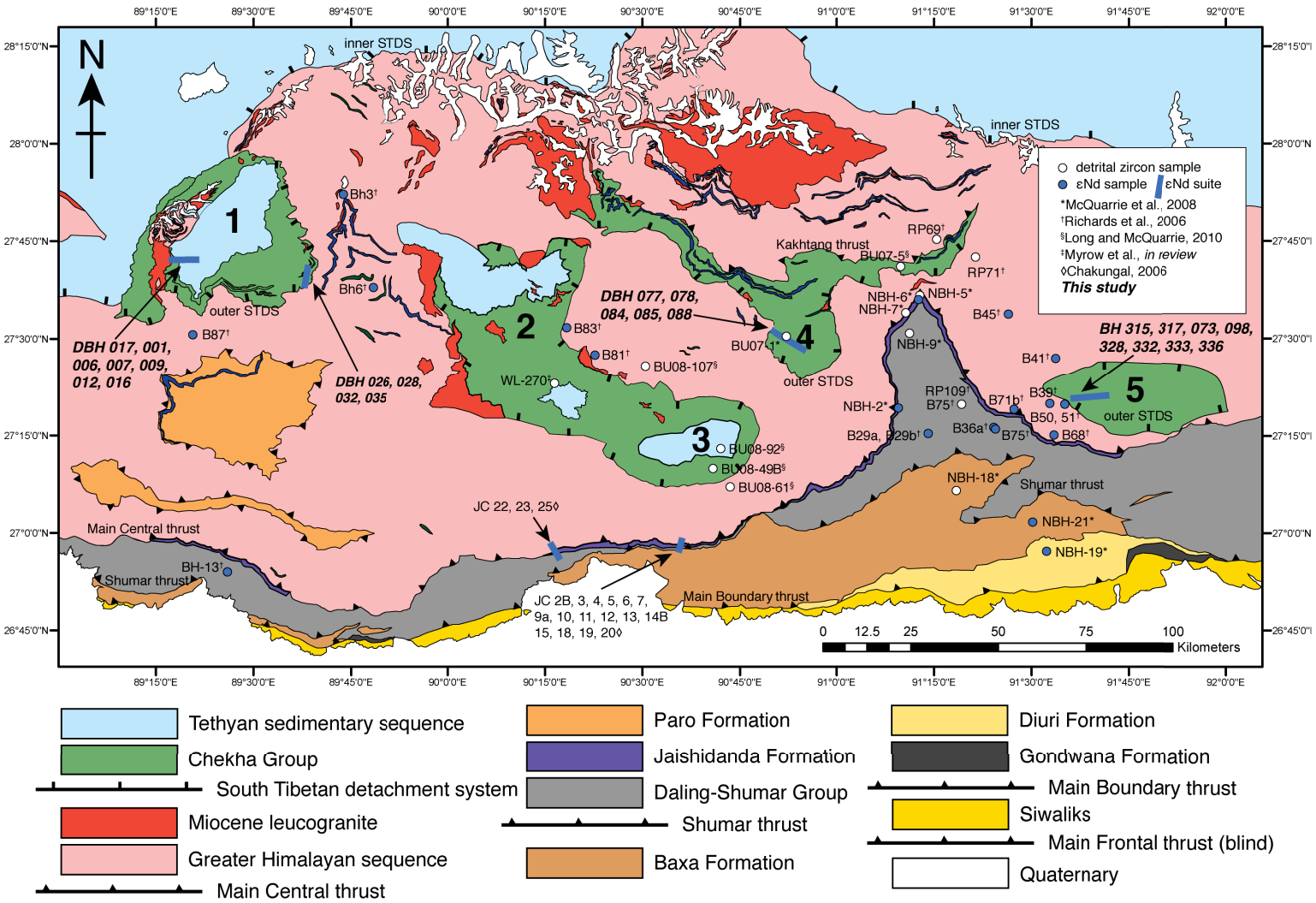
N
inner STDS
outer STDS
1
2
3
4
5
Bh3†
Bh6†
B87†
B83†
B81†
BU08-107§
WL-270†
BU08-92§
BU08-49B§
BU08-61§
JC 22, 23, 25◊
JC 2B, 3, 4, 5, 6, 7, 9a, 10, 11, 12, 13, 14B 15, 18, 19, 20◊
BH-13†
DBH 017, 001, 006, 007, 009, 012, 016
DBH 026, 028, 032, 035
DBH 077, 078, 084, 085, 088
BH 315, 317, 073, 098, 328, 332, 333, 336
Kakhtang thrust
BU07-5§
RP69†
RP71†
NBH-6*
NBH-7*
NBH-5*
B45†
BU07-1*
NBH-9*
B41†
RP109†
B75†
B71b†
B39†
B50, 51†
B68†
NBH-2*
B29a, B29b†
B36a†
NBH-18*
NBH-21*
NBH-19*
Shumar thrust
Main Central thrust
Main Boundary thrust
detrital zircon sample
εNd sample / εNd suite
*McQuarrie et al., 2008
†Richards et al., 2006
§Long and McQuarrie, 2010
‡Myrow et al., in review
◊Chakungal, 2006
This study
0 12.5 25 50 75 100
Kilometers
Tethyan sedimentary sequence
Chekha Group
South Tibetan detachment system
Miocene leucogranite
Greater Himalayan sequence
Main Central thrust
Paro Formation
Jaishidanda Formation
Daling-Shumar Group
Shumar thrust
Baxa Formation
Diuri Formation
Gondwana Formation
Main Boundary thrust
Siwaliks
Main Frontal thrust (blind)
Quaternary

situated between higher-metamorphic grade GHS rocks below and weakly- to un-metamorphosed TSS rocks above (Figs. 5.1; 5.2). This unit is pervasively deformed by Miocene top-to-the-north ductile shearing of the STDS. The Chekha Group is distinguished from the GHS by its distinctly lower metamorphic grade (no anatexis, no sillimanite, prograde zoning preserved in garnets; Chapter 3) and from the TSS by its isoclinal folding, transposed fabrics, abundant intruded Miocene leucogranitic dykes and sills, and up to amphibolite-grade metamorphic assemblages (Grujic et al., 2002; Chapter 3; Chapter 4). Although the GHS and the TSS are recognized orogen-wide as distinct lithotectonic packages, the intervening Chekha Group and its along-strike structural equivalents have been variously identified as belonging to either the GHS (e.g., Searle and Godin, 2003), the TSS (e.g., Myrow et al., 2006), or distinct from either (e.g., Searle et al., 2003). It has been suggested that in the Black Mountain klippe, south-central Bhutan, the GHS, Chekha Group and TSS are in undisturbed stratigraphic position, despite displacement on the STDS (Long and McQuarrie, 2010).

The Jaishidanda Formation, a unit of metasedimentary and meta-igneous rocks, is situated structurally beneath the GHS and above the lower metamorphic grade LHS. It is separated from the GHS by the MCT, and from the LHS below by a yet-unnamed shear zone (Fig. 5.2). The Jaishidanda Formation is distinguished from the GHS by its lower metamorphic grade and hairpin pressure-temperature (P-T) loops, and from the LHS by its contrasting lithology and distinct provenance signature (discussed in detail in §5.4) (Bhargava, 1995; Chakungal, 2006). In the literature, the Jaishidanda Formation has been identified as either part of the LHS (e.g., McQuarrie et al., 2008), the GHS (e.g., Jangpangi, 1974) or distinct from either (e.g., Bhargava, 1995).

The paleogeographic affinities of the GHS-bounding lithotectonic packages, the Chekha Group and the Jaishidanda Formation, hold implications for the geometry of the pre-collision Indian margin, as well as for the definition and evolution of the STDS and MCT. Here we present new whole-rock ϵNd isotopic data for the Chekha Group in three klippen that span the E-W extent of the Bhutan Himalaya. We compare these data and published paleogeographic signatures of the Chekha Group and Jaishidanda Formation to the principal across-strike lithotectonic units of the eastern Himalaya (TSS, GHS, LHS), in order to examine possible configurations for the pre-collision paleogeography of the eastern Himalaya. We conclude by refining the protolith boundaries of the GHS and

discussing the implications for the tectonic history of the eastern Himalaya.

5.3 TECTONOSTRATIGRAPHY OF THE HIMALAYA

5.3.1 MAJOR UNITS AND STRUCTURES

The Himalaya is composed of several tectonostratigraphic packages distinguished by contrasts in provenance, contrasts in metamorphism and deformation, or both, and generally bound by orogen-scale structures (Fig. 5.1; Le Fort, 1975). The Main Frontal thrust (MFT), a blind thrust separating the undeformed foreland basin of the Himalaya from the foothills, marks the southern front of Himalayan deformation. Structurally above are the Sub-Himalaya (only the Siwaliks unit is present in Bhutan), unmetamorphosed clastic and minor carbonate sediments that make up the deformed portion of the foreland basin of the Himalaya (Gansser, 1983; Najman et al., 2004). The Main Boundary thrust (MBT) separates the Sub-Himalaya from the overlying deformed and metamorphosed LHS.

The LHS comprises Paleoproterozoic to Cenozoic stratigraphically-defined units including quartzite, phyllite, dolomite and gneiss. These clastic and carbonate metasedimentary rocks are thought to have been deposited as a proximal passive margin sequence on the northern margin of the Indian plate. Stratigraphically up-section, shallow marine to sub-aerial sedimentary rocks dominate, coinciding with early foreland basin development (Hodges, 2000 and references therein).

The upper boundary of the LHS is typically regarded as the Main Central thrust (MCT), as defined by Gansser (1964). However, in the Bhutan Himalaya, the Jaishidanda Formation, a structurally-bound metasedimentary and metaigneous unit of disputed paleogeographic affinity, occurs between the LHS and the GHS and beneath the defined MCT (Bhargava, 1995; Daniel et al., 2003; Chakungal, 2006).

The GHS is composed of ductilely-deformed, amphibolite- to granulite-facies augen and pelitic gneiss, metapelite, quartzite, marble, calc-silicate, and anatectite, and is intruded by Miocene leucogranite bodies. In Bhutan, the GHS has been tectonically duplicated by out-of-sequence thrusting (Gansser, 1983; Grujic et al., 1996; Hollister and Grujic, 2006).

In the Bhutan Himalaya, the Chekha Group is structurally above the GHS. It is a sequence of lower amphibolite- to greenschist-facies metasedimentary rocks. This package

is deformed by top-to-the-north normal-sense ductile shearing along the STDS (Gansser, 1983; Burchfiel et al., 1985). Along-strike structural equivalents of this unit include (from west to east along the orogen): the Haimanta Group, the Nilgiri (also Dhaulagiri) Limestone, the Larjung (also Annapurna Yellow) Formation, the Everest Series (also North Col Formation) with Yellow Band and the Chekha Group (Wager, 1934; Wager, 1965; Fuchs, 1967; Gansser, 1983; Colchen et al., 1986; Frank et al., 1995).

Above the Chekha Group and above the STDS is the TSS, comprising Paleozoic to Cenozoic weakly- to un-metamorphosed sedimentary rocks. To the north, the TSS is structurally bound by the Indus-Yarlung suture, which marks the northernmost surface extent of Indian crust.

5.3.2 PALEOPROVENANCE SIGNATURES IN THE HIMALAYA

It has been recognized that some lithotectonic packages in the Himalaya can be distinguished on the basis of paleoprovenance signatures such as whole rock ϵNd values and detrital zircon U-Pb age populations, indicating differences in their source regions and source ages (e.g., Parrish and Hodges, 1996). Several studies have established that LHS rocks can be distinguished from GHS rocks on the basis of ϵNd values and detrital zircon age signatures (e.g., Parrish and Hodges, 1996; Whittington et al., 1999; Ahmad et al., 2000; Robinson et al., 2001; Myrow et al., 2003; Richards et al., 2006; McQuarrie et al., 2008). Because most of these studies demonstrated distinct differences in both ϵNd values and detrital zircon signatures between at least parts of the LHS and GHS, these provenance indicators have also been used as tools to identify ambiguous rock packages as having either LHS or GHS affinity, and to locate major structures such as the MCT (e.g., Ahmad et al., 2000; Murphy, 2007; Imayama and Arita, 2008; McQuarrie et al., 2008). Others maintain that structures such as the MCT should be defined solely on the basis of strain localization, and need not coincide with a protolith boundary (Searle et al., 2008). Provenance signature data have also been compared with paleogeography and displacement predictions from numerical models of continental collision (Jamieson et al., 2006). The paleoprovenance of the Sub-Himalaya and LHS have been examined to determine sources of detritus and erosion rates of the various overlying tectonostratigraphic packages into the Himalaya foreland basin (e.g., White et al., 2002; DeCelles et al., 2004).

5.3.2.1 ϵNd signatures

The ϵNd value of a metasedimentary rock is a measure of the weighted average of the Sm/Nd ages of all crustal sources for the sedimentary protolith (McCullogh and Wasserburg, 1978). Sedimentary sequences contain rocks derived from broadly similar source regions. Therefore they may yield a definable range of ϵNd values that are distinct from other sedimentary sequences derived from either different crustal sources or similar sources but in different proportions (e.g., Boghossian et al., 1996). ϵNd signatures of metasedimentary sequences are typically measured in fine-grained clastic rocks (i.e. metapelites).

In the Himalaya, ϵNd values for the LHS were found to be distinctly more negative than those for the GHS (Parrish and Hodges, 1996). However, many authors have since observed that LHS rocks close to the MBT have less negative ϵNd values (generally overlapping with GHS ϵNd values), while LHS rocks directly structurally beneath the GHS have more negative ϵNd values that typically do not overlap with those from GHS rocks (e.g., Richards et al., 2005 and references therein). This division within the LHS, distinguished in both ϵNd data and detrital zircon data, locally coincides with a thrust, such as the Ramgarh thrust in Nepal (e.g., Robinson et al., 2001) or the Shumar thrust in Bhutan (e.g., McQuarrie et al., 2008).

The following ϵNd values are summarized from Parrish and Hodges, 1996; Whittington et al., 1999; Ahmad et al., 2000; Miller et al., 2001; Robinson et al., 2001; Argles et al., 2003; Richards et al., 2005; Richards et al., 2006, and; references therein. All ϵNd values listed here are reported at t=0, and have been recalculated for published data where necessary. Orogen-wide, LHS ϵNd values range from -28 to -10. However, close to the MCT they are centred at -26 to -25, while close to the MBT they are more broadly distributed, typically ranging -22 to -18. GHS ϵNd values range from -20 to -7 with most samples yielding -16 to -14.

The Haimanta Group of NW India, structurally equivalent to the Chekha Group, has yielded ϵNd values ranging from -19 to -11 (Miller et al., 2001), while TSS ϵNd values from central Nepal range from -21 to -6, but from -21 to -16 for the stratigraphically older (Devonian) units (Robinson et al., 2001).

5.3.2.2 Detrital zircon age distributions

Detrital zircon U-Pb age populations provide information on the maximum deposition age of sedimentary protoliths (constrained by the youngest detrital zircon ages), as well

as the ages of various source rocks (e.g., Gehrels and Dickinson, 1995). Detrital zircons are typically sampled from coarse-grained detrital rocks (usually quartzite). Strata of different rock types (e.g., quartzite vs. pelite) within a single basin may be the result of differences in source rocks, weathering processes, and/or depositional environments (e.g., Savage and Potter, 1991). Thus, though detrital zircon studies and Sm-Nd studies can be complementary, they do not necessarily characterize the same sedimentary processes or sources. Furthermore, studies on similarities in detrital zircon age signatures from rocks of similar depositional age, but separated by more than 2000 km along the Himalayan orogenic belt (Myrow et al., 2009; Myrow et al., *in review*) suggest that, particularly in pre-Carboniferous environments when land vegetation was scarce, zircons (known for their robust ability to withstand weathering, transport and depositional processes) can be transported vast distances in braided river systems, and are likely very well mixed prior to deposition (Rahl et al., 2003; Davies and Gibling, 2010). Similarly, wide-scale mixing processes may have homogenized ϵNd signatures in Himalayan sedimentary protoliths to a significant extent.

Detrital zircon U-Pb age populations in the LHS are, as for ϵNd signatures, typically divided into inner (near MCT) and outer (near MBT) LHS groups. The inner LHS, directly beneath the GHS, is distinct from all the other lithotectonic packages of the Himalaya in that it does not contain zircons younger than ca. 1700 Ma, conspicuously lacking the prominent ca. 500 Ma population of zircons preserved in all other lithotectonic units (Parrish and Hodges, 1996; DeCelles et al., 2000; Myrow et al., 2003; Richards et al., 2006; McQuarrie et al., 2008). Both GHS and outer LHS rocks do include significant populations of younger detrital zircon, of ages 1200-800 Ma and ca. 500 Ma (Parrish and Hodges, 1996; DeCelles et al., 2000). TSS rocks also contain detrital zircons in these age ranges, and thus are generally considered indistinguishable from GHS rocks on the basis of detrital zircon signatures (DeCelles et al., 2000; Myrow et al., 2003).

5.4 METHOD: ϵND GEOCHEMISTRY

5.4.1 SAMPLE DESCRIPTIONS

Twenty-four Chekha Group metapelite samples from the Lingshi, Ura and Tashigang klippen were analyzed for whole rock ϵNd geochemistry at Centre national de la recherche

Sample	Latitude (dd°mm.mmm')	Longitude (dd°mm.mmm')	Sub-region	Lithology
BH 073	27°21.753'	91°41.253'	Tashigang	Shaly sandstone
BH 098B	27°22.105'	91°44.086'	Tashigang	Garnet mica schist
BH 315	27°21.619'	91°40.303'	Tashigang	Mica schist
BH 317	27°21.516'	91°40.426'	Tashigang	Garnet mica schist
BH 328	27°17.737'	91°44.912'	Tashigang	Biotite schist
BH 332	27°16.209'	91°55.685'	Tashigang	Pelitic quartzite
BH 333	27°16.808'	91°55.794'	Tashigang	Calc-silicate
BH 336	27°24.932'	91°53.563'	Tashigang	Garnet mica schist
DBH 001	27°41.943'	89°17.552'	NW Bhutan (W)	Calc-silicate/mica schist
DBH 006	27°41.943'	89°17.552'	NW Bhutan (W)	Metapelitic schist
DBH 007	27°41.896'	89°17.929'	NW Bhutan (W)	Metapelitic schist
DBH 009	27°41.936'	89°18.464'	NW Bhutan (W)	Metapelitic schist
DBH 012	27°41.956'	89°19.366'	NW Bhutan (W)	Sericite slate
DBH 016	27°41.831'	89°21.251'	NW Bhutan (W)	Phyllite
DBH 017	27°41.871'	89°17.429'	NW Bhutan (W)	Mica schist
DBH 026	27°38.028'	89°37.887'	NW Bhutan (E)	Phyllitic schist
DBH 028	27°38.087'	89°37.893'	NW Bhutan (E)	Pelitic quartzite
DBH 032	27°39.136'	89°38.630'	NW Bhutan (E)	Pelitic quartzite
DBH 035	27°40.117'	89°38.523'	NW Bhutan (E)	Calc-silicate
DBH 077	27°29.767'	90°49.253'	Ura	Biotite schist
DBH 078	27°29.589'	90°40.265'	Ura	Metapelitic schist
DBH 084	27°30.012'	90°52.172'	Ura	Metapelite/quartzite
DBH 085	27°29.826'	90°52.179'	Ura	Garnet mica schist
DBH 088	27°28.881'	90°54.782'	Ura	Garnet mica schist

Table 5.1: Sample locations for ϵNd analyses.

scientifique in Nancy, France. The sample locations are listed in Table 5.1 and plotted in Fig. 5.2. Sample preparation and analytical procedures are according to Luais et al. (1997) and Luais et al., (2009) and outlined in detail in Appendix K.

5.4.2 RESULTS

Results for ϵNd analyses are shown in Table 5.2 and in Figure 5.3. Chekha Group ϵNd values range from -20 to -11, with overlap in all three klippen between -19 and -16. The western Lingshi klippe yields ϵNd values of -20 to -16, while the central Ura klippe yields values from -19 to -11 and the eastern Tashigang klippe yields values from -20 to -13.

5.5 GEOLOGY AND PALEOPROVENANCE SIGNATURES OF BHUTAN

In Figures 5.3 and 5.4, we present published and our ϵNd and detrital zircon data from the Bhutan Himalaya divided into lithotectonic groups bounded by structures: (a) Baxa/Diuri:

Sample	Sm (ppm)	Nd (ppm)	$^{143}Nd/^{144}Nd$ (0)	2σ error	εNd (0)
BH 073	6.87	44.80	0.511647	0.000016	**-19.3**
BH 098B	10.78	57.43	0.511631	0.000014	**-19.6**
BH 315	8.44	31.58	0.511856	0.000012	**-15.3**
BH 317	27.77	105.22	0.511799	0.000008	**-16.4**
BH 328	7.59	39.53	0.511961	0.000011	**-13.2**
BH 332	10.55	48.54	0.511811	0.000013	**-16.1**
BH 333	7.59	42.56	0.511769	0.000005	**-17.0**
BH 336	8.68	45.02	0.511714	0.000025	**-18.0**
DBH 001	8.96	46.97	0.511779	0.000007	**-16.8**
DBH 006	8.40	45.94	0.511775	0.000013	**-16.8**
DBH 007	6.21	33.50	0.511729	0.000012	**-17.7**
DBH 009	7.40	42.11	0.511806	0.000012	**-16.2**
DBH 012	5.87	31.68	0.511746	0.000007	**-17.4**
DBH 016	7.84	44.77	0.511736	0.000013	**-17.6**
DBH 017	8.52	46.07	0.511712	0.000014	**-18.1**
DBH 026	6.86	39.03	0.511624	0.000006	**-19.8**
DBH 028	1.18	48.62	0.511736	0.000017	**-17.6**
DBH 032	9.09	50.48	0.511762	0.000013	**-17.1**
DBH 035	7.40	45.64	0.511734	0.000012	**-17.6**
DBH 077	7.77	40.27	0.511946	0.000019	**-13.5**
DBH 078	6.57	32.95	0.512025	0.000005	**-12.0**
DBH 084	1.66	7.05	0.511877	0.000013	**-14.8**
DBH 085	7.40	29.09	0.511728	0.000007	**-17.8**
DBH 088	7.07	39.93	0.511712	0.000021	**-18.1**

Table 5.2: ϵNd results. Zero indicates present time.

LHS Baxa and Diuri Formation rocks bounded by the MBT and the Shumar thrust; (b) Daling/Shumar: LHS Daling-Shumar Group rocks bounded by the Shumar thrust and the shear zone at the base of the Jaishidanda Fm.; (c) Jaishidanda: Jaishidanda Fm. with the MCT as its upper boundary; (d) GHS: bounded by the MCT and the STDS; (e) Chekha: Chekha Group rocks bounded by the STDS and; (f) TSS: TSS rocks, which are bounded by the inner STD (see Fig. 5.1), and in the klippen may be stratigraphically continuous with the Chekha Group.

We have reinterpreted some published samples according to our mapping, as well as mapping by Bhargava (1995), Chakungal (2006), Long and McQuarrie (2010) and Chapter 2. For clarity, the original sample numbers of published data are included in Figures 5.3 and 5.4 so that groupings and reassignment of lithotectonic affinity are transparent. In particular, we interpret NBH-2, 5, 6 and 7 of McQuarrie et al. (2008) as Jaishidanda Fm. (previously tentatively interpreted as Baxa Fm.) and BU07-5 of Long and McQuarrie (2010) as Chekha Group (previously interpreted as GHS). BU07-5 was collected from garnet-staurolite schists mapped as the Naspe Formation by Bhargava (1995) (Fig. 5.1). According to our mapping of Chekha Group rocks in the Ura klippe (also

Chapter 2), we did not observe a shear zone or fault separating the undisputed Chekha Group in that klippe from the Naspe Formation of Bhargava (1995). We distinguish the Chekha Group from the GHS on the presence of an intervening high strain zone of top-to-the north shear, prograde chemical zoning in garnet, the absence of sillimanite and the absence of in situ anatectite. Since the Naspe Formation satisfies these criteria, we interpret BU07-5 as part of the Chekha Group.

5.5.1 LESSER HIMALAYA SEQUENCE

In Bhutan, the LHS is made up of four lithologic groups: the Daling-Shumar Group, an interbedded quartzite and phyllite sequence; the Baxa Group of quartzite, dolomite and limestone; the Diuri Formation of interbedded slate and diamictite and; the Gondwana Sequence sandstone, siltstone and shale, distinctive for its coal seams (Gansser, 1983; McQuarrie et al., 2008). These units have been stacked in a repeated thrust sequence making their stratigraphic order uncertain. Mapping by McQuarrie et al. (2008) places the Shumar unit at the stratigraphic base of the LHS, with the following younging sequence: Daling, Baxa, Diuri, Gondwana.

The Gondwana sequence at the structural base of the LHS is the youngest LHS unit, and has been paleontologically dated as Permian (Lakshminarayana, 1995). The Baxa and Diuri Formations structurally overlie the Gondwana sequence. Baxa/Diuri contains detrital zircons at least as young as ca. 500 Ma (McQuarrie et al., 2008), suggesting a probable Paleozoic age. The structurally highest Daling-Shumar Group is bound by the Shumar thrust at its base and a shear zone separates its upper units from the Jaishidanda Fm. Daling/Shumar contains the oldest detrital zircon population in the LHS, and in the Bhutan Himalaya in general, with no zircons younger than 1700 Ma (Fig. 5.4; Richards et al., 2006; McQuarrie et al., 2008). In Bhutan, ϵNd signatures for Baxa/Diuri range from -21 to -19 (only two samples analyzed), while they span -32 to -25 for Daling/Shumar (Fig. 5.3; Richards et al., 2006; McQuarrie et al., 2008).

5.5.2 JAISHIDANDA FORMATION

The Jaishidanda Formation, consisting of highly-deformed garnet-mica schist, micaceous quartzite and augen gneiss, is both lithologically distinct from the underlying Daling/Shumar, and of higher metamorphic grade. While it is lithologically similar to the overlying GHS, peak T estimates indicate lower metamorphic grades, and P-T conditions from

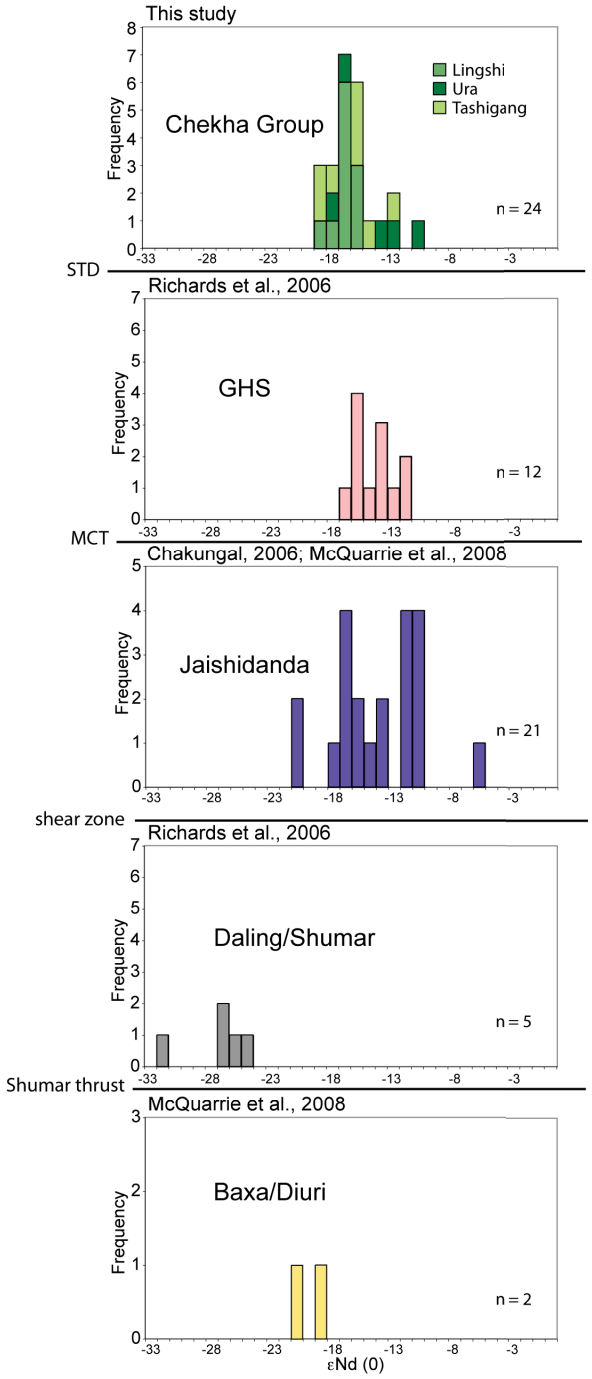

Figure 5.3: ϵNd data. Histograms show ϵNd(0) data from the Chekha Group (this study) compared with values from other lithotectonic packages of Bhutan published in previous studies.

Figure 5.4: Detrital zircon data. Frequency plots of published detrital zircon U-Pb ages from the Chekha Group compared to age distributions from other lithotectonic packages in Bhutan. Where the tectonostratigraphic association is in question, the specific unit is distinguished (e.g., Jaishidanda Fm.).

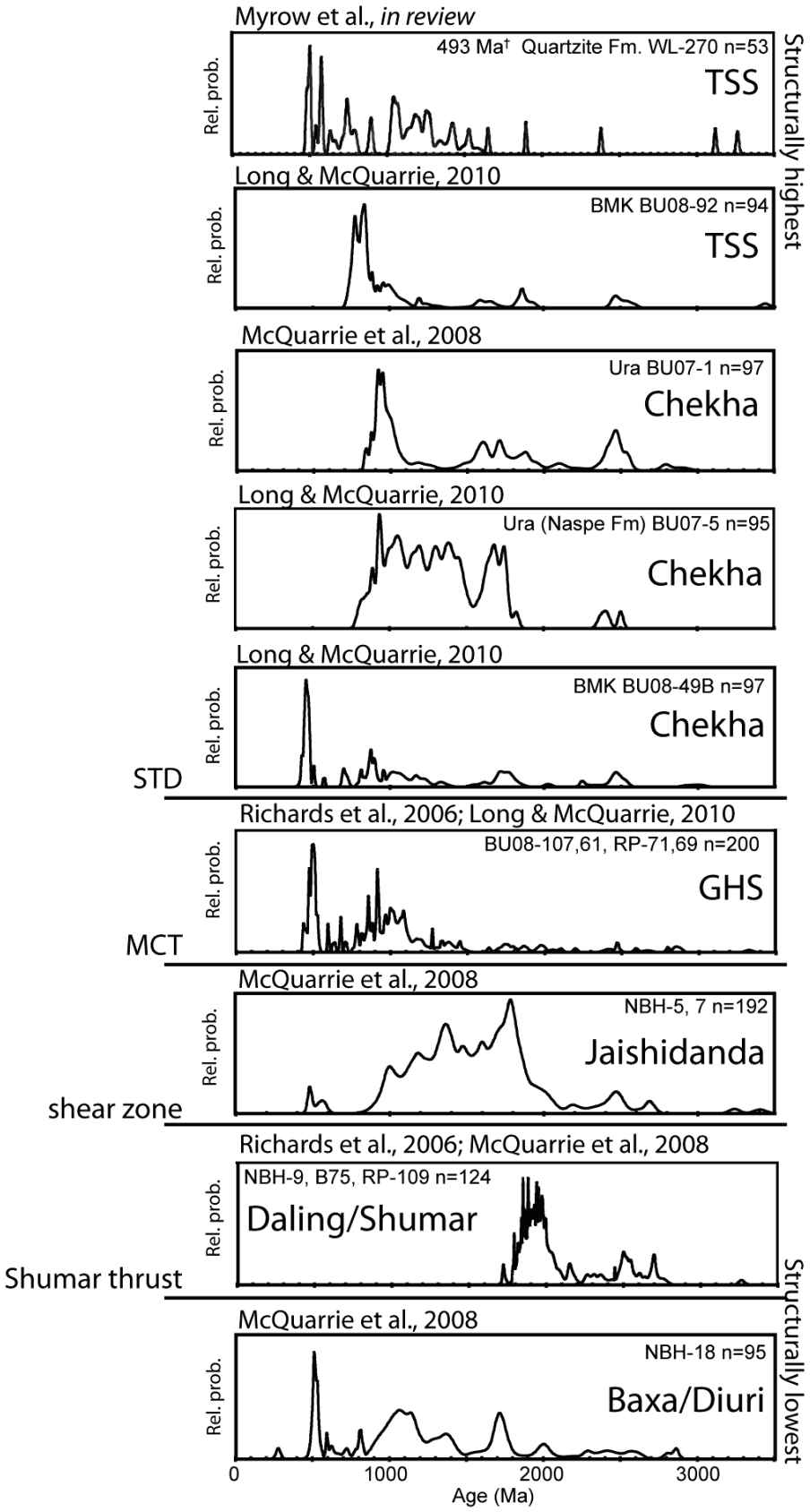
Myrow et al., in review
493 Ma† Quartzite Fm. WL-270 n=53
TSS
Long & McQuarrie, 2010
BMK BU08-92 n=94
TSS
McQuarrie et al., 2008
Ura BU07-1 n=97
Chekha
Long & McQuarrie, 2010
Ura (Naspe Fm) BU07-5 n=95
Chekha
Long & McQuarrie, 2010
BMK BU08-49B n=97
Chekha
STD
Richards et al., 2006; Long & McQuarrie, 2010
BU08-107,61, RP-71,69 n=200
GHS
MCT
McQuarrie et al., 2008
NBH-5, 7 n=192
Jaishidanda
shear zone
Richards et al., 2006; McQuarrie et al., 2008
NBH-9, B75, RP-109 n=124
Daling/Shumar
Shumar thrust
McQuarrie et al., 2008
NBH-18 n=95
Baxa/Diuri
Rel. prob.
Structurally highest
Structurally lowest
0
1000
2000
3000
Age (Ma)

Jaishidanda rocks indicate hairpin loops through P-T space in contrast to broader P-T loops preserved in GHS rocks (Daniel et al., 2003; Chakungal, 2006; Chapter 3). In addition, garnet grains preserve growth zoning, typically absent in garnet from GHS rocks (Daniel et al., 2003; Chakungal, 2006; Chapter 3). Similar hairpin P-T paths have been obtained from LHS rocks in eastern Nepal (Groppo et al., 2009), central Nepal (Catlos et al., 2001; Kohn et al., 2001) and NW India (Caddick et al., 2007). Jaishidanda ϵNd values range from -22 to -6, while its detrital zircon signature is characterized by a small peak at 500 Ma and a broad "plateau" of ages between 800-2100 Ma (Figs. 5.3, 5.4).

5.5.3 Greater Himalayan sequence

The Greater Himalayan sequence in Bhutan comprises amphibolite- to granulite-facies metapelitic gneiss and schist, augen gneiss, quartzite, calc-silicate and marble (Gansser, 1983; Grujic et al., 1996; Daniel et al., 2003; Warren et al., *in review*). The sequence has variable thickness, is migmatized, and has been intruded by Miocene leucogranite. It is pervasively ductilely-deformed (Grujic et al., 1996), and its thickness is duplicated within Bhutan by thrusting along the out-of-sequence Kakhtang thrust (Fig. 5.1; Gansser 1983; Grujic et al., 2002). Within the GHS, ϵNd signatures range from -18 to -12 (Fig. 5.3; Richards et al., 2006). The detrital zircon age distribution of GHS samples is similar to those published for the GHS orogen-wide: it is dominated by ca. 500 Ma and 800-1200 Ma grains, with smaller contributions of Proterozoic and Archean age grains (Fig. 5.4).

5.5.4 Chekha Group

The Chekha Group is exposed in a series of klippen in Bhutan, from west to east: Lingshi, Pele La, Black Mountain, Ura and Tashigang (also Radi) (Fig. 5.2). There is a discrepancy in published maps of the Pele La and Black Mountain klippe as to whether they are distinct or in fact one continuous klippe extending from central to south-central Bhutan (Koike et al., 2002; Long and McQuarrie, 2010). Although we present the klippen as a continuous package in Fig. 5.2, we consider the two areas here as separate klippen because of significant differences in paleoprovenance data.

Samples for our study were collected from the Lingshi, Ura and Tashigang klippen (Fig. 5.2). In the Lingshi klippe, the Chekha Group comprises calc-silicate, mica schist, marble, and limestone (Chapter 3). In Ura, the Chekha Group is composed of alternating mica schist and quartzite layers, with local marble bands and rare amphibolite. The

Tashigang klippe comprises quartzite, garnet+muscovite±staurolite schist, marble, and local amphibolite±garnet interlayers (interpreted as mafic dykes). The Chekha Group in all three klippen is intruded by variably-deformed leucogranite dikes and sills generated by Miocene partial melting of the GHS (Le Fort, 1975; Gansser, 1983). Chekha Group rocks increase in metamorphic grade down structural section from lower greenschist-facies to amphibolite-facies, and have been isoclinally folded and subsequently sheared in the Miocene by the STDS (Chapter 3).

The ϵNd values determined from Chekha Group samples in the three klippen range from -20 to -11 (Fig. 5.3). Chekha Group detrital zircon U-Pb age distributions are available for three samples from the Ura and Black Mountain klippen (McQuarrie et al., 2008; Long and McQuarrie, 2010). All three exhibit a population of 800-1200 Ma grains similar to that observed in the GHS, Jaishidanda Formation and Baxa/Diuri samples (Fig. 5.4). A population of ca. 500 Ma detrital zircons is present in Chekha Group rocks from the Black Mountain klippe, but not the Ura klippe. Chekha Group sample BU07-5 from the Ura klippe is particularly notable for the similarity its detrital zircon age spectrum bears to Jaishidanda (Fig. 5.4). Although the former lacks ca. 500 Ma grains, both contain a broad "plateau" of zircons ages between 800-1900 Ma.

5.5.5 TETHYAN SEDIMENTARY SEQUENCE

The Tethyan sedimentary sequence (TSS) has been mapped in the core of the Lingshi, Pele La and Black Mountain klippen, and is also exposed north of the inner STDS (Fig. 5.2). Within the Pele La klippe, TSS rocks are preserved at Tang Chu and Wachi La (see *a* and *b*, respectively, in Fig. 5.2). In Bhutan, the TSS is weakly- to un-metamorphosed, folded into upright to south-vergent folds, and consists predominantly of limestone and slate of lower Paleozoic to Cretaceous age (Gansser, 1983).

The stratigraphic age of the base of the TSS has been tightly constrained by trilobite fossils in the Quartzite Formation of the Pele La klippe (Wachi La) to 493-494 Ma (Hughes et al., *in review*). Devonian fossils have been identified higher in the TSS section at Wachi La (Termier and Gansser, 1974; Gupta and Termier, 1983). There are no ϵNd data available for the TSS in Bhutan. TSS sample BU08-92 from the Black Mountain klippe yielded a distinct detrital zircon age peak at 700-900 Ma (Long and McQuarrie, 2010), while sample WL-270 from the Pele La klippe yielded several small age peaks between 450 and 1700 Ma (Fig. 5.4; Myrow et al., *in review*).

5.6 DISCUSSION

5.6.1 LESSER HIMALAYAN SEQUENCE

The Baxa/Diuri contains similar zircon populations to structurally higher lithotectonic packages, and is not older than Paleozoic in age. Particularly, it contains a prominent population of ca. 500 Ma zircons, and a population at 800-1200 Ma, as do parts of the GHS, Chekha Group and TSS (Fig. 5.4). In comparison, the Daling/Shumar is likely Proterozoic in age, as it does not contain zircons younger than 1700 Ma (Fig. 5.4; Richards et al., 2006; McQuarrie et al., 2008).

Daling/Shumar yields distinctly more negative ϵNd values ($<$ -24) than all other lithotectonic groups in the Bhutan Himalaya ($>$ -22), including the structurally underlying Baxa/Diuri and overlying Jaishidanda (Fig. 5.3; Chakungal, 2006; Richards et al., 2006; McQuarrie et al., 2008). The distinct detrital zircon and ϵNd signature of the Daling/Shumar package suggests that its provenance is distinct from all other lithotectonic packages in the Himalaya, and that the Shumar thrust is a protolith boundary within the LHS.

5.6.2 JAISHIDANDA

The Jaishidanda has a distinctly different provenance signature from the Daling/Shumar, suggesting that the shear zone separating them is also a protolith boundary. Because the Jaishidanda is only several tens to few hundreds of meters thick and is pervasively sheared in the field, it is not possible to map discrete upper and lower bounding shear zones. However, recent geothermometric data from the LHS in eastern Bhutan obtained by the Raman spectroscopy of carbonaceous material method (Whynot et al., 2010), combined with standard geothermobarometry data (Daniel et al., 2003) indicate that there is a temperature jump in the thermal field gradient of ca. 50 °C across the lower structural boundary of the Jaishidanda, and of ca. 140 °C across the upper boundary. The upper structural boundary is mapped as the MCT (Bhargava, 1995).

However, Jaishidanda metasedimentary rocks are similar in both ϵNd signature and detrital zircon age distribution with the overlying GHS and particularly with the Chekha Group in the Ura klippe (sample BU07-5, Fig. 5.4). Considering these age signature similarities, the Jaishidanda may be age equivalent to parts of both the Chekha Group and GHS, and the overlap in ϵNd values further suggests that it may have originally been deposited proximally to GHS and/or Chekha Group protoliths.

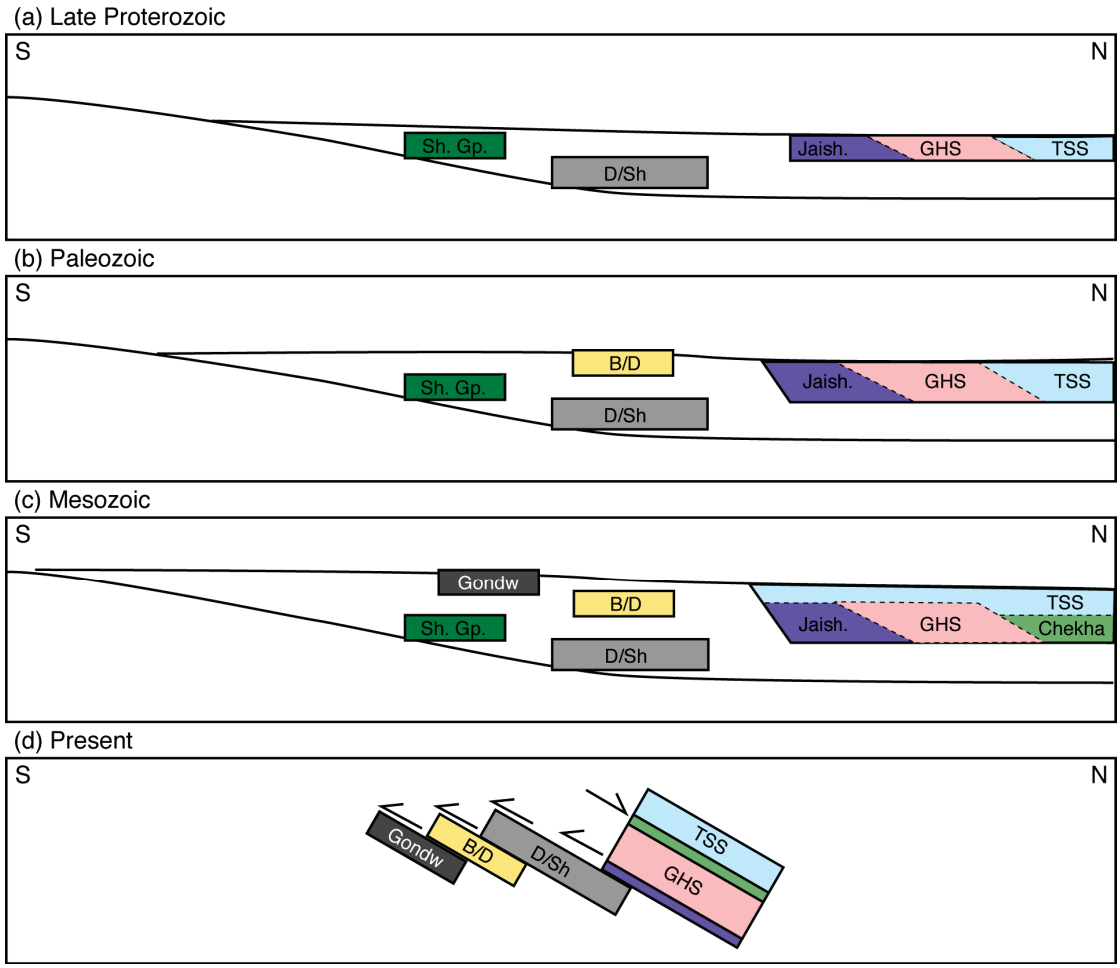

Figure 5.5: Proposed paleogeography of the main lithotectonic units of the Bhutan Himalaya since the Late Proterozoic, as interpreted from our and published ϵNd data, as well as detrital zircon signatures, lithology, and timing of structures from the literature. Sh. Gp.—Shillong Group, Jaish.—Jaishidanda Formation, D/Sh—Daling-Shumar Group, B/D—Baxa and Diuri Formations, Gondw—Gondwana Formation. Colours are according to the legend in Fig. 5.2. The location of the Shillong Group, interpreted in (a) to (c) is not shown in (d) as it is not exposed in the Bhutan Himalaya.

5.6.3 Greater Himalayan sequence

The ϵNd range for the GHS is completely overlapped by Chekha Group and Jaishidanda Formation ϵNd values, but is slightly less negative than Baxa/Diuri samples and significantly less negative than Daling/Shumar samples (Fig. 5.3; Chakungal, 2006; Richards et al., 2006; McQuarrie et al., 2008; this study). The detrital zircon age distribution for the GHS shares similarities with Chekha, Jaishidanda and Baxa/Diuri (particularly ca. 500 Ma grains), suggesting it cannot be distinguished from these units on the basis of detrital zircon signature alone.

5.6.4 Chekha and TSS

Chekha Group ϵNd values between the three klippen show overlap from -19 to -11. Thus, although lithology of the Chekha Group varies along strike (Gansser, 1983; Bhargava 1995; Koike et al., 2002; Long and McQuarrie, 2010; Chapter 2), at least the pelitic units show similar provenance characteristics across the length of Bhutan, which may indicate common source rocks in time and space during deposition of Chekha Group sedimentary protoliths, as well as deposition in a laterally-continuous sedimentary basin. Furthermore, ϵNd values in the Haimanta Group, NW India, (2000 km along-strike of the Chekha Group) also range from -19 to -11 (Miller et al., 2001), suggesting a laterally extensive basin with significant homogenization of sediments during deposition.

There appears to be a large range in depositional age for Chekha Group rocks, overlapping with both GHS and TSS depositional ages. The oldest dated TSS rocks (of depositional age 493-494 Ma) overlie Chekha Groups rocks at Wachi La in the Pele La klippe, suggesting Chekha Group rocks there were deposited before ca. 500 Ma. There are no zircons younger than ca. 800 Ma in the Ura klippe samples, also consistent with a depositional age older than 500 Ma for the Chekha Group. However, Chekha Group rocks from the Black Mountain klippe and local underlying GHS rocks have both yielded detrital zircons as young as 460 Ma (Long and McQuarrie, 2010). There are three possible explanations for this apparent contradiction:

1. Discordant U-Pb zircon ages were included in the detrital zircon age spectra, skewing the age spectra towards younger but false ages. Long and McQuarrie (2010) state that they used a 30% U-Pb discordance cut-off for their detrital zircon data, arguing that it is unlikely for more than one detrital grain to show a similar age from discordance or

inheritance and that their age peaks are determined by at least three overlapping ages. While there is no standard convention for the treatment of discordant data in detrital zircon studies, 5-10% discordance is a typical cut-off value for acceptance of data (Nemchin and Cawood, 2005). The choice of a high discordance cut-off could perhaps explain the discrepancy between paleontological vs. detrital zircon ages.

2. Young metamorphic and/or igneous rim zircon was sampled during detrital zircon core measurements, yielding mixed U-Pb ages with no geological significance. Long and McQuarrie (2010) indicate that each U-Pb measurement was examined for consistency of $^{206}Pb/^{238}U$ and $^{206}Pb/^{207}Pb$ ratios during acquisition. All analyses showing jumps or increases were discarded, which should exclude any analyses in which more than one age domain was sampled.

3. The Chekha Group, GHS and TSS all contain age equivalent units and thus, despite the evidence for deposition in a single sedimentary basin, are not in continuous stratigraphic order/position.

Long and McQuarrie (2010) argue that the absence of an obvious fault or shear zone separating the GHS, Chekha Group and TSS in the Black Mountain klippe indicates that their contacts are stratigraphic. However, this inference is inconsistent outside of the Black Mountain klippe, since Black Mountain GHS and Chekha Group samples must be younger than the TSS in the Pele La klippe, which contain 493 Ma fossils. Thus we conclude that there is a tectonic juxtaposition of original stratigraphic relationships between these three packages, and only the TSS should be considered as a continuous stratigraphic package, and defined stratigraphically. The GHS contains both Proterozoic and Paleozoic protoliths (Ahmad and Tarney, 1991 and references therein; Chakungal et al., 2010; Yin et al., 2010), and we propose that the Chekha Group may similarly contain both Proterozoic and Paleozoic protoliths, both on the basis of detrital zircon data from Bhutan (Fig. 5.4) and on the suggested Proterozoic ages of along-strike lithotectonic equivalents (e.g., Myrow et al., 2009; *in review*).

Detrital zircon ages in the Chekha Group and fossil control in the overlying TSS rocks suggest that the Chekha Group was deposited during late Neoproterozoic to Cambrian, and no earlier than late Cambrian in the Black Mountain klippe. GHS, Jaishidanda and Baxa/Diuri units also contain early Paleozoic metasedimentary rocks (their detrital zircon age spectra include populations of ca. 500 Ma grains). The consistency of ϵNd

range and detrital zircon ages (particularly at 500 Ma, 800-1200 Ma) across Chekha Group klippen and across lithotectonic units suggests that at least parts of the TSS, Chekha Group, GHS, Jaishidanda, and Baxa/Diuri LHS are time equivalent and may have been deposited during the Paleozoic within a single sedimentary basin.

5.6.5 Paleogeography of the Bhutan Himalaya

Paleoprovenance data from the central Himalaya have been shown to support a "continuous margin" origin for the LHS, GHS and TSS lithotectonic packages, and are incompatible with an "accreted terrane" or "crystalline axis" origin for the GHS (DeCelles et al., 2000; Myrow et al., 2003). The similarity in ϵNd values and detrital zircon age signatures for Baxa/Diuri, Jaishidanda, GHS, Chekha Group and TSS rocks from the eastern Himalaya provide further support for a "continuous margin" depositional model (Fig. 5.5b). Furthermore, since the GHS, Chekha Group and TSS in the Bhutan Himalaya contain age equivalent strata, original stratigraphic relationships have not been preserved (Fig. 5.5c, d). This observation has also been made in the central Himalaya (Myrow et al., 2003).

Although TSS rocks appear to be older than Chekha Group rocks across klippe (e.g., Wachi La TSS appears to be older than Black Mountain Chekha), within any particular klippe the available age data is consistent with older Chekha Group rocks underlying younger TSS rocks. These observations lead us to conclude that Chekha Group rocks are metamorphosed and deformed equivalents of the TSS. We suggest that deformation of the TSS has occurred at different stratigraphic levels along the strike of the Bhutan Himalaya for example, at higher stratigraphic level (younger rocks) in the Black Mountain klippe and lower stratigraphic level (older rocks) in the Ura klippe.

Our and published data are consistent with a "continuous margin" depositional model for the eastern Himalaya, in which Baxa/Diuri, Jaishidanda, GHS and Chekha Group/TSS rocks were all deposited in a single, extensive passive margin basin on northeastern margin of India during the Paleozoic (Fig. 5.5b). Baxa/Diuri was deposited most proximally to India, while the TSS/Chekha Group was deposited most distally (Myrow et al., 2003) and the Jaishidanda and GHS were deposited between them. Deposition of Baxa/Diuri appears to have been confined to the Paleozoic. A proximal equivalent of the Late Proterozoic rocks from the Chekha Group and GHS may be the Shilling Group, interpreted to have been deposited proximally in a passive margin on the northeastern continental margin of the Indian craton during a first rifting of India from Antarctica during

ca. 900-560 Ma (Fig. 5.5a; Yin et al., 2010).

5.6.6 THE EXTENT OF THE GHS IN THE BHUTAN HIMALAYA

Detrital zircon data, ϵNd signatures and lithology for the Jaishidanda, GHS and Chekha are notably similar, although the Chekha Group does not contain metaigneous rocks. The primary difference between these lithotectonic units is the lower metamorphic grade and concomitant lack of *in situ* leucogranitic melt in the Jaishidanda and Chekha, compared to the GHS. These data suggest that the three units originated as a single extensive protolith that has been metamorphosed and deformed to varying degrees during the India-Asia collision. While GHS rocks *sensu strictu* were buried in the mid-crust, heated, partially-melted and then returned to the surface via channel flow and extrusion, Jaishidanda Formation and Chekha Group rocks were not entrained into the mid-crustal channel, but only deformed and exhumed by the structures that bounded the extruding portion of the GHS (the MCT and the STDS, respectively). Thus, protolith boundaries of the GHS lie structurally above and below the mapped MCT and the outer STDS in the Bhutan Himalaya. As the Proterozoic and Paleozoic protolith boundaries need not be parallel to the Miocene structures and because the latter cut both up and down section, this observation may not apply elsewhere in the orogen. In addition because original stratigraphic bedding in all the units, including Chekha and Jaishidanda, has been transposed, locating these units astride a structure (e.g. STDS) may not be useful in constraining displacement along the given structure.

Geodynamic models of the Himalaya with particle tracking (e.g., Jamieson et al., 2006) suggest that displacement between adjacent points across the model MCT may be in the order of 400 km. This is probably a geologically un-testable prediction, although the difference in P-T paths and jump in peak temperatures indicate that the MCT is a first order structure, while provenance data indicate that the major stratigraphic discordance is actually structurally further down.

5.7 CONCLUSIONS

The main lithotectonic units of the Bhutan Himalaya, with the exception of the Daling/Shumar Group and Gondwana, share similar ϵNd and detrital zircon provenance signatures, suggesting deposition during the Neo-Proterozoic to Paleozoic in a single

extensive “continuous” passive margin. In the Paleozoic, the Baxa and Diuri Formations were deposited simultaneously with and more proximally to India than the Jaishidanda, GHS, Chekha Group and TSS. In the Late Proterozoic, the Shillong Group (Yin et al., 2010) may have been deposited simultaneously with and more proximally to India than the Jaishidanda Formation, GHS and Chekha Group.

Age equivalent rocks in the GHS, Chekha Group and TSS indicate that original stratigraphic relationships have been disrupted, probably due to deformation and displacement along the STDS.

Similarities in provenance signatures and lithology between the GHS, Jaishidanda Formation and the Chekha Group suggest a common GHS protolith, in which case the STDS and MCT structures in the Bhutan Himalaya do not occur at protolith boundaries.

CHAPTER 6

DISCUSSION AND TECTONIC IMPLICATIONS

6.1 SOUTH TIBETAN DETACHMENT SYSTEM IN BHUTAN

6.1.1 THESIS PROBLEM

The scientific problem stated at the outset of this thesis (§1.4.1) is "The crustal-scale STDS has a normal sense of displacement, but developed within a compressional tectonic regime, challenging traditional concepts of orogenesis. In the eastern Himalaya of Bhutan, the STDS appears to be duplicated. What is the tectonic history of the duplicated STDS in the eastern Himalaya; can it be explained by or used to constrain models of Himalayan orogenesis, and; what are the implications of a duplicated STDS for the evolution of the Himalayan orogen in general?" Specific objectives were formulated in §1.4.2 to answer the above questions:

1. Determine the timing and cooling history of the STDS
2. Characterize the structure and metamorphic field gradient across the STDS
3. Establish pressure-temperature-time paths for tectonites across the STDS
4. Determine the paleo-geographic affinity of the Chekha Group.

Objective 1 was pursued in Chapter 2, in which the tectonic history of the duplicated STDS was determined by U-Pb dating of zircon and $^{40}Ar/^{39}Ar$ dating of muscovite in leucogranites deformed by both fault systems. Objective 2 was investigated in Chapters 3

and 4, in which the metamorphic field gradient across the outer STDS was determined using thermobarometry and thermometry techniques, and the structure of the STDS and its upper crustal hanging wall were described. In Chapter 3, P-T-t paths of tectonites deformed in the older outer STDS were established, as proposed in objective 3. Objective 4 was explored in Chapter 5, in which new and published ϵNd data and published detrital zircon U-Pb age data were compiled to constrain the paleo-geographic affinity of the Chekha Group.

During the above researches, I introduced new nomenclature for the duplicated STDS in Bhutan. I also suggested that the usefulness of "upper" and "lower" nomenclature is limited for understanding the structures that make up the STD system, and proposed that the STDS can rather be described as comprising three types of low-angle normal-sense detachments (LANDs): channel LANDs, extrusion LANDs and destabilization LANDs. These concepts are expanded below in §6.1.2-6.1.5 and in §6.2.

The tectonic history of the STDS in Bhutan has been described in some detail in Chapters 2-5. Below in §6.3, I discuss these data and conclusions in the more regional context of the eastern Himalaya. As described in Chapter 3, channel flow models that produce dome extrusion above a crustal ramp are compatible with P-T-t paths of tectonites in the Bhutan STDS. In §6.3-6.4, these model data are employed to examine the implications of a duplicated STDS for the evolution of the Himalayan orogen in general.

6.1.2 Review of definitions and concepts

The STDS is composed of one to several structures. These structures have been generally referred to as "upper" and "lower" structures within the STDS (Fig. 6.1a). Below I expand on the terminology of the STDS with regards to the duplicated STDS in Bhutan, as well as the characterization of and possible tectonic processes that lead to the formation of "upper" and "lower" STDS structures.

In Chapter 2, I introduced a new nomenclature for the STDS in Bhutan: "outer STDS" for the ductile shear zone exposed at the base of synformal klippen of Chekha Group and TSS rocks and; "inner" STDS for the network of ductile shear zones and brittle faults exposed at the northern margin of Bhutan. This nomenclature, unique to Bhutan, was required for the following two reasons:

(1) The STDS as first described (Burchfiel et al., 1992) is composed of one to several structures (Godin et al., 2006). Collectively, these structures exhibit an increase in

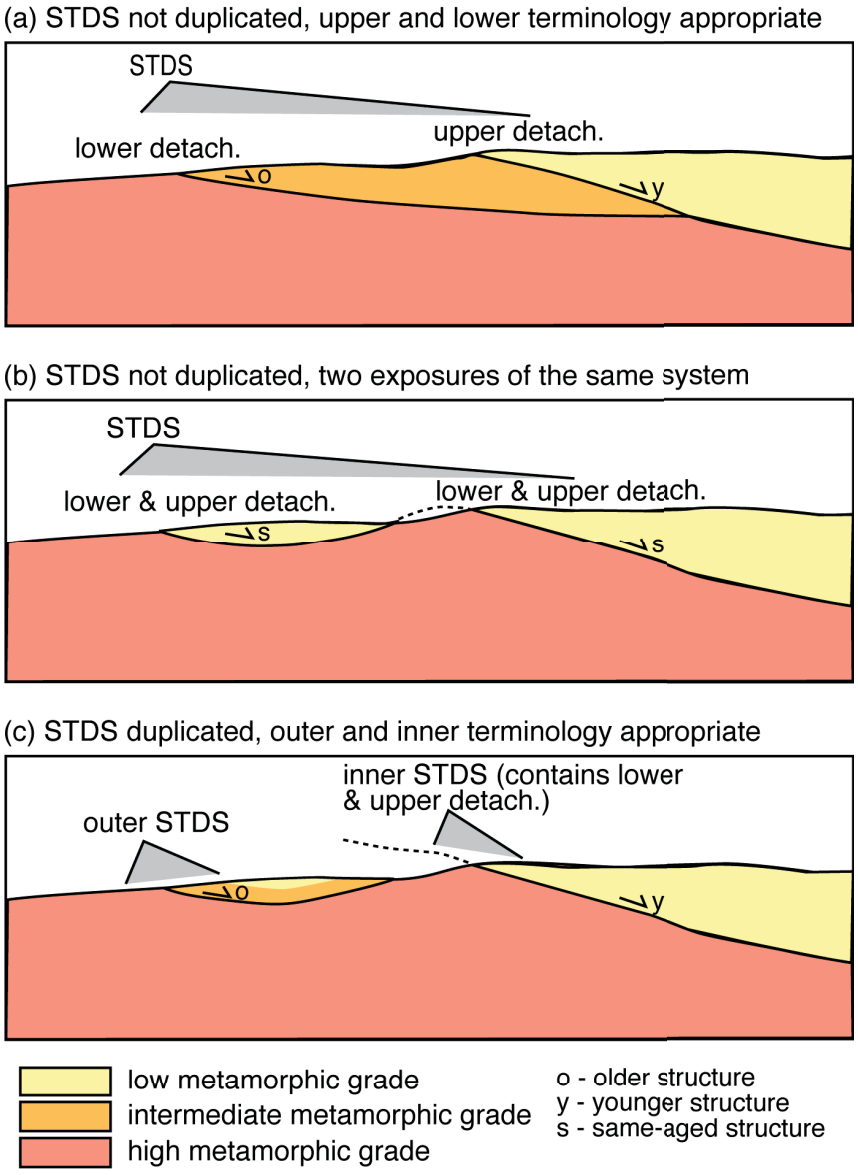

Figure 6.1: Schematic diagrams of the STDS. (a) Upper and lower components of the STDS. The upper detachment is younger and steeper than the lower detachment, and metamorphic grade systematically increases up-section across the STDS. (b) The STDS has a ramp-flat geometry, or has been folded, and intersects the surface more than once, producing a klippe of upper-crustal rocks. The STDS is the same age everywhere it is exposed, and upper and lower detachments similar to those in (a) may be present at each intersection with the surface. (c) The STDS intersects the surface more than once, producing klippe of upper-crustal rocks. The lower detachment in the outer STDS is older than the lower detachment in the inner STDS. There is no upper detachment in the outer STDS. Grey shading delimits the width of the STDS.

metamorphic grade from hanging wall to footwall, such that within the STD "system" of structures, the footwall of the lowermost structure contains the highest metamorphic grade rocks and the hanging wall of the uppermost structure contains the lowest metamorphic grade rocks (e.g., Fig. 6.1a). This is not the case for the STD structures in Bhutan. Both the outer and the inner STDS preserve low- to unmetamorphosed rocks in the hanging wall and high-grade metamorphic rocks in the footwall, such that metamorphic grade does not systematically decrease from the footwall of the outer STDS to the hanging wall of the inner STDS. However, within each set of structures, metamorphic grade does systematically increase from footwall to hanging wall (Fig. 6.1b, c).

(2) One could then argue that the duplicated STDS in Bhutan is one continuous detachment system that has a ramp-flat geometry or has been folded (e.g., Fig. 6.1b). The outer STDS could be an up-dip flat (now folded) while the inner STDS is a ramp, and the observed repetition of the STDS is due to the interaction of topography with structure. However, the distinct difference in duration of ductile shearing along the two structures, demonstrated by U-Pb dating of zircons in deformed leucogranites (Chapter 2), indicates that this is not the case (Fig. 6.1c). Furthermore, the lack of brittle structures overprinting ductile fabrics in the outer STDS compared to the major brittle faults described from the inner STDS indicates that these two sets of structures, though they may have been originally contiguous, have experienced a very different tectonic history since the mid-Miocene. Thus, I conclude that lower and upper STD terminology as it has been used in the literature does not describe the duplication of the STDS in Bhutan. It can, however, be used to describe the individual structures within the outer STDS and within the inner STDS. In Chapter 4, I attributed the upper and lower structures of the STDS, with their distinct structural characteristics, to different tectonic processes. This is expanded below in §6.1.3.

6.1.3 Upper vs. lower STD structures

The STDS comprises one to several LANDs. In general, the lowermost structure is a mylonitic ductile shear zone with migmatite in the footwall and metasedimentary rocks in the hanging wall, and the uppermost structures are ductile-brittle to brittle faults (e.g., Burchfiel et al., 1992). These characteristics were not explicitly stated for, but are useful in, describing the lower and upper STD (Godin et al., 2006a). In Chapter 4, I used RSCM geothermometry data and structural data to show that there is currently no evidence of

brittle faulting or an "upper" STD within the outer STDS (Fig. 6.1c). In comparison, the inner STDS can be described as a "lower" STD ductile shear zone (active < 12 Ma (Chapter 2)) that has been cut by more recent "upper" STD ductile-brittle faulting (Gonto La detachment of Edwards et al., 1996; Edwards et al., 1999) (Fig. 6.1c). Researchers have noted the absence of Paleozoic and Proterozoic rocks in the hanging wall of the inner STDS (e.g., Burchfiel et al., 1992; Edwards et al., 1996). I suggest that this is due to cutting of the "upper" STD structure down section through the "lower" folded, mylonitic STD structure (e.g., Fig. 6.1a).

6.1.4 North Himalayan gneiss domes

To the north of Bhutan, high-grade metamorphic rocks are exposed in antiformal gneiss domes mantled by up to staurolite-kyanite grade Paleozoic metasedimentary rocks, such as the Yala Xiangbo dome to the northeast (e.g., Aikman et al., 2004), Kangmar dome (e.g., Lee et al., 2000) and Kampa dome (e.g., Quigley et al., 2006) to the northwest, and several others further to the west. Geophysical data suggest that the STDS may resurface at the location of the antiformal domes (Hauck et al., 1998).

Shear fabrics in the Kangmar dome preserve either top-to-the-north (Kangmar detachment of Chen et al., 1990; Aoya et al., 2006) or both top-to-the-south and top-to-the-north flow shear-sense with a significant component of pure shear (Lee et al., 2000) that overprints an early south-directed shortening fabric. The ductile shear fabric was deformed by doming and exhumation of the gneiss, which has produced an extensional fabric. Extension in the Kangmar Dome may (Chen et al., 1990) or may not (Lee et al., 2000) have generated one or conjugate LANDs. In the Kampa dome, conjugate top-to-the-north and top-to-the-south LANDs on the northern and southern limbs of the dome, respectively, overprint and dip more steeply than the earlier mylonitic top-to-the-north fabric (Quigley et al., 2006). The ductile shear and overprinting structures described from the Kampa and Kangmar domes are reminiscent of the "lower" and "upper" STD, but the conjugate nature of the overprinting brittle faults is distinct from the north-dipping "upper" STD faults further south.

6.1.5 Channel flow and LANDs

There are three types of LANDs that make up the STDS in the eastern Himalaya: a near-horizontal diffuse top-to-the-north ductile shear zone; a network of shallowly-dipping

discrete top-to-the-north shear zones and faults and; conjugate north and south-dipping low-angle normal faults. All were produced across-strike from one another during the Miocene, coeval with lithospheric contraction, and coeval with strike-parallel thrusts.

Although not explicitly designed to reproduce them, some numerical models of channel flow produce complex LAND structures analogous to those observed in the eastern Himalaya, suggesting that the kinematics of their formation may be the direct result of mid-crustal channel flow. During channel flow, mid-crustal rocks tunnel and flow laterally within the orogen unless/until they are exhumed to the surface by focused erosion (Beaumont et al., 2004). Modeling results indicate that, if sufficiently weak, the upper crust above an orogenic channel can destabilize. This separation results in the passive pro-ward transport of upper crustal material (including the upper boundary of the channel), giving rise to local extension in the upper crust, despite overall lithospheric shortening (Beaumont et al., 2004).

Tectonites from a mid-crustal channel boundary may be exhumed by focused erosion without extrusion, exhibiting little deformation above the brittle/ductile transition zone, and preserving a near-horizontal ductile shear zone separating mid-crustal rocks and anatectite from upper-crustal rocks. Here I define extrusion as the focused exhumation of a paleo-channel between discrete faults or shear zones, driven by channel flow at depth and erosion at the surface, as suggested by Godin et al. (2006a). I propose that channel flow has produced the outer STDS in Bhutan, and the mylonitic LAND in the inner STDS (channel LAND; Fig. 6.2b).

If paleo-channel rocks are extruded to the surface, discrete ductile-brittle and brittle normal fault structures will cut down-section into the paleo-channel, overprinting the ductile structures and cutting out part of the channel LAND structure (extrusion LAND; Fig. 6.2b). This may be analogous to the structures of the inner STDS in Bhutan.

Doming of the channel due to destabilization of the upper crust above a ramp on the basal detachment can exhume paleo-channel material along conjugate low-angle detachments due to local extension of the upper crust. I suggest that top-to-the-north shear zones and conjugate extensional faults in the Kangmar and Kampa domes correspond to channel flow and destabilization LANDs, respectively (Fig. 6.2b).

Figure 6.2: Interpreted cross-sections of the eastern Himalaya. (a) Cross-section through $\sim$90° E showing the main structures of the eastern Himalaya and their timing, the metamorphic grade of rocks exposed at the surface, and interpreted exhumed channel material. [1]Stüwe and Foster, 2001; [2]Meigs et al., 1995; [3]Chapter 2; [4]Burg et al., 1984b; Ratschbacher et al., 1994. Dashed lines indicate dominant foliation of rocks at the surface, and interpreted flow lines of channel material (b) Interpreted locations of channel flow, extrusion and destabilization LANDs in the eastern Himalaya, and the location of Chekha Group rocks relative to these structures. Arrows show relative displacement across faults and shear zones. Cross-hatching - Miocene leucogranites.

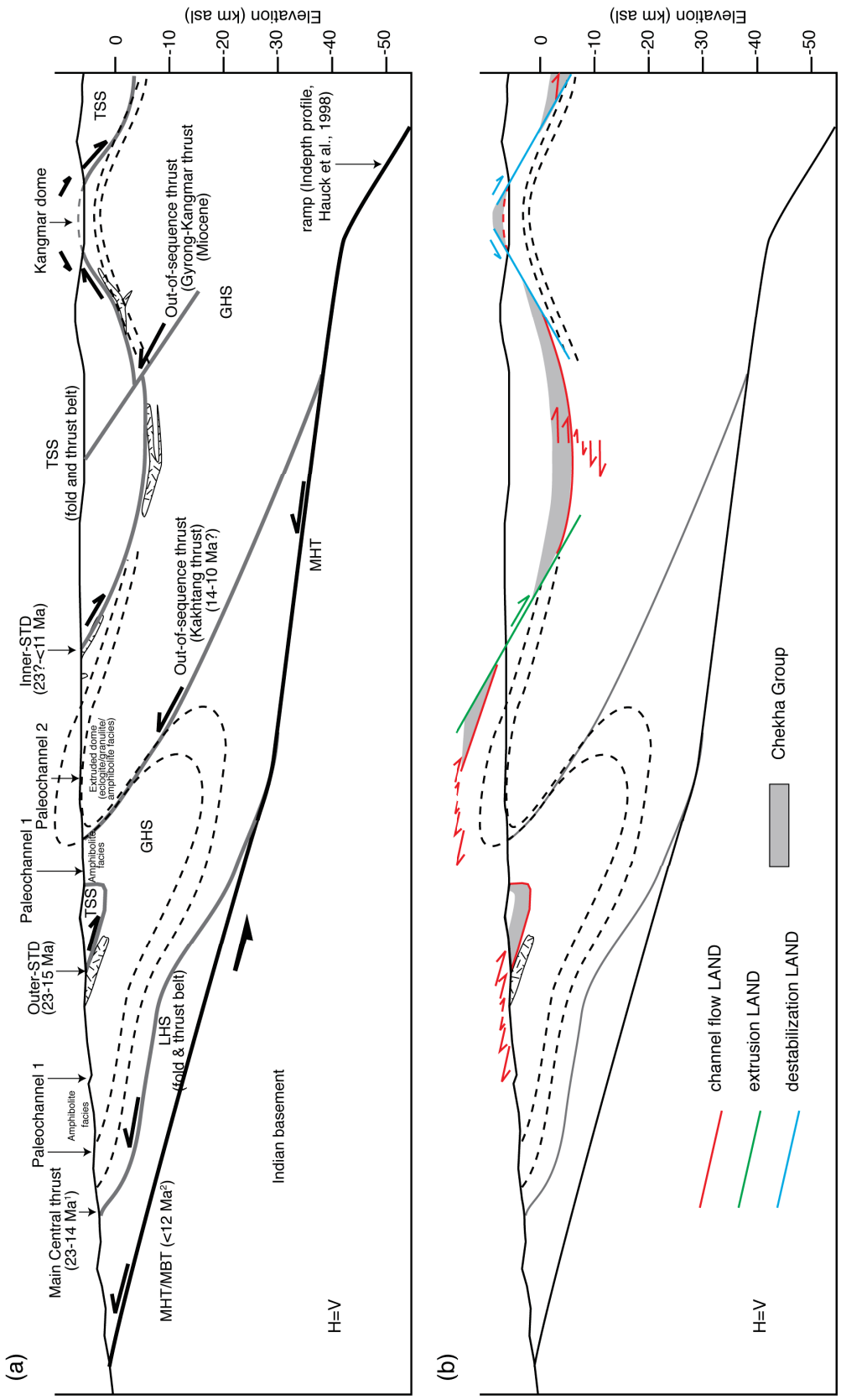
(a)
(b)
Elevation (km asl)
0
-10
-20
-30
-40
-50
Kangmar dome
TSS
TSS
(fold and thrust belt)
Out-of-sequence thrust
(Gyrong-Kangmar thrust
(Miocene)
GHS
ramp (Indepth profile,
Hauck et al., 1998)
Inner-STD
(23?-<11 Ma)
Out-of-sequence thrust
(Kakhtang thrust)
(14-10 Ma?)
MHT
Paleochannel 2
Extruded dome
(migmatite gneiss/
amphibolite facies)
Paleochannel 1
Amphibolite
facies
GHS
TSS
Outer-STD
(23-15 Ma)
LHS
(fold & thrust belt)
Paleochannel 1
Amphibolite
facies
Main Central thrust
(23-14 Ma[1])
MHT/MBT (<12 Ma[2])
Indian basement
H=V
channel flow LAND
extrusion LAND
destabilization LAND
Chekha Group
H=V

6.2 South Tibetan detachment system LANDs

There are several well-described sections of the STDS outside Bhutan, including NW India, central Nepal, Everest, and the Dzakaa Chu and Dinggyê areas which border the Ama Drime massif (Fig. 6.3). In each of these sections, the STDS can be described in terms of channel and extrusion LANDs.

Dèzes et al (1999) described the Zanskar shear zone (STDS) in the northwest Himalaya between ~77-78° E as a 1-km thick shear zone dipping 20° to the northeast. The shear zone preserves a right-way-up metamorphic succession from kyanite- to biotite zone. The footwall is characterized by migmatites and leucogranite intrusion. Shear sense indicators preserve evidence for an early thrust sense of displacement overprinted by normal-sense shear. Leucogranites penetrate and are deformed within the shear zone. The ductile shear zone is overprinted by minor brittle faults, such as the Sarchu fault, that cut down-section into the Zanskar shear zone at high angle (50-70°). The Zanskar shear zone fits the criteria of a channel LAND. The overprinting brittle structures are steeper than LANDs, but otherwise are characteristic of extrusion LANDs, and thus are interpreted to be near surface faults that facilitate extrusion of the channel LAND.

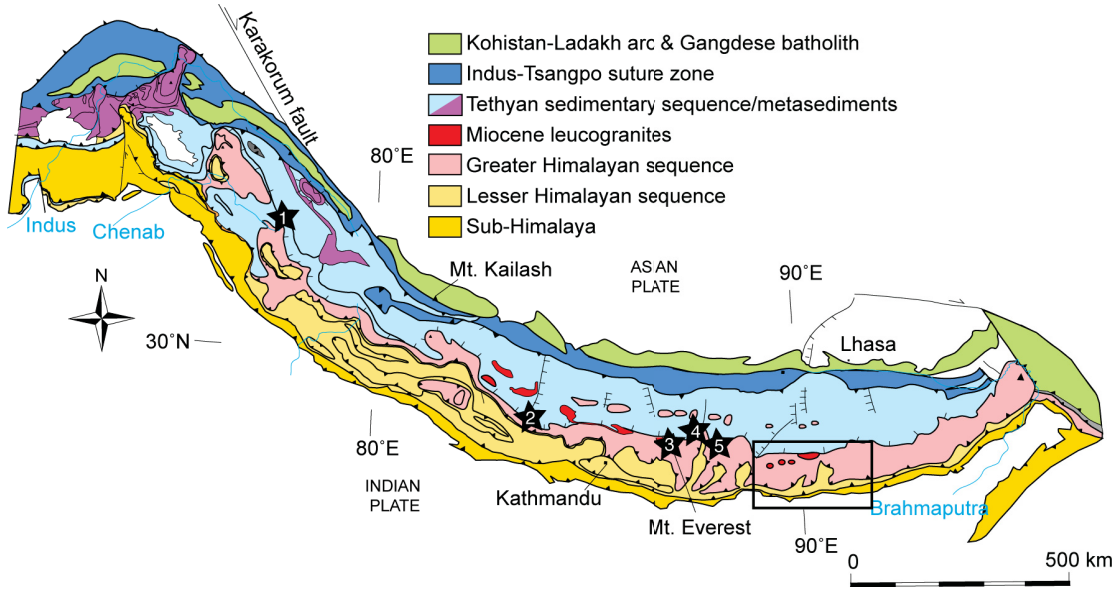

Figure 6.3: Geological map of the Himalayan orogen (from Guillot et al., 2008). The map shows well-characterized sections of the STDS outside of the study area. 1. NW India, 2. Central Nepal, 3. Everest, 4. Dzakaa Chu, 5 Dinggyê. Study area is boxed.

In central Nepal, the Chame detachment (also Deorali and Annapurna detachments)

is a normal-sense, low-angle ductile shear zone that separates North Col Formation marbles in the hanging wall from GHS calc-silicates in the footwall (Hodges et al., 1996; Coleman and Hodges, 1998; Searle and Godin, 2003; Searle, 2010). The shear zone is characterized by a gradual and continuous upward decrease in metamorphic grade, and leucogranite intrusion. The Chame detachment is cut by a younger and structurally higher network of ductile to brittle faults, the Phu detachment (also Machhupuchhare detachment). The Phu detachment dips $< 30^{\circ}$ towards the north-northeast, and separates metasedimentary rocks in the footwall from unmetamorphosed TSS sedimentary rocks in the hanging wall. In places, the Phu detachment places TSS rocks on high-grade gneisses, although it is unclear from the published data whether the Phu detachment cuts down-section. The Chame detachment is here interpreted as a channel LAND, while the Phu detachment is interpreted as an extrusion LAND.

In the Everest region of eastern Nepal and southern Tibet, the STDS comprises two LANDs: the structurally lower Lhotse detachment and the structurally higher Qomolongma detachment (Burchfiel et al., 1992; Carosi et al., 1998; Searle et al., 2003; Jessup et al., 2008). The Lhotse detachment is described as a very shallowly-dipping $\sim$1 km thick ductile LAND that deforms footwall gneisses and sheet-like intrusions of leucogranite and hanging wall amphibolite-facies metasedimentary rocks. Metamorphic grade gradually decreases up-section across the shear zone. The Qomolongma detachment is ductile-brittle, and places weakly metamorphosed TSS rocks in the hanging wall against metasedimentary Everest Series rocks in the footwall. The structure dips slightly more steeply ($\sim$15°), post-dates and cuts down-section into the Lhotse detachment. The Lhotse detachment is here interpreted as a channel LAND, while the Qomolongma detachment is interpreted as an extrusion LAND.

To the north-east and $\sim$50 km down-dip from Mt. Everest, the STDS is exposed in the Dzakaa Chu (Cottle et al., 2007). Here it comprises a single, diffuse ductile shear zone $\sim$1 km thick, with high-metamorphic grade GHS gneisses in the footwall and unmetamorphosed TSS rocks in the hanging wall. Although small, steeply northeast-dipping brittle faults overprint the ductile fabric, there is no overprinting structure present capable of accommodating significant displacement. This section of the STDS bears similarity to the outer STDS in Bhutan, in that it comprises a single channel LAND with no overprinting extrusion LAND. This channel LAND section of the STDS appears to

have been exhumed by major, late NS-striking extensional structures such as the Ama Drime detachment, rather than by an extrusion LAND.

The next described exposure of the STDS to the east, in the Dinggyê area east of the Ama Drime massif, is up-dip of the Dzakaa Chu exposure, and bears greater similarity to the Everest section. The STDS here is characterized by two north-dipping LANDs: a lower diffuse ductile shear zone characterized by an up-section decrease in metamorphic grade (Dinggyê detachment of Burchfiel et al., 1992; STDsz of Kali et al., 2010 and Leloup et al., 2010) and an upper brittle fault with an unmetamorphosed hanging wall (Saer detachment of Burchfiel et al., 1992).

6.3 Tectonic history of the eastern Himalaya

Here the tectonic history of the eastern Himalaya is summarized, based on the results and conclusions of the research chapters of this thesis and published literature, and guided by thermodynamical numerical models of continental collision. The relevant chapters are cited, and the reader is directed to those chapters for detailed reviews of the additional published literature incorporated into this summary.

Paleoprovenance data (Chapter 5) indicate that the main lithotectonic units of the eastern Himalaya were probably all deposited within a single extensive passive margin on Indias northern flank, with the exception of Protorozoic LHS Shumar and Daling rocks, which are the oldest sedimentary rocks deformed by the Himalayan orogen, and have a distinct depositional history. The initial position of the Proterozoic LHS relative to the sedimentary rocks of the other main units (the Paleozoic LHS, Jaishidanda Formation, GHS, Chekha Group and TSS) is unknown, but presumably beneath, craton-ward or both.

Following the onset of continental collision in the Eocene, the more distal components of the passive margin, the TSS and Chekha Group, were shortened and thickened into a south-directed fold and thrust belt (Chapter 4), and probably thrust over the GHS, which experienced burial and prograde metamorphism during the Oligocene (Chapter 3). Following thickening and thermal maturation of the crust, partial melting initiated within the mid-crust (Chapter 2), lowering its viscosity relative to the upper and lower crust. Gravitational potential between the thickened crust beneath the Tibetan plateau and Himalayan orogen and the thinner Indian foreland induced a lateral channel flow of mid-crustal material away from the plateau and towards the orogenic front in the Miocene, producing a

normal sense of shear in the upper part of the channel (channel LAND) and a thrust sense of shear in the lower part of the channel.

Focused erosion on the southern flank of the orogen facilitated extrusion of mid-crustal rocks (Paleochannel 1, Fig. 6.2a). In early Miocene, a frontal ramp on the basal detachment propagated into the orogen. This ramp produced an antiform in the overlying channel, which, after bypassing the ramp, rolled forward and overthrust earlier channel material (Paleochannel 1), producing the out-of-sequence Kakhtang thrust (in places expressed at the surface as a fault propagation fold with a blind out-of-sequence thrust at depth). This process detached the upper crust, deactivating the now outer STDS, and causing Chekha Group and TSS rocks in the hanging wall of Paleochannel 1 to be passively translated together with the GHS towards the foreland on the MHT since ca. 15 Ma. At the line of detachment, extrusion of Paleochannel 2 followed between the Kakhtang and inner STD structures until late Miocene, exhuming deeper and hotter rocks than in Paleochannel 1. All strands of the STDS in the eastern Himalaya appears to have ceased activity by 10 Ma, at which time extension had initiated along NS-striking faults, offsetting STDS structures (Chapter 2 and references therein; Leloup et al., 2010; Kali et al., 2010).

Meanwhile, the ramp continued to propagate into the orogen, producing a second antiform of channel material. Upper crust north of the STDS and above the channel was still translated towards the foreland but varying rates of motion north and south of the antiform may have caused destabilization and detachment of the upper crust (conjugate LANDs). Destabilization produced a local low pressure area towards which channel material flowed, producing a string of domes along the North Himalayan antiform. Some authors suggest that the Gyirong-Kangmar thrust (Fig. 6.2a) may have also contributed to exhumation of the domes (e.g., Lee et al., 2000). The domes did not bypass the ramp, so they did not roll forward and overthrust Paleochannel 2.

The tectonic history described above shares many features with channel flow model HT 111 (Jamieson et al., 2006). Time steps of HT 111 between **10.5** and **0.0 Ma** (where model **Ma**, shown in bold, is millions of years before model end, with collision beginning at **54 Ma**) are shown in Figure 6.4. These snapshots illustrate the development of model structures analogous to the main structures of the eastern Himalaya: MCT, outer and inner STD, KT, Gyirong-Kangmar thrust, and Kangmar dome, and also produces late buckling of rocks between the MCT and inner STD (Chapter 4). The timing of events in this model

predicts tectonic reorganization of the STD and development of the KT and inner STD in latest Miocene, ca. **9 million years** after these structures developed in nature (Fig. 6.4). However, the relative timing of structures is well-reproduced in HT 111. For example, the MCT and STDS were already active by 19.5 Ma, the outer STD became inactive at ca. 15 Ma, and the Kangmar dome formed by ca. 13 Ma. The discrepancy in absolute timing could be the result of differences in convergence and/or erosion rates between HT 111 and nature, which I explore below in §6.4.

HT 111 also accurately predicts the presence of a crustal ramp on the MHT approximately beneath the Kangmar dome. It can be observed in the final two time steps that once the crustal ramp advances as far into the orogen as the Kangmar dome, it remains more or less fixed in place relative to the dome, although material continues to propagate through the ramp and entrain into the active channel (note the red material line in Fig. 6.4e, f). This prediction of a strong crustal ramp will be discussed in §6.4.

6.4 Along-strike variations in structure of the Himalayan orogen

I have demonstrated that the present day geometry of the Bhutan Himalaya can be explained by propagating a crustal ramp on the basal detachment into the orogen. However, outstanding questions remain: how was this ramp produced and what is its lateral extent? Which of the along-strike differences of the Himalayan orogen can or cannot be explained by a crustal ramp? Features of the Himalayan orogen that exhibit along-strike difference include: metamorphic grade of the GHS - greenschist-facies in NW India, upper amphibolite-facies in the central Himalaya, and up to granulite-facies in the eastern Himalaya; increasing separation of the surface traces of the STD and MCT (and hence greater surface exposure of the GHS) towards the east; an apparent increase in size and decrease in age of Miocene granite bodies at the top of the GHS from west to east; emergence of the Himalayan gneiss domes east of 85° E (and particularly east of 87° E); and duplication of the STDS in the Bhutan Himalaya (e.g., Vannay and Hodges, 1996; Grujic et al., 2002; Steck, 2003; Kohn, 2008; Cottle et al., 2009; Corrie et al., 2010; Warren et al., *in review*).

Previous studies articulating similar along-strike tectonic variability in the Himalaya have proposed that it can be explained by: (1) along-strike increase in convergence rate

Figure 6.4: Time steps of thermomechanical model HT 111 (Jamieson et al., 2006; R.A. Jamieson pers. commun.) with model run time indicated on the left (**0 Ma** is end of model run, with collision beginning at **54 Ma**). The horizontal red bar indicates both amount of convergence relative to total convergence (2693 km) and time relative to total model run time (**54 million years**). H = V. Depth and horizontal distance are in kilometers. Interpreted cross-sections on the right show upper-crustal material in grey, a red vertical line is a marker horizon on the underthrust plate. Interpreted outer STDS (O-STDS), MCT, inner STDS (I-STDS), Kakhtang thrust (KT), Kangmar dome (KD), foreland fold and thrust belt (FTB) and Gyirong-Kangmar thrust (GKT) structures are indicated. Model times are clearly younger than actual timing of structures, however, shifting the time by 9 Ma, the relative timing of development of structures appears to be compatible with model HT 111. A crustal ramp that is situated beneath the extruding channel in (a) propagates into the orogen from **10.5 Ma** to $\sim$**5 Ma**.

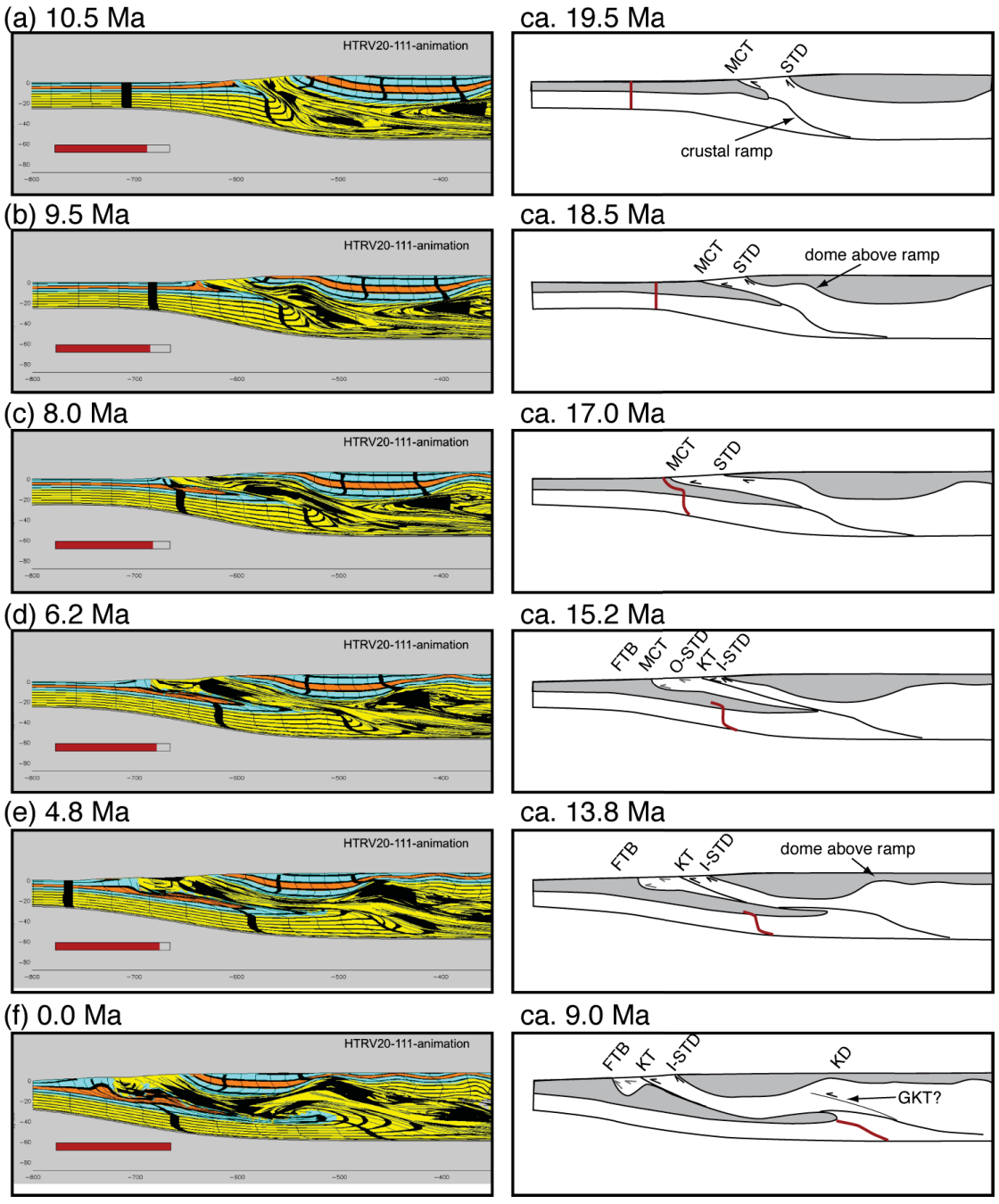
(a) 10.5 Ma
HTRV20-111-animation
ca. 19.5 Ma
MCT
STD
crustal ramp
(b) 9.5 Ma
HTRV20-111-animation
ca. 18.5 Ma
MCT
STD
dome above ramp
(c) 8.0 Ma
HTRV20-111-animation
ca. 17.0 Ma
MCT
STD
(d) 6.2 Ma
HTRV20-111-animation
ca. 15.2 Ma
FTB
MCT
O-STD
KT
I-STD
(e) 4.8 Ma
HTRV20-111-animation
ca. 13.8 Ma
FTB
KT
I-STD
dome above ramp
(f) 0.0 Ma
HTRV20-111-animation
ca. 9.0 Ma
FTB
KT
I-STD
KD
GKT?

(and hence total amount of convergence) since the Eocene from east to west (e.g., Guillot et al., 1999; Yin et al., 2006); (2) along-strike increase in exhumation rate since the Eocene from east to west (e.g., Webb et al., 2007); (3) I additionally consider whether the observed variability could be explained by variability in the pre-collision rheology and/or geometry of the Indian margin. It has been further suggested that the interaction of the Karakorum fault with the Himalayan orogen may explain some of the above described variability, particularly the age and abundance of leucogranites (Leech, 2008). That hypothesis has been critiqued elsewhere (e.g., Parrish, 2009; Searle and Phillips, 2009), and will not be addressed here.

(1) The convergence rate between India and Asia is typically reported as having slowed in the Eocene from ca. 15-20 cm/yr to ca. 5 cm/yr (e.g., Klootwijk et al., 1992), presumably due to collision of the Indian continent with Asia. However, recent reconstructions of the Indian plate determined from relative plate motions of neighbouring plates during the Cenozoic indicate that after this rate change, convergence rates in the easternmost Himalaya may have been consistently 1.3-1.4 times greater than in the westernmost Himalaya throughout the remainder of the Cenozoic (Molnar and Stock, 2009). Converting these rates to values of total convergence, they suggest $\sim$1000 km more total convergence in the eastern compared to the western Himalaya over 54 million years ($\sim$3500 vs. $\sim$2500 km, respectively). If these rates are correct, the eastern Himalaya has accommodated up to 1000 km more lithospheric shortening than the west.

Heat transport in Model HT 111 is dominated by advection due to a high thermal Péclet number, or ratio of heat advection over diffusion (Turcotte and Schubert, 1982). Thus, the different time steps plotted for model HT 111 in Fig. 6.4 may be broadly analogous to different amounts of total convergence and hence different convergence rates (model HT 111 has a fixed convergence of 5 cm/yr; Jamieson et al., 2006). In that case the effect of different amounts of convergence on orogen structure can be hypothesized. In Figure 6.4a, total convergence is $\sim$2150 km, while in Figure 6.4f, total convergence is $\sim$2700 km. There is a significant change in orogen structure between these two time steps, as most of the structures characteristic of the eastern Himalaya have not developed at time step (a), while they are all present at time step (f). In fact, time step (a) is similar in structure to the present day central Nepal Himalaya (e.g., Hodges et al., 2001), while time step (f) is similar to the present day Bhutan Himalaya (Fig. 6.2). I interpret this

observation to reflect that, without invoking any special geometry or physical properties for the subducting Indian crust, a faster convergence rate or greater total convergence will afford less time for the subducting crust to thermally equilibrate. In model HT 111, thermal equilibration to partial melt conditions ($>$700 °C) requires ca. 20 Myr (Beaumont et al., 2004; Jamieson et al., 2006). Colder basement can produce a "thermal" ramp on the basal detachment. If the basement ramp is thermally controlled by convergence rates, it is expected that its prominence would gradually decrease westward, disappearing completely at about central Nepal.

(2) There is no conclusive evidence that cumulative erosion in the eastern Himalaya has been significantly greater that in the west. However, the difference in exposed metamorphic grade of the GHS along strike indicates that rocks in the east have been exhumed from greater depths than rocks in the west. Erosion rates in nature depend on several geological and climatic factors that are spatially and temporally variable, including river incision rates, rock erodibility, precipitation, glaciation, etc. In model HT 111, erosion rate is controlled by local surface slope and a spatial climate function which simulates orographic precipitation on the pro-ward side of the model orogen (e.g. Jamieson et al., 2002). A steeper pro-ward model slope leads to a higher erosion rate at that slope, which in turn can localize deformation by removing colder near-surface rocks and replacing them with hotter rocks, and a positive feedback between erosion rate and tectonic processes results (e.g., Willett, 1999b). Assuming plane strain in the Himalayan orogen, a higher rate of convergence, different precipitation pattern, or a number of other factors may have resulted in steeper local slopes in the eastern Himalaya, which in turn led to higher focused erosion rates. In this case the above argument regarding convergence rates may equally apply to an along-strike difference in erosion rates throughout the duration of the Himalayan orogeny.

(3) A ramp on the basal detachment could also be formed due to variability in the pre-collision rheology and/or geometry of the Indian plate. The ramp interpreted beneath the Kangmar dome from INDEPTH geophysical data has a relief of $>$ 20 km. It is possible that the ramp is the pre-collision rifted northern continental margin of India. In turn, the structure of the Indian continental crust may have included relatively weak (shale or quartzite) and relatively strong (e.g., basement gneiss or granitoid) units. Subduction of relatively strong crust behind relatively weak crust could also produce a ramp on the basal detachment. The extent of the ramp would then depend on the structure and/or

geometry of Indian continental crust, and need not be a function of convergence or erosion rates. In numerical models, laterally-variable crustal strength in a subducting plate during continental collision has been shown to result in the uplift and expulsion of ductile nappes that are transported over the indenting lower plate (Jamieson et al., 2007).

While (1) and (2) predict a gradual disappearance of a ramp along strike to the west, as a function of the decreasing rate of convergence and/or erosion, the basal detachment structure suggested in (3) could have a range of geometries, and could disappear abruptly or gradually towards the east and west along lateral ramps.

Characteristics of the eastern Himalaya that can be explained by underthrusting of a crustal ramp include: higher metamorphic grades in the east (extruded in paleochannel 2); increasing separation of the surface traces of the STDS and the MCT (due to out-of-sequence thrusting within the GHS, increasing its apparent thickness); a decrease in age of Miocene leucogranite bodies (due to more rapid extrusion of anatectite, and by exhumation of younger parts of the channel), and emergence of the North Himalayan gneiss domes.

Importantly, while the above features are present across several hundred kilometers of strike, the out-of-sequence KT appears to be local to Bhutan. The KT, if present regionally, may be difficult to identify, as in its predicted along-strike surface trace it should place gneiss on gneiss. Goscombe et al. (2006) described a zone of mylonite within the GHS in eastern Nepal which they termed the High Himal thrust, and which they predicted is laterally continuous with the KT. Alternatively, it was suggested in Chapter 2 that the KT may die out laterally, continuing to the east and west of its mapped extent as a blind thrust beneath a fault propagation fold. A third possibility is that the KT is not of regional importance, and does not play a significant role in the tectonic history of the eastern Himalaya. Further mapping and detailed P-T-t transects across the GHS between eastern Nepal and central Bhutan are required to determine the true extent of the KT and the High Himal thrust.

Likewise, the outer STDS appears to be local to Bhutan. As discussed in Chapter 2, there is little evidence for similarly preserved segments of the STDS elsewhere in the Himalayan orogen, and particularly not in the eastern Himalaya, where the above described tectonic history predicts it may have formed. I suggest that this is a result of special preservation. At least part of Bhutan has been sheltered since Late Miocene from intense erosion caused by the Indian monsoon by uplift of the Shillong plateau (Grujic et al.,

2006). The plateau created a rain shadow, resulting in a decrease in precipitation and thus decrease in erosion rates, preserving a higher erosion level than areas to the east and west of Bhutan. This attenuation in erosion combined with post-11 Ma buckling of the Bhutan Himalaya, allowed for the preservation of the outer STDS and upper crustal rocks in structural depressions.

6.5 FUTURE WORK

Three types of syn-convergent LANDs were described in this thesis. Channel LANDs require a mid-crustal channel flow to form. The formation of destabilization LANDs appears to require a weak mid-crust dragging a stiffer upper crust, in which case channel flow is a requirement for their formation as well. Extrusion LANDs can be coupled with channel flow at depth as described here for the Himalaya, but perhaps they can be formed by other processes as well.

Numerical thermomechanical modeling results suggest that a channel flow will only form in relatively large and hot orogens such as the Himalaya-Tibet and Grenville orogens (Beaumont et al., 2006). However, apparently syn-convergent LANDs are present in medium-sized orogens such as the Canadian Cordillera and Trans Hudson orogens and small, cold orogens such as the Alps. Comparisons between the LANDs described here and those from other orogens should be made to determine whether syn-convergent LANDs in those smaller orogens are produced due to channel flow, or another mechanism entirely. I suggest that syn-convergent LANDs in smaller orogens may be extrusion LANDs formed by other processes than solely channel flow. Extrusion of a frictional plastic wedge is one possible candidate, although it has not yet been demonstrated to be feasible in finite-element numerical models (Willett 1999a).

Future geophysical studies across the Himalayan orogen should reveal the extent and geometry of the MHT ramp in the eastern Himalaya. The geometry of the ramp may provide a clue as to whether it is a function of the pre-collision geometry of the Indian margin, the rheology of the Indian plate, or a thermal ramp produced by faster convergence and/or erosion rates in the eastern Himalaya.

CHAPTER 7

CONCLUSIONS

Two distinct segments of the South Tibetan detachment system are preserved in the Bhutan Himalaya, here termed the outer and inner South Tibetan detachment system.

The outer South Tibetan detachment system is a low-angle, diffuse ductile shear zone characterized by top-to-the-north shear sense indicators and an up-section continuous decrease in metamorphic grade. It is now preserved at the base of synformal klippen of upper-crustal Chekha Group and Tethyan sedimentary sequence rocks.

Prograde garnet growth in footwall rocks of the outer South Tibetan detachment system preceded partial melting at 22.6 $\pm$ 0.4 Ma. Peak T conditions of $>$ 750 °C in the footwall were reached after ca. 20.5 Ma. In the hanging wall, peak T conditions of $>$ 700 °C were reached by ca. 22-20 Ma. Peak T conditions were followed by ductile normal-sense top-to-the-north shearing under retrograde metamorphic conditions until ca. 15 Ma. Hanging wall tectonites cooled below 425-350 °C by ca. 11 Ma.

The timing of high-T ductile shearing along the outer South Tibetan detachment system coincides with published ages for the timing of shearing along the strike-parallel Main Central thrust, between 23 and 15 Ma.

Chekha Group and Tethyan sedimentary sequence rocks in the hanging wall of the outer South Tibetan detachment system are characterized by pre-Miocene, south-directed shortening structures. In the Lingshi klippe, only the Chekha Group is deformed by Miocene top-to-the-north shearing along the South Tibetan detachment system, and there is no evidence for a detachment between the Chekha Group and the Tethyan sedimentary sequence. Peak T in the Tethyan sedimentary sequence ranges between 200 and 350 °C, while Chekha Group rocks have peak T of 300 to $>$ 700 °C. Both are deformed by post-South Tibetan detachment system low-wavelength buckling and oblique-slip faulting.

The inner South Tibetan detachment system comprises a low-angle diffuse ductile shear zone characterized by top-to-the-north shear in Greater Himalayan sequence gneiss and Miocene leucogranite, that has been overprinted and cut by a steeper low-angle ductile-brittle detachment with Tethyan sedimentary sequence rocks in the hanging wall. The ductile shear zone was active until at least ca. 11 Ma, and its footwall cooled more rapidly than footwall rocks in the outer South Tibetan detachment system.

I propose that the South Tibetan detachment system is made up of three types of syn-convergent low-angle normal-sense detachments (LANDs): channel LANDs formed by channel flow in the mid-crust; extrusion LANDs formed by extrusion of a paleo-channel, and; destabilization LANDs, formed by destabilization of the upper crust accompanying doming of a mid-crustal channel.

Paleoprovenance data indicate that the Jaishidanda Formation below and Chekha Group above may share a common protolith with the Greater Himalaya sequence, in which case the protolith boundaries of the Greater Himalaya sequence do not coincide with its bounding structures, the Main Central thrust and the South Tibetan detachment system. The similarities between ϵNd and detrital zircon signatures for Baxa and Diuri Formation Lesser Himalaya sequence rocks, Jaishidanda Formation, Greater Himalaya sequence, Chekha Group and Tethyan sedimentary sequence suggest deposition in a single continuous passive margin on Indias northern continental margin, at least during the Paleozoic.

Comparisons of the above data with models of channel flow indicate that the tectonic history of the South Tibetan detachment system in the eastern Himalaya can be explained by underthrusting of a crustal ramp into the orogen since early Miocene, causing extrusion of a laterally extensive dome of mid-crustal material above a previously-extruded channel. A crustal ramp may explain several other tectonic features characteristic of the eastern Himalaya, including gneiss domes exposed in the North Himalayan antiform, increasing metamorphic grade of the Greater Himalaya sequence from west to east, greater surface exposure of the Greater Himalaya sequence, and out-of-sequence thrusting within the Greater Himalaya sequence.

A crustal ramp may have preferentially occurred in the eastern Himalaya due to higher convergence and/or erosion rates compared to the western Himalaya, or due to the underthrusting of a block of relatively strong Indian crust behind relatively weaker crust.

The above results provide detailed empirical data that can be used for future research

into the mechanisms behind the formation of syn-convergent LANDs, structures that have been recognized in several different orogens of varying temperature and magnitude around the world.

REFERENCES

Ahmad, T., and Tarney, J., 1991, Geochemistry and petrogenesis of Garhwal volcanics: implications for evolution of the north Indian lithosphere: Precambrian Research, v. 50, no. 1-2, p. 69-88.

Ahmad, T., Harris, N., Bickle, M., Chapman, H., Bunbury, J., Prince, C., 2000, Isotopic constraints on the structural relationships between the Lesser Himalayan Series and the High Himalayan Crystalline Series, Garhwal Himalaya: GSA Bulletin, v. 112, no. 3, p. 467-477.

Aikman, A. B., Harrison, T. M., and Lin, D., 2008, Evidence for Early (> 44 Ma) Himalayan Crustal Thickening, Tethyan Himalaya, southeastern Tibet: Earth and Planetary Science Letters, p. 14-23.

Anders, E., and Grevesse, N., 1989, Abundances of the elements—Meteoritic and solar: Geochimica et Cosmochimica Acta, v. 53, no. 1, p. 198-200.

Anders, M. H., Christie-Blick, N., and Walker, C. D., 2006, Distinguishing between rooted and rootless detachments: A case study from the Mormon Mountains of southeastern Nevada: The Journal of Geology, v. 114, no. 6, p. 645-664.

Anderson, E. M., 1951, The dynamics of faulting: Edinburgh and London, Oliver and Boyd, 206 p.

Andronicos, C. L., Velasco, A.A., and Hurtado, J.M.Jr., 2007, Large-scale deformation in the India-Asia collision constrained by earthquakes and topography: Terra Nova, v. 19, no. 2, p. 105-119.

Aoya, M., Wallis, S.R., Kawakami, T., Lee, J., Wang, Y., and Maeda, H., 2006, The Malashan gneiss dome in south Tibet: comparative study with the Kangmar dome with special reference to kinematics of deformation and origin of associated granites, *in* Law, R., Searle, M.P., Godin, L., ed., Channel Flow, Ductile Extrusion and Exhumation in Continental Collision Zones: London, Geological Society Special Publications, p. 471-495.

Argles, T., Foster, G., Whittington, A., Harris, N., George, M., 2003, Isotope studies reveal a complete Himalayan section in the Nanga Parbat syntaxis: Geology, v. 31, no. 12, p. 1109-1112.

Armijo, R., Tapponier, P. and Tonglin, H., 1989, Late Cenozoic right-lateral strike-slip faulting in southern Tibet: Journal of Geophysical Research, v. 94, no. B3, p. 2787-2838.

Armstrong, R., 1972, Low-angle (denudation) faults, hinterland of the Sevier orogenic belt, eastern Nevada and western Utah: Geological Society of America Bulletin, v. 83, no. 6, p. 1729.

Avouac, J. P., 2003, Mountain building, erosion, and the seismic cycle in the Nepal Himalaya: Advances in Geophysics, v. 46, p. 1-80.

Axen, G. J., 2004, Low-angle normal fault mechanics and crustal strength: *in* Rheology and Deformation in the Lithosphere at Continental Margins, Tikoff, B., ed, EOS Transactions, AGU, v. 85, no. 39, p. 46-91.

Axen, G. J., 2007, Research Focus: Significance of large-displacement, low-angle normal faults: Geology, v. 35, no. 3, p. 287.

Baule, S., 2004, Clockwise rotation and fold axis distribution in the Tethyan Himalaya of Bhutan: constraints from palaeomagnetic remnances and anisotropy of magnetic susceptibility (unpublished Dipl. Thesis): Tuebingen, Eberhard Karls University.

Beaumont, C., Jamieson, R.A., Nguyen, M.H., and Lee, B., 2001, Himalayan tectonics explained by extrusion of a low-viscosity crustal channel coupled to focused surface denudation: Nature, v. 414, p. 738-742.

Beaumont, C., Jamieson, R.A., Nguyen, M.H., and Medvedev, S., 2004, Crustal channel flows: 1. Numerical models with applications to the tectonics of the Himalayan-Tibetan orogen: Journal of Geophysical Research, v. 109, no. B06406, p. doi: 10.1029/2003JB002809.

Beaumont, C., Nguyen, M.H., Jamieson, R.A., and Ellis, S., 2006, Crustal flow modes in large hot orogens: *in* Channel Flow, Ductile Extrusion, and Exhumation in Continental Collision Zones, Law, R., Searle, M.P., and Godin, L., ed., Geological Society, London, Special Publications, v. 268 p. 91-145.

Beyssac, O., Goffé, B., Chopin, C., and Rouzaud, J.N., 2002, Raman spectra of carbonaceous material in metasediments: a new geothermometer: Journal of Metamorphic Geology, v. 20, p. 859-871.

Beyssac, O., Bollinger, L., Avouac, J.-P., and Goffé, B., 2004, Thermal metamorphism in the lesser Himalaya of Nepal determined from Raman spectroscopy of carbonaceous material: Earth and Planetary Science Letters, v. 225, p. 233-241.

Beyssac, O., Simoes, M., Avouac, J.-P., Farley, K.A., Chen, Y.G., Chan, Y.C., and Goffé, B., 2007, Late Cenozoic metamorphic evolution and exhumation of Taiwan: Tectonics, v. 26, TC6001, doi:10.1029/2006TC002064.

Bhargava, O.N., 1995, The Bhutan Himalaya, a Geological Account, Special Publication, Geological Survey of India, 245 p.

Biswas, S., Coutand, I., Grujic, D., Hager, C., Stöckli, D., and Grasemann, B., 2007, Exhumation and uplift of the Shillong plateau and its influence on the eastern Himalayas: New constraints from apatite and zircon (U-Th-[Sm])/He and apatite fission track analyses: Tectonics, v. 26, no. 6, doi:10.1029/2007TC002125

Boghossian, N. D., Patchett, P. J., Ross, G. M., and Gehrels, G. E., 1996, Nd isotopes and the source of sediments in the miogeocline of the Canadian Cordillera: The Journal of Geology, v. 104, no. 3, p. 259-277.

Bollinger, L., and Janots, E., 2006, Evidence for Mio-Pliocene retrograde monazite in the Lesser Himalaya, far western Nepal: European Journal of Mineralogy, v. 18, no. 3, p. 289-297.

Bollinger, L., Henry, P., and Avouac, J.-P., 2006, Mountain building in the Nepal Himalaya: Thermal and kinematic model: Earth and Planetary Science Letters, v. 244, no. 1-2, p. 58-71.

Booth, A.L., Zeitler, P.K., Kidd, W.S.F., Wooden, J., Liu, Y., Idleman, B., Hren, M., and Chamberlain, C.P., 2004, U-Pb zircon constraints on the tectonic evolution of southeastern Tibet, Namche Barwa area: American Journal of Science, v. 304, no. 10, p. 889-929.

Boyer, S.E., and Elliott, D., 1982, Thrust Systems: The American Association of Petroleum Geologists Bulletin, v. 66, no. 9, p. 1196-1230.

Brichau, S., Ring, U., Carter, A., Monié, P., Bolhar, R., Stöckli, D., and Brunel, M., 2007, Extensional faulting on Tinos Island, Aegean Sea, Greece: How many detachments?: Tectonics, v. 26, no. 4, TC4009, doi:10.1029/2006TC001969.

Brown, R.L. and Nazarchuk, J.H., 1993, Annapurna detachment fault in the Greater Himalaya of central Nepal: *in* Treloar, P.J., Searle, M.P., ed., Himalayan Tectonics: Special Publications: London, Geological Society, v. 74, p. 461-473.

Brown, R.L. and Gibson, H.D., 2006, An argument for channel flow in the southern Canadian Cordillera and comparison with Himalayan tectonics: *in* Channel Flow, Ductile Extrusion, and Exhumation in Continental Collision Zones, Law, R., Searle, M.P., and Godin, L., ed., Geological Society, London, Special Publications, v. 268 p. 543-560.

Brown, W.L., and Parsons, I., 1989, Alkali feldspars: ordering rates, phase transformations and behaviour diagrams for igneous rocks: Mineralogical Magazine, v. 53, no. 369, p. 25-42.

Brunel, M., Arnaud, N., Tapponnier, P., Pan, Y., and Wang, Y., 1994, Kongur Shan normal fault: Type example of mountain building assisted by extension (Karakoram fault, eastern Pamir): Geology, v. 22, no. 8, p. 707-710.

Burchfiel, B.C., Royden, L.H., 1985, North-south extension within the convergent Himalayan region: Geology, v. 13, p. 679-682.

Burchfiel, B.C., Chen, Z., Hodges, K.V., Liu, Y., Royden, L.H., Deng, C., and Xu, J., 1992, The South Tibet Detachment System, Himalayan orogen: extension contemporaneous with and parallel to shortening in a collisional mountain belt: Geological Society of America Special Paper, v. 269, p. 1-41.

Burg, J.P., Chen, G.M., 1984, Tectonics and structural zonation of southern Tibet, China: Nature, v. 311, p. 219-223.

Burg, J.P., Brunel, M., Gapais, D., Chen, G.M., Liu, G.H., 1984a, Deformation of leucogranites of the crystalline Main Central Sheet in southern Tibet (China): Journal of Structural Geology, v. 6, no. 5, p. 535-542.

Burg, J.P., Guiraud, M., Chen, G.M., and Li, G.C., 1984b, Himalayan metamorphism and deformations in the North Himalayan Belt (southern Tibet, China): Earth and Planetary Science Letters, v. 69, no. 2, p. 391-400.

Caddick, M. J., Bickle, M. J., Harris, N. B. W., Holland, T. J. B., Horstwood, M. S. A., Parrish, R. R., and Ahmad, T., 2007, Burial and exhumation history of a Lesser Himalayan schist: Recording the formation of an inverted metamorphic sequence in NW India: Earth and Planetary Science Letters, v. 264, no. 3-4, p. 375-390.

Carosi, R., Lombardo, B., Molli, G., Musumeci, G., and Pertusati, P.C., 1998, The south Tibetan detachment system in the Rongbuk valley, Everest region. Deformation features and geological implications: Journal of Southeast Asian Earth Sciences, v. 16, no. 2-3, p. 299-311.

Carosi, R., Lombardo, B., Musumeci, G., and Pertusati, P. C., 1999, Geology of the higher Himalayan crystallines in Khumbu Himal (eastern Nepal): Journal of Asian Earth Sciences, v. 17, no. 5-6, p. 785-803.

Carosi, R., Montomoli, C., Rubatto, D., Visonà, D., 2006, Normal-sense shear zones in the core of the Higher Himalayan Crystallines (Bhutan Himalaya): evidence for extrusion?, *in* Law, R., Searle, M.P., Godin, L., ed., Channel Flow, Ductile Extrusion and Exhumation in Continental Collision Zones: London, Geological Society, p. 425-444.

Carr, S.D., Parrish, R.R., and Brown, R.L., 1987, Eocene structural development of the Valhalla complex, southeastern British Columbia: Tectonics, v. 6, p. 175-196.

Catlos, E. J., Harrison, T. M., Kohn, M. J., Grove, M., Ryerson, F. J., Manning, G. E., and Upreti, B. N., 2001, Geochronologic and thermobarometric constraints on the evolution of the Main Central Thrust, central Nepal Himalaya: Journal of Geophysical Research, v. 106, no. B8, p. 16,177-16,204.

Catlos, E. J., Dubey, C.S., Harrison, T.M. and Edwards, M.A., 2004, Late Miocene movement within the Himalayan Main Central Thrust shear zone, Sikkim, north-east India: Journal of Metamorphic Geology, v. 22, p. 207-226.

Cesare, B., Marchesi, C., Hermann, J., and Gomez-Pugnaire, M.T., 2003, Primary melt inclusions in andalusite from anatectic graphitic metapelites: Implications for the position of the Al_2SiO_5 triple point: Geology, v. 31, no. 7, p. 573-576.

Chakungal, J., 2006, Geochemistry and metamorphism of metabasites, and spatial variation of P-T paths across the Bhutan Himalaya: Implications for the exhumation of the Greater Himalayan sequence (unpublished Ph.D. thesis): Halifax, Dalhousie University, 169 p.

Chakungal, J., Dostal, J., Grujic, D., Duchêne, S., and Ghalley, K. S., 2010, Provenance of the Greater Himalayan sequence: Evidence from mafic granulites and amphibolites in NW Bhutan: Tectonophysics, v. 480, p. 198-212.

Chambers, J.A., 2008. Thermal evolution of the mid-crust from the Himalayan orogen (unpublished Ph.D. thesis): Milton Keynes, The Open University, United Kingdom, 304 p.

Chambers, J., Caddick, M., Argles, T., Horstwood, M., Sherlock, S., Harris, N., Parrish, R., and Ahmad, T., 2009, Empirical constraints on extrusion mechanisms from the upper margin of an exhumed high-grade orogenic core, Sutlej valley, NW India: Tectonophysics, v. 477, no. 1-2, p. 77-92.

Chen, Z., Liu, Y., Hodges, K.V., Burchfiel, B. C., Royden, L.H., and Deng, C., 1990, The Kangmar dome: A metamorphic core complex in southern Xizang (Tibet): Science, v. 250, no. 4987, p. 1552-1556.

Claiborne, L.L., Miller, C.F., Walker, B.A., Wooden, J.L., Mazdab, F.K., and Bea, F., 2006, Tracking magmatic processes through Zr/Hf ratios in rocks and Hf and Ti zoning in zircons: An example from the Spirit Mountain batholith, Nevada: Mineralogical Magazine, v. 70, no. 5, p. 517-543.

Clarke, D.B., Dorias, M., Barbarin, B., Barker, D., Cesare, B., Clarke, G., El Baghdadi, M., Erdmann, S., Forster, H.-J., Gaeta, M., Gottesmann, B., Jamieson, R.A., Kontak, D.J., Koller, F., Gomes, C.L., London, D., Morgan, G.B., Neves, L.J.P.F., Pattison, D.R.M., Pereira, A.J.S.C., Pichavant, M., Rapela, C.W., Renno, A.D., Richards, S., Roberts, M., Rottura, A., Saavedra, J., Sial, A.N., Toselli, A.J., Ugidos, J.M., Uher, P., Villaseca, C., Visonà, D., Whitney, D.L., Williamson, B., Woodard, H.H. , 2005, Occurrence and origin of andalusite in peraluminous felsic igneous rocks: Journal of Petrology, v. 46, no. 3, p. 441-472.

Clement, S.W.J., and Compston, W., 1994, Ion probe parameters for very high resolution without loss of sensitivity, U.S. Geological Survey Circular 1107, p. 62.

Clift, P. D., Giosan, L., Blusztajn, J., Campbell, I.H., Allen, C., Pringle, M., Tabrez, A.R., Danish, M., Rabbani, M.M., and Alizai, A., 2008, Holocene erosion of the Lesser Himalaya triggered by intensified summer monsoon: Geology, v. 36, no. 1, p. 79-82.

Colchen, M., Le Fort, P., Pêcher, A., 1986, Recherches Géologiques dans l'Himalaya du Népal: Annapurna-Manaslu-Ganesh Himal: Editions du Centre National de la Recherche Scientifique, 136 p.

Coleman, M., Hodges, K., 1998, Contrasting Oligocene and Miocene thermal histories from the hanging wall and footwall of the South Tibetan detachment in the central Himalaya from $^{40}Ar/^{39}Ar$ thermochronology, Marsyandi Valley, central Nepal: Tectonics, v. 17, no. 5, p. 726-740.

Corfu, F., Hanchar, J. M., Hoskin, P. W. O., and Kinny, P., 2003, Atlas of Zircon Textures: Reviews in Mineralogy and Geochemistry, v. 53, no. 1, p. 469-500.

Corrie, S. L., Kohn, M. J., and Vervoort, J. D., 2010, Young eclogite from the Greater Himalayan Sequence, Arun Valley, eastern Nepal: PTt path and tectonic implications: Earth and Planetary Science Letters, v. 289, p. 406-416.

Cottle, J.M., Jessup, M.J., Newell, D.L., Searle, M.P., Law, R.D., and Horstwood, M.S.A., 2007, Structural insights into the early stages of exhumation along an orogen-scale detachment: The South Tibetan Detachment System, Dzakaa Chu section, Eastern Himalaya: Journal of Structural Geology, v. 29, no. 11, p. 1781-1797.

Cottle, J.M., Horstwood, M.S.A., and Parrish, R.R., 2009a, A new approach to single shot laser ablation analysis and its application to in situ Pb/U geochronology: Journal of Analytical Atomic Spectrometry, v. 24, p. 1355-1363.

Cottle, J.M., Jessup, M.J., Newell, D.L., Horstwood, M.S.A., Noble, S.R., Parrish, R.R., Waters, D.J., and Searle, M.P., 2009b, Geochronology of granulitized eclogite from the Ama Drime Massif: Implications for the tectonic evolution of the South Tibetan Himalaya: Tectonics, v. 28, no. 1, TC1002, doi:10.1029/2008TC002256.

Cottle, J.M., Searle, M.P., Horstwood, M.S.A., and Waters, D.J., 2009c, Timing of Mid-crustal Metamorphism, Melting, and Deformation in the Mount Everest Region of Southern Tibet Revealed by U (-Th)-Pb Geochronology: The Journal of Geology, v. 117, no. 6, p. 643-664.

Crouzet, C., Dunkl, I., Paudel, L., Árkai, P., Rainer, T.M., Balogh, K., and Appel, E., 2007, Temperature and age constraints on the metamorphism of the Tethyan Himalaya in Central Nepal: A multidisciplinary approach: Journal of Asian Earth Sciences, v. 30, no. 1, p. 113-130.

Dahlen, F. A., 1990, Critical Taper Model of Fold-and-Thrust Belts and Accretionary Wedges: Annual Review of Earth and Planetary Sciences, v. 18, p. 55-99.

Daniel, C.G., Hollister, L.S., Parrish, R.R., Grujic, D., 2003, Exhumation of the Main Central Thrust from Lower Crustal Depths, Eastern Bhutan Himalaya: Journal of Metamorphic Geology, v. 21, p. 317-334.

Dasgupta, S., 1995, Jaishidanda Formation, *in* Bhargava, O.N., ed., The Bhutan Himalaya: a Geological Account: Special Publication 39, Geological Survey of India, Calcutta, p. 79-88.

Davidson, C., Grujic, D.E., Hollister, L.S., and Schmid, S.M., 1997, Metamorphic reactions related to decompression and synkinematic intrusion of leucogranite, High Himalayan Crystallines, Bhutan: Journal of Metamorphic Geology, v. 15, p. 593-612.

Davies, N. S., and Gibling, M. R., 2010, Paleozoic vegetation and the Siluro-Devonian rise of fluvial lateral accretion sets: Geology, v. 38, no. 1, p. 51-54.

Davis, G.H., and Coney, P.J., 1979, Geologic development of the Cordilleran metamorphic core complexes: Geology, v. 7, no. 3, p. 120-124.

de Sigoyer, J., Chavagnac, V., Blichert-Toft, J., Villa, I.M., Luais, B., Guillot, S., Cosca, M., and Mascle, G., 2000, Dating the Indian continental subduction and collisional thickening in the northwest Himalaya: Multichronology of the Tso Morari eclogites: Geology, v. 28, p. 487-490.

DeCelles, P. G., Gehrels, G.E., Quade, J., LaReau, B., Spurlin, M., 2000, Tectonic implications of U-Pb zircon ages of the Himalayan orogenic belt in Nepal: Science, v. 288, p. 497-499.

DeCelles, P. G., Gehrels, G.E., Najman, Y., Martin, A.J., Carter, A., Garzanti, E., 2004, Detrital geochronology and geochemistry of Cretaceous-Early Miocene strata of Nepal: implications for timing and diachroneity of initial Himalayan orogenesis: Earth and Planetary Science Letters, v. 227, p. 313-330.

Deniel, C., Vidal, P., Fernandez, A., Le Fort, P., Peucat, J.-J., 1987, Isotopic study of the Manaslu granite (Himalaya, Nepal): inferences on the age and source of Himalayan leucogranites: Contributions to Mineralogy and Petrology, v. 96, p. 78-92.

Dettman, D.L., Fang, X., Garzione, C.N., and Li, J., 2003, Uplift-driven climate change at 12 Ma: a long δO^{18} record from the NE margin of the Tibetan plateau: Earth and Planetary Science Letters, v. 214, no. 1-2, p. 267-277.

Dèzes, P. J., Vannay, J.-C., Steck, A., Bussy, F., Cosca, M., 1999, Synorogenic extension: Quantitative constraints on the age and displacement of the Zanskar shear zone (northwest Himalaya): GSA Bulletin, v. 111, no. 3, p. 364-374.

Di Vincenzo, G., Carosi, R., and Palmeri, R., 2004, The Relationship between Tectonometamorphic Evolution and Argon Isotope Records in White Mica: Constraints from in situ $^{40}Ar/^{39}Ar$ Laser Analysis of the Variscan Basement of Sardinia: Journal of Petrology, v. 45, no. 5, p. 1013-1043.

Drukpa, D., Velasco, A.A., Doser, D.I., 2006, Seismicity in the Kingdom of Bhutan (1937-2003): Evidence for crustal transcurrent deformation: Journal of Geophysical Research, v. 111, no. B06301, p. doi:10.1029/2004JB003087.

Edwards, M.A., and Harrison, T.M., 1997, When did the roof collapse? Late Miocene north-south extension in the high Himalaya revealed by Th-Pb monazite dating of the Khula Kangri Granite: Geology, v. 25, no. 6, p. 543-546.

Edwards, M.A., Kidd, W.S.F., Li, J., Yue, Y., Clark, M., 1996, Multi-stage development of the southern Tibet detachment system near Khula Kangri. New data from Gonto La: Tectonophysics, v. 260, no. 1-3, p. 1-19.

Edwards, M.A., Pêcher, A., Kidd, W.S.F., Burchfiel, B.C., Royden, L.H., 1999, Southern Tibet detachment system at Khula Kangri, eastern Himalaya: A large-area, shallow detachment stretching into Bhutan?: The Journal of Geology, v. 107, p. 623-631.

Ferry, J.M., Watson, E.B., 2007, New thermodynamic models and revised calibrations for the Ti-in-zircon and Zr-in-rutile thermometers: Contributions to Mineralogy and Petrology, v. 154, no. 4, p. 429-437.

Fitzsimons, I.C.W., Kinny, P.D., Wetherley, S., and Hollingsworth, D.A., 2005, Bulk chemical control on metamorphic monazite growth in pelitic schists and implications for U-Pb age data: Journal of Metamorphic Geology, v. 23, no. 4, p. 261-277.

Foster, G., Gibson, H.D., Parrish, R., Horstwood, M., Fraser, J., and Tindle, A., 2002, Textural, chemical and isotopic insights into the nature and behaviour of metamorphic monazite: Chemical Geology, v. 191, no. 1-3, p. 183-207.

France-Lanord, C., and Le Fort, P., 1988, Crustal melting and granite genesis during the Himalayan collision orogenesis: Transactions of the Royal Society of Edinburgh. Earth Sciences, v. 79, no. 2-3, p. 183-195.

Frank, W., Hoinkes, G., Miller, C., Purtscheller, F., Richter, W., and Thöni, M., 1973, Relations between metamorphism and orogeny in a typical section of the Indian Himalayas: Mineralogy and Petrology, v. 20, no. 4, p. 303-332.

Frank, W., Grasemann, B., Guntli, P., and Miller, C., 1995, Geological map of the KishtwarChambaKulu region (NW Himalayas, India): Jahrbuch der Geologischen Bundesanstalt, v. 138, p. 299308.

Fu, B., Page, F.Z., Cavosie, A.J., Fournelle, J., Kita, N.T., Lackey, J.S., Wilde, S.A., and Valley, J.W., 2008, Ti-in-zircon thermometry: applications and limitations: Contributions to Mineralogy and Petrology, v. 156, doi: 10.1007/s00410-008-0281-5.

Fuchs, G., 1967, Zum Bau des Himalaya, Osterreichische akademie der wissenschaften mathematisch-naturwissenschafliche klasse denkschriften: Vienna, Springer-Verlag, 211 p.

Gansser, A., 1964, Geology of the Himalayas: New York, Interscience, 289 p.

Gansser, A., 1983, Geology of the Bhutan Himalaya: Basel, Birkhäuser Verlag, 181 p.

Garzanti, E., 1999, Stratigraphy and sedimentary history of the Nepal Tethys Himalaya passive margin: Journal of Asian Earth Sciences, v. 17, p. 805-827.

Gehrels, G.E., and Dickinson, W.R., 1995, Detrital zircon provenance of Cambrian to Triassic miogeoclinal and eugeoclinal strata in Nevada: American Journal or Science, v. 295, p. 18-48.

Gemmer, L., Ings, S. J., Medvedev, S., and Beaumont, C., 2004, Salt tectonics driven by differential sediment loading: stability analysis and finite-element experiments: Basin Research, v. 16, no. 2, p. 199-218.

Gibson, H.D., Carr, S.D., Brown, R.L., and Hamilton, M.A., 2004, Correlations between chemical and age domains in monazite, and metamorphic reactions involving major pelitic phases: an integration of ID-TIMS and SHRIMP geochronology with Y-Th-U X-ray mapping: Chemical Geology, v. 211, no. 3-4, p. 237-260.

Glodny, J., Ring, U., and Kühn, A., 2008, Coeval high-pressure metamorphism, thrusting, strike-slip, and extensional shearing in the Tauern Window, Eastern Alps: Tectonics, v. 27, no. 4.

Godin, L., 2003, Structural evolution of the Tethyan sedimentary sequence in the Annapurna area, central Nepal Himalaya: Journal of Asian Earth Sciences, v. 22, p. 307-328.

Godin, L., Parrish, R.R., Brown, R.L. and Hodges, K.V., 2001, Crustal thickening leading to exhumation of the Himalayan metamorphic core of central Nepal: insight from U-Pb geochronology and $^{40}Ar/^{39}Ar$ thermochronology: Tectonics, v. 20, no. 5, p. 729-747.

Godin, L., Grujic, D., Law, R., and Searle, M.P., 2006a, Crustal Flow, Extrusion, and Exhumation in Continental Collision Zones: An Introduction, *in* Law, R., Searle, M.P., Godin, L., ed., Channel Flow, Ductile Extrusion, and Exhumation in Continental Collision Zones: Special Publication: London, Geological Society, p. 1-23.

Godin, L., Gleeson, T., Searle, M.P., Ullrich, T.D., and Parrish, R.R., 2006b, Locking of southward extrusion in favour of rapid crustal-scale buckling of the Greater Himalayan sequence, Nar valley, central Nepal, *in* Law, R., Searle, M.P., Godin, L., ed., Channel Flow, Ductile Extrusion and Exhumation in Continental Collision zones: London, Geological Society of London, p. 269-292.

Gordon, S.M., Grove, M., Whitney, D.L., Schmitt, A.K., and Teyssier, C., 2009, Time-temperature-fluid evolution of migmatite dome crystallization: Coupled U-Pb age, Ti thermometry, and O isotopic ion microprobe depth profiling of zircon and monazite: Chemical Geology, v. 262, no. 3-4, p. 186-201.

Goscombe, B., Gray, D., and Hand, M., 2006, Crustal architecture of the Himalayan metamorphic front in eastern Nepal: Gondwana Research, v. 10, no. 3-4, p. 232-255.

Grambling, J.A., and Williams, M.L., 1985, The effects of Fe^{3+} and Mn^{3+} on aluminum silicate phase relations in north-central New Mexico, U.S.A.: Journal of Petrology, v. 26(2), p. 324-354.

Groppo, C., Rolfo, F., and Lombardo, B., 2009, PT evolution across the Main Central Thrust zone (Eastern Nepal): hidden discontinuities revealed by petrology: Journal of Petrology, v. 50, no. 6, p. 1149.

Grujic, D., 2006, Channel flow and continental collision tectonics: an overview: *in* Channel Flow, Ductile Extrusion, and Exhumation in Continental Collision Zones, Law, R., Searle, M.P., and Godin, L., ed., Geological Society, London, Special Publications, v. 268, p. 25-37.

Grujic, D., Casey, M., Davidson, C., Hollister, L.S., Kündig, R., Pavlis, T., and Schmid, S., 1996, Ductile extrusion of the Higher Himalayan Crystalline in Bhutan: evidence from quartz microfabrics: Tectonophysics, v. 260, p. 21-43.

Grujic, D., Hollister, L.S. and Parrish, R.R., 2002, Himalayan metamorphic sequence as an orogenic channel: insight from Bhutan: Earth and Planetary Science Letters, v. 198, p. 177-191.

Grujic, D., Coutand, E., Bookhagen, B., Bonnet, S., Blythe, A., Duncan, C., 2006, Climatic forcing of erosion, landscape, and tectonics in the Bhutan Himalayas: Geology, v. 34, no. 10, p. 801-804.

Guillot, S., Cosca, M., Allemand, P., and Le Fort, P., 1999, Contrasting metamorphic and geochronologic evolution along the Himalayan belt: *in* Macfarlane, A., Sorkhabi, R.B. and Quade, J., ed., Himalaya and Tibet: Mountain Roots to Mountain Tops, Geological Society of America Special Paper v. 328, p. 117-128.

Guillot, S., Replumaz, A., Hattori, K. H., and Strzerzynski, P., 2007, Initial geometry of western Himalaya and ultrahigh-pressure metamorphic evolution: Journal of Asian Earth Sciences, v. 30, no. 3-4, p. 557-564.

Guillot, S., Mahéo, G., de Sigoyer, J., Hattori, K.H., and Pêcher, A., 2008, Tethyan and Indian subduction viewed from the Himalayan high-to ultrahigh-pressure metamorphic rocks: Tectonophysics, v. 451, no. 1-4, p. 225-241.

Gupta, V. J., and Termier, G., 1983, Middle Devonian Corals from Central Bhutan: Journal of the Geological Society of India, p. 212-214.

Hames, W. E., Bowring, S.A., 1994, An empirical evaluation of the argon diffusion geometry in muscovite: Earth and Planetary Science Letters, v. 124, no. 1-4, p. 161-169.

Hanchar, J.M., and Miller, C.F., 1993, Zircon zonation patterns as revealed by cathodo-luminescence and backscattered electron images: implications for interpretation of complex crustal histories: Chemical Geology, v. 110, no. 1-3, p. 1-13.

Harris, N.B.W., Caddick, M., Kosler, J., Goswami, S., Vance, D. and Tingle, A.G., 2004, The pressure-temperature-time path of migmatites from the Sikkim Himalaya: Journal of Metamorphic Geology, v. 22, p. 249-264.

Harrison, T.M., Grove, M., Lovera, O.M., and Catlos, E.J., 1998, A model for the origin of Himalayan anatexis and inverted metamorphism: Journal of Geophysical Research, v. 103, no. B11, p. 27017-27032.

Harrison, T.M., Célérier, J., Aikman, A.B., Hermann, J., and Heizler, M.T., 2009, Diffusion of ^{40}Ar in muscovite: Geochimica et Cosmochimica Acta, v. 73, p. 1039-1051.

Hauck, M. L., Nelson, K.D., Brown, L.D., Zhao, Wenjin and Ross, A.R., 1998, Crustal structure of the Himalayan orogen at ∼90 east longitude from Project INDEPTH deep reflection profiles: Tectonics, v. 17, no. 4, p. 481-500.

Herren, E., 1987, Zanskar shear zone: Northeast-southwest extension within the Higher Himalayas (Ladakh, India): Geology, v. 15, no. 5, p. 409-413.

Hodges, K.V., 2000, Tectonics of the Himalaya and southern Tibet from two perspectives: GSA Bulletin, v. 112, no. 3, p. 324-350.

Hodges, K.V., Parrish, R.R., Housh, T.B., Lux, D.R., Burchfiel, B.C., Royden, L.H., Chen, Z., 1992, Simultaneous Miocene extension and shortening in the Himalayan orogen: Science, v. 258, p. 1466-1469.

Hodges, K. V., Parrish, R.R. and Searle, M.P., 1996, Tectonic evolution of the central Annapurna Range, Nepalese Himalayas: Tectonics, v. 15, no. 6, p. 1264-1291.

Hodges, K.V., Hurtado, J.M., and Whipple, K.X., 2001, Southward extrusion of Tibetan crust and its effect on Himalayan tectonics: Tectonics, v. 20, no. 6, p. 799-809.

Holdaway, M.J., 1971, Stability of andalusite and the aluminum silicate phase diagram: American Journal of Science, v. 271, no. 2, p. 97.

Holland, T.J.B., and Powell, R., 1998, An internally consistent thermodynamic data set for phases of petrological interest: Journal of Metamorphic Geology, v. 16, p. 309-344.

Hollister, L.S., 1966, Garnet zoning: an interpretation based on the Rayleigh fractionation model, ©1966 by the American Association for the Advancement of Science, p. 1647-1651.

Hollister, L.S., Grujic, D., 2006, Pulsed channel flow in Bhutan, *in* Law, R., Searle, M.P., Godin, L., ed., Channel Flow, Ductile Extrusion and Exhumation in Continental Collision Zones: Special Publications: London, Geological Society, v. 268, p. 415-423.

Holtz, F., Becker, A., Freise, M., and Johannes, W., 2001, The water-undersaturated and dry Qz-Ab-Or system revisited. Experimental results at very low water activities and geological implications: Contributions to Mineralogy and Petrology, v. 141, no. 3, p. 347-357.

Horstwood, M.S.A., Foster, G.L., Parrish, R.R., Noble, S.R., and Nowell, G.M., 2003, Common-Pb corrected in situ UPb accessory mineral geochronology by LA-MC-ICP-MS: Journal of Analytical Atomic Spectrometry, v. 18, no. 8, p. 837-846.

Hughes, N., Myrow, P.M., McKenzie, N.R., Harper, D.A.T., Bhargava, O.N., Tangri, S.K., Ghalley, K.S. and Fanning, C. M., *in review*, Cambrian rocks and faunas of the Black Mountain Klippe, Bhutan: Geological Magazine.

Hurtado, J.M.J., Hodges, K.V. and Whipple, K.X., 2001, Neotectonics of the Thakkhola graben and implications for recent activity on the South Tibetan fault system in the central Nepal Himalaya: GSA Bulletin, v. 113, no. 2, p. 222-240.

Imayama, T., and Arita, K., 2008, Nd isotopic data reveal the material and tectonic nature of the Main Central Thrust zone in Nepal Himalaya: Tectonophysics, v. 451, no. 1-4, p. 265-281.

Ireland, T.R. and Williams, I.S., 2003, Considerations in zircon geochronology by SIMS, Zircon: *in* Reviews in Mineralogy and Geochemistry, Hanchar, J.M. and Hoskins, P.W.O., ed., v. 53, p. 215-241.

Jamieson, R. A., Beaumont, C., Fullsack, P., and Lee, B., 1998, Barrovian regional metamorphism: where's the heat?: Geological Society London Special Publications, v. 138, no. 1, p. 23.

Jamieson, R. A., Beaumont, C., Nguyen, M.H., Lee, B., 2002, Interaction of metamorphism, deformation and exhumation in large convergent orogens: Journal of Metamorphic Geology, v. 20, p. 9-24.

Jamieson, R. A., Beaumont, C., Medvedev, S., and Nguyen, M. H., 2004, Crustal channel flows: 2. Numerical models with implications for metamorphism in the Himalayan-Tibetan orogen: Journal of Geophysical Research, v. 109, p. 124.

Jamieson, R.A., Beaumont, C., Nguyen, M.H., and Grujic, D., 2006, Provenance of the Greater Himalayan Sequence and associated rocks: Predictions of channel flow models: *in* Law, R., Searle, M.P., Godin, L., ed., Channel Flow, Ductile Extrusion and Exhumation in Continental Collision Zones: Special Publications: London, Geological Society, v. 268, p. 165-182.

Jamieson, R. A., Beaumont, C., Nguyen, M. H., and Culshaw, N. G., 2007, Synconvergent ductile flow in variable-strength continental crust: Numerical models with application to the western Grenville orogen: Tectonics, v. 26, no. 5, doi:10.1029/2006TC002036.

Jangpangi, B.S., 1974. Stratigraphy and tectonics of parts of eastern Bhutan. Himalayan Geology, 4, 117136.

Jessup, M.J., Law, R.D., Searle, M.P., and Hubbard, M.S., 2006, Structural evolution and vorticity of flow during extrusion and exhumation of the Greater Himalayan Slab, Mount Everest Massif, Tibet/Nepal: implications for orogen-scale flow partitioning: *in* Law, R., Searle, M.P., Godin, L., ed., Channel Flow, Ductile Extrusion and Exhumation in Continental Collision Zones: Special Publications: London, Geological Society, v. 268, p. 379-414.

Jessup, M.J., Cottle, J.M., Searle, M.P., Law, R.D., Newell, D.L., Tracy, R.J., and Waters, D.J., 2008, PTtD paths of Everest Series schist, Nepal: Journal of Metamorphic Geology, v. 26, no. 7, p. 717-739.

Johnson, M.R.W., Oliver, G.J.H., Parrish, R.R., and Johnson, S.P., 2001, Synthrusting metamorphism, cooling, and erosion of the Himalayan Kathmandu Complex, Nepal: Tectonics, v. 20, no. 3, p. 394-415.

Johnson, T.E., Brown, M., and Solar, G.S., 2003, Low-pressure subsolidus and suprasolidus phase equilibria in the MnNCKFMASH system: Constraints on conditions of regional metamorphism in western Maine, northern Appalachians: American Mineralogist, v. 88, no. 4, p. 624-638.

Kali, E., Leloup, P.H., Arnaud, N., Mahéo, G., Liu, D., Boutonnet, E., Van der Woerd, J., Liu, Xiaohan, Liu-Zeng, Jing and Li, Haibing, 2010, Exhumation history of the deepest central Himalayan rocks, Ama Drime range: Key pressure-temperature-deformation-time constraints on orogenic models: Tectonics, v. 29, doi:10.1029/2009TC002551.

Kawakami, T., Aoya, M., Wallis, S.R., Lee, J., Terada, K., Wang, Y., and Heizler, M., 2007, Contact metamorphism in the Malashan dome, North Himalayan gneiss domes, southern Tibet: an example of shallow extensional tectonics in the Tethys Himalaya: Journal of Metamorphic Geology, v. 25, no. 8, p. 831-853.

Keller, L.M., Fugenschuh, B., Hess, M., Schneider, B., and Schmid, S.M., 2006, Simplon fault zone in the western and central Alps: Mechanism of Neogene faulting and folding revisited: Geology, v. 34, p. 317-320.

Kellett, D.A., and Godin, L., 2009, Pre-Miocene deformation of the Himalayan superstructure, Hidden valley, central Nepal: Journal of the Geological Society, v. 166, no. 2, p. 261-275.

Kellett, D.A., Grujic, D., and Erdmann, S., 2009, Miocene structural reorganization of the South Tibetan detachment, eastern Himalaya: implications for continental collision: Lithosphere, v. 1, no. 5, p. 259-281.

Kellett, D.A., Grujic, D., Warren, C., Cottle, J., Jamieson, R., and Tenzin, T., *in press*, Metamorphic history of a syn-convergent orogen-parallel detachment: The South Tibetan detachment system, Bhutan Himalaya: Journal of Metamorphic Geology.

Klootwijk, C.T., Gee, J.S., Peirce, J. W., Smith, G.M., and McFadden, P.L., 1992, An early India-Asia contact: Paleomagnetic constraints from Ninetyeast Ridge, ODP Leg 121: Geology, v. 20, no. 5, p. 395-398.

Kohn, M.J., 2008, PTt data from central Nepal support critical taper and repudiate large-scale channel flow of the Greater Himalayan Sequence: Geological Society of America Bulletin, v. 120, no. 3, p. 259-273.

Kohn, M. J., and Spear, F., 2000, Retrograde net transfer reaction insurance for pressure-temperature estimates: Geology, v. 28, no. 12, p. 1127-1130.

Kohn, M. J., Catlos, E. J., Ryerson, F. J., and Harrison, T. M., 2001, Pressure-temperature-time path discontinuity in the Main Central thrust zone, central Nepal: Geology, v. 29, no. 7, p. 571-574.

Koike, R., Chettri, I.K., Tapa, T.P., and Ghalley, K.S., 2002. The Geological Mapping at the Black Mountain Area, Central Bhutan.

Kretz, R., 1983, Symbols for rock-forming minerals: American Mineralogist, v. 68, no. 1-2, p. 277-279.

Kuiper, Y.D., Williams, P.F. and Kruse, S., 2006, Possibility of channel flow in the southern Canadian Cordillera: a new approach to explain existing data: *in* Law, R., Searle, M.P., Godin, L., ed., Channel Flow, Ductile Extrusion and Exhumation in Continental Collision Zones: Special Publications: London, Geological Society, v. 268, p. 589-611.

Kuiper, K.F., Deino, A., Hilgen, F.J., Krijgsman, W., Renne, P.R., and Wijbrans, J.R., 2008, Synchronizing rock clocks of Earth history, Science, v. 320, p. 500-504.

Kündig, R., 1988. Kristallisation und Deformation im Higher Himalaya, Zanskar (NW-Indien), (unpublished Ph.D. thesis), ETH Zürich, 188 p.

Lakshminarayana, G., 1995, Damuda Supergroup: *in* Bhargava, O.N., ed., The Bhutan Himalaya: a Geological Account: Geological Survey of India Special Publication 39, p. 2933.

Larson, K.P., 2009, The tectonometamorphic evolution of the Greater Himalayan sequence as exposed in central Nepal and adjacent south-central Tibet (unpublished Ph.D. thesis): Kingston, Queen's University, Canada, 222 p.

Lavé, J., and Avouac, J.P., 2000, Active folding of fluvial terraces across the Siwaliks Hills, Himalayas of central Nepal: Journal of Geophysical Research, v. 105, p. 5735-5770.

Law, R.D., Searle, M.P. and Simpson, R.L., 2004, Strain, deformation temperatures and vorticity of flow at the top of the Greater Himalayan Slab, Everest Massif, Tibet: Journal of the Geological Society, London, v. 161, p. 305-320.

Le Fort, P., 1975, Himalayas: the collided range. Present knowledge of the continental arc.: American Journal of Science, v. 275-A, p. 1-44.

Lee, J., Hacker, B.R., Dinklage, W.S., Wang, Y., Gans, P., Calvert, A., Wan, J, Chen, W., Blythe, A.E. and McClelland, W., 2000, Evolution of the Kangmar Dome, southern Tibet: structural, petrologic, and thermochronologic constraints: Tectonics, v. 19, no. 5, p. 872-895.

Lee, J., Hacker, B., and Wang, Y., 2004, Evolution of North Himalayan gneiss domes: structural and metamorphic studies in Mabja Dome, southern Tibet: Journal of Structural Geology, v. 26, no. 12, p. 2297-2316.

Leech, M.L., 2008, Does the Karakoram fault interrupt mid-crustal channel flow in the western Himalaya?: Earth and Planetary Science Letters, v. 276, no. 3-4, p. 314-322.

Leech, M.L., Singh, S., Jain, A.K., Klemperer, S.L., and Manickavasagam, R.M., 2005, The onset of IndiaAsia continental collision: Early, steep subduction required by the timing of UHP metamorphism in the western Himalaya: Earth and Planetary Science Letters, v. 234, no. 1-2, p. 83-97.

Leloup, P.H., Mahéo, Arnaud, M., Kali, E., Boutonnet, E., Liu, Dunyi, Xiaohan, Liu, and Haibing, Li, 2010, The South Tibet detachment shear zone in the Dinggye area. Time constraints on extrusion models of the Himalayas: Earth and Planetary Science Letters, v. 292, doi:10.1016/j.epsl.2009.12.035.

Lombardo, B., Pertusati, P., and Borghi, S., 1993, Geology and tectonomagmatic evolution of the eastern Himalaya along the Chomolungma-Makalu transect: *in* Treloar, P.J., Searle, M.P., ed., Himalayan Tectonics: Special Publications: London, Geological Society, v. 74, p. 341.

Long, S., and McQuarrie, N., 2010, Placing limits on channel flow: Insights from the Bhutan Himalaya: Earth and Planetary Science Letters, v. 290, no. 3-4, p. 375-390.

Long, S., McQuarrie, N. and Tobgay, T. *in review*, Geometry and crustal shortening of the Himalayan fold-thrust belt, Eastern and Central Bhutan: GSA Bulletin.

Luais, B., Telouk, P., and Albaréde, F., 1997, Precise and accurate neodymium isotopic measurements by plasma-source mass spectrometry: Geochimica et Cosmochimica Acta, v. 61, p. 4847-4854.

Luais, B., Le Carlier de Veslud, C., Géraud, Y., and Gauthier-Lafaye, F., 2009, Comparative behavior of Sr, Nd and Hf isotopic systems during fluid-related deformation at middle crust levels: Geochimica et Cosmochimica Acta, v. 73, p. 2961-2977.

Ludwig, K.R., 2001, Squid, A users manual: Berkeley Geochronology Center Special Publication No. 2.

Ludwig, K.R., 2003, Isoplot 3.00, a geochronological toolkit for Excel, Berkeley Geochronology Center Special Publication No. 4.

MacDougall, I., and Harrison, T.M., 1988, Geochronology and thermochronology by the $^{40}Ar/^{39}Ar$ method: Oxford University Press, New York, 212 p.

Makovsky, Y., Klemperer, S.L., Liyan, H. and Deyuan, L., 1996, Structural elements of the southern Tethyan Himalaya crust from wide-angle seismic data: Tectonics, v. 15, no. 5, p. 997-1005.

Maluski, H., Matte, P., Brunel, M., and Xiao, X., 1988, Argon 39-Argon 40 dating of metamorphic and plutonic events in the north and high Himalaya belts (southern Tibet-China): Tectonics, v. 7, no. 2, p. 299-326.

Mancktelow, N., 1985, The Simplon line: a major displacement zone in the western Lepontine Alps: Eclogae Geologicae Helvetiae, v. 78, no. 1, p. 73-96.

Mancktelow, N.S., and Pavlis, T.L., 1994, Fold-fault relationships in low-angle detachment systems: Tectonics, v. 13, no. 3, p. 668-685.

Martin, A.J., DeCelles, P.G., Gehrels, G.E., Patchett, P.J., Isachsen, C., 2005, Isotopic and structural constraints on the location of the Main Central thrust in the Annapurna Range, central Nepal Himalaya: GSA Bulletin, v. 117, no. 7/8, p. 926-944.

Martin, A.J., Gehrels, G.E., and DeCelles, P.G., 2007, The tectonic significance of (U, Th)/Pb ages of monazite inclusions in garnet from the Himalaya of central Nepal: Chemical Geology, v. 244, no. 1-2, p. 1-24.

Massonne, H. J., and Schreyer, W., 1987, Phengite geobarometry based on the limiting assemblage with K-feldspar, phlogopite, and quartz: Contributions to Mineralogy and Petrology, v. 96, no. 2, p. 212-224.

Mazdab, F.K., and Wooden, J.L., 2006, Trace element analysis in zircon by ion microprobe (SHRIMP-RG): Technique and applications: Geochimica et Cosmochimica Acta, v. 70, p. 405-405.

McCulloch, M.T., and Wasserburg, G.J., 1978, Sm-Nd and Rb-Sr chronology of continental crust formation: Science, v. 200, no. 4345, p. 1003-1011.

McDonough, W.F., and Sun, S., 1995, The composition of the Earth: Chemical Geology, v. 120, no. 3-4, p. 223-253.

McQuarrie, N., Robinson, D., Long, S., Tobgay, T., Grujic, D., Gehrels, G., and Ducea, M., 2008, Preliminary stratigraphic and structural architecture of Bhutan: Implications for the along strike architecture of the Himalayan system: Earth and Planetary Science Letters, v. 272, no. 1-2, p. 105-117.

Meade, B.J., 2007, Present-day kinematics at the India-Asia collision zone: Geology, v. 35, no. 1, p. 81-84.

Means, W. D., 1990, One-dimensional kinematics of stretching faults: Journal of Structural Geology, v. 12, no. 2, p. 267-272.

Meigs, A.J., Burbank, D.W., and Beck, R.A., 1995, Middle-late Miocene (>10 Ma) formation of the Main Boundary thrust in the western Himalaya: Geology, v. 23, no. 5, p. 423-426.

Meyer, M.C., Wiesmayr, G., Brauner, M., Häusler, H., and Wangda, D., 2006, Active tectonics in Eastern Lunana (NW Bhutan): Implications for the seismic and glacial hazard potential of the Bhutan Himalaya: Tectonics, v. 25, no. 3, doi:10.1029/2005-TC001858.

Miller, C., Thöni, M., Frank, W., Grasemann, B., Klötzli, U., Guntli, P., and Draganits, E., 2001, The early Palaeozoic magmatic event in the Northwest Himalaya, India: Source, tectonic setting and age of emplacement: Geological Magazine, v. 138, no. 03, p. 237-251.

Molnar, P., 1984, Structure and Tectonics of the Himalaya: Constraints and Implications of Geophysical Data: Annual Reviews in Earth and Planetary Sciences, v. 12, no. 1, p. 489-516.

Molnar, P., and Stock, J.M., 2009, Slowing of India's convergence with Eurasia since 20 Ma and its implications for Tibetan mantle dynamics: Tectonics, v. 28, no. 3, doi:10.1029/2008TC002271.

Mukul, M., Jade, S., Bhattacharyya, A., and Bhusan, K., 2010, Crustal shortening in convergent orogens: Insights from global positioning system (GPS) measurements in northeast India: Journal of the Geological Society of India, v. 75, p. 302-312.

Murphy, M.A., 2007, Isotopic characteristics of the Gurla Mandhata metamorphic core complex: Implications for the architecture of the Himalayan orogen: Geology, v. 35, no. 11, p. 983-986.

Myrow, P. M., Hughes, N.C., Paulsen, T.S., Williams, I.S., Parcha, S.K., Thompson, K.R., Bowring, S.A., Peng, S.-C.. Ahluwalia, A.D., 2003, Integrated tectonostratigraphic analysis of the Himalaya and implications for its tectonic reconstruction: Earth and Planetary Science Letters, v. 212, p. 433-441.

Myrow, P. M., Thompson, K.R., Hughes, N.C., Paulsen, T.S., Sell, B.K., Parcha, S.K., 2006, Cambrian stratigraphy and depositional history of the northern Indian Himalaya, Spiti Valley, north-central India: GSA Bulletin, v. 118, no. 3/4, p. 491-510.

Myrow, P.M., Hughes, N.C., Searle, M.P., Fanning, C.M., Peng, S.C., and Parcha, S.K., 2009, Stratigraphic correlation of CambrianOrdovician deposits along the Himalaya: Implications for the age and nature of rocks in the Mount Everest region: Geological Society of America Bulletin, v. 121, p. 323-332.

Myrow, P.M., Hughes, N.C., Goodge, J.W., Fanning, C.M., Williams, I.S., Shanchi Peng, Bhargava, O.M., Parcha, S.K. and Pogue, K.R., *in review*. Extraordinary transport and mixing of sediment across Himalayan central Gondwana during the Cambrian-Ordovician.

Najman, Y., 2006, The detrital record of orogenesis: A review of approaches and techniques used in the Himalayan sedimentary basin: Earth-Science Reviews, v. 74, p. 1-72.

Najman, Y., Pringle, M., Godin, L. and Oliver, G., 2001, Dating of the oldest continental sediments from the Himalayan foreland basin: Nature, v. 410, p. 194-197.

Najman, Y., Johnson, K., White, N., and Oliver, G., 2004, Evolution of the Himalayan foreland basin, NW India: Basin Research, v. 16, no. 1, p. 1-24.

Negro, F., Beyssac, O., Goffé, B. Saddiqi, O., and Bouybaouène, M.L., 2006, Thermal structure of the Alboran Domain in the Rif (northern Morocco) and the Western Betics (southern Spain). Constraints from Raman spectroscopy of carbonaceous material: Journal of Metamorphic Geology, v. 24, p. 309-327.

Nelson, K.D., Zhao, W., Brown, L.D., Kuo, J., Che, J., Liu, X., Klemperer, S.L., Makovsky, Y., Meissner, R., Mechie, J., Kind, R., Wenzel, F., Ni, J., Nabelek, J., Leshou, C., Tan, H., Wei, W., Jonew, A.G., Booker, J., Unsworth, M., Kidd, W.S.F., Hauck, M., Alsdorf, Ross, A., Cogan, M., Wu, C., Sandvol, E. and Edwards, M., 1996, Partially molten middle crust beneath southern Tibet: synthesis of Project INDEPTH results: Science, v. 274, no. 5293, p. 1684-1688.

Nemchin, A.A., and Cawood, P.A., 2005, Discordance of the U-Pb system in detrital zircons: Implication for provenance studies of sedimentary rocks: Sedimentary Geology, v. 182, no. 1-4, p. 143-162.

Neumayer, J., Wiesmayr, G., Janda, C., Grasemann, B., and Draganits, E., 2004, Eohimalayan fold and thrust belt in the NW-Himalaya (Lingti-Pin Valleys): Shortening and depth to detachment calculation: Austrian Journal of Earth Sciences, v. 95, p. 28-36.

Ni, J., and Barazangi, M., 1984, Seismotectonics of the Himalayan collision zone: Geometry of the underthrusting Indian plate beneath the Himalaya: Journal of Geophysical Research-Solid Earth, v. 89, no. B2, p. 1147-1163.

Paquette, J.L., Nèdèlec, A., Moine, B., and Rakotondrazafy, M., 1994, U-Pb, single zircon Pb-evaporation, and Sm-Nd isotopic study of a granulite domain in SE Madagascar: The Journal of Geology, v. 102, no. 5, p. 523-538.

Parrish, R.R., 2009, Comment on: "Does the Karakoram fault interrupt mid-crustal channel flow in the western Himalaya?" by Mary L. Leech, Earth and Planetary Science Letters 276 (2008) 314-322: Earth and Planetary Science Letters, v. 286, p. 586-588.

Parrish, R. R., Hodges, K.V., 1996, Isotopic constraints on the age and provenance of the Lesser and Greater Himalayan sequences, Nepalese Himalaya: GSA Bulletin, v. 108, no. 7, p. 904-911.

Passchier, C.W., and Trouw, R.A.J., 2005, Microtectonics: Springer-Verlag, Berlin, 366 p.

Pattison, D.R.M., 1992, Stability of andalusite and sillimanite and the Al_2SiO_5 triple point: constraints from the Ballachulish Aureole, Scotland: The Journal of Geology, v. 100. p. 423-446.

Price, R.A., 1986, The southeastern Canadian Cordillera: thrust faulting, tectonic wedging, and delamination of the lithosphere: Journal of Structural Geology, v. 8, no. 3-4, p. 239-254.

Quigley, M., Liangjun, Y., Xiaohan, L., Wilson, C.J.L., Sandiford, M., and Phillips, D., 2006, 40Ar/39Ar thermochronology of the Kampa Dome, southern Tibet: Implications for tectonic evolution of the North Himalayan gneiss domes: Tectonophysics, v. 421, no. 3-4, p. 269-297.

Rahl, J.M., Reiners, P.W., Campbell, I.H., Nicolescu, S., and Allen, C.M., 2003, Combined single-grain (U-Th)/He and U/Pb dating of detrital zircons from the Navajo Sandstone, Utah: Geology, v. 31, no. 9, p. 761-764.

Rahl, J.M., Anderson, K.M., Brandon, M.T., Fassoulas, C., 2005, Raman spectroscopic carbonaceous material thermometry of low-grade metamorphic rocks: Calibration and application of tectonic exhumation in Crete, Greece: Earth and Planetary Science Letters, v. 240, p. 339-354.

Rantitsch, G., Sachsenhofer, R.F., Hasenhüttl, C., Russegger, B., and Rainer, T., 2005, Thermal evolution of an extensional detachment as constrained by organic metamorphic data and thermal modeling: Graz Paleozoic Nappe Complex (Eastern Alps): Tectonophysics, v. 411, no. 1-4, p. 57-72.

Ratschbacher, L., Frisch, W., Liu, Guanghua and Chen, Chengsheng, 1994, Distributed deformation in southern and western Tibet during and after the India-Asia collision: Journal of Geophysical Research, v. 99, no. B10, p. 19,917-19,945.

Richards, A., Argles, T., Harris, N., Parrish, R., Ahmad, T., Darbyshire, F., Draganits, E., 2005, Himalayan architecture constrained by isotopic tracers from clastic sediments: Earth and Planetary Science Letters, v. 236, p. 773-796.

Richards, A., Parrish, R., Harris, N., Argles, T., Zhang, L., 2006, Correlation of lithotectonic units across the eastern Himalaya, Bhutan: Geology, v. 34, no. 5, p. 341-344.

Richardson, S.W., Gilbert, M.C., and Bell, P.M., 1969, Experimental determination of kyanite-andalusite and andalusite-sillimanite equilibria; the aluminum silicate triple point: American Journal of Science, v. 267, no. 3, p. 259-272.

Ring, U., Glodny, J., Will, T., and Thomson, S., 2007, An Oligocene extrusion wedge of blueschist-facies nappes on Evia, Aegean Sea, Greece: implications for the early exhumation of high-pressure rocks: Journal of the Geological Society, v. 164, no. 3, p. 637-652.

Robinson, D.M., 2008, Forward modeling the kinematic sequence of the central Himalayan thrust belt, western Nepal: Geosphere, v. 4, no. 5, p. 785-801.

Robinson, D.M., DeCelles, P.G., Patchett, P.J. and Garzione, C.N., 2001, The kinematic evolution of the Nepalese Himalaya interpreted from Nd isotopes: Earth and Planetary Science Letters, v. 192, p. 507-521.

Robinson, D.M., DeCelles, P.G., Garzione, C.N., Pearson, O.N., Harrison, T.M., and Catlos, E.J., 2003, Kinematic model for the Main Central thrust in Nepal: Geology, v. 31, no. 4, p. 359-362.

Robinson, D.M., DeCelles, and P. Copeland, 2006, Tectonic evolution of the Himalayan thrust belt in western Nepal: Implications for channel flow models: GSA Bulletin, v. 118, no. 7-8, p. 865-885.

Rosenberg, C.L., and Handy, M.R., 2005, Experimental deformation of partially melted granite revisited: implications for the continental crust: Journal of Metamorphic Geology, v. 23, no. 1, p. 19-28.

Rowley, D.B., 1996, Age of initiation of collision between India and Asia: a review of stratigraphic data: Earth and Planetary Science Letters, v. 145, p. 1-13.

Rowley, D.B., 1998, Minimum age of initiation of collision between India and Asia north of Everest based on the subsidence history of the Zhepure mountain section: The Journal of Geology, v. 106, p. 229-235.

Royden, L.H., and Burchfiel, B.C., 1987, Thin-skinned NS extension within the convergent Himalayan region: gravitational collapse of a Miocene topographic front: Geological Society London Special Publications, v. 28, no. 1, p. 611-619.

Rubatto, D., 2002, Zircon trace element geochemistry: partitioning with garnet and the link between U-Pb ages and metamorphism: Chemical Geology, v. 184, p. 123-138.

Rubatto, D., Gebauer, D., 2000, Use of cathodoluminescence for U-Pb zircon dating by ion microprobe: some examples from the western Alps, *in* Pagel, M., ed., Cathodoluminescence in Geosciences: Berlin; New York, Springer, p. 373-400.

Sakai, H., Sawada, M., Takigami, Y., Orihashi, Y., Danhara, T., Iwano, H., Kuwahara, Y., Dong, Q., Cai, H., and Li, J., 2005, Geology of the summit limestone of Mount Qomolangma (Everest) and cooling history of the Yellow Band under the Qomolangma detachment: The Island Arc, v. 14, no. 4, p. 297-310.

Savage, K. M., and Potter, P. E., 1991, Petrology of modern sands of the Rios Guaviare and Inirida, southern Colombia: Tropical climate and sand composition: The Journal of Geology, v. 99, no. 2, p. 289-298.

Sawyer, E. W., 1999, Criteria for the recognition of partial melting: Physics and Chemistry of the Earth, Part A: Solid Earth and Geodesy, v. 24, no. 3, p. 269-279.

Scaillet, B., and Searle, M. P., 2006, Mechanisms and timescales of felsic magma segregation, ascent and emplacement in the Himalaya: *in* Law, R., Searle, M.P., Godin, L., ed., Channel Flow, Ductile Extrusion and Exhumation in Continental Collision Zones: Special Publications: London, Geological Society, v. 268, no. 1, p. 293-308.

Scaillet, B., Pichavant, M., and Roux, J., 1995, Experimental crystallization of leucogranite magmas: Journal of Petrology, v. 36, no. 3, p. 663-705.

Schärer, U., 1984, The effect of initial ^{230}Th disequilibrium on young U-Pb ages: the Makalu case, Himalaya: Earth and Planetary Science Letters, v. 67, p. 191-204.

Searle, M.P., 1999, Extensional and compressional faults in the Everest-Lhotse Massif, Khumbu Himalaya, Nepal: Journal of the Geological Society, v. 156, no. 2, p. 227-240.

Searle, M.P., 2001, Dating the Indian continental subduction and collisional thickening in the northwest Himalaya: Multichronology of the Tso Morari eclogites: Comment and Reply: Geology, v. 29, no. 2, p. 191-192.

Searle, M.P., 2010, Low-angle normal faults in the compressional Himalayan orogen; Evidence from the Annapurna-Dhaulagiri Himalaya, Nepal: Geosphere, v. 6, no. 4, p. 296-315.

Searle, M., and Godin, L., 2003, The South Tibetan Detachment and the Manaslu Leucogranite: a structural reinterpretation and restoration of the Annapurna-Manaslu Himalaya, Nepal.: The Journal of Geology, v. 111, p. 505-523.

Searle, M. P., and Phillips, R. J., 2009, Comment on: "Does the Karakoram fault interrupt mid-crustal channel flow in the western Himalaya?" by Mary L. Leech, Earth and Planetary Science Letters 276 (2008) 314-322: Earth and Planetary Science Letters, v. 286, p. 589-591.

Searle, M., Simpson, R.L., Law, R.D., Parrish, R.R., and Waters, D.J., 2003, The structural geometry, metamorphic and magmatic evolution of the Everest massif, High Himalaya of Nepal-South Tibet: Journal of the Geological Society, London, v. 160, p. 345-366.

Searle, M. P., Law, R. D., Godin, L., Larson, K. P., Streule, M. J., Cottle, J. M., and Jessup, M. J., 2008, Defining the Himalayan Main Central Thrust in Nepal: Journal of the Geological Society, v. 165, no. 2, p. 523-534.

Sibson, R.H., 1977, Fault rocks and fault mechanisms: Journal of Geological Society, v. 133, no. 3, p. 191-213.

Simonetti, A., Heaman, L.M., Chacko, T., and Banerjee, N. R., 2006, In situ petrographic thin section UPb dating of zircon, monazite, and titanite using laser ablationMCICP-MS: International Journal of Mass Spectrometry, v. 253, no. 1-2, p. 87-97.

Simpson, R.L., Parrish, R. R., Searle, M. P., and Waters, D. J., 2000, Two episodes of monazite crystallization during metamorphism and crustal melting in the Everest region of the Nepalese Himalaya: Geology, v. 28, no. 5, p. 403-406.

Sirbescu, M.-L.C., and Nabelek, P.I., 2003, Crustal melts below 400 °C: Geology, v. 31, no. 8, p. 685-688.

Srivastava, P., and Mitra, G., 1994, Thrust geometries and deep structure of the outer and lesser Himalaya, Kumaon and Garhwal (India): Implications for evolution of the Himalayan fold-and-thrust belt: Tectonics, v. 13, no. 1, p. 89-109.

St.-Onge, M. R., Searle, M.P., and Wodicka, N., 2006, Trans-Hudson orogen of North America and Himalaya-Karakorum-Tibetan orogen of Asia: structural and thermal characteristics of the lower and upper plates: Tectonics, v. 25, p. doi: 10.1029/2005-TC001907.

Steck, A., 2003, Geology of the NW Indian Himalaya: Swiss Journal of Geosciences, v. 96, no. 2, p. 147-196.

Stipp, M., Stünitz, H., Heilbronner, R., and Schmid, S. M., 2002, Dynamic recrystallization of quartz: correlation between natural and experimental conditions: *in* The Interpretation of Microstructures and Textures, Geological Society London Special Publications, v. 200, no. 1, p. 171-190.

Stüwe, K., and Foster, D., 2001, $^{40}Ar/^{39}Ar$ pressure, temperature and fission track constraints on the age and nature of metamorphism around the main central thrust in the eastern Bhutan Himalaya: Journal of Asian Earth Sciences, v. 19, no. 1-2, p. 85-95.

Tapponier, P., Zhiqin, X., Roger, F., Meyer, B., Arnaud, N., Wittlinger, G. and Jingsui, Y., 2001, Oblique stepwise rise and growth of the Tibet Plateau: Science, v. 294, p. 1671-1677.

Termier, G., and Gansser, A., 1974, Les series devoniennes du Tang Chu (Himalaya du Bhoutan): Eclogae Geologicae Helvetiae, v. 67, no. 3, p. 587-596.

Turcotte, D.L., and Schubert, G., 1982, Geodynamics: Applications of Continuum Physics to Geological Problems, John Wiley, Hoboken, N.J. 450 p.

Twiss, R.J., and Moores, E.M., 2007, Structural Geology: NewYork, Freeman & Co., 736 p.

Upreti, B.N., 1999, An overview of the stratigraphy and tectonics of the Nepal Himalaya: Journal of Asian Earth Sciences, v. 17, no. 5-6, p. 577-606.

Vannay, J.-C., and Hodges, K.V., 1996, Tectonometamorphic evolution of the Himalayan metamorphic core between the Annapurna and Dhaulagiri, central Nepal: Journal of Metamorphic Geology, v. 14, p. 635-656.

Vernon, R. H., 2000, Review of Microstructural Evidence of Magmatic and Solid-State Flow: Visual Geosciences, v. 5, no. 2, p. 1-23.

Villa, I.M., 2004, Geochronology of metamorphic rocks: Periodico di Mineralogia, v. 73, p. 259271.

Visonà, D. and Lombardo, B., 2002, Two-mica and tourmaline leucogranites from the Everest-Makalu region (Nepal-Tibet). Himalayan leucogranite genesis by isobaric heating?: Lithos, v. 62, p. 125-150.

Wager, L.R., 1934, A review of the geology and some new observations *in* Ruttledge, H., ed., Everest 1933: Hodder and Stoughton, London, 312336.

Wager, L.R., 1965, Injected granite sheets of the Rongbuk valley and the north face of Mount Everest, DN Wadia commemorative volume: India Mining, Geology and Metallurgy Institute, p. 358379.

Warren, C.J., Grujic, D., Kellett, D.A., Cottle, J., Jamieson, R.A. and Ghalley, K.S., *in review*. Probing the depths of the India-Asia collision: U-Pb monazite chronology of granulites from NW Bhutan: Tectonics.

Watson, E.B., and Harrison, T.M., 2005, Zircon thermometer reveals minimum melting conditions on earliest Earth: Science, v. 308, p. 841-844.

Watson, E.B., Wark, D.A., and Thomas, J.B., 2006, Crystallization thermometers for zircon and rutile: Contributions to Mineralogy and Petrology, v. 151, no. 4, p. 413-433.

Webb, A.A.G., Yin, A., Harrison, T.M., Célérier, J., and Burgess, W.P., 2007, The leading edge of the Greater Himalayan Crystalline complex revealed in the NW Indian Himalaya: Implications for the evolution of the Himalayan orogen: Geology, v. 35, no. 10, p. 955.

Wei, C., Clarke, G., Tian, W., and Qiu, L., 2007, Transition of metamorphic series from the kyanite- to andalusite-types in the Altai orogen, Xinjiang, China: Evidence from petrography and calculated KMnFMASH and KFMASH phase relations: LITHOS, v. 96, no. 3-4, p. 353-374.

Wernicke, B., 1981, Low-angle normal faults in the Basin and Range Province: nappe tectonics in an extending orogen: Nature, v. 291, p. 645-648.

Wernicke, B., 2009, The detachment era (1977-1982) and its role in revolutionizing continental tectonics: Geological Society London Special Publications, v. 321, no. 1, p. 1-8.

Wernicke, B., and Burchfiel, B.C., 1982, Modes of extensional tectonics: Journal of Structural Geology, v. 4, no. 2, p. 105-115.

Whitney, D.L., and Evans, B.W., 2010, Abbreviations for names of rock-forming minerals: American Mineralogist, v. 95, no. 1, p. 185-187.

White, N.M., Pringle, M., Garzanti, E., Bickle, M., Najman, Y., Chapman, H., and Friend, P., 2002, Constraints on the exhumation and erosion of the High Himalayan Slab, NW India, from foreland basin deposits: Earth and Planetary Science Letters, v. 195, no. 1-2, p. 29-44.

Whittington, A., Foster, G., Harris, N., Vance, D., and Ayres, M., 1999, Lithostratigraphic correlations in the western Himalaya; an isotopic approach: Geology, v. 27, no. 7, p. 585-588.

Whynot, N., Grujic, D., Long, S. and McQuarrie, N., 2010, Apparent temperature gradient across the Lesser Himalayan sequence: Raman spectroscopy on carbonaceous material in the eastern Bhutan Himalaya. 25th Himalayan-Karakorum-Tibetan Workshop abstract.

Wiesmayr, G., Grasemann, B., 2002, Eohimalayan fold and thrust belt: Implications for the geodynamic evolution of the NW-Himalaya (India): Tectonics, v. 21, no. 6, p. doi:10.1029/2002TC001363.

Wiesmayr, G., Edwards, M.A., Meyer, M., Kidd, W.S.F., Leber, D., Häusler, H., Wangda, D., 2002, Evidence for steady fault-accommodated strain in the High Himalaya: progressive fault rotation of the southern Tibet detachment system in NW Bhutan, *in* de Meer, S., Drury, M.R., de Bresser, J.H.P., Pennock, G.M., ed., Deformation Mechanisms, Rheology and Tectonics: Current Status and Future Perspectives: London, Geological Society, v. 200, p. 371-386.

Willett, S. D., 1999a, Rheological dependence of extension in wedge models of convergent orogens: Tectonophysics, v. 305, no. 4, p. 419-435.

Willett, S.D., 1999b, Orogeny and orography: The effects of erosion on the structure of mountain belts: Journal of Geophysical Research, v. 104, no. B12, p. 28957-28981.

Williams, I.S., 1997, U-Th-Pb geochronology by ion microprobe: not just ages but histories: Society of Economic Geologists Reviews in Economic Geology, v. 7, p. 1-35.

Williams, I.S., and Hergt, J.M., 2000, UPb dating of Tasmanian dolerites: a cautionary tale of SHRIMP analysis of high-U zircon: Beyond 2000: New Frontiers in Isotope Geoscience Conference, p. 185188.

Wopenka, B., Pasteris, J.D., 1993, Structural characterization of kerogens to granulite-facies graphite: Applicability of Raman microprobe spectroscopy: American Mineralogist, v. 78, p. 533-557.

Wu, C., Nelson, K.D., Wortman, G., Samson, S.D., Yue, Y., Li, J., Kidd, W.S.F., and Edwards, M.A., 1998, Yadong cross structure and South Tibetan Detachment in the east central Himalaya (89°-90°E): Tectonics, v. 17, no. 1, p. 28-45.

Xypolias, P., and Kokkalas, S., 2006, Heterogeneous ductile deformation along a mid-crustal extruding shear zone: an example from the External Hellenides (Greece): *in* Law, R., Searle, M.P., Godin, L., ed., Channel Flow, Ductile Extrusion and Exhumation in Continental Collision Zones: Special Publications: London, Geological Society, v. 268, p. 497-516.

Yardley, B.W.D., 1977, An empirical study of diffusion in garnet: American Mineralogist, v. 62, no. 7-8, p. 793-800.

Yin, A., 2006, Cenozoic tectonic evolution of the Himalayan orogen as constrained by along-strike variation of structural geometry, exhumation history, and foreland sedimentation: Earth Science Reviews, v. 76, no. 1-2, p. 1-131.

Yin, A., Dubey, C.S., Kelty, T.K., Gehrels, G.E., Chou, C.Y., Grovel, M., and Lovera, O., 2006, Structural evolution of the Arunachal Himalaya and implications for asymmetric development of the Himalayan orogen: Current Science, v. 90, no. 2, p. 195-200.

Yin, A., Dubey, C.S., Webb, A.A.G., Kelty, T.K., Grove, M., Gehrels, G.E., and Burgess, W.P., 2010, Geologic correlation of the Himalayan orogen and Indian craton: Part 1. Structural geology, U-Pb zircon geochronology, and tectonic evolution of the Shillong Plateau and its neighboring regions in NE India: Geological Society of America Bulletin, v. 122, no. 3-4, p. 336-359.

APPENDIX A

FIELD DATA

Field data is available electronically in an Excel data file at the back of this thesis.

APPENDIX B

SUMMARY OF AUTHOR CONTRIBUTIONS, CHAPTERS 2-5

B.1 CHAPTER 2

This chapter was written by D. Kellett. Field sampling and mapping of the Lingshi and Ura field areas was conducted by D. Kellett. Field sampling and mapping of the Masang Kang field area was conducted by D. Grujic. D. Kellett did all mineral separations and conducted SHRIMP analyses in 2007 and 2008 at Stanford University with assistance by D. Grujic. K. Taylor conducted $^{40}Ar/^{39}Ar$ analyses in 2007 and 2008 at Dalhousie University. S. Erdmann provided in-depth granite petrology, and critical review of the manuscript. A version of this chapter has been published as: Kellett, D.A., Grujic, D. and Erdmann, S., 2009, Miocene structural reorganization of the South Tibetan detachment, eastern Himalaya: implications for continental collision. Lithosphere, 1(5), 259-281.

B.2 CHAPTER 3

This chapter was written by D. Kellett, with critical review and minor contributions from all other authors. Field sampling and mapping of the Lingshi and Ura field areas was conducted in 2006 by D. Kellett, and in 2008 by D. Kellett with the assistance of T. Tenzin. D. Kellett described samples, collected electron microprobe analyses for pressure-temperature-time analyses and monazite characterization, and conducted LA-ICP-MS U-Pb analyses in 2009 at the NERC Isotope Geosciences Laboratory with assistance from J. Cottle, C. Warren and M. Horstwood. C. Warren collected electron microprobe analyses

for those samples described in Appendix G. R. Jamieson was involved in discussion and writing of a comparison of the results with numerical model predictions. A version of this chapter has been published as: Kellett, D.A., Grujic, D., Warren, C., Cottle, J, Jamieson, R.A. and Tenzin, T., 2010, Metamorphic history of a syn-convergent orogen-parallel detachment: The South Tibetan detachment system, Bhutan Himalaya. Journal of Metamorphic Geology, 28, 785-808.

B.3 CHAPTER 4

This chapter was written by D. Kellett with contributions from and critical review by D. Grujic. Field sampling and mapping of the Lingshi field area was conducted by D. Grujic and D. Kellett with assistance from I Coutand and C. Warren. D. Kellett prepared and described the samples and collected Raman spectra with guidance from K. Hewitt and assistance from L. Hilchie and N. Whynot. A version of the chapter is in preparation for submission to Earth and Planetary Science Letters for peer review as: Kellett, D.A. and Grujic, D., Structure and metamorphism from mid- to upper crust in the Bhutan Himalaya: defining the South Tibetan detachment system.

B.4 CHAPTER 5

This chapter was written by D. Kellett, with critical review by D. Grujic. Field sampling and mapping was conducted by D. Kellett and D. Grujic. Samples for ϵNd analysis were prepared by D. Kellett, and analyzed by S. Duchêne in Nancy, France.

APPENDIX C

THERMOBAROMETRY OF MAGMATIC ANDALUSITE

Andalusite makes up to $\leq$3 vol % of BH 225, forming $\leq$1 mm large, subhedral to euhedral single crystals, or clusters of crystals that are $\sim$50-1000 mm large, anhedral to subhedral, and randomly oriented (Fig. C.1a). Most andalusite grains display concentric or sector zoning, are inclusion-free and are partially replaced by sillimanite and muscovite. Andalusite occurs in interstitial spaces between phenocrysts, along grain boundaries, or as marginal inclusions in zoned magmatic plagioclase and cordierite. Similar andalusite has previously been described from Miocene leucogranites of the Everest-Makalu region (e.g., Searle, 1999; Visonà and Lombardo, 2002). The andalusite- and sillimanite-bearing leucogranites of the Everest-Makalu region have been interpreted as peritectic magmatic minerals and possibly as restite crystals (Visonà and Lombardo, 2002).

The presence of andalusite in BH 225 therefore indicates that the leucogranite crystallized at low pressures. The maximum P-T-X stability for andalusite remains controversial, given difficulties to constrain the exact locations of the andalusitesillimanite field boundary and the position of the granite solidus for specific compositional systems (e.g., Clarke et al., 2005). Assuming the water-saturated granite solidi of Scaillet et al. (1995) or Holtz et al. (2001), and the andalusite—sillimanite stability field proposed by Richardson et al. (1969), andalusite may crystallize at a pressure as high as ca. 4.8-5.2 kbar at 630-650 °C. Assuming the andalusitesillimanite stability field proposed by Pattison (1992), which has found support in most recent studies (e.g., Cesare et al., 2003; Johnson et al., 2003; Wei et al., 2007), andalusite may have its maximum stability at only 2.6-3.0 kbar at 640-660 °C.

For BH 225, we suggest that andalusite crystallized close to or at the solidus (given its interstitial occurrence), and therefore at a pressure of probably $\leq$2.8 kbar (medium grey field, Fig. C.1c), or at maximum $\leq$5.0 kbar (light grey field, Fig. C.1c).

Evidence for significant deformation during magmatic evolution is lacking. The rock fabrics discussed above indicate that the leucogranites were deformed at sub-solidus conditions. Locally developed shear bands host muscovite and fibrolitic sillimanite, which partly rim magmatic andalusite. To crystallize sillimanite following andalusite, pressure or temperature must have increased, or the composition of the system must have changed in a way that reduced the andalusite stability to lower temperatures or pressures (e.g., by reducing Mn or Fe^{3+} concentrations; Grambling and Williams, 1985). A pressure increase seems unlikely since all thermobarometric studies to date suggest continuous decompression for the GHS at that time (e.g., Hollister and Grujic, 2006 and references therein). On the other hand, a small, short-term temperature increase and/or compositional modification of the system during high-temperature, sub-solidus deformation, seem both probable. Hot fluids, liberated from large granite intrusions may have facilitated deformation, and percolated along the shear bands, permitting the crystallization of sillimanite over magmatic andalusite.

Figure C.1: Andalusite thermobarometry. (a) Subhedral, single andalusite crystal interstitial to plagioclase and quartz, partly replaced by muscovite. Photomicrograph with crossed polarizers. (b) Andalusite, sillimanite, and muscovite along a leucogranite micro-shear band. Andalusite is randomly oriented (different grey scales in image), and rimmed by oriented sillimanite and muscovite. Photomicrograph with crossed polarizers. (c) Temperature and pressure locations of experimentally-determined stability fields for aluminum silicate polymorphs and wet granite solidi curves. Solidi are from Scaillet et al. (1995) and from Holtz et al. (2001); aluminum silicate stability fields are from Richardson et al. (1969) (R 69), Holdaway (1971) (H 71), and Pattison (1992) (P 92). The light grey field outlines the estimated maximum stability field for andalusite in our samples. The dark grey field highlights the estimated pressure for the crystallization and re-equilibration of muscovite along shear bands (after Massonne and Schreyer, 1987). The black field shows the most probable pressure and temperature conditions for muscovite formation and re-equilibration. The star marks the estimated conditions for the final crystallization of leucogranite BH 225.

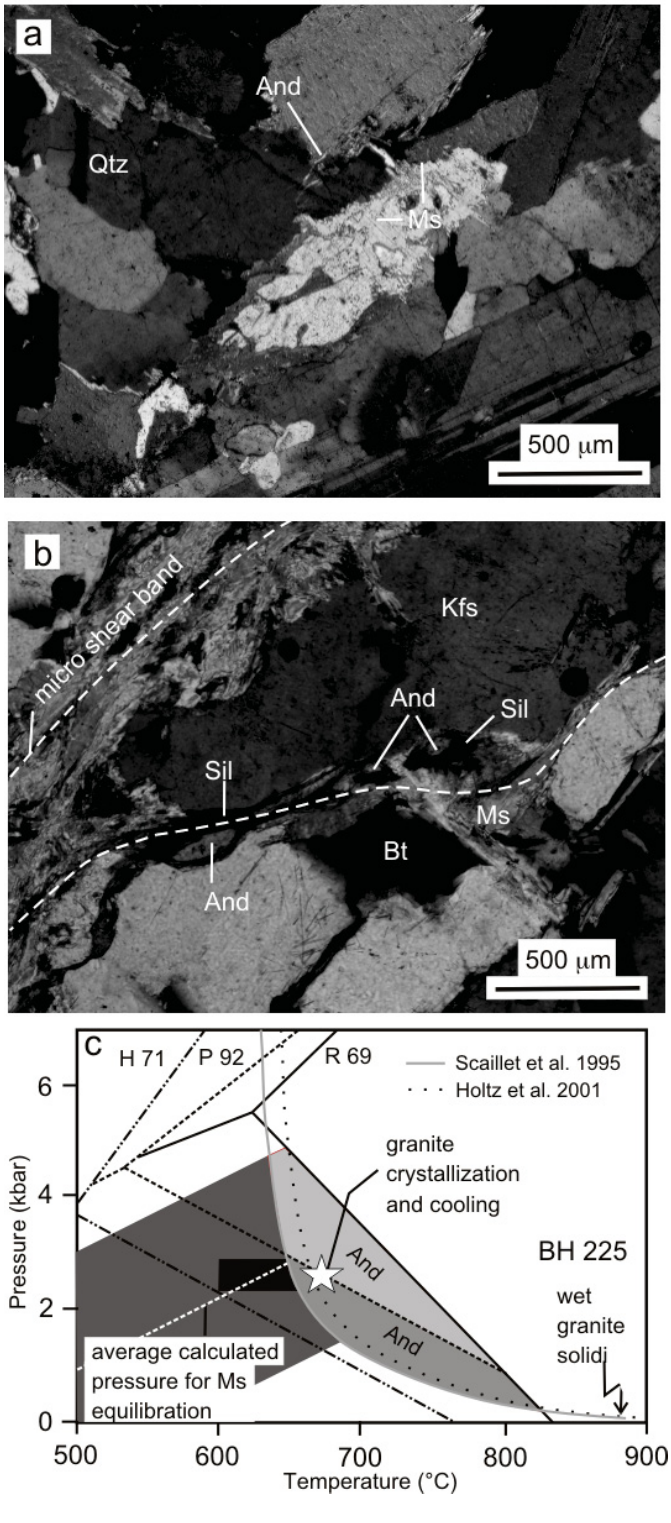
a
And
Qtz
Ms
500 μm
b
micro shear band
Kfs
And
Sil
Sil
Ms
Bt
And
500 μm
c
H 71
P 92
R 69
Scaillet et al. 1995
Holtz et al. 2001
granite
crystallization
and cooling
BH 225
wet
granite
solidi
And
And
average calculated
pressure for Ms
equilibration
Pressure (kbar)
Temperature (°C)
0
2
4
6
500
600
700
800
900

APPENDIX D

SHRIMP-RG ANALYTICAL PROCEDURES

D.1 SHRIMP-RG ANALYTICAL PROCEDURE FOR U-PB GEOCHRONOLOGY AND TRACE-ELEMENT GEOCHEMISTRY

Minerals, concentrated by standard heavy mineral separation processes and hand picked for final purity, were mounted on double-stick tape on glass slides in 1 x 6 mm rows, cast in epoxy, ground and polished to a 1 μm finish on a 25 mm diameter by 4 mm thick disc. All grains were imaged with transmitted light and reflected light (and incident light if needed) on a petrographic microscope, and with cathodoluminescence and back scattered electrons (for older zircons) as needed on a JEOL 5600 SEM to identify internal structure, inclusions and physical defects. Fractures observed in the zircons during imaging are likely a result of the separation process (crushing and milling) since the least fractured grains are found in sample BH 225, which was separated by Selfrag. The fractures also coincide with porous areas of the zircon grains, which are likely weaker zones. The mounted grains were washed with 1N HCl or EDTA solution (if acid soluble) and distilled water, dried in a vacuum oven, and coated with Au. Mounts typically sat in a loading chamber at high pressure (10-7 torr) for several hours before being moved into the source chamber of the SHRIMP-RG. Secondary ions were generated from the target spot with an O_2^- primary ion beam varying from 4-6 nA. The primary ion beam produced a spot with a diameter of 20-40 μm and a depth of 1-2 μm for an analysis time of 9-12 minutes. Nine peaks were measured sequentially for zircons (the SHRIMP-RG is limited to a single collector, usually an EDP electron multiplier): $^{90}Zr_2{}^{16}O$, ^{204}Pb, Bgd (0.050 mass units above ^{204}Pb), ^{206}Pb,

^{207}Pb, ^{208}Pb, ^{238}U, ^{248}Th^{16}O, ^{254}U^{16}O. Autocentering on selected peaks and guide peaks for low or variable abundance peaks (i.e. ^{96}Zr^{216}O 0.165 mass unit below ^{204}Pb) were used to improve the reliability of locating peak centers. The number of scans through the mass sequence and counting times on each peak were varied according to sample age and U and Th concentrations to improve counting statistics and age precision. Measurements were made at mass resolutions of 6000-8000 (10% peak height) which eliminated all interfering atomic species. The SHRIMP-RG was designed to provide higher mass resolution than the standard forward geometry of the SHRIMP I and II (Clement and Compston, 1994). This design also provides very clean backgrounds and combined with the high mass resolution, the acid washing of the mount, and rastering the primary beam for 90-120 seconds over the area to analyzed before data is collected, assures that any counts found at mass ^{204}Pb are actually Pb from the zircon and not surface contamination. In practice greater than 95% of the spots analyzed have no common Pb. Concentration data for zircons are standardized against zircon standard R33 (419 Ma, quartz diorite of Braintree complex, Vermont, John Aleinikoff, pers. comm.) which are analyzed repeatedly throughout the duration of the analytical session. Data reduction follows the methods described by Williams (1997) and Ireland and Williams (2003) and uses the Squid and Isoplot programs of Ken Ludwig (Ludwig, 2001; 2003). Between U-Pb analyses and Ti-in-zircon analyses the zircon mounts were repolished and recoated with gold.

D.2 ZIRCON CHARACTERIZATION

Zircons were imaged under cathodoluminescence (CL) and back-scattered electrons (BSE) using a JEOL scanning electron microscope (Fig. A1; Hanchar and Miller, 1993). The five samples collected from leucogranites within the hanging wall of the lower STD share many characteristics. Sample DBH 003 zircons are small (50-200 μm along long axis), while the other grains range from 150-500 μm. Some grains display both terminations, but many are fractured, possibly by crushing during sample preparation due to the porous structure of many of the grains. DBH 003 and DBH 036 yielded a few zircons with distinctive bright xenocrystic cores rimmed by either thick, sector-zoned, dark under CL (low U) rims (i.e., Fig. D.1a, grains 11 and 14) or by zircon with a mottled texture (i.e., Fig. D.1a, grains 8 and 9). However, most of the grains lack xenocrystic cores and the interiors of the zircons are mottled, containing numerous holes and inclusions, while their

concentrically-zoned igneous-type rims are typically free of holes and inclusions (see BSE images, Fig. D.1b). In sample DBH 031 zoned rims are typically observed only at pyramid terminations, not along the prism faces, and there are thin, bright under CL (low U) rims ringing some crystals, perhaps indicating late local recrystallization (Corfu et al., 2003; see CL images, Fig. D.1c). Sample DBH 036 zircons generally exhibit thick ($\leq$50 μm thick), concentrically-zoned rims (Fig. D.1d) and grain interiors composed of mottled zircon with holes and inclusions (Fig. D.1d grain 3), except for one grain that has a more complex internal texture of zonation (Fig. D.1d grain 10). DBH 080 zircons rims are only locally concentrically-zoned. Grain interiors have the mottled texture, with abundant inclusions and holes, although some sections also appear cloudy and dark under CL (e.g., Fig. D.1e).

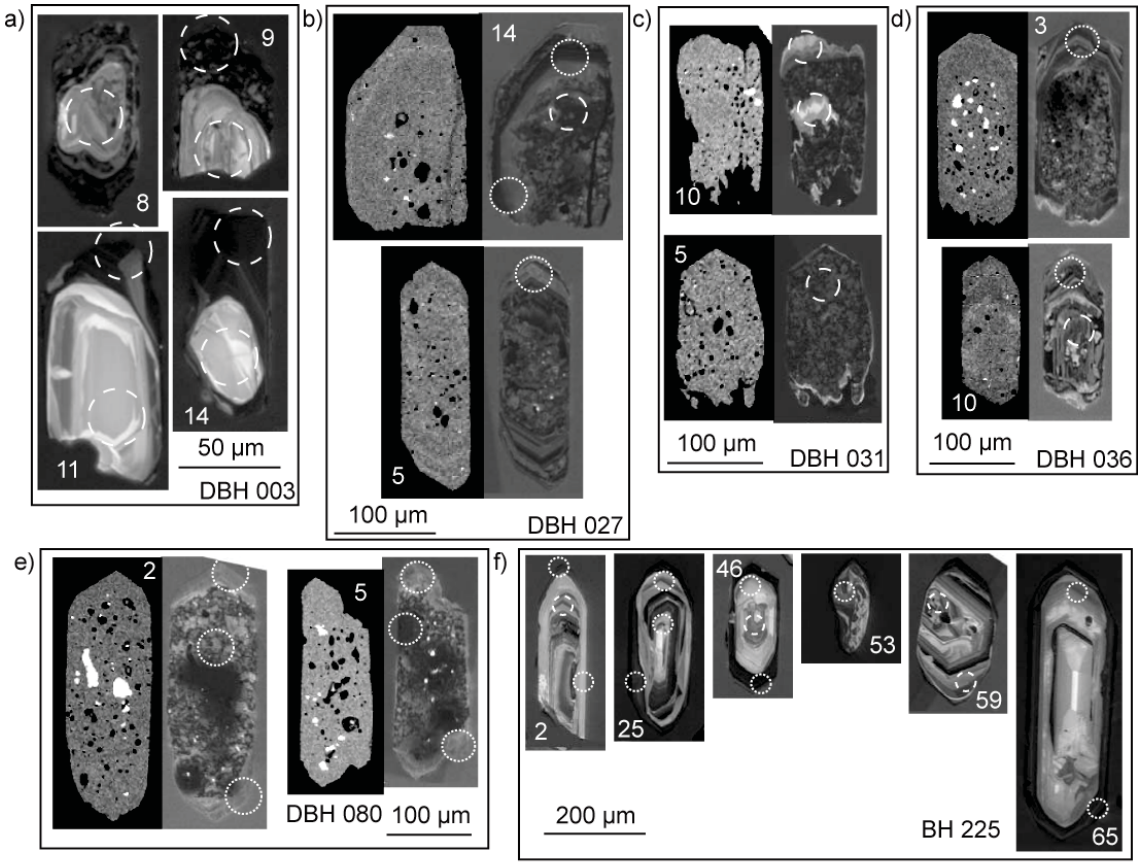

Figure D.1: Zircon characterization. (a) and (f) are imaged by cathodoluminescence (CL) only, while for (b)-(e), back-scattered electron images are on the left and CL images of the same grains are on the right. Dashed circles denote spots for U-Pb analyses while dotted circles denote spots for both U-Pb and Ti-in-zircon analyses.

There are at least three texturally-distinct growth phases present in the zircons

described above. Bright xenocrystic cores in DBH 003 and the zoned core in DBH 036 are probably relicts from protoliths. All samples (with the exception of DBH 003) contain zircons with concentrically zoned rims, although growth zoning is only locally observed in DBH 080. Oscillatory rims are widely described as in the literature as magmatic. Here the oscillatory, concentrically zoned rims likely grew during crystallization of the leucogranites. The dark (under CL, light under BSE) color of both the rims and the mottled texture indicates the generally high U content of the zircons (Rubatto and Gebauer, 2000). The origin of the mottled zircon texture, which comprises a significant component of almost all zircon grains, is uncertain. It has been observed elsewhere in zircons from leucogranites derived from partial melting and crystallization under low P/low T conditions (Booth et al., 2004). A locally observed faint oscillatory zonation (e.g., Fig. 2.4a grain 8) and young intermediate ages (between detrital core and magmatic rim ages) suggest sub-solidus recrystallization. However, the texture is not one typically observed in recrystallized zircons (i.e., Rubatto and Gebauer, 2000). It could possibly be a product of a highly fractionated, trace element-rich early partial melt. The high U content, abundant holes and inclusions and uncertain origin of the mottled zircon texture make it difficult to interpret U-Pb results from this phase. Thus, they will not be considered further, and interpretation of U-Pb ages will be confined to the cores and rims, although results from mottled zircon are included in the data tables. Thin bright rims found surrounding some zircon crystals (e.g., Fig. D.1c grain 5) may reflect another growth phase but as these rims are too thin to sample, their ages cannot be determined.

BH 225 zircons are texturally distinct from the lower STD zircons described above, and contain from two to four distinct growth phases. In general, cores display a range of sector zoning (Fig. D.1f grain 65), concentric zoning (Fig. D.1f grain 25), or more complex convoluted zoning (Fig. D.1f grain 53), suggesting a sedimentary protolith (Rubatto and Gebauer, 2000). Cores are often embayed and surrounded by grey-under-CL zircon with weak or no concentric zoning (i.e., Fig. D.1f grain 2) and then rimmed by zircon that is concentrically zoned and dark under CL. The grey-under-CL zircon may be magmatic or metamorphic. Dating of this texture yielded detrital ages, mixed ages and ages coincident with dark rims. Again, the dark, oscillatory-zoned rims are likely magmatic in origin, crystallizing in the leucogranite. The mottled texture ubiquitous to zircons found in the lower STD is not observed in this sample, and the grains are relatively free of holes

and inclusions, except for isolated large inclusions commonly observed in the cores (i.e., Fig. D.1f grain 59).

D.3 TRACE-ELEMENT GEOCHEMISTRY OF MOTTLED ZIRCON

The trace element geochemistry of mottled zircon is similar to that of the zircon rims. Most of the mottled zircons display a small positive Ce anomaly, and a large negative Eu anomaly. Mottled zircon from sample DBH 003 is variable and distinct from the other samples, ranging from a small positive to a small negative Ce anomaly, a small to no Eu anomaly and an abundance of light rare earth elements (LREEs). This variability in trace element geochemistry may indicate contamination by inclusions, a different protolith source, or that it is not an analogous growth phase to the mottled zircon in the other four samples.

APPENDIX E

ZIRCON TRACE-ELEMENT DATA

Chondrite-normalized trace-element values for zircon used to plot trace-element patterns. Chondrite-normalizing values are from McDonough and Sun (1995). For sample labels: bold=rims, regular=mottled, italics=cores, grey=BH 225 grey interior, grey fill=anomalous REE pattern (not plotted in Fig. 5). §Calculated from Anders and Grevesse (1989). *Calculated, not measured. N subscript denotes that values were chondrite-normalized before calculation.

	La	Ce	Pr§	Nd	Sm	Eu	Gd	Tb	Dy	Ho	Er	Tm	Yb	Lu	$(Sm/La)_N$	Ce/Ce*	Hf (ppm)	Eu/Eu*	Th/U	$(Yb/Gd)_N$
DBH 003																				
1.1	389.482	120.69	112.39	60.38	68.90	98.18	127.8		519		1078		4085		0.2	0.48	9883	0.9981	1.0804	31.95
10.1	125.919	39.50	31.29	15.60	14.59	9.99	47.5		285		822		2686		0.1	0.50	9482	0.3217	0.0662	56.53
11.1	1.604	2.28	1.04	0.83	15.34	5.81	194.3		877		1853		2610		9.6	1.73	10657	0.0554	0.0132	13.44
11.2	0.365	17.42	0.79	1.15	8.64	3.27	54.8		188		507		870		23.7	30.28	9639	0.1030	0.4191	15.88
12.1	7.853	12.36	10.34	11.87	73.51	21.30	466.3		2358		5270		12948		9.4	1.36	10930	0.0789	0.0984	27.77
14.1R	11.726	12.33	5.51	3.78	36.41	16.75	333.5		964		1639		1966		3.1	1.43	10560	0.0906	0.0359	5.89
14.2C	0.192	46.13	0.91	1.96	18.37	16.26	158.4		493		1196		1432		95.4	84.04	10139	0.1840	0.3564	9.04
2.1	25.505	6.19	10.62	6.86	25.35	5.49	118.5		432		1123		3093		1.0	0.34	10572	0.0763	0.0229	26.10
3.1	2.376	2.08	1.51	1.20	5.69	1.43	31.5		301		1168		4816		2.4	1.07	10936	0.0771	0.1996	152.80
4.1	4.100	5.64	2.97	2.52	17.31	7.11	149.1		816		1713		2812		4.2	1.60	10066	0.0855	0.0344	18.86
5.1	1.171	1.34	0.75	0.60	8.53	1.10	92.6		512		1106		1639		7.3	1.40	8964	0.0218	0.0200	17.70
5.2C	2707.946	2181.95	1251.61	850.91	763.80	74.59	762.6		637		1323		3071		0.3	1.10	10176	0.0977	0.8441	4.03
6.1	2.321	3.28	1.50	1.21	15.53	5.27	203.0		1489		3509		6106		6.7	1.72	9257	0.0482	0.0136	30.08
7.1	19.366	26.37	18.18	17.62	61.30	6.76	170.4		686		2164		8895		3.2	1.40	10209	0.0583	1.0569	52.21
8.1	6.192	14.98	4.42	3.73	9.14	4.88	48.0		205		677		1684		1.5	2.82	10352	0.1709	0.1399	35.11
9.1	85.020	18.04	32.79	20.36	36.71	18.02	92.9		375		1047		3998		0.4	0.31	10202	0.2782	0.6898	43.04
9.2	13.704	39.94	8.35	6.51	36.82	14.87	189.0		460		1069		1623		2.7	3.62	10023	0.1317	0.7047	8.59
DBH 027																				
2.2	0.000	0.57	0.00	0.25	9.39	1.35	171.7	717	1119	1047	1055	1130	1120	762			29951	0.0336	0.0040	5.40
A4.1	0.028	0.37	0.07	0.10	4.99	1.14	89.9	389	653	697	714	836	881	721	180	8.5	27945	0.0540	0.0031	8.11
A2.1	0.073	0.43	0.13	0.17	5.10	0.35	65.2	266	428	503	456	537	594	599	70	4.5	30434	0.0193	0.0073	7.53
6.1	1.655	1.05	0.53	0.30	8.31	1.60	149.9	622	1029	1033	1127	1377	1590	1237	5	1.1	27586	0.0452	0.0039	8.78
2.1	0.020	0.53	0.08	0.16	4.68	0.72	78.8	348	571	626	678	824	884	751	236	13.3	26530	0.0372	0.0033	9.29
14.1	0.864	1.47	1.24	1.48	14.71	1.76	155.9	603	1045	1112	1288	1534	1652	1193	17	1.4	22503	0.0368	0.0044	8.78
17.1	3.281	1.77	0.58	0.24	3.63	0.85	49.5	200	359	414	426	510	572	465	1	1.3	23236	0.0632	0.0033	9.57
1.1	0.087	0.64	0.09	0.10	4.53	0.57	83.8	368	602	649	679	901	979	899	52	7.1	27452	0.0294	0.0035	9.67
14.3	0.020	0.61	0.11	0.25	7.86	1.35	128.2	517	937	1089	1315	1717	1910	1585	397	13.1	20227	0.0426	0.0044	12.33
19.2	0.046	0.37	0.08	0.10	2.53	0.45	46.9	202	360	435	523	710	794	780	54	6.1	36031	0.0417	0.0042	14.02
A11.1	0.039	0.58	0.09	0.14	3.59	0.55	48.7	197	371	439	585	808	919	926	91	9.7	23904	0.0420	0.0037	15.62
20.1	0.219	0.55	0.21	0.20	1.84	0.49	25.7	114	225	299	384	517	569	557	8	2.6	21937	0.0713	0.0024	18.31
15.1	0.082	0.45	0.07	0.06	2.54	0.42	34.9	152	294	420	504	703	795	725	31	5.9	19454	0.0449	0.0029	18.83
1.2	0.048	0.42	0.08	0.10	2.04	0.32	34.7	131	258	340	446	611	700	660	42	6.9	20351	0.0384	0.0020	16.69
A11.2	0.127	0.52	0.13	0.14	2.50	1.42	39.2	187	356	459	583	808	983	1000	20	4.0	23356	0.1438	0.0035	20.74
19.1	0.365	1.04	0.39	0.41	3.19	4.26	35.4	146	289	406	491	670	815	756	9	2.7	21630	0.4008	0.0430	19.05
A4.2	0.086	0.48	0.06	0.05	1.85	0.44	28.4	130	245	319	426	596	733	703	21	6.8	19821	0.0612	0.0026	21.35
A3.1	0.124	0.63	0.30	0.46	6.20	0.68	66.8	262	450	570	711	1079	1419	1501	50	3.3	20022	0.0336	0.0042	17.60
5.1	0.046	0.40	0.10	0.14	1.68	0.33	28.9	139	280	398	528	742	938	889	36	6.0	28530	0.0479	0.0084	26.88
A12.1	0.037	0.40	0.05	0.07	1.89	0.29	31.5	150	290	394	580	792	1103	1187	50	8.8	24196	0.0375	0.0031	29.02
A1.2	0.044	0.34	0.08	0.12	2.34	0.64	44.5	162	350	547	784	1179	1551	1653	53	5.6	24905	0.0627	0.0033	28.84
A1.1	0.119	0.31	0.07	0.05	2.14	0.46	29.5	150	312	479	746	1099	1497	1602	18	3.5	26923	0.0576	0.0035	42.03
9.1	2.880	1.77	0.68	0.33	3.33	1.23	29.8	151	362	581	906	1431	1909	2010	1	1.3	33052	0.1239	0.0066	52.95
11.1	7.206	4.40	0.86	0.30	2.64	2.42	39.1	164	352	539	883	1539	2228	2649	0	1.8	26639	0.2378	0.0061	47.16

	La	Ce	Pr§	Nd	Sm	Eu	Gd	Tb	Dy	Ho	Er	Tm	Yb	Lu	$(Sm/La)_N$	Ce/Ce*	Hf (ppm)	Eu/Eu*	Th/U	$(Yb/Gd)_N$
A5.1	0.393	0.62	0.21	0.16	1.36	0.85	20.8	89	196	346	550	954	1347	1640	3	2.2	19341	0.1600	0.0033	53.70
DBH 031																				
10.1	0.646	1.77	0.16	0.08	1.31	0.04	12.2		97		192		452		2.0	5.56	39797	0.0099	0.0813	30.60
10.2	0.622	1.63	0.33	0.24	2.69	0.14	22.1		135		267		797		4.3	3.60	41103	0.0186	0.0531	29.88
12.1	1.727	2.05	0.62	0.37	2.41	0.12	17.8		127		321		1114		1.4	1.99	37752	0.0186	0.0294	51.94
15.1	0.385	1.55	0.22	0.16	1.50	0.11	10.8		94		218		753		3.9	5.34	40906	0.0274	0.0349	57.46
15.2	1.029	2.01	1.08	1.11	15.06	0.19	84.8		291		414		1078		14.6	1.90	37345	0.0052	0.0197	10.52
16.1	2.444	2.43	0.52	0.24	1.48	1.23	12.3		99		170		381		0.6	2.15	35934	0.2882	0.0710	25.61
2.1	2.223	2.37	1.38	1.08	21.25	0.46	171.3		657		649		1226		9.6	1.35	44530	0.0076	0.0197	5.93
25.1	933.958	253.89	97.24	31.38	30.83	2.68	69.3		232		325		812		0.0	0.84	32084	0.0580	0.0436	9.70
28.1	7.949	4.88	2.57	1.46	3.94	0.13	20.8		125		259		924		0.5	1.08	36231	0.0141	0.0157	36.80
3.1	3.009	3.27	3.16	3.24	45.55	0.55	217.7		704		844		2139		15.1	1.06	39145	0.0055	0.0518	8.13
4.1	0.217	1.14	0.07	0.04	0.64	0.15	7.0		65		193		615		2.9	9.40	39042	0.0709	0.0679	72.25
5.1	1.378	1.65	1.30	1.26	24.60	0.20	135.5		417		558		1339		17.8	1.24	30773	0.0035	0.0133	8.18
8.1	0.828	1.23	0.90	0.93	15.60	0.06	93.0		317		367		1063		18.8	1.43	52046	0.0017	0.0177	9.45
9.1	3.585	5.32	6.13	8.02	109.62	0.76	488.4		1356		1347		2976		30.6	1.13	52762	0.0033	0.0253	5.04
31.1	1.280	2.43	2.38	3.24	53.59	0.32	227.9		484		559		1395		41.9	1.39	50529	0.0029	0.0273	5.07
DBH 036																				
1.1	0.024	0.40	0.06	0.09	4.41	0.13	61.3	288	516	554	744	1192	1635	1529	183	10.6	37510	0.0080	0.0140	22.09
2.1	0.907	2.39	1.23	1.44	20.66	0.17	134.6	409	635	675	928	1420	1757	1584	23	2.3	35156	0.0033	0.0227	10.81
3.1	0.077	0.58	0.10	0.11	2.67	0.22	35.0	182	413	625	1108	2131	3331	3771	35	6.7	34198	0.0225	0.0218	78.71
4.1	0.047	0.31	0.09	0.12	2.53	0.14	36.1	142	278	387	568	886	1173	1251	53	4.9	21826	0.0146	0.0052	26.88
5.2	0.837	1.77	1.22	1.48	7.21	0.99	67.6	204	397	503	1228	2405	4213	5441	9	1.8	26119	0.0449	0.0135	51.58
6.1	0.009	0.42	0.03	0.05	3.38	0.02	39.6	193	364	410	613	941	1401	1380	360	25.9	33052	0.0021	0.0091	29.27
8.1	1.292	0.66	0.21	0.08	2.40	0.19	25.9	119	230	314	436	684	914	973	2	1.3	31504	0.0241	0.0065	29.28
9.1	0.574	0.95	0.60	0.62	5.88	0.40	47.9	176	312	463	608	982	1370	1557	10	1.6	27037	0.0240	0.0101	23.69
10.1	0.000	0.60	0.00	0.07	1.84	1.05	23.3	72	102	99	96	105	110	94			19487	0.1599	0.0112	3.90
11.1	0.449	0.85	0.43	0.42	7.08	0.16	94.6	401	647	677	764	987	1108	1029	16	1.9	27565	0.0063	0.0061	9.70
13.1	0.230	0.98	0.56	0.87	15.63	1.39	205.4	749	1481	2096	3262	4719	6010	6162	68	2.7	22659	0.0246	0.0065	24.22
14.1	0.052	0.53	0.11	0.15	2.92	0.02	49.6	239	446	535	728	1202	1790	1763	56	7.1	35533	0.0019	0.0104	29.89
15.1	2.634	1.62	0.60	0.28	5.42	0.75	70.6	256	498	697	1066	1706	2405	2748	2	1.3	24614	0.0385	0.0054	28.17
16.1	0.731	3.67	1.06	1.27	17.24	0.05	145.5	451	602	608	721	1095	1425	1252	24	4.2	64358	0.0009	0.0195	8.10
19.1	1.160	0.83	0.29	0.14	2.11	0.09	25.6	114	232	307	454	749	1074	1162	2	1.4	30010	0.0123	0.0073	34.71
20.1	0.842	1.16	0.48	0.36	4.07	1.28	89.1	354	643	736	1189	1715	2286	2353	5	1.8	22349	0.0672	0.0093	21.25
25.1	0.120	0.54	0.12	0.12	2.11	0.10	31.8	111	168	151	180	237	284	246	18	4.5	41626	0.0126	0.0132	7.39
28.1	0.714	0.82	0.29	0.18	2.77	0.22	40.3	192	386	514	699	1030	1335	1371	4	1.8	30983	0.0211	0.0097	27.41
DBH 080																				
1.1	0.049	0.43	0.09	0.11	5.09	0.12	59.6	131	100	54	34	43	34	33	104	6.6	39934	0.0070	0.0092	0.57
2.1	0.049	0.45	0.07	0.08	2.75	0.13	38.3	144	187	136	138	184	241	223	57	7.8	31209	0.0129	0.0062	6.29
2.3	2.352	9.82	8.40	15.87	109.28	0.53	207.0	395	365	260	250	337	421	388	46	2.2	31501	0.0035	0.0326	2.03
5.1	0.078	0.40	0.14	0.18	4.35	0.14	77.9	220	196	113	90	102	98	92	56	3.9	30621	0.0078	0.0062	1.26
5.3	0.954	3.30	2.70	4.53	32.61	0.30	80.6	169	133	83	63	71	82	78	34	2.1	33775	0.0058	0.0364	1.02
9.2	0.050	0.36	0.11	0.15	4.48	0.13	45.4	133	138	95	80	86	92	69	90	4.9	39748	0.0093	0.0067	2.02

	La	Ce	Pr§	Nd	Sm	Eu	Gd	Tb	Dy	Ho	Er	Tm	Yb	Lu	$(Sm/La)_N$	Ce/Ce*	Hf (ppm)	Eu/Eu*	Th/U	$(Yb/Gd)_N$
14.1	0.098	0.49	0.09	0.09	3.07	0.15	39.2	136	151	102	94	130	145	140	31	5.1	31375	0.0135	0.0062	3.69
15.1	0.060	0.31	0.07	0.08	4.16	0.09	47.2	114	94	47	36	34	32	32	69	4.8	36431	0.0068	0.0072	0.69
17.1	0.040	0.29	0.06	0.08	5.10	0.06	59.8	136	128	94	93	134	184	170	126	5.9	42314	0.0033	0.0119	3.07
22.1	0.048	0.46	0.06	0.06	2.77	0.13	40.4	130	136	94	97	116	145	127	57	8.7	33397	0.0127	0.0062	3.58
22.2	0.053	0.42	0.07	0.09	3.21	0.13	50.6	139	127	75	65	75	83	75	60	6.7	30122	0.0103	0.0060	1.65
25.1	0.055	0.32	0.05	0.05	3.13	0.09	42.3	114	97	56	42	41	48	48	57	6.0	31983	0.0081	0.0052	1.14
27.1	0.057	0.34	0.05	0.05	2.74	0.09	49.1	140	133	76	60	74	80	72	48	6.3	31088	0.0074	0.0055	1.64
1.2	0.631	1.78	1.49	2.28	32.03	0.31	213.8	558	658	520	449	513	537	447	51	1.8	29568	0.0038	0.0091	2.51
2.2	0.384	1.07	0.87	1.30	16.07	0.07	81.4	190	222	190	240	388	536	542	42	1.9	28591	0.0019	0.0050	6.59
2.2B	0.329	1.07	0.72	1.07	14.69	0.04	124.9	338	390	284	295	389	468	411	45	2.2	31463	0.0010	0.0110	3.74
5.2	0.802	1.48	1.80	2.71	28.16	0.29	126.8	303	395	447	656	1257	1961	2340	35	1.2	29555	0.0048	0.0278	15.47
9.1	0.579	1.71	1.27	1.88	47.41	0.30	396.6	827	675	381	259	222	196	124	82	2.0	46375	0.0022	0.0286	0.49
11.1	0.230	0.72	0.35	0.44	11.53	0.07	128.0	298	274	161	127	119	123	86	50	2.5	28716	0.0017	0.0106	0.96
12.1	0.180	0.56	0.22	0.24	5.15	0.07	55.4	154	184	136	151	209	262	268	29	2.8	30968	0.0039	0.0115	4.74
16	0.020	1.08	0.08	0.17	16.55	0.15	214.7	620	611	366	266	260	227	158	814	26.1	73091	0.0025	0.0244	1.06
16.2	0.903	0.83	0.71	0.63	15.46	0.50	177.0		292	140	86	75	61	41	17	1.0	48045	0.0095	0.0236	0.35
BH 225																				
13.1DRK	0.033	0.75	0.20	0.47	9.21	1.58	137.7	431	964	1912	3312	4831	6057	6641	275	9.25	15301	0.0443	0.0262	36.40
15.1DKR	0.066	7.68	0.36	0.85	17.57	4.41	204.6	561	1084	2062	3400	4659	5786	6424	266	49.59	14889	0.0736	0.1320	23.41
2.1DKR	0.171	0.96	0.44	0.70	14.48	3.10	197.7	548	1188	2264	3891	5659	7094	7506	85	3.52	16422	0.0580	0.0328	29.71
21.2GInt	0.016	0.25	0.03	0.04	1.04	0.15	10.8	42	109	234	492	1002	1694	2274	63	10.88	16876	0.0462	0.0020	129.87
22.1GR	0.553	1.56	0.61	0.64	11.14	2.73	144.2	463	996	1903	3164	4694	5837	6441	20	2.68	15658	0.0682	0.0329	33.50
23.1DKR	0.034	1.20	0.24	0.65	10.88	2.09	132.4	479	984	1966	3429	5320	7293	8726	316	13.11	14810	0.0552	0.0105	45.59
23.2GInt	0.044	0.76	0.15	0.27	6.92	1.90	90.8	275	566	1043	1725	2432	3096	3749	157	9.48	14472	0.0759	0.0154	28.22
25.3DRK	0.010	0.65	0.13	0.46	9.26	1.66	123.7	369	801	1577	2721	4052	4996	5240	926	18.10	15955	0.0490	0.0238	33.43
27.1DRK	0.036	0.90	0.23	0.59	12.06	2.44	170.8	528	1233	2394	4218	6157	7770	8364	339	9.95	15439	0.0538	0.0255	37.64
3.1DKR	0.022	7.30	0.24	0.78	14.05	4.26	247.4	684	1506	2989	5005	7079	9073	10206	644	101.50	12331	0.0723	0.1202	30.36
3.2GInt	0.094	0.72	0.11	0.12	1.13	1.01	14.3	31	57	90	124	165	185	230	12	7.04	12019	0.2527	0.0884	10.67
30.2GInt	0.149	7.23	1.46	4.57	34.14	17.64	216.7	405	640	1067	1501	1908	2197	2467	229	15.50	9202	0.2051	0.8866	8.39
34.1DKR	0.168	1.06	0.31	0.42	7.50	1.39	109.2	361	816	1594	2685	3991	5125	5805	45	4.66	17087	0.0485	0.0172	38.86
35.1DKR	0.083	1.04	0.41	0.90	10.25	1.85	134.7	420	907	1760	3048	4413	5704	6158	124	5.65	16179	0.0498	0.0228	35.04
35.3GInt	0.023	0.20	0.03	0.03	0.27	0.15	0.4	3	9	29	98	226	504	919	12	7.74	13428	0.4527	0.0298	1068.39
39.1DKR	0.049	1.23	0.28	0.67	12.45	3.02	172.9	525	1130	2065	3618	5121	6431	6891	252	10.43	16249	0.0651	0.0335	30.78
42.2DKR	4.332	3.34	1.38	0.77	4.95	1.08	61.1	209	455	759	1384	2515	3954	4660	1	1.37	20590	0.0620	0.0038	53.58
43.1DKR	0.135	0.59	0.28	0.40	9.61	2.02	144.6	471	1080	2144	3698	5397	6795	7545	71	3.07	15565	0.0541	0.0282	38.91
46.1DKR	0.010	9.55	0.26	1.30	21.68	4.93	282.5	745	1415	2697	4528	6328	8048	9039	2168	188.71	13165	0.0630	0.1365	23.58
49.1DKR	0.349	1.19	0.52	0.64	12.49	2.43	155.4	472	1008	1935	3329	4858	5954	6514	36	2.78	16896	0.0551	0.0274	31.72
5.1DKR	0.046	0.62	0.12	0.20	6.49	1.00	87.5	306	713	1442	2606	3919	4939	5577	142	8.35	16320	0.0420	0.0159	46.74
65.1DKR	6.403	5.25	1.76	0.92	7.51	2.13	94.4	305	717	1335	2504	4029	5664	6509	1	1.56	20678	0.0799	0.0117	49.68

APPENDIX F

^{40}AR/^{39}AR STEP-HEATING ANALYTICAL PROCEDURE

McDougall and Harrison (1988) described the principles and method of $^{40}Ar/^{39}Ar$ dating. Coarse, pristine muscovite grains were hand picked from material crushed by a jaw crusher. The separated mica concentrates were individually wrapped in aluminum foil, and then stacked in an aluminum irradiation canister. Interspersed among the samples were five to seven aliquots of the flux monitor, Fish Canyon tuff sanidine, which has an apparent K-Ar age of 28.205 $\pm$ 0.046 Ma (Kuiper et al., 2008). The canister was irradiated with fast neutrons in the nuclear reactor at McMaster University in Hamilton, Ontario, Canada. At Dalhousie University, a double-vacuum tantalum resistance furnace was used to carry out the step-heating. Isotopic analyses were made in a VG3600 mass spectrometer using both Faraday and electron multiplier collectors to measure the abundance of ^{39}Ar for $^{40}Ar/^{39}Ar$ and $^{36}Ar/^{39}Ar$ ratios, respectively. Errors are reported at the 2σ level and include the uncertainty in the irradiation parameter, J, but do not incorporate uncertainty in the assumed age of the flux monitor.

APPENDIX G

THERMOBAROMETRY SAMPLE LOCATIONS

Sample	Analysis	Latitude (N)	Longitude (E)
DBH 088	PT	27° 30.044’	90° 53.974’
DBH 086	PT	27° 29.826’	90° 52.179’
DBH 071	PT	27° 25.170’	90° 54.386’
DBH 068	PTt	27° 24.938’	90° 55.698’
DBH 005	PT	27° 41.935’	89° 17.506’
DBH 063	PTt	27° 24.939’	90° 56.293’
DBH 113	PTt	27° 35.138’	89° 30.800’
DBH 061	PT	27° 37.642’	89° 37.702’
CWB-08-04	PTt	27° 30.932’	90° 48.670’
DBH 122	PTt	27° 33.761’	89° 31.013’
DBH 095	PTt	27° 32.577’	89° 29.423’
DBH 020	PT	27° 35.903’	89° 37.882’

APPENDIX H

THERMOBAROMETRY

H.1 SAMPLE DESCRIPTIONS

The following additional samples were used for P-T estimates: DBH 088, DBH 086, DBH 071, DBH 005, and DBH 061 (locations shown in Fig. H.1). Samples are discussed below from structurally highest to structurally lowest (approximate structural positions are indicated in Table 3.2 and Figure 3.9).

DBH 088 is a garnet-biotite-staurolite schist in the Chekha Group. Biotite, aligned muscovite and elongated quartz grains define the main schistose foliation. Garnets exhibit a well-developed internal foliation preserving biotite-rich and quartz-rich domains and crenulation cleavage. The cores are inclusion rich and the rims are inclusion poor. Inclusions are quartz, ilmenite, plagioclase, biotite and apatite. Although the internal foliation in garnet (S_i) is at high angle to the external schistose foliation (S_e) of the rock, the inclusion trails do bend sharply towards S_e at the rims, suggesting that garnet rims are syntectonic with the schistose foliation. Pressure shadows around garnet contain quartz, biotite and chlorite, and garnet rims are embayed. Staurolite grains have quartz-chlorite pressure shadows and are fractured by late shear bands that also deform biotite. The schistose fabric is overprinted by a crenulation cleavage.

DBH 086 is a garnet-biotite schist of the Chekha Group. The schistose fabric is defined by intergrown muscovite and biotite, which bends around garnet grains. Garnets are largely idioblastic and contain quartz, biotite, ilmenite and apatite inclusions that preserve a spiral S_i in rare grains. Garnet cores contain more inclusions than garnet rims. S_i where preserved is at an angle to S_e. Pressure shadows are small and contain coarse biotite. Garnet rims are surrounded by fine-grained biotite.

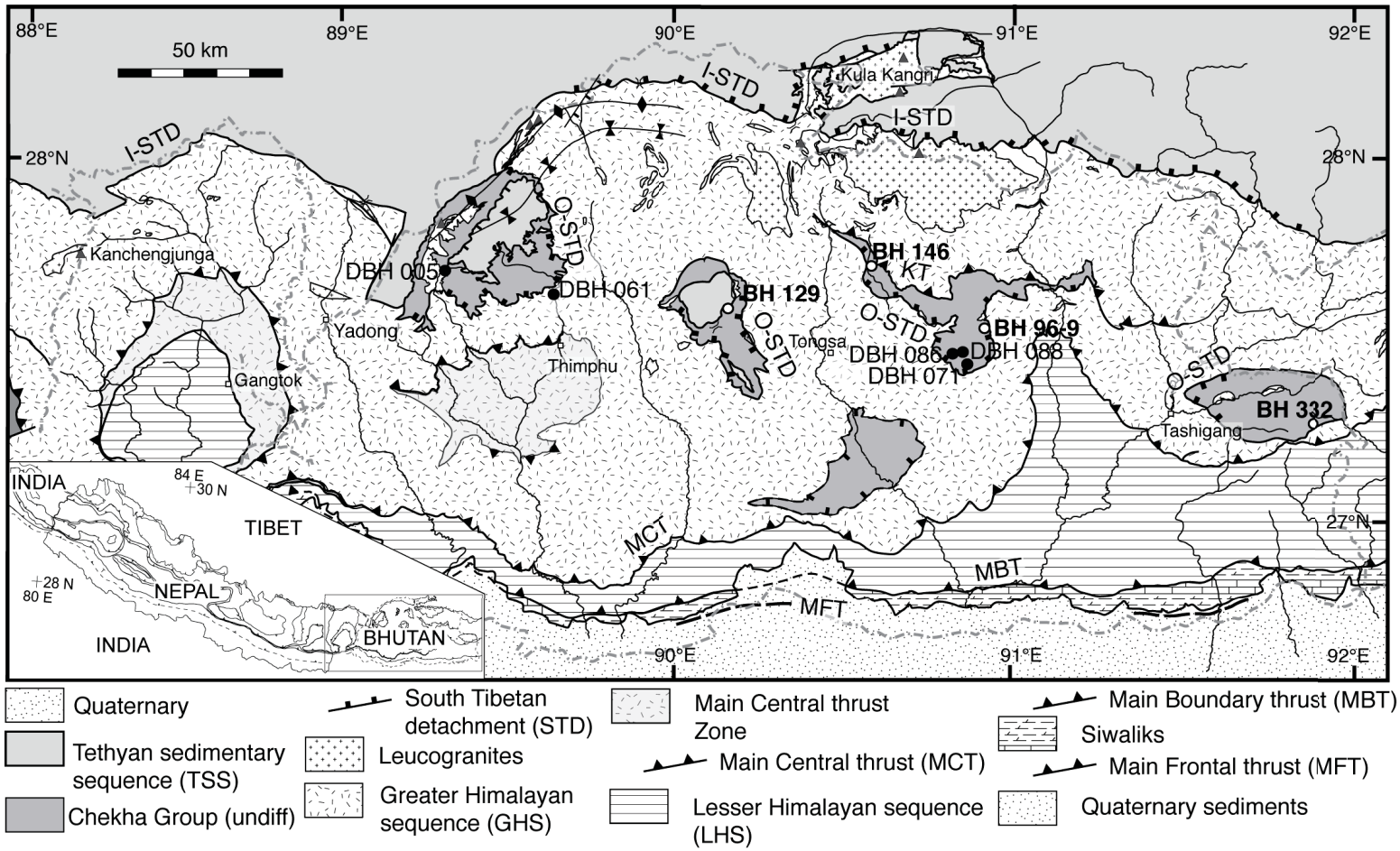

Figure H.1: Thermobarometry sample locations. Chekha Group klippe are labeled in bold. Samples used for P-T estimates are labeled in standard text. Chekha Group samples from other locations in Bhutan that also exhibit prograde garnet zoning are labeled in bold.

DBH 071 is a garnet-biotite schist of the Chekha Group. The schistose fabric is defined by alternating layers of aligned biotite-muscovite-chlorite and quartz-plagioclase. It is overprinted by a well-developed symmetric crenulation cleavage at high angle to the schistose fabric. Garnets are subidioblastic to idioblastic. Inclusions in garnet are biotite, plagioclase, muscovite and ilmenite, and form sinuous S_i in garnet that is broadly continuous with S_e. Inclusions are finer in garnet cores, coarsening toward the rims, and are finer-grained than the matrix minerals. Pressure shadows around garnets contain polygonal quartz grains, plagioclase and rare biotite. Chlorite forms strain caps on garnets, and chlorite also overgrows the schistose fabric.

Sample DBH 005 is a garnet-biotite-amphibole schist of the Chekha Group adjacent to the contact with a large leucogranite body in the Lingshi klippe. The matrix is fine grained, with alternating layers of quartz-biotite-muscovite-chlorite and hornblende-quartz-chlorite defining the schistosity. Biotite porphyroblasts are crenulated and there is chlorite growth along crenulations. Garnets are skeletal in the amphibole-rich layers and subidioblastic in the biotite-rich layers, and contain abundant coarse-grained inclusions of quartz, plagioclase, K-feldspar, biotite, chlorite and ilmenite with no preserved S_i. Some garnet grains are elongate and aligned parallel to the foliation plane.

The Greater Himalayan sequence sample examined for P-T is DBH 061, a garnet-biotite augen gneiss. Feldspar augen and garnets are within a matrix of quartz and biotite. Garnets are subidioblastic and fractured, with biotite replacing garnet along fracture surfaces. They contain few, medium-grained inclusions of quartz, plagioclase, biotite and muscovite that do not form an internal fabric.

H.2 THERMOBAROMETRIC ESTIMATES

Selected garnet grains in polished thin section from each sample were imaged with backscattered electrons (BSE) and then mapped for Ca, Mg, Mn, Fe, $\pm$Y, $\pm$Al by wave-dispersive spectrometry on the JEOL 8200 electron microprobe at Dalhousie University, using an accelerating voltage of 15 kV and a beam current of $\tilde{1}0$ nA. The compositional maps were used to characterize zoning patterns and to guide quantitative point analyses. Pressures and temperatures for interpreted stable metamorphic assemblages were calculated using THERMOCALC version 326i (©rp/tjbh 2005), and the internally consistent dataset of Holland and Powell (1998). Table 3.2 lists the resulting calculated P-T conditions

(electron microprobe analyses used for P-T calculations can be found in Appendix 9). Uncertainties in P and T are reported at the 2σ level.

Four of the additional samples examined are Chekha Group metapelites. Garnet mapping of DBH 088 indicates prograde zoning is preserved (cores are elevated in Mn and Ca and depleted in Mg and Fe compared to rims), and there is no evidence for Mn resorption at the rims. Garnet cores yield a P-T estimate of 6.9±1.2 kbars at 558±32 °C, while rims yield 8.4±1.1 at 650±26 °C (Table 3.2). DBH 086 also preserves strong chemical growth zoning in garnet with an absence of Mn resorption at the rim. Garnet cores yield 8.6±1.2 kbars at 618±31 °C and rims yield 7.7±1.0 kbars at 607±27 °C. Prograde garnet chemical zoning is present in DBH 071, and appears truncated where garnet is in contact with biotite, suggesting garnet breakdown. Garnet core P-T is estimated at 8.7±1.9 kbars at 576±44 °C while the P-T estimate for rims is 8.6±1.1 kbars at 604±27 °C. DBH 005 garnets show slight Mn enrichment and Mg depletion in the cores. Garnet rim and matrix compositions yield a P-T estimate of 8.7±2.9 kbars at 721±90 °C.

Greater Himalayan sequence sample DBH 061 was also studied for P-T estimates. Garnet maps from DBH 061 show a lack of zoning for Ca or Fe. The rims are elevated in Mn and depleted in Mg, suggesting post-garnet growth resorption of Mn. Garnet cores yield a P-T estimate of 8.1±1.6 kbars at 748±41 °C, while near rim and matrix compositions yield a lower pressure of 6.2±1.7 kbars at 725±49 °C.

H.3 CHEKHA GROUP GARNETS AND PROGRADE ZONING

Garnets in Chekha Group samples collected from several of the klippe in Bhutan (Pele La, Ura and Radi), as well as in the footwall of the Kakhtang thrust (Fig. H.1), have identical elemental zoning to garnets in the samples used in this study for P-T estimates (above) and P-T-t estimates in the main text, demonstrating the along-strike consistency of general metamorphic conditions for the Chekha Group (Fig. H.2). Garnet-staurolite schists in the footwall of the Kakhtang thrust were originally mapped by Gansser (1983) as being part of the GHS, and by Bhargava (1995) as the Naspe Formation. However, recent mapping (Chapter 2) indicates that the schists are continuous with Chekha Group rocks of the Ura klippe. Based on that mapping and the similarity of growth-zoned garnets (dominantly almandine-rich, with minor components of pyrope, spessartine and grossular) in these garnet-staurolite schists (see BH 146 in Fig. H.2 as well as sample 93Bs27 of Davidson et

al. (1997)), we argue that they are Chekha Group garnets. As shown in Figure H.2, they typically exhibit prograde zoning, with elevated Ca and Mn in the cores and elevated Mg in the rims.

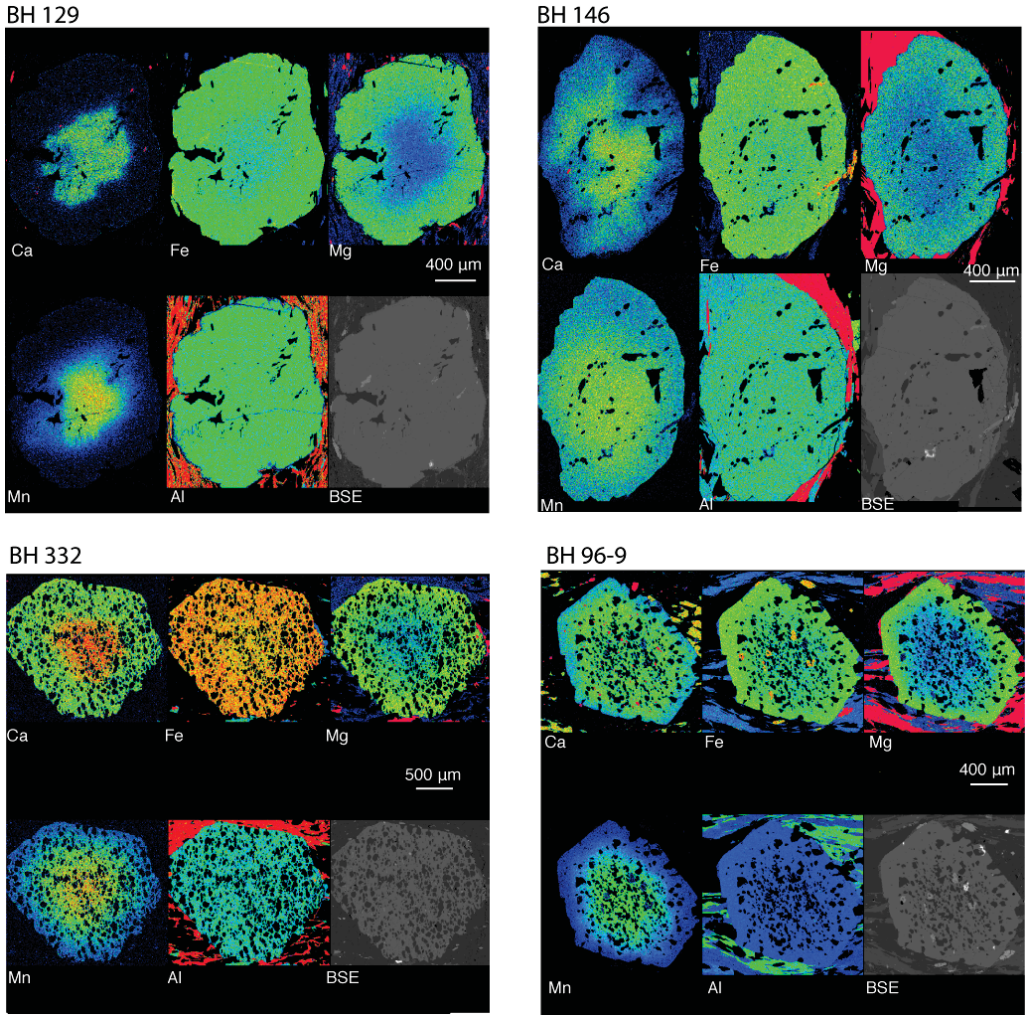

Figure H.2: Chekha Group garnet compositional maps produced by electron microprobe. Warm colours represent relatively high values and cool colours represent relatively low values.

APPENDIX I

ELECTRON MICROPROBE ANALYSES USED FOR THERMOBAROMETRY

AX (version 0.3, Intel) was used to calculate relative components of Fe_2O_3 and FeO, cations and activities. Dash denotes below detection limits.

DBH 063									
CORE	ingrt	plingrt	core	ingrt	**RIM**	mtx	nrgrt	aver	ingrt
Min	biotite	plagioclase	garnet	muscovite	Min	biotite	plagioclase	garnet	muscovite
SiO_2	35.19	62.79	36.27	46.52	SiO_2	35.43	62.57	36.19	47.79
TiO_2	1.27	0	0	0.52	TiO_2	1.33	0	0.01	0.74
Al_2O_3	19.89	23.74	20.45	36.67	Al_2O_3	20.41	23.52	20.34	35.94
Cr_2O_3	0.01	0	0	0.01	Cr_2O_3	0	0	0.02	0.03
Fe_2O_3	0	0.46	1.55	1.14	Fe_2O_3	0	0.27	1.33	0.1
FeO	20.55	0	33.76	0.44	FeO	20.26	0	34.04	1.1
MnO	0.14	0	2.52	0.02	MnO	0.14	0.02	2.52	0
MgO	7.9	0	2.33	0.57	MgO	7.51	0	2.33	0.7
CaO	0.02	4.37	2.16	0	CaO	0	4.31	1.93	0.01
Na_2O	0.21	8.88	0.01	0.9	Na_2O	0.23	9.5	0	0.97
K_2O	8.78	0.12	0.03	8.43	K_2O	8.78	0.12	0.02	8.42
Totals	93.97	100.36	98.92	95.22	Totals	94.1	100.31	98.6	95.8
Oxygens	11	8	12	11	Oxygens	11	8	12	11
Si	2.719	2.768	2.968	3.056	Si	2.725	2.766	2.974	3.116
Ti	0.074	0	0	0.026	Ti	0.077	0	0.001	0.036
Al	1.812	1.234	1.973	2.84	Al	1.851	1.226	1.97	2.763
Cr	0.001	0	0	0.001	Cr	0	0	0.001	0.002
Fe^{3+}	0	0.015	0.095	0.056	Fe^{3+}	0	0.009	0.082	0.006
Fe^{2+}	1.328	0	2.311	0.024	Fe^{2+}	1.303	0	2.339	0.059
Mn	0.009	0	0.175	0.001	Mn	0.009	0.001	0.175	0
Mg	0.91	0	0.284	0.056	Mg	0.861	0	0.285	0.068
Ca	0.002	0.206	0.189	0	Ca	0	0.204	0.17	0.001
Na	0.031	0.759	0.002	0.115	Na	0.034	0.814	0	0.123
K	0.865	0.007	0.003	0.707	K	0.861	0.007	0.002	0.7
Sum	7.75	4.99	8	6.881	Sum	7.721	5.027	8	6.875
Activities: phl 0.0346, ann 0.067, east 0.034, an 0.32, ab 0.79, py 0.00136, gr 0.00032, alm 0.44, spss 0.00018, mu 0.76, pa 0.204					Activities:phl 0.0318, ann 0.063, east 0.033, an 0.30, ab 0.80, py 0.00132, gr 0.00023, alm 0.46, spss 0.00019, mu 0.69, pa 0.29				

DBH 068										
CORE	dbh68	plingrt	core	nxtgrt	**RIM**	dbh68mtx	ploutgrtaverim	rim	nxtgrtave	nxtgrt
Min	biotite	plagioclase	garnet	muscovite	Min	biotite	plagioclase	garnet	muscovite	staurolite
SiO_2	36.09	59.27	36.29	45.98	SiO_2	35.23	61.29	36.43	45.98	26.52
TiO_2	0.43	0.01	0.06	0.46	TiO_2	1.04	0	0.01	0.46	0.58
Al_2O_3	21.29	24.8	20.7	35.76	Al_2O_3	20.19	23.05	20.96	35.76	54.45
Cr_2O_3	0.02	0	0	0	Cr_2O_3	0.01	0	0.02	0	0.01
Fe_2O_3	0	0.37	0.86	0	Fe_2O_3	0	0.24	0.66	0	0
FeO	15.77	0	26.69	1.1	FeO	19.63	0	35.14	1.1	11.92
MnO	0.05	0.05	7.85	0.01	MnO	0.07	0	1.21	0.01	0.1
MgO	11.1	0	1.04	0.59	MgO	8.78	0	2.8	0.59	1.28
CaO	0	6.39	5.37	0	CaO	0.01	4.26	1.61	0	0.01
Na_2O	0.09	8.04	0.01	1.33	Na_2O	0.19	9.18	0.02	1.33	0.1
K_2O	8.54	0.09	0.01	8.47	K_2O	8.2	0.1	0.02	8.47	0.02
Totals	93.39	99.02	98.79	93.71	Totals	93.36	98.12	98.81	93.71	94.99
Oxygens	11	8	12	11	Oxygens	11	8	12	11	46
Si	2.723	2.67	2.972	3.077	Si	2.715	2.768	2.973	3.077	7.517
Ti	0.024	0	0.004	0.023	Ti	0.06	0	0.001	0.023	0.124
Al	1.894	1.317	1.998	2.821	Al	1.834	1.227	2.016	2.821	18.194
Cr	0.001	0	0	0	Cr	0.001	0	0.001	0	0.002
Fe^{3+}	0	0.012	0.053	0	Fe^{3+}	0	0.008	0.04	0	0
Fe^{2+}	0.995	0	1.828	0.062	Fe^{2+}	1.265	0	2.398	0.062	2.826
Mn	0.003	0.002	0.545	0.001	Mn	0.005	0	0.084	0.001	0.024
Mg	1.248	0	0.127	0.059	Mg	1.008	0	0.341	0.059	0.541
Ca	0	0.308	0.471	0	Ca	0.001	0.206	0.141	0	0.003
Na	0.013	0.702	0.002	0.173	Na	0.028	0.804	0.003	0.173	0.055
K	0.822	0.005	0.001	0.723	K	0.806	0.006	0.002	0.723	0.007
Sum	7.724	5.018	8	6.938	Sum	7.725	5.019	8	6.938	29.292
Activities: phl 0.084, ann 0.028, east 0.072, an 0.47, ab 0.70, py 0.000191, gr 0.0045, alm 0.22, spss 0.0057, mu 0.69, cel 0.0100, fcel 0.0104, pa 0.47.					Activities: phl 0.044, ann 0.056, east 0.042, an 0.31, ab 0.80, py 0.0023, gr 0.00016, alm 0.50, spss 0.000020, mu 0.69, cel 0.0095, fcel 0.0099, pa 0.45, mst 0.00077, fst 0.48.					

DBH 113				DBH 122				
CORE Min	ave biotite	pl plagioclase	core garnet	**RIM** Min	ave biotite	ave plagioclase	rim garnet	rim muscovite
SiO_2	35.06	59.94	35.09	SiO_2	34.94	58.93	35.22	45.55
TiO_2	2.75	0	0.06	TiO_2	2.06	0	0	0.97
Al_2O_3	20.28	24.44	19.8	Al_2O_3	20.12	24.31	20.35	34.7
Cr_2O_3	0.08	0	0.01	Cr_2O_3	0	0	0	0
Fe_2O_3	0	0.26	1.9	Fe_2O_3	0	0.13	0.77	0
FeO	17.64	0	27.58	FeO	17.98	0	25.97	1.49
MnO	0.19	0.02	6.27	MnO	0.28	0.01	9.12	0
MgO	8.55	0	2.97	MgO	9.02	0	2.45	0.65
CaO	0	5.6	2.15	CaO	0.01	6.04	1.9	0
Na_2O	0.27	8.36	0	Na_2O	0.2	7.99	0.01	0.43
K_2O	9.28	0.21	0.01	K_2O	9.43	0.18	0.02	10.18
Totals	94.11	98.83	95.65	Totals	94.05	97.59	95.73	93.98
Oxygens	11	8	12	Oxygens	11	8	12	11
Si	2.677	2.699	2.954	Si	2.678	2.689	2.967	3.073
Ti	0.158	0	0.004	Ti	0.119	0	0	0.049
Al	1.826	1.298	1.965	Al	1.818	1.308	2.021	2.76
Cr	0.005	0	0.001	Cr	0	0	0	0
Fe^{3+}	0	0.009	0.12	Fe^{3+}	0	0.005	0.049	0
Fe^{2+}	1.127	0	1.942	Fe^{2+}	1.153	0	1.83	0.084
Mn	0.012	0.001	0.447	Mn	0.018	0	0.651	0
Mg	0.973	0	0.373	Mg	1.03	0	0.308	0.065
Ca	0	0.27	0.194	Ca	0.001	0.295	0.172	0
Na	0.04	0.73	0	Na	0.03	0.707	0.002	0.056
K	0.904	0.012	0.001	K	0.922	0.01	0.002	0.876
Sum	7.722	5.019	8	Sum	7.77	5.014	8	6.965
Activities: phl 0.034, ann 0.037, east 0.043, an 0.38, ab 0.73, py 0.0029, gr 0.00037, alm 0.26, spss 0.0030.				Activities:phl 0.042, ann 0.043, east 0.046, an 0.40, ab 0.70, py 0.0016, gr 0.00026, alm 0.22, spss 0.010, mu 0.72, cel 0.0121, fcel 0.016, pa 0.172.				

CWB-08-04								
RIM	ave	ave	rim	**RIM**	ave	ave	rim	rim
Min	biotite	plagioclase	garnet	Min	biotite	plagioclase	garnet	muscovite
SiO_2	36.4	63.43	35.56	SiO_2	35.49	62.98	35.33	44.96
TiO_2	1.74	0	0.01	TiO_2	3.07	0	0	0.64
Al_2O_3	20.34	22.29	20.25	Al_2O_3	19.45	22.5	20.2	34.18
Cr_2O_3	0.01	0	0.01	Cr_2O_3	0.02	0	0.01	0
Fe_2O_3	0	0.12	1.14	Fe_2O_3	0	0.04	1.55	0
FeO	15.82	0	30.89	FeO	17.44	0	30.42	1.08
MnO	0.08	0	2.72	MnO	0.1	0	2.75	0.01
MgO	10.77	0	3.6	MgO	9.54	0	4.17	0.82
CaO	0	3.26	1.83	CaO	0.01	3.39	1.17	0
Na_2O	0.27	9.76	0.02	Na_2O	0.28	9.76	0.01	0.87
K_2O	8.59	0.22	0.01	K_2O	8.86	0.08	0.02	9.1
Totals	94.03	99.08	95.93	Totals	94.27	98.75	95.48	91.67
Oxygens	11	8	12	Oxygens	11	8	12	11
Si	2.733	2.827	2.969	Si	2.695	2.816	2.956	3.089
Ti	0.098	0	0.001	Ti	0.175	0	0	0.033
Al	1.801	1.171	1.993	Al	1.741	1.186	1.993	2.768
Cr	0.001	0	0.001	Cr	0.001	0	0.001	0
Fe^{3+}	0	0.004	0.072	Fe^{3+}	0	0.001	0.098	0
Fe^{2+}	0.994	0	2.157	Fe^{2+}	1.108	0	2.129	0.062
Mn	0.005	0	0.192	Mn	0.006	0	0.195	0.001
Mg	1.205	0	0.448	Mg	1.08	0	0.52	0.084
Ca	0	0.156	0.164	Ca	0.001	0.162	0.105	0
Na	0.039	0.843	0.003	Na	0.041	0.846	0.002	0.116
K	0.823	0.013	0.001	K	0.858	0.005	0.002	0.798
Sum	7.699	5.014	8	Sum	7.708	5.016	8	6.951
Activities: phl 0.064, ann 0.026, east 0.062, an 0.26, ab 0.84, py 0.0054, gr 0.00030, alm 0.36, spss 0.00024.				Activities: phl 0.041, ann 0.036, east 0.044, an 0.22, ab 0.84, py 0.0071, gr 0.000074, alm 0.35, spss 0.00025, mu 0.68, cel 0.0163, fcel 0.0120, pa 0.325.				

DBH 095								
CORE	incl3-1	aveplincl	3coreave	**RIM**	avemtx	aveplmtx	kspmtx	2coreave
Min	biotite	plagioclase	garnet	Min	biotite	plagioclase	K-feldspar	garnet
SiO_2	23.72	37.2	37.2	SiO_2	34.08	59.64	61.55	36.67
TiO_2	0.02	0	0	TiO_2	1.6	0	0.03	0.01
Al_2O_3	20.62	21.01	21.01	Al_2O_3	19.85	22.77	17.61	20.78
Cr_2O_3	0.02	0	0	Cr_2O_3	0.04	0	0	0
Fe_2O_3	4.4	34.01	1.76	Fe_2O_3	0	0.28	0.02	1.59
FeO	22.44	0	29.01	FeO	19.47	0	0	31.27
MnO	0.1	1.96	1.96	MnO	0.15	0	0	3.5
MgO	12.74	4.38	4.38	MgO	8.49	0	0	3.58
CaO	0.03	4.31	4.31	CaO	0.02	5.3	0.04	1.9
Na_2O	0.03	0.02	0.02	Na_2O	0.2	9.2	1.6	0.03
K_2O	0.08	0.02	0.02	K_2O	9.59	0.18	14.06	0.03
Totals	84.2	102.91	99.5	Totals	93.5	97.37	94.93	99.2
Oxygens	11	8	12	Oxygens	11	8	8	12
Si	2.056	1.828	2.963	Si	2.657	2.733	2.987	2.965
Ti	0.001	0	0	Ti	0.094	0	0.001	0.001
Al	2.108	1.217	1.973	Al	1.824	1.23	1.007	1.981
Cr	0.001	0	0	Cr	0.002	0	0	0
Fe^{3+}	0.287	1.258	0.106	Fe^{3+}	0	0.01	0.001	0.097
Fe^{2+}	1.627	0	1.933	Fe^{2+}	1.269	0	0	2.114
Mn	0.007	0.082	0.132	Mn	0.01	0	0	0.24
Mg	1.646	0.321	0.52	Mg	0.986	0	0	0.431
Ca	0.003	0.227	0.368	Ca	0.002	0.26	0.002	0.165
Na	0.005	0.002	0.003	Na	0.03	0.817	0.151	0.005
K	0.009	0.001	0.002	K	0.954	0.011	0.87	0.003
Sum	7.751	4.936	8	Sum	7.829	5.061	5.019	8
Activities: phl 0.000652, ann 0.00072, east 0.0088, an 0.99, py 0.0097, gr 0.0030, alm 0.24, spss 0.000074.				Activities: phl 0.039, ann 0.060, east 0.043, an 0.33, ab 0.76, san 0.86, ab 0.44, py 0.0044, gr 0.00025, alm 0.34, spss 0.00047.				

APPENDIX J

RAMAN SPECTRA RESULTS

Raman spectra results.

Spot	Peak Area D1	D2	D3	G	R2	Peak Height D1	G	R1	T1 (°C)	T2 (°C)
DBH 021										
1	25694	2635		13261	0.618	285	456	0.625	366	247
2	9601	1084		12859	0.408	169	483	0.350	460	405
3	16390	927		13090	0.539	242	331	0.729	401	353
4	10444	1118		6683	0.572	165	195	0.848	386	341
5	11216	719		6698	0.602	172	210	0.821	373	304
6	7414	1868		5948	0.487	142	203	0.699	424	403
7	14610	2213		12013	0.507	251	409	0.614	416	363
8	17187	2437		13992	0.511	294	420	0.700	413	377
9	8214	476		5347	0.585	129	146	0.882	381	333
10	13841	2260		8741	0.557	236	260	0.910	393	368
11	20845	1768		29098	0.403	370	1032	0.358	462	412
12	20837	2386		23219	0.449	435	804	0.541	441	408
13	13701	1735		8809	0.565	217	270	0.804	390	340
14	12110	1682		19537	0.363	234	680	0.345	479	451
15	11494	1150		8472	0.544	181	258	0.702	399	342
Mean					**0.51**			**0.66**	**412**	**363**
1σ					**0.08**			**0.19**	**35**	**50**
DBH 011										
1	22402	1262		18878	0.527	366	450	0.814	407	383
2	21680	2044		25811	0.438	399	562	0.711	446	458
3	19275	1674		16225	0.518	263	322	0.817	410	392
4	22667	2102		24880	0.457	403	550	0.733	438	442
5	34259	2348		31939	0.500	598	701	0.854	419	419
6	34425	3016		30977	0.503	565	675	0.837	417	412
7	26365	1487		21541	0.534	444	472	0.939	403	398
8	24028	2438		22632	0.489	404	526	0.769	423	414
9	20094	1490		16329	0.530	318	360	0.883	405	392
10	20671	2920		16317	0.518	347	369	0.942	411	415
11	26270	3754		30969	0.431	480	624	0.770	449	477
Mean					**0.49**			**0.82**	**421**	**419**
1σ					**0.04**			**0.08**	**17**	**29**
DBH 009										
1	14536	1915		11915	0.512	204	327	0.625	413	360
2	10417	928		7205	0.562	112	176	0.638	391	310
3	16660	2543		16034	0.473	220	372	0.592	431	394
4	17641	2898		21249	0.422	216	701	0.308	453	378
5	12116	3904		10215	0.462	146	253	0.577	435	403
6	11673	3289		16567	0.370	171	447	0.382	476	453
7	11234	1824		5943	0.591	158	135	1.174	378	372
8	9357	1259		10112	0.451	181	336	0.540	440	405
9	14629	1493		13786	0.489	231	385	0.599	423	379
10	8302	2482		7826	0.446	149	250	0.595	442	424
Mean					**0.52**			**0.62**	**412**	**355**
1σ					**0.06**			**0.23**	**29**	**39**
DBH 050										
1	103140	5668	7627	46512	0.664	1229	755	1.629	345	338
2	85584	4310	5744	43490	0.642	1026	710	1.445	355	348
3	95136	4835	5883	43358	0.664	1091	700	1.558	346	333
4	102490	5783	6495	45442	0.667	1278	803	1.592	344	332
5	100640	8882	10120	36483	0.689	1201	697	1.722	334	315
6	51990	9314	7256	13586	0.694	737	331	2.226	332	311
7	69445	11163	7573	16300	0.717	850	400	2.123	322	290
8	53516	10098	9488	13222	0.696	729	323	2.255	331	308
9	53367	8809	9419	15308	0.689	718	351	2.047	335	321
10	61647	10806	10952	13083	0.721	842	362	2.324	320	279
11	68953	10709	10837	20132	0.691	949	461	2.059	334	319
12	33585	5250	4469	8938	0.703	470	228	2.063	328	306
Mean					**0.69**			**1.92**	**336**	**317**
1σ					**0.02**			**0.31**	**10**	**20**
DBH 051										
1	199670	7722	28991	84299	0.685	2001	1491	1.342	336	292
2	135820	4374	18017	53333	0.702	1391	994	1.399	329	280
3	286730	18398	41183	104750	0.700	2769	1939	1.428	330	285
4	51641	1546	5131	22564	0.682	562	417	1.348	338	296
5	164370	5718	16644	65154	0.699	1666	1201	1.387	330	282
6	199610	14705	27069	74971	0.690	2082	1382	1.506	334	301

Spot	Peak Area				Peak Height		T1	T2	Spot	Peak Area
	D1	D2	D3	G	R2	D1	G	R1		D1
7	160490	11286	22701	63211	0.683	1633	1156	1.413	337	301
8	114860	4000	10449	46156	0.696	1142	867	1.317	331	277
9	125110	6703	14222	43811	0.712	1293	870	1.485	324	276
10	273980	27969	39801	93866	0.692	2614	1826	1.431	333	293
11	262720	28750	41266	90261	0.688	2690	1774	1.516	335	304
12	208990	18356	32295	73710	0.694	2134	1453	1.468	332	294
Mean					**0.69**			**1.42**	**332**	**290**
1σ					**0.01**			**0.07**	**4**	**10**
DBH 052										
1	63080	3149	6638	19070	0.740	608	377	1.612	312	256
2	899960	80080	210690	217060	0.752	6455	4115	1.569	306	240
3	450410	27291	100570	110560	0.766	3018	1849	1.633	300	229
4	175460	11926	24598	61682	0.704	1784	1198	1.489	328	285
5	369280	37089	70441	101010	0.728	3757	2167	1.733	317	275
6	320380	36268	57667	89309	0.718	3308	1926	1.717	321	284
7	77474	6397	7372	25214	0.710	810	461	1.755	325	294
8	569240	41084	147840	128480	0.770	4455	2578	1.728	298	229
9	298110	22991	76945	64491	0.773	2213	1304	1.697	297	225
10	1206000	85105	342940	309610	0.753	8579	5592	1.534	306	236
11	563350	36635	155050	136480	0.765	4602	2792	1.648	301	231
12	533680	41142	141180	126930	0.760	4218	2556	1.650	303	236
Mean					**0.75**			**1.65**	**310**	**252**
1σ					**0.02**			**0.08**	**11**	**26**
DBH 053										
1	353360	20922	25865	129850	0.701	4338	2582	1.680	329	301
2	180620	14053	13730	64362	0.697	2416	1339	1.804	331	310
3	316940	35545	14110	111900	0.682	4611	2582	1.786	337	325
4	63144	6364	4439	20281	0.703	843	465	1.816	328	304
5	273890	26535	22874	85490	0.710	3519	1886	1.866	325	298
6	182090	17753	16370	57603	0.707	2415	1327	1.820	326	300
7	400950	45616	30332	135410	0.689	5289	3046	1.736	334	316
8	172280	19392	16302	49897	0.713	2223	1237	1.796	324	293
9	189950	24832	21206	57139	0.699	2366	1334	1.774	330	307
10	216340	27170	36260	58767	0.716	2479	1431	1.732	323	288
11	191440	26330	28276	48649	0.719	2799	1241	2.255	321	284
12	206060	28899	28566	58296	0.703	2574	1456	1.768	328	303
Mean							**0.70**			**1.82**
1σ					**0.01**			**0.15**	**5**	**12**
DBH 054										
1	72659	7152	4623	22672	0.709	967	478	2.022	326	300
2	68219	6747	4195	21738	0.705	859	454	1.894	327	303
3	227030	30356	26106	66966	0.700	2876	1452	1.981	330	310
4	125190	13783	10658	38324	0.706	1647	826	1.994	327	303
5	120780	15689	4401	46910	0.659	1788	1031	1.734	348	349
6	75168	11144	3702	31499	0.638	1186	677	1.752	357	371
7	56318	6357	2913	20573	0.677	804	450	1.789	340	331
8	124100	17598	16710	31264	0.718	1514	717	2.111	322	290
9	69158	10894	3558	21886	0.678	981	531	1.845	339	331
10	49369	7210	1892	16197	0.678	748	398	1.878	339	332
11	211860	31284	14570	66148	0.685	3171	1606	1.975	336	326
12	100600	17534	7594	27809	0.689	1408	710	1.984	334	321
Mean					**0.69**			**1.91**	**335**	**322**
1σ					**0.02**			**0.12**	**10**	**23**
DBH 055 poor spectra - removed										
1	115360	28494	4562	64363	0.554	1784	953	1.873	394	464
2	94068	14452	3213	53885	0.579	1433	874	1.639	383	429
3	65500	14463	2300	39328	0.549	954	587	1.626	397	460
4	78357	16945	3178	52991	0.528	1340	814	1.646	406	483
5	71683	17394	3156	49644	0.517	1218	745	1.634	411	495
6	81252	26073	3442	62476	0.479	1489	898	1.658	428	537
7	67215	14986	3158	42932	0.537	1162	661	1.758	402	479
8	471560	30333	151620	164210	0.708	3091	2676	1.155	326	245
9	98049	20583	3204	55822	0.562	1442	864	1.669	391	449
10	137630	23314	5553	66334	0.606	1952	1066	1.831	372	408
11	98732	15427	3682	33060	0.671	1454	731	1.989	343	341
Mean					**0.57**			**1.68**	**387**	**436**

Spot	Peak Area D1	D2	D3	G	Peak Height R2	D1	T1 G	T2 R1	Spot	Peak Area D1
1σ					**0.07**			**0.21**	**30**	**81**
B 653										
1	55897	5294		64298	0.445	1023	2037	0.503	443	402
2	35614	3397		36253	0.473	629	1095	0.574	430	390
3	37869	3089		79020	0.316	695	2391	0.291	501	487
4	8744	197		73696	0.106	210	2686	0.078	594	649
5	28951	3985		60389	0.310	478	1638	0.292	503	493
6	37720	3291		48323	0.422	718	1602	0.448	453	414
7	141890	6272		143710	0.486	1930	2322	0.831	425	429
8	22729	2852		45571	0.319	452	1464	0.309	499	488
9	19220	4039		60413	0.230	405	1708	0.237	539	564
10	24228	2051		61974	0.275	477	1847	0.258	519	522
11	122880	22627		158870	0.404	1018	3781	0.269	461	387
Mean					**0.34**			**0.37**	**488**	**475**
1σ					**0.12**			**0.20**	**52**	**82**
B 654										
1	36927	2841	2433	14871	0.676	336	338	0.995	340	256
2	16214	15262	8855	21309	0.307	298	662	0.450	504	538
3	46737	20606	11044	34659	0.458	776	1104	0.703	437	434
4	70353	12151		101900	0.382	1065	1989	0.536	471	479
5	11489	15157	9741	62984	0.128	360	1332	0.270	584	681
6	33762	6116		58771	0.342	680	1338	0.508	489	514
7	19803	40902	39336	74100	0.147	427	1194	0.358	576	685
8	60824	15069		71693	0.412	1230	1430	0.861	458	514
9	298400	42175	36061	194170	0.558	1798	2883	0.624	393	311
10	27277	6977		61879	0.284	497	1258	0.395	515	549
11	17780	10002		53071	0.220	437	1149	0.380	543	613
12	28068	6189		41641	0.370	614	924	0.664	476	520
Mean					**0.36**			**0.56**	**505**	**553**
1σ					**0.16**			**0.22**	**49**	**83**
B 655										
1	816200	37050	175100	346940	0.680	6819	5968	1.143	338	273
2	834410	36194	153500	325250	0.698	7275	5668	1.284	331	272
3	1144200	52665	238760	479940	0.682	8955	8337	1.074	337	261
4	998220	53214	192630	351370	0.712	7887	6124	1.288	324	258
5	410620	14092	59884	177000	0.682	3777	3081	1.226	337	281
6	959840	40736	156700	367970	0.701	7953	6719	1.184	329	256
7	1314400	76126	350230	600210	0.660	9767	9314	1.049	347	281
8	910720	43345	133680	405720	0.670	7976	6967	1.145	343	284
9	153090	6934	19377	64317	0.682	1452	1104	1.315	337	292
10	581840	27858	106800	268750	0.662	5265	4386	1.200	346	300
11	711340	32787	116660	322760	0.667	6013	5256	1.144	344	287
12	729880	32840	146990	257640	0.715	6176	5105	1.210	323	244
Mean					**0.68**			**1.19**	**337**	**274**
1σ					**0.02**			**0.08**	**8**	**17**
B 656										
1	224190	16068	49419	88957	0.681	1773	1456	1.218	338	282
2	215820	16051	54410	75155	0.703	1883	1523	1.236	328	261
3	298420	29633	76185	107410	0.685	2479	1952	1.270	336	284
4	261060	23781	66138	94854	0.688	2178	1711	1.272	335	281
5	367750	35172	116530	122690	0.700	2832	2117	1.338	330	276
6	207860	23112	66540	68567	0.694	1569	1216	1.290	332	277
7	239560	20933	59703	85945	0.691	1979	1555	1.273	333	277
8	296330	29702	72180	99569	0.696	2433	1781	1.366	331	282
9	290680	29775	59716	99254	0.693	2474	1840	1.345	333	284
10	221240	21193	46533	80321	0.685	1986	1513	1.313	336	288
11	214440	21586	46362	76851	0.685	1811	1383	1.309	336	288
12	207880	19877	55316	72451	0.692	1692	1287	1.315	333	281
Mean					**0.69**			**1.30**	**333**	**280**
1σ					**0.01**			**0.04**	**3**	**7**
B 657										
1	637710	54562	65870	246830	0.679	5949	4177	1.424	338	273
2	733310	66116	86270	280090	0.679	6848	4734	1.447	331	272
3	647380	54879	74001	258260	0.674	6301	4364	1.444	337	261
4	931060	82659	105210	333330	0.691	9059	5632	1.608	324	258

Spot	Peak Area				Peak Height		T1	T2	Spot	Peak Area
	D1	D2	D3	G	R2	D1	G	R1		D1
5	971920	64626	245730	432670	0.662	7334	6284	1.167	337	281
6	790550	53949	133960	312810	0.683	6082	4587	1.326	329	256
7	743820	44848	121760	326480	0.667	6478	5073	1.277	347	281
8	737840	46284	103310	297200	0.682	6437	4860	1.325	343	284
9	796170	44664	127550	334060	0.678	6924	5195	1.333	337	292
10	677660	30758	88786	262170	0.698	5904	4431	1.332	346	300
11	757630	39730	109040	335050	0.669	7142	5652	1.264	344	287
Mean					**0.68**			**1.36**	**339**	**300**
1σ					**0.01**			**0.12**	**5**	**10**
B 658										
1	1131100	129320	216780	310410	0.720	8205	5416	1.515	321	270
2	673280	30946	135240	185340	0.757	4286	3526	1.215	304	201
3	810630	60182	205020	244140	0.727	5765	4449	1.296	317	242
4	875240	64428	157360	247610	0.737	6136	4775	1.285	313	230
5	1039100	38292	174650	332890	0.737	7182	6379	1.126	313	210
6	1008600	51063	241810	272380	0.757	7274	5556	1.309	304	211
7	1324400	114000	423800	407380	0.718	7910	6887	1.149	322	234
8	825390	48635	236590	223300	0.752	5612	4535	1.237	306	208
9	953340	46436	234770	273260	0.749	6830	5363	1.273	308	216
10	1036800	54303	237510	294130	0.748	7296	5818	1.254	308	214
11	1112000	65341	303590	328650	0.738	8075	6351	1.272	312	227
12	612250	23764	137880	179120	0.751	3921	3457	1.134	307	196
Mean					**0.74**			**1.26**	**311**	**222**
1σ					**0.01**			**0.10**	**6**	**20**
B 661										
1	247790	16860	62594	80387	0.718	1748	1467	1.191	321	239
2	468680	40991	187400	160810	0.699	2945	2437	1.208	330	261
3	496810	30916	140200	161800	0.721	3313	2888	1.147	320	231
4	342350	22263	91374	105070	0.729	2283	1939	1.178	317	226
5	278080	21995	85589	88297	0.716	1936	1561	1.240	322	247
6	373970	30529	95412	110580	0.726	2532	1990	1.273	318	240
7	384630	34086	112130	132300	0.698	2546	2130	1.195	330	261
8	453220	43893	141210	128680	0.724	3071	2334	1.315	319	247
9	452680	45654	156670	131380	0.719	2872	2236	1.284	321	249
10	436670	39567	156960	173390	0.672	2687	2490	1.079	342	272
11	352010	29127	85215	118860	0.704	2440	2027	1.204	328	256
12	416120	36001	111750	133920	0.710	2722	2229	1.221	325	251
Mean					**0.71**			**1.21**	**325**	**248**
1σ					**0.02**			**0.06**	**7**	**7**
B 662										
1	350670	38525	73392	141410	0.661	2879	3037	0.948	347	264
2	386000	43269	79633	151820	0.664	3202	3231	0.991	345	267
3	381850	44175	79362	146810	0.667	3151	3143	1.003	344	267
4	360820	42762	68054	142010	0.661	2980	3049	0.978	347	268
5	376490	42719	75215	143150	0.669	3137	3081	1.018	343	266
6	346150	40281	74283	135940	0.663	2849	2890	0.986	346	268
7	369420	40548	75034	138350	0.674	2993	2962	1.010	341	260
8	423270	52593	86852	158510	0.667	3476	3434	1.012	344	268
9	353420	40527	74777	139310	0.663	2902	3001	0.967	346	265
10	413510	49434	79875	164220	0.659	3373	3504	0.962	348	268
11	409870	50521	79892	159510	0.661	3341	3458	0.966	347	267
12	362960	37023	67903	158880	0.649	2936	3313	0.886	352	265
Mean					**0.66**			**0.98**	**346**	**266**
1σ					**0.01**			**0.04**	**3**	**2**
B 663										
1	331520	43251	158610	107800	0.687	2019	2083	0.969	335	240
2	345370	34858	110740	129270	0.678	2202	2793	0.788	339	217
3	242620	23688	82283	94002	0.673	1494	1858	0.804	341	225
4	192750	18288	75505	75322	0.673	1188	1488	0.798	341	224
5	157180	19709	29587	76640	0.620	1121	1561	0.718	365	265
6	376800	41763	73209	158080	0.653	2535	2891	0.877	350	259
7	257900	21484	47815	108740	0.664	1689	1989	0.849	345	243
8	422060	38884	75699	175880	0.663	2795	2989	0.935	346	260
9	237360	21987	42825	106310	0.649	1573	1807	0.871	352	263
10	348830	38520	70459	156250	0.642	2469	3095	0.798	355	257

Spot	Peak Area				Peak Height		T1	T2	Spot	Peak Area
	D1	D2	D3	G	R2	D1	G	R1		D1
11	378960	38490	68500	162680	0.653	2583	3223	0.801	350	246
12	501980	38515	98569	206730	0.672	3185	4094	0.778	342	221
Mean					**0.66**			**0.83**	**347**	**243**
1σ					**0.01**			**0.10**	**3**	**12**
B 666										
1	208770	9527	55158	96102	0.664	1780	1609	1.106	346	285
2	143880	6243	13098	82265	0.619	1735	1650	1.051	365	325
3	479450	23578	163320	148030	0.736	3893	2768	1.407	313	243
4	297660	8364	39294	118270	0.702	2969	2698	1.101	329	244
5	514820	18206	171570	165380	0.737	4804	3516	1.366	313	239
6	331020	12124	110880	187000	0.624	2559	2337	1.095	363	326
7	459140	40575	193190	146170	0.711	3025	2296	1.317	325	262
8	103440	5782	21027	80810	0.544	931	1255	0.742	399	350
9	289450	31677	126570	173630	0.585	1816	2121	0.856	381	329
10	196620	12016	21033	84902	0.670	2238	1885	1.187	343	290
11	543590	45875	161520	178310	0.708	4168	3017	1.382	326	271
12	320900	24153	63595	131640	0.673	3258	2257	1.443	341	314
Mean					**0.66**			**1.17**	**340**	**284**
1σ					**0.06**			**0.22**	**22**	**35**
B 667										
1	1130900	53068	128130	456950	0.689	8082	7622	1.060	334	252
2	767570	36052	92010	307330	0.691	5479	5132	1.067	334	251
3	935900	33071	120410	383300	0.692	6678	6401	1.043	333	246
4	1050400	40126	161630	412810	0.699	7199	6870	1.048	330	240
5	980030	41088	134240	397900	0.691	7815	6549	1.193	334	269
6	769560	26585	118720	322270	0.688	5498	5325	1.032	335	248
7	1054800	40143	160870	441320	0.687	7763	7291	1.065	335	255
8	1147300	39594	217850	426430	0.711	7871	7612	1.034	325	224
9	790030	29688	123450	291930	0.711	5419	5204	1.041	325	226
10	1056600	43945	188020	403090	0.703	7846	7208	1.088	328	241
11	949380	31023	192910	350860	0.713	7042	6758	1.042	324	223
12	687540	24438	116440	265910	0.703	5006	4744	1.055	328	236
Mean					**0.70**			**1.06**	**330**	**243**
1σ					**0.01**			**0.04**	**4**	**14**
B 670										
1	1383300	137150	420730	637970	0.641	8618	11341	0.760	356	251
2	1068700	89490	296430	323620	0.721	5853	6208	0.943	320	199
3	1447500	150930	419610	479340	0.697	9146	10275	0.890	331	216
4	1447700	151060	420070	477140	0.697	9136	10298	0.887	331	214
5	184530	18166	66750	58208	0.707	1127	1320	0.854	326	198
6	1822600	110400	653080	535990	0.738	9629	11348	0.849	313	164
7	2501800	263760	712760	1158000	0.638	14269	19643	0.726	357	248
8	1007100	72770	271570	377410	0.691	5935	8199	0.724	333	190
9	2236100	179490	722650	877420	0.679	11753	14504	0.810	339	220
10	1711700	159330	333420	785430	0.644	10249	14043	0.730	354	241
11	434290	50461	80897	192390	0.641	2666	3499	0.762	356	251
12	1551200	138610	262870	585590	0.682	9548	9710	0.983	338	247
Mean					**0.68**			**0.83**	**338**	**220**
1σ					**0.03**			**0.09**	**15**	**28**
B 671										
1	722120	85681	282490	347310	0.625	3749	4635	0.809	363	277
2	383740	46820	160380	211980	0.597	1995	2512	0.794	375	304
3	551550	81078	319170	268600	0.612	2839	3380	0.840	369	297
4	314000	44482	173900	181780	0.581	1480	2033	0.728	382	308
5	761710	72817	354610	333310	0.652	4216	4525	0.932	351	270
6	716060	74688	222060	315250	0.647	4157	4190	0.992	353	285
7	468610	43059	141400	205530	0.653	2635	2593	1.016	350	283
8	160680	14682	60100	88302	0.609	800	979	0.818	370	296
9	607230	58863	197400	337540	0.605	3139	3806	0.825	372	302
10	835820	97782	236270	471920	0.595	4567	5302	0.861	376	319
11	1483100	114720	363040	848850	0.606	6507	9204	0.707	371	277
12	722120	85681	282490	347310	0.625	3749	4635	0.809	363	277
Mean					**0.62**			**0.85**	**367**	**243**
1σ					**0.03**			**0.10**	**11**	**15**
B 672										

Spot	Peak Area				Peak Height		T1	T2	Spot	Peak Area
	D1	D2	D3	G	R2	D1	G	R1		D1
1	659830	25034	106390	280790	0.683	5599	4671	1.199	337	277
2	791700	43190	176980	317270	0.687	6934	5608	1.236	335	278
3	870470	37610	146310	354970	0.689	8000	6580	1.216	334	273
4	602020	62568	158710	195370	0.700	4867	3809	1.278	329	269
5	706060	44793	174280	276410	0.687	5994	4896	1.224	335	276
6	760230	53691	136110	288800	0.689	6736	5501	1.225	334	274
7	628460	31886	150440	221460	0.713	4967	4205	1.181	324	243
8	1464900	106230	358710	432510	0.731	12183	8673	1.405	316	249
9	887070	76874	210110	290060	0.707	7883	5824	1.354	326	269
10	1048800	132660	556020	376810	0.673	7500	6372	1.177	341	285
11	930700	80842	191940	328790	0.694	7860	6185	1.271	332	274
12	1250200	114880	337910	438980	0.693	10432	8120	1.285	333	277
Mean					**0.70**			**1.25**	**331**	**270**
1σ					**0.02**			**0.70**	**7**	**12**
B 674										
1	300410	26241	73423	106760	0.693	2452	1989	1.233	333	271
2	559900	51501	205170	164830	0.721	3917	2990	1.310	320	250
3	397830	42159	157420	113130	0.719	2911	2181	1.334	321	254
4	486540	55262	155530	134070	0.720	3408	2569	1.326	321	253
5	329820	30367	104330	94306	0.726	2469	1916	1.289	318	243
6	507990	51670	162620	149240	0.717	3834	2998	1.279	322	251
7	472820	39388	190620	121850	0.746	3288	2321	1.417	309	234
8	385840	40297	135860	114820	0.713	2989	2285	1.308	324	258
9	260440	30303	75848	81666	0.699	2074	1702	1.219	330	262
10	346070	28968	111600	102270	0.725	2587	2016	1.283	318	243
11	382810	31230	124100	119680	0.717	3001	2450	1.225	322	244
12	320320	28514	103310	93295	0.724	2408	1766	1.363	319	252
Mean					**0.72**			**1.30**	**321**	**251**
1σ					**0.01**			**0.06**	**6**	**10**
B 675B										
1	1496300	70057	336560	450810	0.742	10258	8801	1.166	311	210
2	1328000	43906	331640	396310	0.751	8519	7372	1.156	307	199
3	1293200	42453	296450	368110	0.759	8010	6832	1.172	303	193
4	1904100	90415	477410	524640	0.756	11914	10320	1.155	305	194
5	1225800	60965	326580	322030	0.762	7616	6358	1.198	302	193
6	1457600	66440	386520	357690	0.775	8763	7117	1.231	296	184
7	1348500	129600	321870	376070	0.727	7895	6449	1.224	317	233
8	606120	87674	197970	186630	0.688	3415	2618	1.304	335	284
9	625550	97106	215870	212580	0.669	3556	2749	1.293	343	304
10	782380	89497	239780	230850	0.709	4595	3158	1.455	325	276
11	847190	100120	281170	269320	0.696	4785	3679	1.301	331	275
12	564290	34778	121040	148090	0.755	3591	2509	1.432	305	226
Mean					**0.73**			**1.26**	**315**	**231**
1σ					**0.03**			**0.10**	**15**	**43**
B 677										
1	277130	26869	27663	108280	0.672	3402	2045	1.664	337	277
2	132570	11019	12699	53214	0.674	1521	994	1.530	335	278
3	344200	48688	44518	107440	0.688	4202	2330	1.803	334	273
4	133650	13839	8735	50508	0.675	1835	902	2.035	329	269
5	116690	12174	4820	45820	0.668	1512	858	1.762	335	276
6	79051	9450	4868	26970	0.685	1084	519	2.088	334	274
7	246260	32804	24097	91087	0.665	2454	1659	1.479	324	243
8	1168900	101640	358240	542680	0.645	7278	6605	1.102	316	249
9	210340	24602	12468	83236	0.661	2675	1534	1.743	326	269
10	303770	40693	44515	118410	0.656	3405	2092	1.628	341	285
11	128920	16772	13280	44022	0.680	1330	842	1.579	332	274
12	329510	34570	28413	122850	0.677	3970	2221	1.788	333	277
Mean					**0.67**			**1.68**	**343**	**329**
1σ					**0.01**			**0.26**	**5**	**12**
B 678B										
1	221130	13806		129030	0.608	3576	2308	1.549	311	210
2	134500	11114		95673	0.557	2385	1849	1.290	307	199
3	128880	8987		67216	0.628	2094	1171	1.789	303	193
4	173370	11871		110040	0.587	2935	2023	1.450	305	194
5	135090	6260		73761	0.628	2194	1222	1.796	302	193

Spot	Peak Area				Peak Height		T1	T2	Spot	Peak Area
	D1	D2	D3	G	R2	D1	G	R1		D1
6	157030	7771		89001	0.619	2481	1368	1.813	296	184
7	111020	6468		62299	0.618	1853	1096	1.690	317	233
8	202020	12416		127650	0.591	3335	2313	1.442	335	284
9	71500	4551		37446	0.630	1185	673	1.760	343	304
10	157070	6241		92569	0.614	2527	1589	1.591	325	276
11	113070	5472		61437	0.628	1825	1019	1.791	331	275
12	61707	3633		37131	0.602	1055	678	1.556	305	226
Mean					**0.61**			**1.63**	**370**	**394**
1σ					**0.02**			**0.17**	**10**	**12**
B 680										
1	83001	5967		95118	0.451	1404	2193	0.640	440	429
2	35809	3021		41218	0.447	588	970	0.606	442	425
3	80875	6550		96647	0.439	1327	2408	0.551	445	421
4	45915	2889		52733	0.452	778	1138	0.684	440	437
5	46256	2945		67457	0.397	907	1691	0.536	465	463
6	153970	17146		166440	0.456	1871	2901	0.645	438	424
7	79106	7185		108440	0.406	1395	2716	0.514	460	447
8	75109	7892		66038	0.504	1190	1476	0.806	417	406
9	55985	5121		57157	0.473	944	1376	0.686	430	414
10	55380	4609		64679	0.444	992	1531	0.648	443	437
11	75268	8781		91428	0.429	1302	2391	0.545	450	430
12	32913	3429		43875	0.410	584	1035	0.564	458	455
Mean					**0.44**			**0.62**	**444**	**432**
1σ					**0.03**			**0.08**	**13**	**17**

APPENDIX K

ϵND ANALYTICAL PROCEDURE

Metapelite samples were trimmed using a circular rock saw to remove all weathered surfaces. Samples which had pervasive weathering, veining or alteration were discarded. Once rocks were trimmed, any surfaces with metallic deposits from the circular saw were sanded until the deposits were removed. Samples were then crushed to 7 mm in a jaw crusher with Ni-based alloy plates. Forty mg of each whole rock sample were powdered and dissolved in a 3:1 concentrated HF/HNO_3 mixture at 150 °C within ©Teflon BOLA bombs for eight days. A few drops of $HClO_4$ were added before evaporation to dryness. Samples were then dissolved in 6 mL of 6 N HCl and evaporated to dryness to remove the last $HClO_4$ condensates and then dissolved again in 4 mL of 6 N HCl. Bombs were left in the oven for 1 day and evaporated again to dryness in a Teflon beaker. Details of the above sample preparation are as described in Luais et al. (2009). Residues were redissolved in 0.5 cc of 2.5 N HCl in an AG50X12 resin. After elution of the major elements, Rb, Sr and the rare earth elements (REE) were collected and then loaded in a 0.5 cc of 0.16 N HCl for elution onto a HDEHP resin. Sm and Nd are eluted in 0.16 N and 0.5 N HCl, respectively. This technique is described in Luais et al. (1997). Sm and Nd were analyzed by thermal ionization mass spectrometry on a Finnigan MAT 262 at the Centre de Recherches Pétrographiques et Géochimiques, Nancy, France.